

LUDWIG-MAXIMILIANS-UNIVERSITÄT  
MÜNCHEN

FAKULTÄT FÜR PHYSIK

**Thermal Non-Equilibria Promote  
Prebiotic DNA and RNA  
Polymerization**

DISSERTATION

Christina Felicitas DIRSCHERL

München 2023





LUDWIG-MAXIMILIANS-UNIVERSITÄT  
MÜNCHEN

FAKULTÄT FÜR PHYSIK

**Thermal Non-Equilibria Promote  
Prebiotic DNA and RNA  
Polymerization**

DISSERTATION

zur Erlangung des Grades  
Doktor der Naturwissenschaften (Dr. rer. nat.)

an der Fakultät für Physik  
der Ludwig-Maximilians-Universität  
München

vorgelegt von  
**Christina Felicitas DIRSCHERL**  
aus München

München, den 18.10.2022



Für meinen Bruder Markus Dirscherl  
1968 - 2016

*“¡Mañana otro día!”*



Erstgutachter: Prof. Dr. Dieter Braun  
Zweitgutachter: Prof. Dr. Hannes Mutschler

Eingereicht am: 18.10.2022  
Tag der mündlichen Prüfung: 30.01.2023



# Zusammenfassung

Das Leben basiert auf den Informationspolymeren DNA und RNA. Für ihre Polymerisation sind hohe Konzentrationen von initialen Monomerbausteinen erforderlich. Bevor es auf der frühen Erde zur Kompartimentierung kam, litt die präbiotische de novo Strangbildung von Nukleinsäuren unter der Verdünnung ihrer Edukte und Produkte. In dieser Doktorarbeit zeige ich, dass die allgegenwärtigen Nicht-Gleichgewichtsbedingungen in erhitzten Unterwasser-Gesteinsspalten auf der frühen Erde ein natürliches Habitat für eine erhöhte RNA- und DNA-Polymerisation gebildet haben können. Diese Studie zeigt, wie die Ausbeute von ansonsten ineffizienten primordialen Polymerisationsreaktionen durch ein physikalisches Nicht-Gleichgewicht, das durch thermische Gradienten angetrieben wird, erhöht wird.

Wärmeströme durch dünne Gesteinsrisse akkumulieren die monomeren Bausteine von DNA und RNA, was deren Polymerisation fördert. Auch bleiben die entstehenden Polymere bleiben über lange Zeiten im Inneren der Pore lokalisiert und vor Diffusion geschützt. Eingeschlossene Gasblasen können zusätzlich mikroskopische Nass-Trocken-Zyklen auslösen und eine trockene Polymerisationsreaktion in einer wasserhaltigen Umwelt ermöglichen. In einem geschlossenen System wurde nach 24 Stunden eine 10-fache Aufkonzentration von Nukleotiden am Boden des im Labor nachgebauten Risses gefunden, mit einer  $10^4$ -fachen relativen Akkumulation für die gewählte 40 mm hohe Pore. Eine bis zu 25-fach erhöhte Polymerisation von aminoimidazolisierten DNA-Nukleotiden und 2',3'-zyklischen RNA-Nukleotiden konnte nachgewiesen werden. Es ist bekannt, dass die Aktivität dieser Substrate unter normalen, isothermen Bedingungen im Bulk sehr begrenzt ist. Darüber hinaus zeigte die gemeinsame Polymerisation von 2',3'-cGMP und 2',3'-cCMP in der thermischen Falle eine erhöhte Heterogenität in der Sequenzzusammensetzung im Vergleich zur isothermen Trocknung, wodurch der kodierte Sequenzraum vergrößert wird. Finite-Elemente-Simulationen auf langen Zeitskalen zeigten, wie offene Poren mit kontinuierlicher Anreicherung von Reagenzien eine aktive Polymerisationsreaktion über Jahre hinweg beherbergen können, während das Entweichen der Oligonukleotide aus dem Riss vernachlässigbar war.

Dieses einfache physikalische Nichtgleichgewichtshabitat einer geheizte, wassergefüllten Gesteinspore schafft ein aktives, zellähnliches Kompartiment, das Nukleotide für die Polymerisation akkumuliert und RNA- und DNA-Stränge zurückbehält, wodurch eine präzelluläre Nichtgleichgewichtsumgebung für die ersten Schritte der molekularen Evolution entsteht.



# Abstract

Life is based on informational polymers such as DNA or RNA. For their polymerization, high concentrations of monomer building blocks are required. Before compartmentalization occurred on early Earth, prebiotic de novo strand formation of nucleic acids suffered from dilution of reagents and products. In this doctoral thesis, I show that the ubiquitous non-equilibrium conditions within heated underwater rock cracks on early Earth could have formed a natural habitat for nurturing RNA and DNA polymerization. This study demonstrates how the yield of otherwise inefficient primordial polymerization reactions is enhanced by a physical non-equilibrium triggered by thermal gradients.

Heat fluxes across a thin rock crack accumulate the monomeric building blocks of DNA and RNA which enhances their polymerization. Also the resulting polymers are localized inside the pore over long times and protected against diffusion. Enclosed gas bubbles can additionally trigger micro-scale wet-dry cycles and enable dry-based reaction. In a closed system, I found nucleotides concentrate 10-fold at the bottom of the lab-built crack after 24 hours with a  $10^4$ -fold relative accumulation for the chosen 40 mm high crack. I found enhanced polymerization from aminoimidazolized DNA nucleotides and 2',3'-cyclic RNA nucleotides, up to 25-fold. The activity of these substrates is known to be very limited under isothermal bulk conditions. Moreover, co-polymerization of 2',3'-cGMP and 2',3'-cCMP in the thermal trap showed an increased heterogeneity in sequence composition compared to isothermal drying, enlarging the encoded sequence space. Finite element simulations on long time-scales showed how open pores with continuous collection of reagents can accommodate an active polymerization reaction over years while the escape of the nucleotides from the crack is negligible.

This simple physical non-equilibrium habitat of a heated, water-filled rock pore creates an active, cell-like compartment that accumulates nucleotides for polymerization and traps RNA strands, providing a pre-cellular non-equilibrium setting for the first steps of molecular evolution.



# Contents

<b>1</b>	<b>Motivation</b>	<b>7</b>
<b>2</b>	<b>Scientific Approach</b>	<b>8</b>
2.1	Molecule Accumulation by Thermophoresis . . . . .	10
2.2	Gas-Water-Interfaces in a Thermal Gradient . . . . .	10
2.3	Implementation via a Thermogravitational Trap . . . . .	11
2.4	De Novo Strand Formation from DNA and RNA Monomers . . . . .	11
2.4.1	Aminoimidazolized DNA Monomers . . . . .	12
2.4.2	2',3'-Cyclic RNA Monomers . . . . .	12
2.5	Finite Element Simulations of Polymerization in Thermal Non-Equilibria . .	13
<b>3</b>	<b>Results and Discussion</b>	<b>15</b>
3.1	Monomer Accumulation in a Thermal Trap . . . . .	15
3.2	AImpdA Monomer Polymerization in a Thermogravitational Trap . . . . .	19
3.3	2',3'-Cyclic Monomer Polymerization in a Bubble Trap . . . . .	23
3.4	Longtime Extrapolation of De Novo Polymerization in Thermal Non-Equilibria	27
<b>4</b>	<b>Conclusion</b>	<b>30</b>
<b>5</b>	<b>Methods and Materials</b>	<b>31</b>
5.1	Trap Building and Setup . . . . .	31
5.2	Sample Preparation . . . . .	33
5.3	Measurements and Analysis . . . . .	35
5.3.1	HPLC-MS Measurements . . . . .	35
5.3.2	Masses . . . . .	37
5.3.3	Peak Analysis and Product Quantification . . . . .	40
5.4	Chemistry . . . . .	48
5.4.1	dAMP Accumulation . . . . .	48
5.4.2	AImpdA DNA Monomers . . . . .	48
5.4.3	2',3'-Cyclic RNA Monomers . . . . .	49
	<b>Bibliography</b>	<b>51</b>
	<b>Acknowledgements</b>	<b>57</b>
	<b>Appendix</b>	<b>59</b>
1	Data Repository . . . . .	59
2	Associated First Author Publication . . . . .	63
3	Associated Publications . . . . .	63



# Chapter 1

## Motivation

The Origins of Life are a riddle to those who emerged from this process, yet the search for it goes as far back as human consciousness. Due to the lack of direct evidence that we can dig out from the earth crust, read up in manuals or extract from our own memory on how self-replicating, thermodynamically open and darwinianly evolving matter arose [1], the scientific community dedicated to the Origins of Life takes a different approach: we use the accessible evidence on the conditions on early Earth, reconstruct prebiotically plausible scenarios in our laboratories and try to show how within these boundaries necessary building blocks for modern life could have emerged and how their assembly process to more complex structures could have taken place.

This scientific approach is used in the present doctoral thesis and is in my opinion a valuable one, taken into account how much time nature had and how vast its playground was on behalf of the different physical conditions that were present on early Earth - “finetuning for free” so to say and multiplexing at its best.

Life uses a multitude of complex structures and systems and unites them to an intricate, highly interlocked meta-process. The path of understanding and retracing a complex question has to be taken in small steps and this work is devoted to the question of how elongated DNA and RNA strands could have emerged from their single building blocks.

DNA and RNA in modern life are the basis of a living cell’s replication and sustaining process and are constructed from four different building blocks: cytosine-, guanine-, adenine- and thymine-/uracil-nucleotides. Billion of times repeated, they encode all necessary information for the continuation of a cell’s life and its complex superstructure.

Prebiotically plausible chemical mechanisms have been found that enable de novo strand formation by polymerizing nucleic acid monomers to longer strands starting from their single building blocks [2, 3, 4]. But to yield products, they require high concentrations of starting material, something that was not readily available in a dilute primordial ocean [5]. Also, chemical systems naturally relax into their thermodynamic equilibrium that then erases all reached complexity. So, which environmental conditions on early Earth could have allowed RNA and DNA to evolve into long informational macromolecules and could have sustained a rich pool of these complex structures from where other mechanisms could have taken over for further steps towards the Origins of Life? This is the question that the present PhD thesis seeks to suggest an answer for.

## Chapter 2

# Scientific Approach

What are the given conditions at the time point on early Earth where we allocate our research in? We only assume the most abundant geologic realities: water, gases and volcanoes with the porous rock material they produce and heat fluxes across them (see Fig. 2.1a and b). We also assume that we are sitting at a time point on Earth's history when the single building blocks of DNA and RNA, called monomers or nucleotides, are already available. [6, 7, 8, 9] showed how they could have emerged on a primordial Earth and its restricted chemical possibilities. Equally prebiotically feasible are the de novo strand formation chemistries that are used for this work: preactivated monomers by imidazolization ([10, 11, 12, 13], see Fig. 2.4) or 2',3'-cyclization ([4, 14, 15], see Fig. 2.5) trigger the oligomerization of short RNA or DNA strands (see Chapter 2.4).

On early Earth, however, it is far from obvious where high enough initial concentrations of monomers could have come from to start and sustain a polymerization reaction [13, p.58] and how the first oligomers could have been kept from being instantly diluted after their formation. This issue is commonly called the concentration problem [16, 17] and runs through many Origins of Life processes that require a certain threshold concentration. Other examples for that are the lipid vesicle formation [18] or the salt concentration for ribozymes starting to function [19]. In order to obtain a persistent pool of informational macromolecules, their formation from building blocks must outpace their destruction and their removal by diffusion.

Heat fluxes across water-filled rock cracks and pores are considered a ubiquitous scenario on early Earth [20, 21]. The non-equilibrium forces caused by thermal gradients generate convection and thermophoresis inside the water-filled pore (see Fig. 2.1c and Chapter 2.1) inducing strong accumulation of dissolved molecules towards the pore bottom for a range of different geometries and thermal gradients [18, 22, 23, 24, 25, 26]. In laboratory conditions it was previously shown that mimics of such liquid-filled pores in thermal gradients (see Chapter 2.3) act as thermogravitational accumulation traps for DNA polymers [5]. In this work, I show that such pores actively collect and concentrate the monomeric RNA and DNA starting material (see Chapter 3.1) despite its high diffusivity ( $0.75 \cdot 10^5 \text{ cm}^2 \text{ s}^{-1}$ , [27]). In comparison, vesicles lack a directed accumulation process to transport molecules towards the inside and coacervates in published cases trade localization of molecules for a similarly reduced reactivity [28, 29].

The thermal non-equilibrium systems described in this study provide the unique possibility to actively enhance the concentration of the monomeric starting material without restricting its reactivity under conditions that also boost its polymerization. Moreover, the polymerized products are retained at the bottom of the pore (see Chapter 3.2) while fresh monomers are supplied from the top of the pore without diluting the reaction at the bottom. This is in contrast to the usual exchange of volume to supply a reaction with fresh reactants where

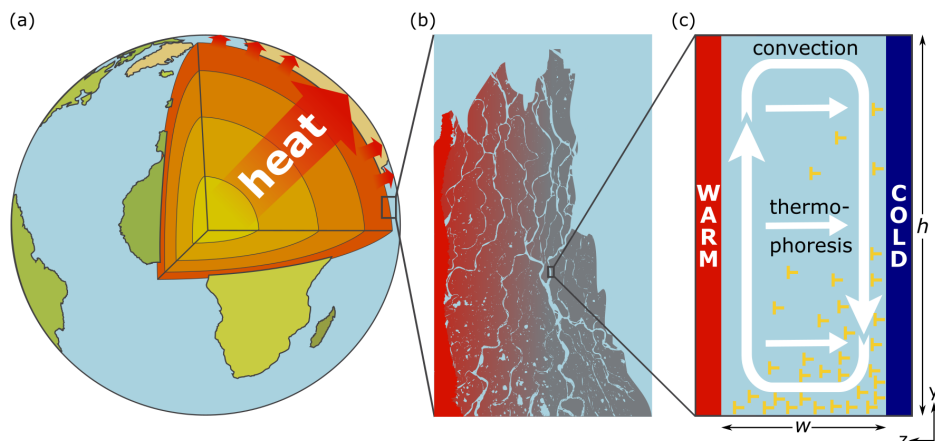


**Figure 2.1: Sketch of the heat dissipation on early Earth.** (a) The hot Earth core releases heat towards the Earth crust [31]. (b) Heat fluxes across water-filled rock cracks on early Earth are for example found in subsea hydrothermal vents [32]. (c) Molecules are accumulated by the superposition of heat-flow driven convection of water (light blue) and thermophoresis of the dissolved molecules (yellow) in a water-filled pore subjected to a thermal gradient. The accumulation of preactivated monomers at the bottom of the pore with height  $h$  and width  $w$  enables an improved polymerization by the enhanced concentration and retains the products over long times.

feeding is accompanied by dilution of the polymerization products [30]. In the chosen non-equilibrium setting, however, the thermophoretic accumulation of the molecule decouples the feeding process with monomers from an inflow of the solvent water.

Liquid filled rock pores naturally can contain gas bubbles, for example by incomplete filling of the volume or due to degassing. When a gas bubble is trapped inside a heated pore, convection and thermophoresis are joined by microscale wet-dry cycles at the air-water interface [33, 34] (see Fig. 2.2 and Chapter 2.2). Macroscopic wet-dry cycles, like for example evaporative lakes [35, 36, 37], lose water through evaporation but are rehydrated with buffers in forms of rivers or splashes from larger reservoirs. As seen also on modern Earth [38], this imbalance leads to runaway salt concentrations and large pH shifts [39]. In a heated pore with a bubble, however, microscale wet-dry cycles happen in a closed system: water evaporates on the warm side and re-enters as dew droplets at the cold side. This prevents a global increase in salt concentration or a shift in pH. In this study, I found that a bubble at the bottom of a thermogravitational trap drove polymerization reactions that normally require dry conditions. The yield of the oligomerization was enhanced by both, the accumulation properties of the heated pore and the constant wet-dry cycling (see Chapters 3.3 and 3.4), while the pH and salt conditions of the reaction were under control of the wet system.

In addition to my experimental research, I could rationalize the observations in detail by finite element simulations and extrapolate the study to long time-scales that are experimentally still inaccessible (see Chapter 3.4).

This study exploits the physical characteristics of thermogravitational traps to accelerate the de novo strand polymerization of RNA and DNA over their degradation. This work suggests a plausible setting on early Earth, in which prebiotic molecules could have become sufficiently concentrated and stayed reactive enough to trigger an efficient polymerization of nucleotides into longer sequences of increased complexity. Once created, thermophoresis would keep the formed polymers in place over prolonged periods of time. My experiments suggest that heat fluxes across narrow pores form this type of physical non-equilibrium and could have tipped the balance in favor for complexity.

The following sub-chapters describe the underlying theory of my research shortly, providing the basics for the findings of this study presented in Chapter 3. A more in-depth description of methods, materials and background can be found in Chapter 5 at the end of this thesis.

## 2.1 Molecule Accumulation by Thermophoresis

The thermal gradient across a water-filled pore induces two physical phenomena inside. The bulk solution undergoes a circular convection motion due to the heat-induced density differences within the liquid. Also, the dissolved molecules in the liquid experience thermophoresis, a drift along the temperature gradient which moves the charged DNA/RNA molecules towards the colder side of the pore [40, 41]. The superposition of these two effects leads to an exponential concentration increase of molecules towards the bottom cold corner of the pore (see Fig. 2.1c and Movie M5). The resulting accumulation of molecules is balanced by diffusion, seeking a homogeneous concentration. In the steady state the concentration distribution inside the pore can be described by the following equation ([23, 42, 43], derivation see Chapter 2.5):

$$\frac{c_{bot}(h)}{c_{top}} \propto \exp(S_T \cdot r \cdot \Delta T) \quad \text{with } r = h/w, \quad (2.1)$$

where  $c_{bot}(h)$  is the concentration at the bottom of a pore with height  $h$  and width  $w$ ,  $S_T = D_T/D$  the Soret coefficient,  $D_T$  the thermodiffusion coefficient,  $D$  the ordinary diffusion coefficient,  $\Delta T$  the applied temperature difference and  $r = h/w$  the aspect ratio (height over width) of the pore.

## 2.2 Gas-Water-Interfaces in a Thermal Gradient

The evaporation of a droplet on a surface leads to the so called “coffee-ring-effect” where the combination of capillary forces and surface tension accumulates the molecules, which are dissolved in the droplet, at its rim [44, 45]. After drying, a ring of concentrated material is left on the surface. When a bubble is submerged in water heated by a temperature gradient, the same effect is driven continuously [33]: molecules accumulate at the air-water-interface and are deposited in layers on the hot side (see Fig. 2.2).

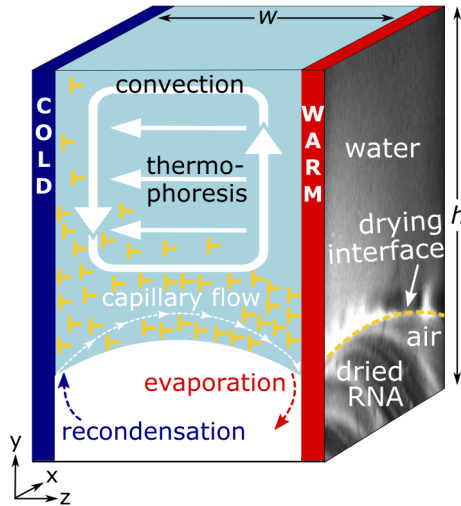


**Figure 2.2: Scheme of a thermophoretic bubble trap.** Monomers polymerize and accumulate in a thermal gradient across a water-filled pore of width  $w$  and height  $h$  with a gas bubble at its bottom. Water evaporates at the warm side, nucleotides dry out and are deposited there in layers until they are washed back into the bulk by re-condensing dew droplets and a moving gas-water-interface.

They are rehydrated by growing water droplets condensing at the cold side. When these drops re-enter the main fluid phase the location of the water-air interface is shifted and re-

dissolves the dried molecules at the cold side. A new cycle of drying and rehydration can begin (see Movie M6).

In this dissertation the aim was to combine the accumulation of a thermogravitational trap with the continuous, accumulative wet-dry-cycling of a heated air-water-interface. For this, a gas bubble was introduced at the bottom of the pore where the thermogravitational accumulation takes place and convection and thermophoresis were now joined by evaporation at the hot side and recondensation at the cold side of the pore.

## 2.3 Implementation via a Thermogravitational Trap

To implement the described non-equilibrium setting, the microfluidic pore structure was cut out from Teflon foil of  $170\ \mu\text{m}$  width and sandwiched between two thermally conducting sapphire plates. In order to create a temperature gradient, cooling on one side and Ohmic heating on the other side was applied (see Chapter 5.1). The samples were inserted through holes in the back-sapphire of the chamber. The accumulation behavior in the pore was visualized in-situ by fluorescent microscopy of low concentrations of Cy5 molecules which co-accumulated with the DNA nucleotides (see Fig. 2.3b and Movie M5).

To understand the accumulation processes in more detail, the pore content was extracted at the end of the experiment in individual stripes along its height by quick freezing to  $-80\ ^\circ\text{C}$ , cutting and subsequent extraction in separate volume sections (details of the freeze extraction procedure see Chapter 5.2 and Movie M4). The local concentrations of molecules in each trap section were then measured by HPLC-MS (see Chapter 5.3).

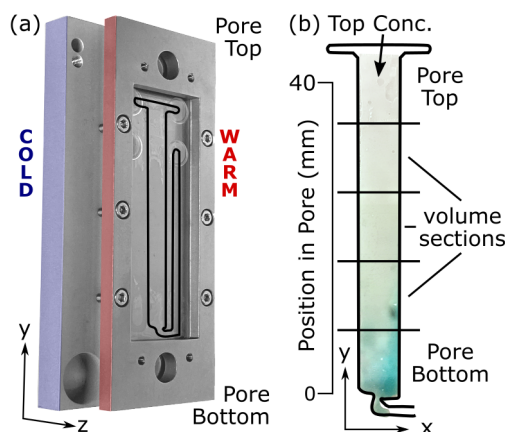


**Figure 2.3: Experimental implementation of a thermogravitational trap and its accumulation behaviour.** (a) Photo of the microfluidic assembly. The prebiotic pore is mimicked by a Teflon foil cutout ( $170\ \mu\text{m} \times 7\ \text{mm} \times 40\ \text{mm}$ ) enclosed between two sapphire plates. These are cooled by a waterbath and heated by Ohmic heaters (see Chapter 5.1) and held in place between a steel frame screwed onto an aluminium backplate. The pore can contain a total liquid volume of  $62\ \mu\text{L}$ . (b) The effect of accumulation is visualized by the exemplary accumulation of the dye-molecule Cy5 for 24 h in a thermal gradient of  $\Delta T = 22\ ^\circ\text{C}$  across the chamber. Horizontal lines indicate the volume partitions extracted for analysis after accumulation and fast freezing, the black border shows the outline of the pore.

## 2.4 De Novo Strand Formation from DNA and RNA Monomers

The RNA-World hypothesis [46] states that at the origins of life, RNA molecules might have sufficed to catalyse their own synthesis and hence form a self-replicating network. However the question remains how to get to RNA of sufficient lengths in order to have enzymatic properties which are necessary to assemble themselves from a nucleotide soup? The formation of a long polymer from its single building blocks gets more improbable with increasing length.

The lead-idea of this work is that for RNA polymers on early Earth the aforementioned naturally existing thermogravitational traps could have introduced the necessary bias towards “length” as a measure for complexity and hence as the door-opener for the polymers to gain secondary properties. This preference of the traps for forming and retaining longer strands is initiated and held upright by the temperature gradient which keeps pumping energy into the physical non-equilibrium system. This will be studied for the two following prebiotically relevant polymerization chemistries:

### 2.4.1 Aminoimidazolized DNA Monomers

Orgel [10], Ferris [11], McGown [12] and others [13, chapter 7.2] have shown that the preactivation of monomers with imidazoles triggers the oligomerization of short RNA molecules. Other studies [7, 8, 9] have shown the formation of deoxyribonucleotide monomers under relevant prebiotic conditions in water and have suggested that DNA could have evolved much earlier than assumed. Here, an imidazole activation is used on the more stable DNA nucleotides to trigger and enhance DNA polymerization (see Fig. 2.4) in thermogravitational pores, exploring how longer DNA oligomers could have formed in prebiotic settings.

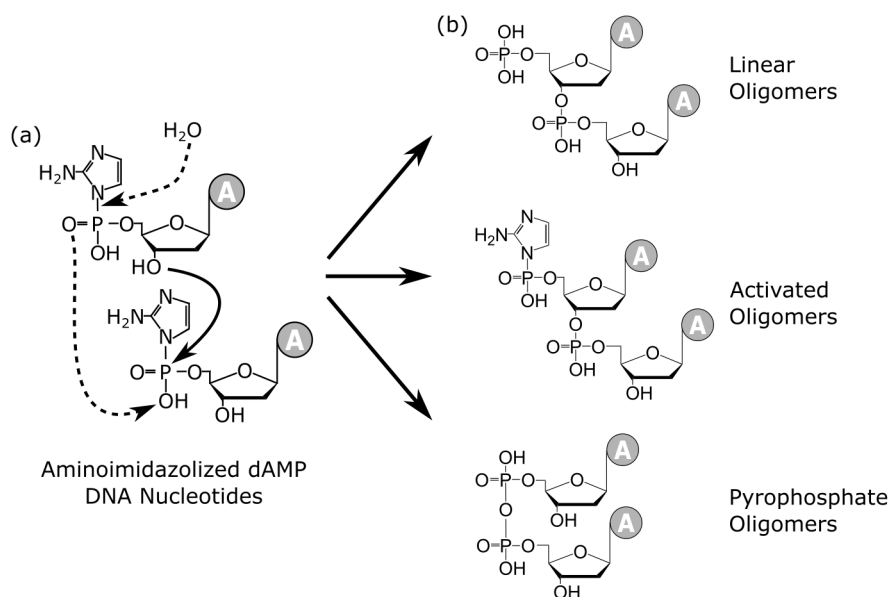


**Figure 2.4: AImpdA monomer polymerization.** (a) Reaction paths of aminoimidazolized dAMP monomers. (b) Polymerization from AImpdA produces linear, activated and pyrophosphate oligomers, analyzed in my experiments by HPLC and ESI-TOF mass spectrometry.

### 2.4.2 2',3'-Cyclic RNA Monomers

The start of a polymerization reaction from 2',3'-cyclic nucleotides is especially attractive since cyclized products are a competing by-product of each polycondensation reaction [13, p.58]. [47] shows that 2',3'-cyclic nucleosides could have formed under prebiotic conditions. Best polymerization yields were found for dry-state polymerization reactions. RNA polymerization from 2',3'-cyclic nucleotides was studied in the past for AMP with the help of various catalysts [4, 15]. Only recently, it was found that 2',3'-cGMP itself can trigger polymerization in the dry at elevated pH without ions or catalysts [14], then leading the way to co-polymerization with other bases.

In this study, I used 2',3'-cyclic GMP and -CMP nucleotides [4, 14, 15], basing the experimental protocols on previous experiments using 3',5'-cyclic GMP [48, 49]. In an alkaline environment a trans-phosphoesterification leads to the formation of a new phosphodiester

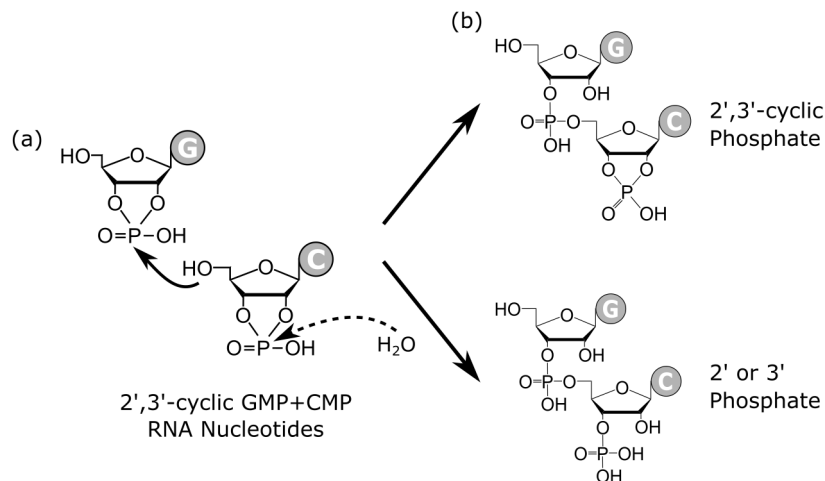


**Figure 2.5: 2',3'-cGMP/CMP monomer polymerization.** (a) Reaction paths of 2',3'-cyclic-CMP and -GMP RNA monomers. (b) The polymerization from 2',3'-cyclic RNA monomers yields oligomers that are still activated with a 2',3'-cyclic phosphate ring or have inactivated endings with a phosphate at the 2' or 3' position of the sugar ring.

bond with another mononucleotide. Possibly aided by the G-base in a yet unknown dry stacking arrangement, the 5'-hydroxyl attacks the 2',3'-cyclic phosphate and leads to the opening of the phosphate ring either at the 2'- or the 3'-oxygen of the sugar. The product is an oligomer with 2',5'- or 3',5'-phosphodiester bonds and either an open (3'P or 2'P) or a closed (2',3'-cP) phosphate ring (Figure 2.5).

One could argue that dry conditions are alien to modern living systems, which need water-based environments to replicate and evolve the information stored in their DNA. The conditions in this study couple water-based accumulation by thermophoresis to the wet-dry cycles at a gas bubble in a thermal pore. This enables the molecules to shuttle in a short time between the wet and the dry environment, allowing reactions in both media in parallel [33, 34]. It enables to keep the dry-polymerization reaction running inside a wet environment while also increasing its polymerization efficiency.

## 2.5 Finite Element Simulations of Polymerization in Thermal Non-Equilibria

The theoretical simulation presented in the following chapters are 2- or 3-dimensional finite element simulations performed with COMSOL Multiphysics v5.4. There I simulated the interplay of the heat transfer in the chamber, the convection of the bulk liquid, the transport of the diluted species and the polymerization kinetics and was able to model the experimental results. The full chamber model used for the experiments was recreated in a 3D CAD software and imported into the finite element software (see Figure 2.6a). Thermal conductivities were taken from COMSOL's internal database or from the product data sheets of the materials used and are  $k_{H_2O} = 0.62 \text{ W m}^{-1} \text{ K}^{-1}$  for water,  $k_{Steel} = 44.5 \text{ W m}^{-1} \text{ K}^{-1}$  for the steel frames,  $k_{Alu} = 237 \text{ W m}^{-1} \text{ K}^{-1}$  for the aluminium elements,  $k_{Sapphire} = 35 \text{ W m}^{-1} \text{ K}^{-1}$  for the sapphire elements and  $k_{FEP} = 0.2 \text{ W m}^{-1} \text{ K}^{-1}$  the FEP-Teflon foil. Since the space around the actual water-filled pocket is fully covered by teflon, an insulating thermal boundary condition for the heat flow through the outer surfaces of the COMSOL model was assumed, i.e.  $q_{extSurface} = 0$ . The heat conduction was then calculated according to the heat-flow-equation

$$\rho c_p \left( \frac{\partial T}{\partial t} + \mathbf{u} \nabla T \right) + \nabla (k \nabla T) = \dot{q} \quad (2.2)$$

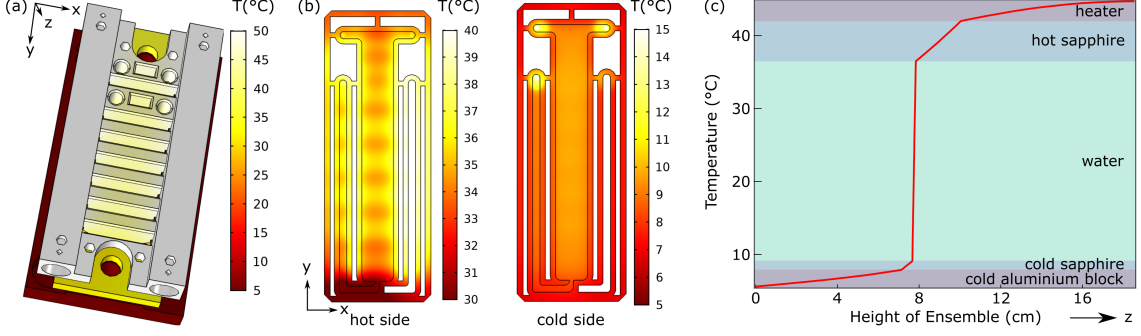


**Figure 2.6: Simulated geometric model and heat conduction simulation.** (a) The full three-dimensional model with color coding for the calculated temperatures for exemplarily applied temperatures of  $T_{cold} = 5^\circ\text{C}$  and  $T_{hot} = 50^\circ\text{C}$ . (b) For the experiments it was important that the temperature distribution in the  $x$ - $y$ -plane of the chamber was as uniform as possible. Along the  $z$ -axis, i.e. in the direction of the heat flow vertically through the thin water layer, the temperature drop should be as linear as possible. Additionally, optical observation of the sample in the heat flow cell was needed. This was achieved by the insertion of a relatively thick sapphire (2 mm) on the hot chamber side, which compensates for thermal unevenness due to the viewing windows in the slit aluminum heater (see (a)). The two-dimensional temperature plot in the  $x$ - $y$ -plane depicts the calculated temperature distribution on the  $x$ - $y$  surface on the hot and the cold side of the water-filled pore, showing that the temperature distribution is quite homogeneous in the  $x$ - $y$ -plane with maximum deviations of about  $2^\circ\text{C}$  on the hot side of the solution and less than  $0.5^\circ\text{C}$  on the cold side of the solution. (c) One-dimensional temperature plot along the  $z$ -axis of the whole model. Most of the temperature difference falls off across the  $170\ \mu\text{m}$  thick microfluidic chamber filled with aqueous solution (around 70% of the entire temperature drop,  $\sim \Delta T = 37^\circ\text{C}$ ).

and solved for the entire structure, where  $\rho$  is the density,  $c_p$  the specific heat capacity,  $k$  the thermal conductivity of the respective material,  $T$  the temperature,  $q$  the heat flow and  $\mathbf{u}$  the velocity vector of the solution in the chamber. In the stationary case and assuming a very slow fluid velocity  $\mathbf{u}$ , due to the small dimensions of the pore and the resulting strong laminarity of the liquid flows, equation (2.2) simplifies to

$$\nabla(k\nabla T) = \dot{q} \quad (2.3)$$

whose solution is shown in Figure 2.6.

The resulting temperature distribution within the fluid was then coupled into the Navier-Stokes equation via the temperature dependent density  $\rho(T)$  and viscosity  $\eta(T)$ :

$$\rho(T)(\mathbf{u}\nabla)\mathbf{u} = \nabla[-p + \eta(T)((\nabla\mathbf{u} + (\nabla\mathbf{u})^\dagger) - \frac{2}{3}\eta(T)(\nabla\mathbf{u})] - \mathbf{e}_y g \rho(T) \quad (2.4)$$

where  $\mathbf{u}$  is the velocity vector of the fluid,  $p$  is the local pressure,  $\mathbf{e}_y$  is the unit vector in  $y$ -direction (gravitation direction) and  $g$  is the gravitational acceleration. After setting a non-slip boundary condition at all surfaces, a complete numerical solution for  $\mathbf{u}$  could be found.

To determine the concentration of the dissolved molecules the pore, the numerical model was further extended by a drift-diffusion-component. This includes thermophoresis, i.e. the movement of the molecule along the temperature gradient, normal diffusion, which counteracts local concentration gradients as well as the coupling to the velocity field of the solution:

$$\nabla(-D\nabla c + (\mathbf{u} + S_T D\nabla T)c) = 0, \quad (2.5)$$

where  $D$  is the normal diffusion coefficient,  $c$  the local concentration and  $S_T$  the Soret coefficient of the molecules. The coupling of equation (2.5) to equations (2.3) and (2.4) is achieved by the temperature  $T$  and the velocity field  $\mathbf{u}$ . The solutions  $c(x, y, z, t)$  of equation (2.5) give the concentration simulation results (see eq. (2.1)). They themselves are coupled to one another via the rate equations of the polymerization kinetics.

## Chapter 3

# Results and Discussion

The line of argument I am going to pursue in in this doctoral work in order to evidence the scientific idea presented above is

- first, to show that and how much small molecules such as monomers are able to be accumulated by the primordial non-equilibrium setting,
- then, to proof the enhancement of a prebiotic wet DNA-polymerization scheme with one base (dA) by the thermogravitational accumulation of a thin pore subjected to a thermal gradient,
- after that, to widen the non-equilibrium setting so that it fosters and enhances a prebiotically plausible RNA-polymerization scheme with two complementary bases (G and C) which requires dry conditions, by the combination of thermogravitational accumulation and thermally driven wet-dry cycling at a bubble boundary, and to show that these conditions also facilitate the emergence of a larger sequence space of the formed strands,
- in the end, to extrapolate the findings to long timescales which are experimentally inaccessible but geologically determining.

I am going to follow this reasoning experimentally and at each step give a more general intuition about the findings by theoretical simulations.

### 3.1 Monomer Accumulation in a Thermal Trap

To tackle the problem of low concentration of the starting material for the polymerization reactions, already past studies have shown that an out-of-equilibrium hydrothermal pore can localize and concentrate many types of molecules, like lipids, ribozymes and ions [33, 19]. To show which amount of accumulation of the starting material for the polymerization was to be expected by the trap, the pore was filled with unactivated 2.5 mM, 20 mM or 300 mM dAMP DNA-mononucleotides in 100 mM MOPS buffer (filling procedure see Movie M1) and operated at a temperature gradient of  $\Delta T = 22^\circ\text{C}$ , with the hot temperature at  $30^\circ\text{C}$  and the cold temperature at  $8^\circ\text{C}$  at the front and back of the solution. The content of the pore was extracted after 24 h in individual stripes along its height by quick freezing, cutting and subsequent extraction in separate volume sections (see Figure 3.1a, details of the freeze-extraction procedure see Chapter 5.2). The local concentration of molecules in each section was then measured with HPLC-MS (see Chapter 5.3).

Figure 3.1b shows that after a runtime of 24 h an up to 10-fold absolute accumulation of dAMP DNA monomers was achieved at the bottom of the pore compared to the starting

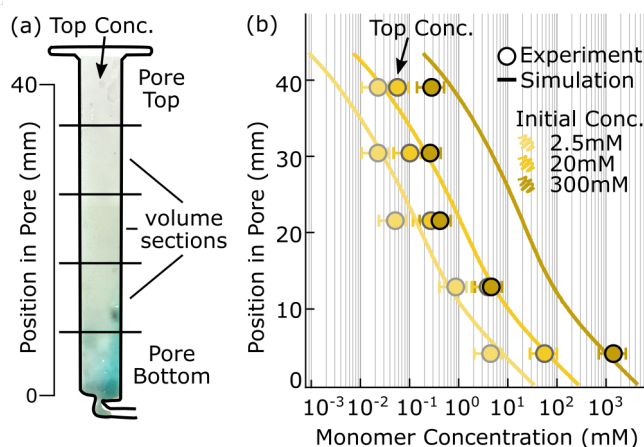


**Figure 3.1: A primordial non-equilibrium habitat accumulates nucleotides and promotes their polymerization.** (a) Photo of a trap after 24 h of thermophoretic accumulation (cold side  $8^{\circ}\text{C}$ , hot side  $30^{\circ}\text{C}$ , temperature gradient  $\Delta T = 22^{\circ}\text{C}$  across a  $170\ \mu\text{m}$  wide sapphire chamber), showing the exemplary accumulation of blue Cy5 dye molecules (see Movie M6). The horizontal black lines indicate the volume sections for freeze extraction, the black border shows the outline of the pore. (b) Nucleotides are accumulated and polymerized by the superposition of heat-flow driven convection and thermophoresis in a water-filled pore subjected to a thermal gradient. After 24 h, the concentration distribution of thermophoretically accumulated nucleotides spreads over four orders of magnitude along the pore height (circles). This accumulation is independent of the initial starting concentrations of 2.5, 20 or 300 mM dAMP and is confirmed by a finite element simulation of fluid flow and thermophoresis (solid lines). Error bars indicate a  $\pm 50\%$  error, taken from triplicates on representative experiments.

concentration. The top concentration depleted simultaneously, yielding an about  $10^4$ -fold relative accumulation. This effect persisted over three orders of magnitude of starting concentrations (light yellow, yellow, dark yellow) as expected from the general finding that thermophoretic properties do depend on the molecule concentration only in highly crowded conditions [40, 50].

For estimating the errors of the experiments shown in Figure 3.1b, the relative errors for all datapoints of the experiments in Figure 3.7, that were gained from the standard deviations of replication experiments, were averaged. This allowed us to get an estimate of a generalized error introduced by thermal pore experiments and measurements by HPLC/ESI-TOF. These errors in average amount to 47.5%, which made us assume an error of  $\pm 50\%$  for all datapoints in Fig. 3.1.

By a finite element simulation with COMSOL Multiphysics, I simulated the heat transfer, the convection, the diffusion and the thermophoresis of DNA nucleotides in a differentially heated chamber (see Chapter 2.5 for details). The simulation (solid lines) showed good agreement with the experimental accumulation behaviour of the DNA monomers in the thermal pore and confirmed the experimental observations (circles). RNA has very similar thermophoretic properties and is expected to behave very similarly [40, 51].

The parameters obtained by fitting the simulation to the experimental results are given in Table 3.1. The same parameter set optimizes the fit for all three different starting concentrations, showing the universality of the simulation. A time-lapse of the accumulations process of monomers in a simulated thermophoretic pore is visualized by Figure 3.2.

Heated rock pores on the volcanic, early Earth were ubiquitous in a wide range of shapes and sizes and were subjected to very different temperature conditions. To give an insight into how robust the accumulation behavior of nucleotides is in primordial pores, I mapped out the effect of different temperature gradients ( $\Delta T = 5 - 50^{\circ}\text{C}$ ) and different pore widths (between  $200\ \mu\text{m}$  and  $400\ \mu\text{m}$ ) in the simulation (see Fig. 3.3). Across this broad range of conditions, I observed stable accumulation of nucleotides, however differences in the time

Parameter	Value	Explanation
Pore Width	170 $\mu\text{m}$	width of pore
Pore Height	43.5 mm	height of pore
Tcold	8 $^{\circ}\text{C}$	temperature of cold side of pore
$\Delta T$	25 K	temperature gradient between hot and cold side of pore (fit-parameter)
n	0.2	fit-parameter for molecule properties
D	$643n^{-0.46} \mu\text{m}^2 \text{s}^{-1}$	formula for diffusion coefficient of molecules [5]
ST	$(5.3 + 5.7n^{0.73})10^{-3} \text{K}^{-1}$	formula for Soret coefficient of molecules [5]
A1L	2.5 mM	initial monomer concentration of 2.5 mM experiments
A1M	20 mM	initial monomer concentration of 20 mM experiments
A1H	300 mM	initial monomer concentration of 300 mM experiments

**Table 3.1: Simulation parameters for monomer accumulation in a thermogravitational pore.** The same parameter set could be used to model all three starting concentrations of the monomer accumulation experiments in a thermophoretic pore. The fit-parameter of  $\Delta T = 25 \text{ K}$  fits quite well with the measured  $\Delta T = 22 \text{ K}$ .

evolution of the accumulation occurred. My experimental settings were optimized for fast accumulation, accepting a rather steep thermal gradient. Even if heated with much more shallow thermal gradients, a similar but slower accumulation is expected [25, 26]. A thinner pore width delays the steady state but results in a higher final concentration at the bottom of the trap (see Fig. 3.3). The demonstrated geometrical versatility provides a wide range of possible rocky environments where temperature gradients could have helped in the concentration and dilution problem on early Earth. The diffusion and Soret coefficient values for theoretical monomers of  $D = 643 \mu\text{m}^2 \text{s}^{-1}$  and  $S_T = 0.001 \text{ K}^{-1}$  were taken from [4]. The Comsol files of the simulations are provided in Dataset D5.

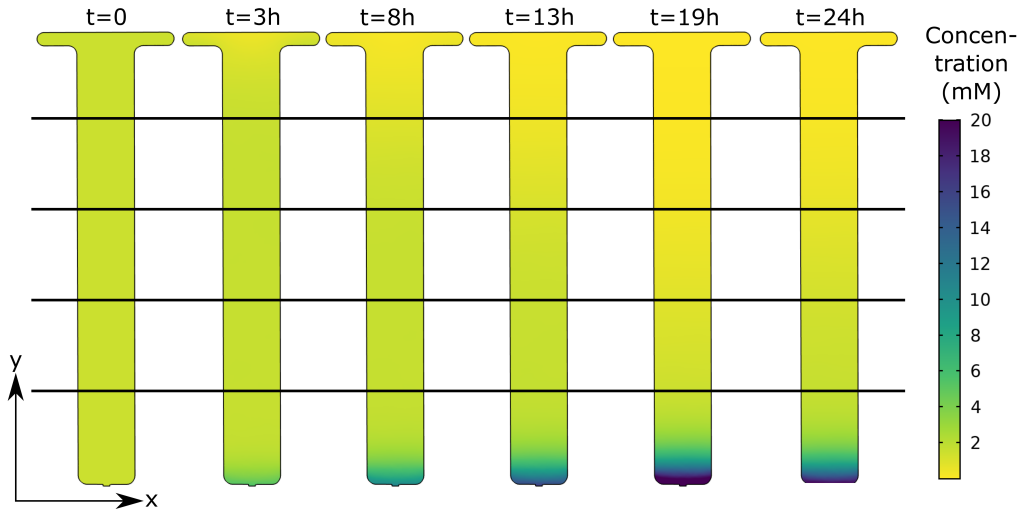


**Figure 3.2: Coupled solution of heat conduction, Navier-Stokes flow and thermal drift diffusion for the dAMP monomer accumulation.** Simulated concentration distribution of dAMP monomers (1.5 mM starting concentration) in the x-y-plane of a pore at different timepoints of the accumulation process with  $\Delta T = 22 \text{ }^{\circ}\text{C}$  and a pore width of  $w = 170 \mu\text{m}$ .

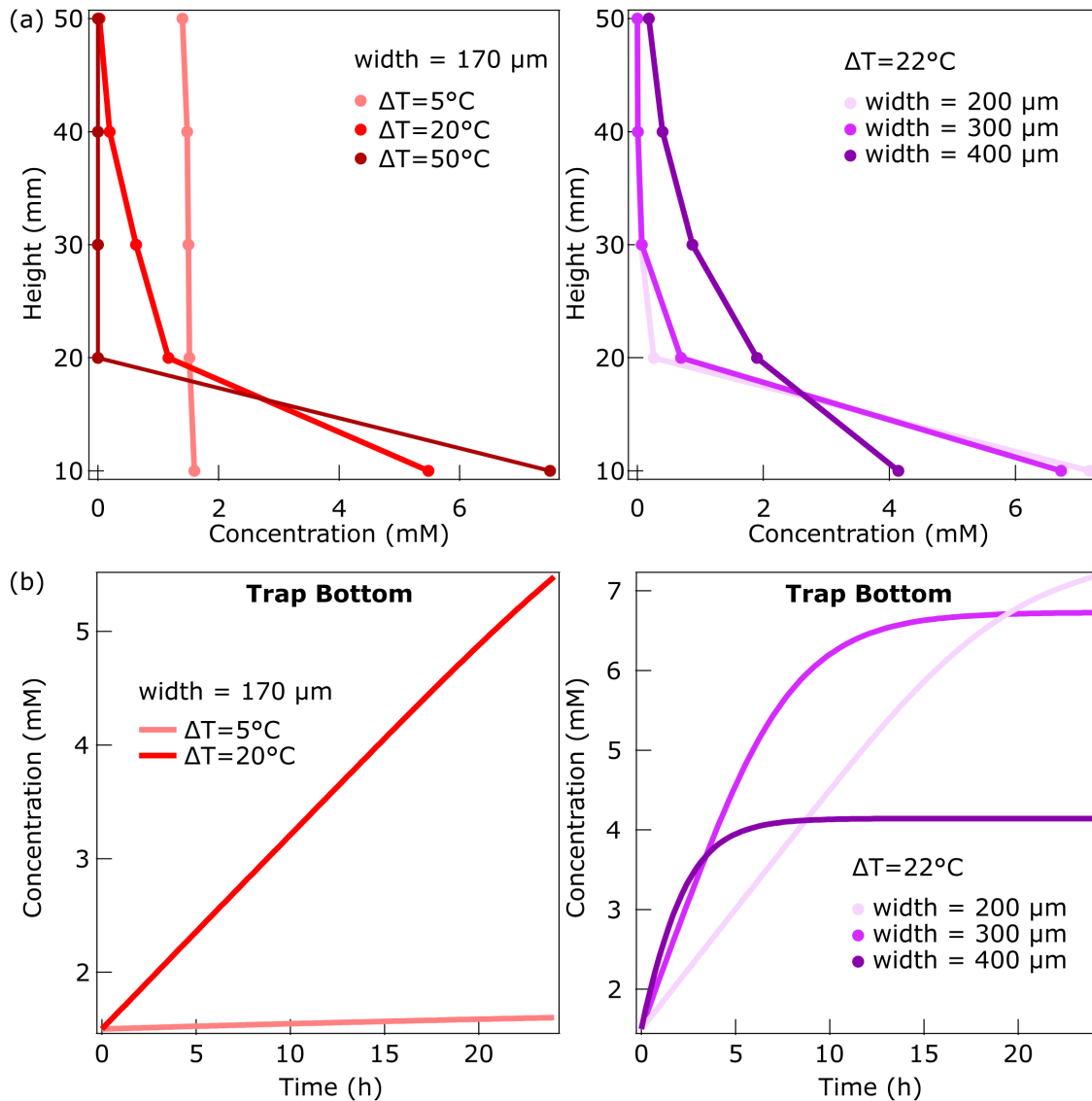


**Figure 3.3: Accumulation simulation for dAMP monomer accumulation for different temperature and width parameters.** (a) Concentration distribution of integrated over the single volume sections along the height of a simulated pore filled with 1.5 mM dAMP monomers after 24 h with  $w = 170 \mu\text{m}$  and  $\Delta T = 5^\circ\text{C}$  (light red),  $\Delta T = 20^\circ\text{C}$  (red) and  $\Delta T = 50^\circ\text{C}$  (dark red) as well as with  $\Delta T = 22^\circ\text{C}$  and  $w = 200 \mu\text{m}$  (light purple),  $w = 300 \mu\text{m}$  (purple) and  $w = 400 \mu\text{m}$  (dark purple). Steeper temperature gradients and thinner widths lead to a stronger accumulation along the height of the pore due to the quicker convection flow and stronger thermophoresis. (b) Simulated concentration evolution at the bottom stripe of a pore over time with 1.5 mM dAMP monomer starting concentration with  $w = 170 \mu\text{m}$  and  $\Delta T = 5^\circ\text{C}$  (light red),  $\Delta T = 20^\circ\text{C}$  (red) and  $\Delta T = 50^\circ\text{C}$  (dark red) as well as with  $\Delta T = 22^\circ\text{C}$  and  $w = 200 \mu\text{m}$  (light purple),  $w = 300 \mu\text{m}$  (purple) and  $w = 400 \mu\text{m}$  (dark purple). A steeper temperature gradient leads to a quicker and stronger accumulation, a smaller pore width leads to an later reaching of the steady stated however a higher concentration at the bottom.

## 3.2 AImpdA Monomer Polymerization in a Thermogravitational Trap

De novo strand polymerization of imidazolized RNA and DNA nucleotides has been studied under various conditions [52, 53]. I applied this activation scheme to DNA dAMP monomers and found DNA oligomerization in water (see Fig. 3.5). In order to show the enhancement of this prebiotic wet DNA-polymerization by the thermogravitational accumulation of a thin pore subjected to a thermal gradient, 2'-aminoimidazole-preactivated dAMP monomers (AImpdA) were mixed at concentrations of 2.5, 20 or 300 mM in a 100 mM MOPS buffer at pH 6.5 without further addition of salts and the samples were incubated for 24 h in the pore under a thermal gradient of  $\Delta T = 30^\circ\text{C} - 8^\circ\text{C} = 22^\circ\text{C}$  and as a control were incubated in bulk under homogeneous temperatures of  $8^\circ\text{C}$  or  $30^\circ\text{C}$ . Experiments were conducted using different starting concentrations of AImpdA to show robustness. The reaction was stopped by freezing the pore and the bulk test tubes at  $-80^\circ\text{C}$ . The content of the pore was then extracted in individual stripes along its height, product concentrations and composition were measured with HPLC-MS for each volume section (details of the analysis see Chapter 5.3). By a combined HPLC-MS analysis I could identify and quantify the different types of oligomerization products for each length (see Figure 3.5a): (i) linear oligomers in which all bonds are 3',5'-phosphodiester bonds, (ii) activated oligomers which are linear oligomers that still have the aminoimidazole activation-group at the 5'-end and (iii) pyrophosphate oligomers in which exactly one monomer linkage is a pyrophosphate bond (the rest are 3',5'-phosphodiester bonds). Obtaining heterogeneous backbones with pyrophosphate linkages should not be detrimental, arguing along the lines of [54] that DNA pyrophosphate linkages stabilizes the base pairing of mixed DNA-RNA duplexes. No cyclized oligomer products could be detected. The results are shown in Figure 3.5b. I found up to 4mers for pyrophosphate and activated oligomers, linear oligomers formed up to a length of 3 nt. It was important to find oligomers with their active group still on as this enables oligomers to polymerize also amongst one another. At the pore bottom, the polymerization concentration was 2- to 6-fold higher for each single lengths and types of oligomers than in the control reaction at isothermal bulk conditions. In sum the thermally induced non-equilibrium accumulation behavior of the pore enhanced the efficiency of oligomerization up to 24-fold compared to the bulk experiments for each of the three different types of oligomers (Figure 3.4 and Table 3.2).

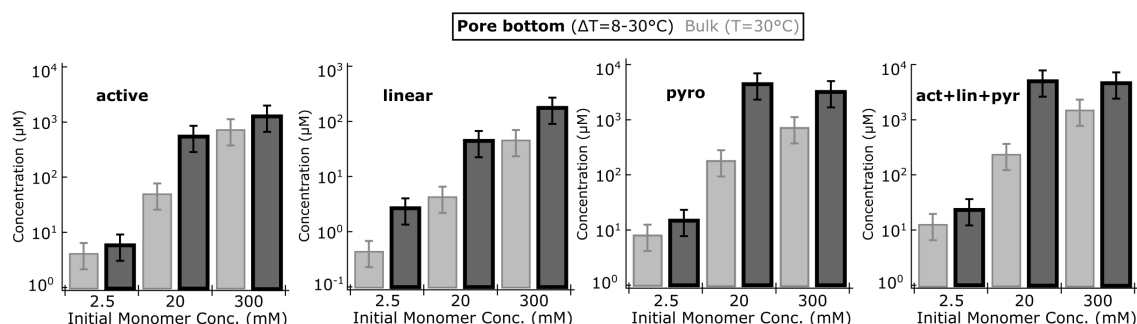


**Figure 3.4: AImpdA polymerization is enhanced by the thermogravitational pore.** For active, linear and pyrophosphate oligomers (all lengths summed) the bottom of the pore (black) yielded a stronger polymerization result than the respective bulk control (grey) for all starting monomer concentrations (2.5/20/300 mM AImpdA). The percentages of yield-enhancement by the non-equilibrium conditions of the pore can be found in Table 3.2. Error bars indicate 50 % error estimates, taken from triplicates on representative polymerization experiments.

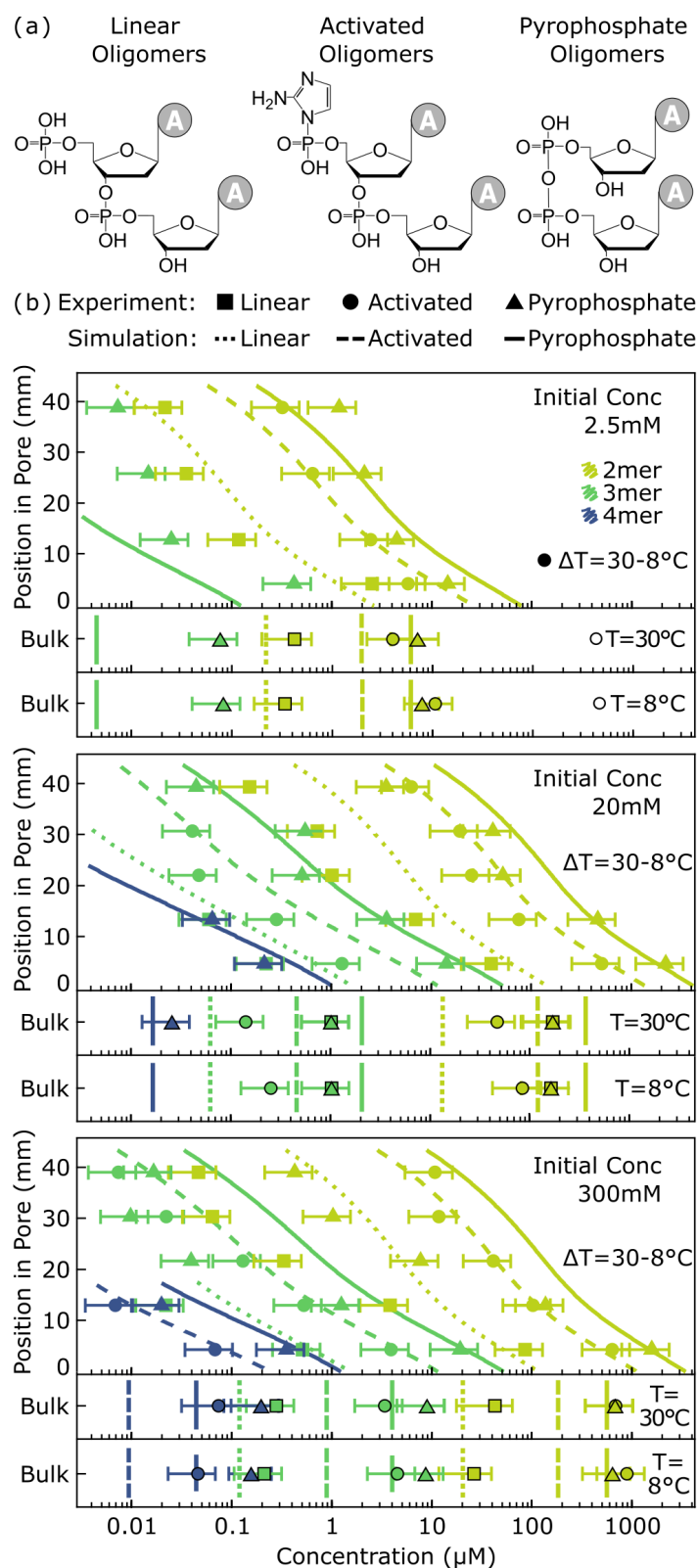


**Figure 3.5: Enhanced DNA polymerization in a thermal gradient.** (a) Polymerization from aminoimidazolized dAMP monomers produces activated, linear and pyrophosphate oligomers, identified by HPLC and ESI-TOF mass spectrometry. (b) Heat-flow enhanced DNA polymerization in a thermophoretic pore at a temperature gradient of  $\Delta T = 22^\circ\text{C}$  formed up to 4mers after 24 h. At the pore bottom, the polymerization concentration was 2- to 6-fold higher for each single lengths and types of oligomers than in the control reaction at isothermal bulk conditions. This experimental result (markers) is confirmed by finite element calculations of a combined polymerization and thermogravitational accumulation theory (lines) for all tested starting concentration (2.5/20/300 mM AImpdA). Error bars indicate 50% error estimates, taken from triplicate experiments on representative polymerization experiments.

Initial AImpdA Concentration	Active Oligomers	Linear Oligomers	Pyrophosphate Oligomers	Sum of all Oligomer Types
2.5 mM	42 %	491 %	86 %	85 %
20 mM	1015 %	928 %	2378 %	2063 %
300 mM	77 %	284 %	346 %	213 %

**Table 3.2: Percentages of yield-enhancement by the non-equilibrium conditions of the pore in comparison to the bulk experiments.** See Figure 3.4.

The parameters for the simulations for all three different starting concentrations were adopted from the previously found parameters of the pure monomer accumulation and completed by on-rates for the polymerization equations and deactivation-rates for the imidazolization and can be found in Table 3.4. The Comsol file of the simulation is provided in Dataset D5. Polymerization of AImpdA occurred throughout the whole chamber volume but was enhanced nonlinearly by the increased monomer concentration at the bottom. Monomers and polymers were similarly accumulated by the heat flow condition. It is important to note that even though the polymer concentration was highest at the bottom of the pore, polymerization also occurred in the upper parts (see Figure 3.5b). The polymers formed there were then actively pushed to the bottom by the mechanisms of convection and thermophoresis explained above. The concentration of oligomers was hence locally increased by the non-equilibrium conditions, instead of being heavily diluted in the bulk water as under equilibrium conditions. In this way, by increasing the proximity of oligomerization products to each other, the probability that they react amongst one another is expected to be enlarged. This can be supported since it was confirmed by mass spectrometry analysis that about 30 % of the oligomerization products still have their activation group (see Figure 3.5), so that they themselves can act again as nucleophilic attackers for other oligomers in their immediate vicinity.

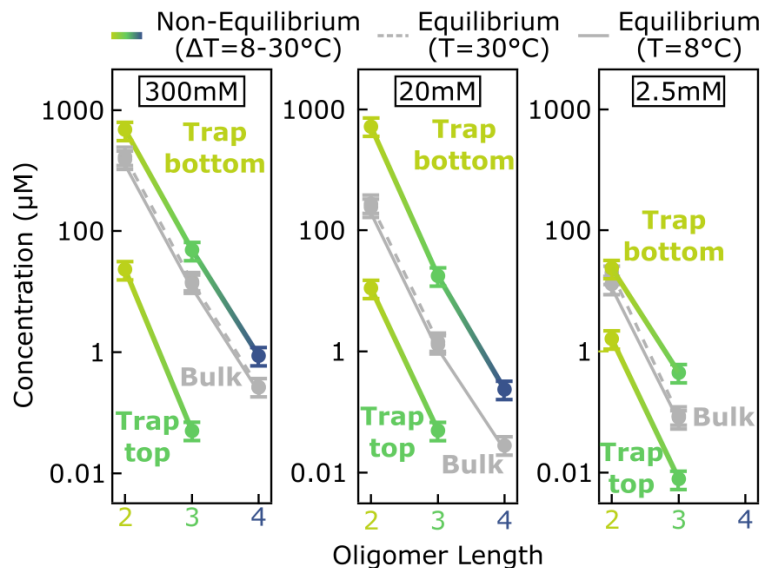


**Figure 3.6: Accumulation in a heated rock pore enhances the polymerization of preactivated DNA monomers compared to bulk experiments in thermal equilibrium for all lengths.** AImpdA monomer polymerization subjected to a temperature gradient of  $\Delta T = 30 - 8^\circ\text{C} = 22^\circ\text{C}$  for 24 h (colorful) exceeds the product concentration in isothermal bulk solution at  $T = 8^\circ\text{C}$  and  $T = 30^\circ\text{C}$  (grey) for all starting concentrations of 2.5, 20 and 300 mM AImpdA and for all oligomer lengths. Error bars indicate 50 % error estimates, taken from triplicates on representative polymerization experiments. Lines are guides to the eye.

Hence, it is expected that if the system was run on the large time scales of the early Earth, the polymerization scheme could be triggered to leave its usual monomer-addition regime that it pursues in equilibrium conditions and grow into more efficient modes of polymerization. If fed from the top of the pore which can be connected to a large reservoir and if run over larger time scales, the polymerization is expected to continue since thermophoresis efficiently prevents monomers and oligomers to leave the thermal trap.

For estimating the errors of the experiments shown in Figure 3.5b, I calculated the relative errors for all datapoints of the experiments in Figure 3.7 that were gained from the standard deviations of replication experiments. This allowed us to get an estimate of a generalized error introduced by thermal pore experiments and measurements by HPLC/ESI-TOF. This errors in average amounts to 47.5%, which made us assume an error of  $\pm 50\%$  for all datapoints in Figures 3.4, 3.5 and 3.6.

Species	Rate Equation
Activated Monomer (A1):	$d(A1)/dt = -op * A1 - 4 * on * A1 * A1 - 2 * on * A1 * A2 - 2 * on * A1 * A3 - 1 * on * A1 * L1 - 1 * on * A1 * L2 - 1 * on * A1 * L3 - 2 * onp * A1 * A1 - 1 * onp * A1 * A2 - 1 * onp * A1 * A3 - 1 * on * A1 * P2 - 1 * on * A1 * P3$
Activated Dimer (A2):	$d(A2)/dt = -op * A2 - 2 * on * A2 * A1 - 4 * on * A2 * A2 + 2 * on * A1 * A1 - 1 * on * A2 * L1 - 1 * on * A2 * L2 - 1 * onp * A2 * A1 - 2 * onp * A2 * A2 - 1 * on * A2 * P2$
Activated Trimer (A3):	$d(A3)/dt = -op * A3 - 2 * on * A3 * A1 + 2 * on * A1 * A2 - 1 * on * A3 * L1 - 1 * onp * A3 * A1$
Activated Tetramer (A4):	$d(A4)/dt = -op * A4 + 2 * on * A1 * A3 + 2 * on * A2 * A2$
Linear Monomer (L1):	$d(L1)/dt = +op * A1 - 1 * on * L1 * A1 - 1 * on * L1 * A2 - 1 * on * L1 * A3 - 1 * onp * A1 * L1 - 1 * onp * A2 * L1 - 1 * onp * A3 * L1$
Linear Dimer (L2):	$d(L2)/dt = +op * A2 + 1 * on * A1 * L1 - 1 * on * L2 * A1 - 1 * on * L2 * A2 - 1 * onp * A1 * L2 - 1 * onp * A2 * L2$
Linear Trimer (L3):	$d(L3)/dt = +op * A3 + 1 * on * A1 * L2 + 1 * on * A2 * L1 - 1 * on * L3 * A1 - 1 * onp * A1 * L3$
Linear Tetramer (L4):	$d(L4)/dt = +op * A4 + 1 * on * A1 * L3 + 1 * on * A3 * L1 + 1 * on * A2 * L2$
Pyrophosphate Dimer (P2):	$d(P2)/dt = +1 * onp * A1 * A1 - 1 * on * P2 * A1 - 1 * on * P2 * A2$
Pyrophosphate Trimer (P3):	$d(P3)/dt = +1 * onp * A1 * A2 + 1 * on * A1 * P2 - 1 * on * P3 * A1$
Pyrophosphate Tetramer (P4):	$d(P4)/dt = +1 * onp * A1 * A3 + 1 * onp * A2 * A2 + 1 * on * A1 * P3 + 1 * on * A2 * P2 + 1 * onp * A2 * L2 + 1 * onp * A1 * L3 + 1 * onp * A3 * L1$

Table 3.3: AImpdA Oligomerization Rate Equations

Parameter	Value	Explanation
Pore Width	170 $\mu\text{m}$	width of pore
Pore Height	43.5 mm	height of pore
Tcold	8 $^{\circ}\text{C}$	temperature at cold side of pore
$\Delta T$	19 K	temperature gradient between hot and cold side of pore (fit-parameter)
n	0.2	fit-parameter for molecule properties
D	$643n^{-0.46} \mu\text{m}^2 \text{s}^{-1}$	formula for diffusion coefficient of molecules [5]
ST	$(5.3 + 5.7n^{0.73})10^{-3} \text{K}^{-1}$	formula for Soret coefficient of molecules [5]
A <small>small</small>	2.5 mM	initial monomer concentration of 2.5 mM experiments
A <small>middle</small>	20 mM	initial monomer concentration of 20 mM experiments
A <small>large</small>	25 mM	initial monomer concentration of 300 mM experiments (fit-parameter)
op	$1.6 * 10^{-6} \text{s}^{-1}$	deactivation off-rate of imidazole activation (fit-parameter)
on	$2.5 * 10^{-9} \text{m}^3 \text{s}^{-1} \text{mol}^{-1}$	on-rate into active or linear oligomers (fit-parameter)
onp	$5.6 * on$	on-rate into pyrophosphate oligomers (fit-parameter)

**Table 3.4: Simulation parameters for combined AImpdA accumulation and polymerization.** The same parameter set could be used to model all three starting concentrations of the AImpdA polymerization and accumulation experiments in a thermophoretic pore. The starting concentration for the largest initial AImpdA concentration was weighed in to be 300 mM but had to be modeled to 25 mM in the simulation to fit the experimental results: this is explainable by the fact, that already by eye a precipitation of the dissolved molecules took place in the pore due to their strong accumulation in the thermophoretic pore.

### 3.3 2',3'-Cyclic Monomer Polymerization in a Bubble Trap

It was previously shown that gas bubbles in contact with differentially heated surfaces can accumulate [34], phosphorylate [33] and enzymatically polymerize [55] DNA and RNA strands by the created local wet-dry cycles. In this dissertation, I study the recently established polymerization from 2',3'-cyclic RNA monomers, initiated by the dry polymerization of 2',3'-cGMP [14]. The conditions in this study combine the accumulation of a water-based thermogravitational trap with the continuous wet-dry-cycling of a heated air-water-interface (see Chapter 2.2). This implements the dry polymerization of RNA in a wet surrounding and enhanced the reaction's yield.

For this, a gas bubble was introduced at the bottom of the pore where the thermogravitational accumulation takes place. Convection and thermophoresis were now joined by evaporation at the hot side and recondensation at the cold side of the pore. The trap was operated for 18 h at a temperature difference of  $\Delta T = 70^{\circ}\text{C} - 40^{\circ}\text{C} = 30^{\circ}\text{C}$ . 10 mM 2',3'-cyclic-GMP and 50 mM 2',3'-cyclic-CMP were dissolved in RNase-free water and the pH was adjusted to pH 10.5 with KOH. The higher concentration of cCMP reflects its higher solubility and compensates for a reduced reactivity in the copolymerization of the two bases. The mixture was inserted in the heated pore while at the same time leaving a gas bubble at its bottom (filling procedure see Movie M2). As a control, 20  $\mu\text{L}$  of the same mixture were incubated in test tubes for 18 h at  $40^{\circ}\text{C}$  or  $70^{\circ}\text{C}$  with the tube lid open to induce dry conditions or the tube lid closed to probe aqueous-only conditions. After 18 h of reaction, the dried tube samples were rehydrated into 20  $\mu\text{L}$  of RNase-free water and all tubes and the trap were

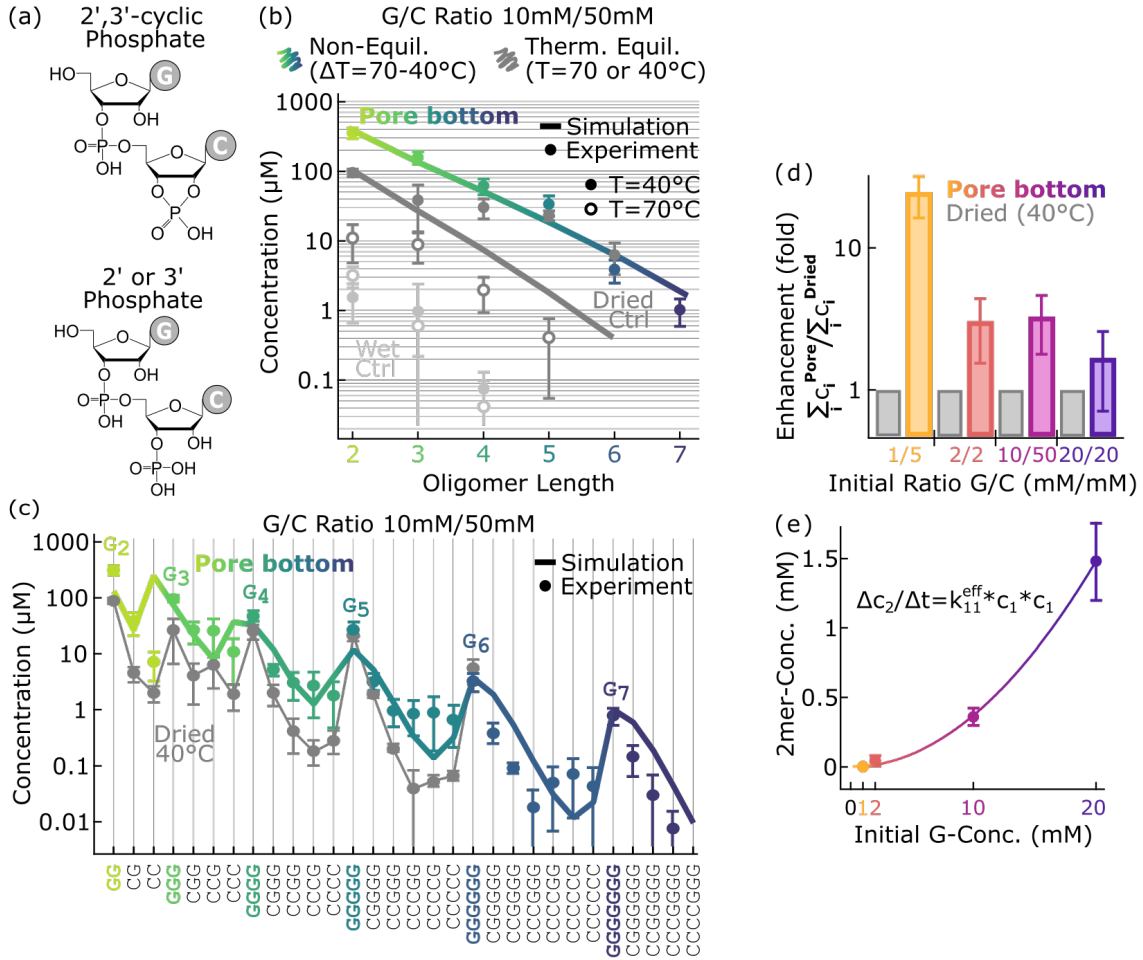


**Figure 3.7: Thermogravitational accumulation combined with interfacial drying drives RNA polymerization.** (a) The polymerization from 2',3'-cyclic RNA monomers yields oligomers with open and closed phosphate rings. (b) Polymerization of 10 mM 2',3'-cGMP and 50 mM 2',3'-cCMP is enhanced in the thermal gradient setting at  $\Delta T = 30^\circ\text{C}$  (colored circles) and exceeds polymerization in pure drying conditions (dark grey circles) or in bulk solution at isothermal conditions (light grey circles) in terms of length and product concentration. The continuous wet-dry cycles at the bubble boundaries allow the thermophoretically concentrated monomers to efficiently polymerize up to 7mers. The drying controls only showed up to 5- or 6mers within the detection limit whereas the wet controls only yielded 4mers. This effect was confirmed by finite element simulation (lines) of a combined accumulation and polymerization theory in terms of length distribution and the yield enhancement. The polymerization was captured in the model using a reduced dimer on-rate  $k_{11} = k_{on}/60 = 15.8 \cdot 10^{-6} \text{s}^{-1} \text{M}^{-1}$  and estimating the hydrolysis of 2',3'-cyclic phosphate to the inactive 2' or 3' phosphate with  $k_{off} = 1/\text{day}$ , both motivated by the results of the same reaction in the dry state [?]. All error bars indicate the standard deviation of the mean of the triplicate experiment. (c) By HPLC/ESI-TOF analysis I could determine the base compositions of the oligomers formed (colored circles). As the polymerization process is governed by a cGMP-quadruplexation [14], naturally the base G dominated the polymer products. This behaviour could be recreated theoretically (solid line) by differential on-rates between the different bases. I found that inside the thermal non-equilibrium setting, C-nucleotides are incorporated more readily into the strands compared to the pure drying protocol at isothermal conditions (grey circles). For that also see Figure 3.8. (d) The enhancement of total oligomer yield at the pore bottom compared to isothermal dry polymerization is independent of the initial G/C monomer ratio and initial monomer concentration. The concentration of oligomers at the pore bottom surmounts dry polymerization especially for the lowest initial G-concentration (24-fold). (e) At the level of dimers I found a quadratic dependency of the yield on the G-monomer initial concentration (least square fit: solid line) with an effective  $k_{11}^{eff} = 5.7 \pm 0.1 \cdot 10^{-6} \text{s}^{-1} \text{M}^{-1}$ . The fitted  $k_{11}^{eff}$  is about one order of magnitude higher than what is needed to fit the polymerization in the microscopic model in 3.7b and c that includes thermophoresis. The higher effective rate shows in a nutshell the efficient enhancement of polymerization by the heated crack.

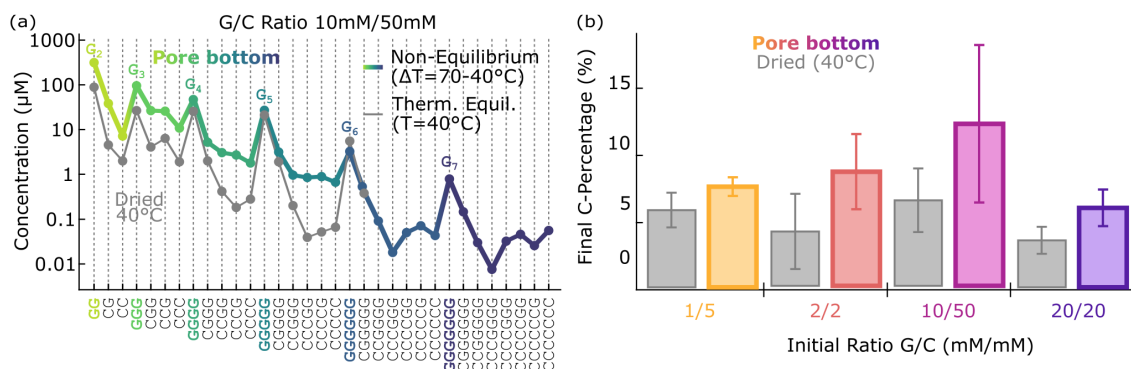


**Figure 3.8: The thermal pore enhances the incorporation of the disfavoured 2',3'-cCMP nucleotide.** (a) The base compositions of the oligomers formed were determined by HPLC/ESI-TOF analysis. The base G dominates the polymer products. However, inside the thermal trap (colored circles) cCMPs nucleotides are incorporated more readily into the strands compared to the pure drying protocol at isothermal conditions (grey circles). The lines in this figure are guides to the eye. (b) The thermal pore increases the formation of mixed sequences and up to doubles the rate of incorporation of C-nucleotides independently for all tested initial monomer compositions and concentrations.

frozen at  $-80^{\circ}\text{C}$  to stop the reaction. The pore sample was again cut and freeze-extracted in individual volume sections along the pore height. The oligomer concentrations were measured with HPLC and ESI-TOF after ethanol precipitation (see Chapter 5.2). Both cyclic and linear phosphate endings of the oligomeric products (Figure 3.7a) were analyzed independently, but displayed as a sum together in the graphs for simplicity.

A direct comparison between the reaction yields at the pore bottom versus the control experiments showed that the thermal non-equilibrium pore triggered the formation of an around 3-fold higher yield for all lengths and 1-2 nt longer oligomers for the 10 mM 2',3'-cGMP/50 mM 2',3'-cCMP experiment (Figure 3.7b, circles), despite the fact that only a very small fraction near the bottom bubble of the pore volume was subjected to drying. Hence, the relative yield per area can be considered much higher. 7mers could be detected at the pore bottom while only 5mers and 6mers were found in the pure drying experiments at isothermal conditions. The bulk control without any drying merely yielded 4mers. One should consider that at the bottom of the chamber drying conditions were implemented only by the air bubble while in the dry sample the full volume has been dried. However, the thermophoretic pore accumulated and confined the monomeric starting material and the oligomer products at the bubble boundary by thermophoresis and convection and consequently could enlarge the efficiency of the polymerization reaction.

The experimental observations (circles) could be rationalized in great detail by a combined accumulation and polymerization simulation (Figures 3.7b and c, solid lines) with COMSOL Multiphysics (see Chapter 2.5 for details), where the polymerization reaction was implemented only in a small section near the bottom of the chamber representing the water-air interface of the bubble.

For the simulation, equation (2.5) was calculated for all oligomer lengths and base compositions that were detected in the experiment (GG, GC, CC, GGG, GGC, ..., GCCC-CCC, CCCCCC) and were coupled by the rate equations that are given in Dataset D6. The self-coded LabVIEW program that calculated the rate equations is also provided in D6 (Kinetics\_ADP\_polymerization\_7.0.vi). The parameters for the simulations were adopted from previously found parameters of pure monomer accumulation and completed by length- and sequence-dependent on-rates for the polymerization rate equations and an off-rate for the deactivation of the 2',3'-cyclic phosphate ends to either a 2' or 3' phosphate. Parameters are given in Table 3.5. The Comsol file of the simulation can be found in Dataset D5.

Parameter	Value	Explanation
Pore Width	170 $\mu\text{m}$	width of pore
Pore Height	43.5 mm	height of pore
Tcold	40 $^{\circ}\text{C}$	temperature at cold side of pore
$\Delta T$	30 K	temperature gradient between hot and cold side of pore (fit-parameter)
n	0.2	fit-coefficient for molecule properties
D	$643n^{-0.46} \mu\text{m}^2 \text{s}^{-1}$	formula for diffusion coefficient of molecules [5]
ST	$(5.3 + 5.7n^{0.73})10^{-3} \text{K}^{-1}$	formula for Soret coefficient of molecules [5]
reaction-height	Pore Width	zone inside the pore in which polymerization can take place, modelling the zone where the air-water interface in the experiment is triggering wet-dry cycles and hence the polymerization
Cinit	50 mM	initial monomer concentration for 2',3'-cCMP monomers in the 10/50 experiments
Ginit	10 mM	initial monomer concentration for 2',3'-cGMP monomers in the 10/50 experiments
kon	$9.5 * 10^{-7} \text{m}^3 \text{s}^{-1} \text{mol}^{-1}$	general on-rate for general polymerization (not monomer-to-monomer-polymerization), fit-parameter
k11	kon/60	on-rate when two monomers are polymerized (fit-parameter)
kGG	1	factor to modulate the on-rate when two GMPs are polymerized (fit-parameter)
kGC	0.03	factor to modulate the on-rate when a GMP and a CMP are polymerized (fit-parameter)
kCC	0.04	factor to modulate the on-rate when two CMPs are polymerized (fit-parameter)
koff	1/day	off-rate for the opening (deactivation) of the 2',3'-cyclic phosphate end

**Table 3.5: Simulation parameters for combined 2',3'-cyclic polymerization and accumulation** To simulate the very peculiar hammock distribution of the base-composition in the strands emerging from the 2',3'-cyclic polymerization (also see Figure 3.8) a lower  $k_{on}$  rate for the reaction of two monomers with one another ( $k_{11}$ ) than for any other polymerization reaction between two other strand lengths had to be included. To attribute for the strong G-preference in the strand formation reaction of this chemistry, I included factors that attenuate the reaction between a G- and a C- or a C- and a second C-base nucleotide.

As shown in [14], the polymerization process of 2',3'-cyclic monomers strongly depends on the efficient stacking of the 2',3'-cGMP, which introduces a natural G-preference into the sequences of the oligomers formed. Using mass spectrometry, it was possible to identify the different base compositions of the formed strands (Figure 3.7c and Figure 3.8a). Pure G-strands were the dominant species, also despite an initial 5:1 concentration bias towards cCMP, since cCMP has a lower probability for incorporation. This is also reflected in the simulation by a damping-factor of  $k_{CC} = 0.03$  and  $k_{CG} = 0.04$  that attenuate the on-rate of a C-monomer polymerizing to a G- or C-end of an already formed strand. Interestingly, the non-equilibrium setting was able to double the incorporation efficiency of 2',3'-cCMP into the oligomers compared to the dry polymerization regardless of the initial monomer concentrations or the initial G/C ratios (Figure 3.8b). This can be explained by an enhanced up-concentration of C as compared to G in the thermogravitational pore due to C's higher solubility. The non-equilibrium setting yielded more strands with a mixed base composition

and hence provided a richer pool of initial sequences which can be advantageous for further evolutionary reactions.

Figure 3.7d shows that for all tested monomer starting concentrations and G/C starting ratios, the total oligomer concentration was consistently 3-fold to 24-fold higher in the non-equilibrium pore compared to the dry polymerization. The highest 24-fold enhancement of polymerization was seen at the lowest initial G-concentration experiment with 1 mM 2',3'-cGMP and 5 mM 2',3'-cCMP.

In addition, the numerical polymerization model suggested rate limiting, slow formation of dimers with a rate equation of  $k_{11} * (c_{mono})^2$  with  $k_{11} = k_{on}/60$  being 60-times smaller than the on-rate for the other polymerization reactions. Dimer concentrations are expected to scale quadratically with the initial concentration of 2',3'-cGMP. This is found convincingly in the data (Figure 3.7e). There, however, the fitted  $k_{11}^{eff} = 5.7 \pm 0.1 * 10^{-5} s^{-1} M^{-1}$ , is about one order of magnitude higher than what is needed to fit the monomer-to-monomer-polymerization  $k_{11} = k_{on}/60 = 15.8 * 10^{-6} s^{-1} M^{-1}$  in the microscopic model in Figure 3.7b and c which includes thermophoresis. The higher effective rate shows in a nutshell the efficient enhancement of polymerization by the heated crack.

The RNA polymerization experiments were repeated three times with the same parameters (except for the pore experiment of G/C ratio 1 mM/5 mM which was repeated twice). The experimental results were averaged and the mean values were plotted into the graphs. The error bars of the data points are the standard deviations of the triplicates (or of the duplicate). I want to underline that the 2',3'-cyclic RNA polymerization performed in the thermal pore took place under mainly wet conditions, where the wet-dry cycles were localized only in a small region of the sample instead of requiring the sample to become completely dry. The latter are conditions that are alien to living systems which replicate and evolve in water-based environments. Overall I found that the non-equilibrium setting yielded more and longer strands with a more balanced and mixed base composition. This makes the formed sequences more likely to hybridize with each other, offering an increasingly likely pathway towards downstream evolutionary reactions.

### 3.4 Longtime Extrapolation of De Novo Polymerization in Thermal Non-Equilibria

In order to retrace the long term effects of thermal non-equilibria on the polymerization systems in my experiments, I extended the finite element simulations used in Chapter 3.1 for monomer accumulation by a thermogravitational pore to times scales of up to one year which are not accessible to lab experiments.

In a closed pore as used in the experiments, I find in the simulation that after about one day the concentration at the bottom of the pore reaches a steady state where accumulated monomers are retained by the temperature gradient but not further concentrated (Figure 3.9a, solid line). The monomer accumulation is 10-fold compared to the starting concentration within 24 h, both in my experiments (Chapter 3.1) and in the steady state of the 2D simulation (Figure 3.9).

For an open pore with feeding, the top boundary of the pore was set to a constant concentration of 1  $\mu$ M, which simulated the connection of a real pore to a large reservoir with 1  $\mu$ M monomer concentration, like for example a primordial ocean or a larger network of cracks. There the exponential accumulation of monomers at the bottom of the trap continues for the whole calculated time span (dotted line). Consequently, an active polymerization reaction can be accommodated there for years by the constant addition of fresh starting material and can progress to longer and longer oligomers. It also offers near perfect retention of the accumulated molecules (Figure 3.9a) after switching off the feeding. Even if the top depletes,

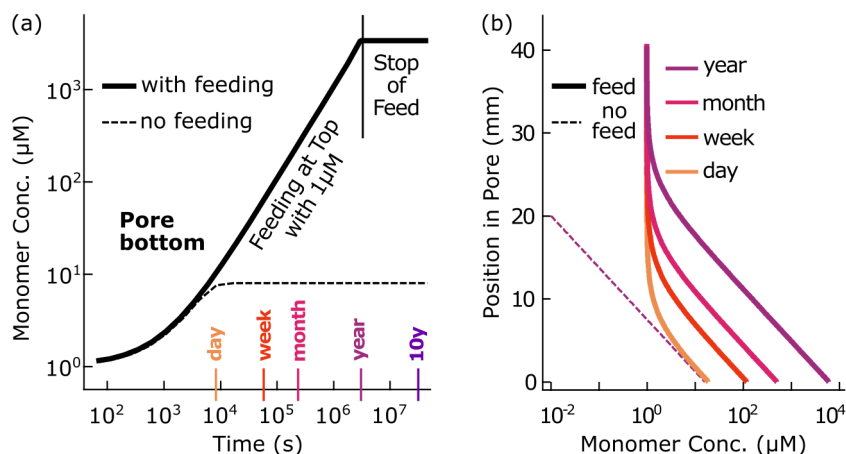


**Figure 3.9: Thermal non-equilibrium pores enable feeding without dilution.** (a) 2D finite element simulation of the monomer accumulation in a thermal pore with and without feeding at the top calculated from fluid flow and thermophoresis with the parameters from Figure 3.1b for an initial monomer concentration of 1 μM. In contrast to a closed pore (solid line) which reaches a steady state after one day, an open heat flow pore ( $\Delta T = 22^\circ\text{C}$ ) is continuously fed from the top with 1 μM of monomers by the connection to a large reservoir, for example a primordial ocean, and can accumulate monomers at its bottom over years while no molecules are expected to leave the setting after the feeding stops. (b) In a closed setting, the absolute concentration raises due to the accumulation at the bottom to 10 μM, but depletes strongly at its top (broken line). High absolute concentrations could be reached if the pore top is connected to a 1 μM reservoir: This feeding is slow, but reaches bottom monomer concentrations of more than  $10^4 \cdot 1 \mu\text{M}$  and over time fills up the whole volume of the pore with monomers (solid lines).

none of the molecules escape the setting over the time scale of many years, in a way very similar to how Earth is able to keep its atmosphere over long times. This is especially interesting for the polymerization reaction whose informational polymers are kept in place for long times and have ample time to recycle and react further without being lost by diffusion. Figure 3.9b shows that the top of a closed trap becomes depleted up to  $10^4$ -fold relatively, while an open pore with the top connected to an outside reservoir of an arbitrary low concentration, for example 1 μM, is being filled up with more and more monomers along its whole height. Hence also a larger volume of the pore gains a constantly increasing monomer concentration and the thermogravitational trapping will in the long run lead to a  $10^4$ -fold accumulation in the whole trap. This is however a slow process and simulations of other settings, for example a feeding flow throughout the whole trap [24, 19] show that filling the trap from the top is actually a worst case scenario, taking significantly longer than a year to completely fill the crack.

The notable point in this feeding scenario triggered by a thermal non-equilibrium in a thin pore is that the addition of fresh starting material takes place without the addition of bulk water and hence without the dilution of already formed products that any other feeding mechanisms would suffer from.

Figure 3.10 extrapolates the impact of feeding for the 2',3'-cyclic polymerization theory with a 0D finite element simulation. Due to the diminishing of dimensions it was possible to ramp up the length of simulated strands to 21 nt (250 sequence-diverse species and rate equations, provided in Dataset D6, lengths), for simplicity only plotted till 12mers in Figure 3.10. The dimensionless parameters for the 0D simulations were adopted from the previously found parameters of the 2',3'-cyclic polymerization in 2D from Chapter 3.3 and can be found in Table 3.6.

Without additional feeding, a steady state of the polymerization reaction is reached after about one day due to the hydrolysis of the active 2',3'-cyclic phosphate end with an off-rate of  $k_{off} = 1/\text{day}$ , resulting in all polymers ending up in a deactivated state which stops further polymerization (Figure 3.10, broken lines).

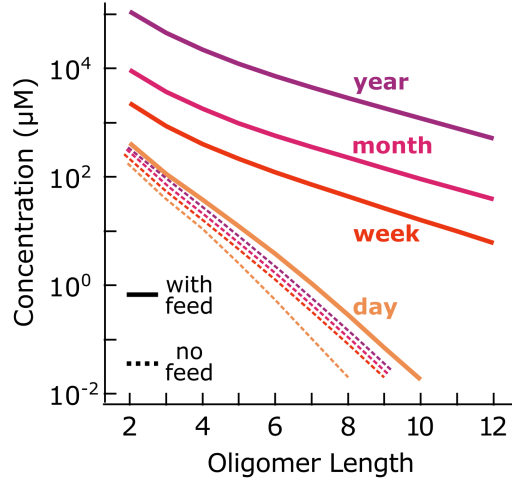


**Figure 3.10: Thermogravitational feeding of a 2',3'-cyclic monomer polymerization reaction.** (a) 0D longtime extrapolation of the 2',3'-cyclic-polymerization theory. To simulate optimal feeding (solid lines), the concentration of monomers is kept constant. Without feeding (broken lines) no fresh molecules are entering the reaction. For a closed reaction, a steady state profile is reached due to the hydrolysis of the active 2',3'-cyclic phosphate end with  $k_{off} = 1/day$ , leading to passive molecules (broken lines). We modelled optimal feeding by keeping the concentration of the monomers in the polymerizing bottom region of the crack constant at 10mM cGMP and 50mM cCMP. As a result, polymers are continuously formed and reach high lengths and concentrations (solid lines).

To simulate optimal feeding at the bottom of the pore, the concentrations of 2',3'-cCMP and 2',3'-cGMP monomers are kept constant representing the permanent refill of monomers to an accumulation trap that has reached its steady state. This simple feeding model showed a strongly enhanced length distribution of the oligomers (Figure 3.10, solid lines). This implies that feeding from a cold reservoir connected to the top of a pore could be a compelling strategy for long term experiments.

Parameter	Value (a.u.)	Explanation
Cinit	50000	initial monomer concentration for 2',3'-cCMP monomers in the 10/50 experiments
Ginit	10000	initial monomer concentration for 2',3'-cGMP monomers in the 10/50 experiments
kon	$9.5 * 10^{-10}$	general on-rate for general polymerization (not monomer-to-monomer polymerization)
k11	kon/60	on-rate when two monomers are polymerized
kGG	1	factor to modulate the on-rate when two GMPs are polymerized
kGC	0.03	factor to modulate the on-rate when a GMP and a CMP are polymerized
kCC	0.04	factor to modulate the on-rate when two CMPs are polymerized
koff	1/day	off-rate for the opening (deactivation) of the 2',3'-cyclic phosphate end

**Table 3.6: Simulation parameters for 0D longtime 2',3'-cyclic monomer polymerization with and without feeding.** The parameters for the 0D simulations were adopted from the previously found parameters of the 2',3'-cyclic polymerization in 2D (see Table 3.5) without units due to the dimensionless 0D simulation.

## Chapter 4

# Conclusion

This doctoral project demonstrates how physical non-equilibria can enhance prebiotically relevant DNA and RNA monomer polymerization reactions. Water-filled rock pores subjected to heat fluxes - a ubiquitous energy source on early Earth - induce a strong accumulation of reagents and products, enhancing the efficiency of de novo strand formation for both DNA and RNA polymerization.

In contrast to equilibrium settings, the accumulation in a thermophoretic pore avoids the need for high starting concentrations of DNA/RNA monomers or other reagents. Even more importantly, the heat flux prevents the diffusional dilution of polymerization products after their creation and maintains the information over timescales only set by the geological heat flow itself. The feeding of the polymerization reaction is simple and is not accompanied by dilution. If monomeric molecules are present at the top of the crack, they are added and accumulated continuously to the reaction at the bottom, enabling a long term setting for continuous reactions with informational molecules.

The incorporation of a gas bubble inside the rock pore, a spontaneous event that can arise for example from water degassing, introduces additional microscale wet-dry cycles. These in turn enable and enhance a polymerization scheme in a dew environment that usually needs dry conditions. This polymerization of RNA in a non-equilibrium setting was also found to create sequences with a more balanced G/C composition, approaching the ability to base pair and increasing the sequence space encoded by the strands. This is an important requisite to enter more efficient modes of strand formation like templated ligation.

The experiments explore a missing piece between the phosphorylation of nucleosides [33] and the templated replication triggered by strand separation [34, 55] found for heated air-water interfaces. By exploiting a thermal non-equilibrium in a thin pore, a rich and localized pool of oligomers with a diverse sequence composition could be created experimentally, that on early Earth could have facilitated the first step towards starting a minimal form of molecular Darwinian evolution.

# Chapter 5

## Methods and Materials

### 5.1 Trap Building and Setup

Developing the thermogravitational traps to the level that enabled the experiments described above was a long process, which is specified in-depth in [56]. The non-equilibrium experiments for this thesis were performed in a chamber ( $170\ \mu\text{m} \times 7\ \text{mm} \times 52\ \text{mm}$ , total volume:  $62\ \mu\text{L}$ ) cut from a thin Teflon foil ( $170\ \mu\text{m}$  thickness, FEP-Teflon, Holscot, Netherlands) which was placed between a transparent cooled back sapphire of  $0.5\ \text{mm}$  thickness (with four laser-cut holes of  $1\ \text{mm}$  diameter, Kyburz, Switzerland) and a heated front sapphire of  $2\ \text{mm}$  thickness (no holes, Kyburz, Switzerland).

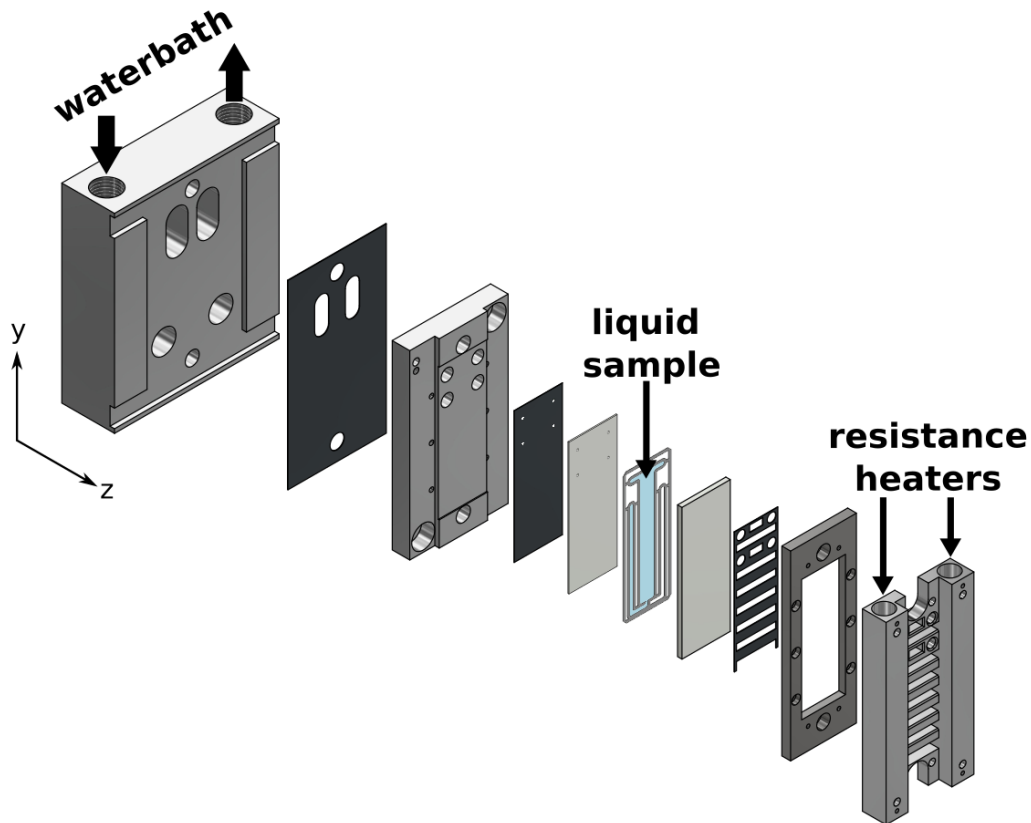


**Figure 5.1: Schematic of the chamber.** From left to right: waterbath-cooled aluminum block, heat conducting graphite foil ( $200\ \mu\text{m}$  thickness), aluminum back plate, heat conducting graphite foil ( $25\ \mu\text{m}$  thickness), bottom sapphire ( $0.5\ \text{mm}$  thickness) with holes, Teflon cutout ( $170\ \mu\text{m}$ ) containing the liquid sample, top sapphire ( $2\ \text{mm}$  thickness), heat conducting graphite foil ( $200\ \mu\text{m}$  thickness), steel frame for fixing the sapphire-teflon-sapphire sandwich on the back plate, aluminum element holding the resistance rod heaters.

The shape of the Teflon foil was designed in Inventor (Autodesk) and cut with a cutting plotter (CE6000-40 Plus, Graphtec). The sapphires were lined with two heat-conducting graphite foils (one of 25  $\mu\text{m}$  thickness in the back, EYGS091203DP, 1600  $\text{W m}^{-1} \text{K}^{-1}$ , Panasonic, one of 200  $\mu\text{m}$  thickness in the front, EYGS0811ZLGH, 400  $\text{W m}^{-1} \text{K}^{-1}$ , Panasonic) to ensure a good thermal connection to an aluminum plate at the back and to the resistance rod heaters at the front. The layers were screwed with a steel frame to the back plate with a torque of 0.2 N m, the heater was screwed to the front sapphire with a torque of 0.16 N m. This sandwich is screwed to a waterbath-cooled (TXF200, Grant Instruments (Cambridge) Ltd) second aluminum block with a torque of 0.5 N m and with another 200  $\mu\text{m}$  thick graphite foil in between. All aluminum parts were designed in Inventor and fabricated in the university workshop. Four microfluidic teflon tubings (KAP 100.969, Techlab) were connected with fittings and ferrules (VBM 100. 823 and VBM 100.632, Techlab) to the sapphire back wall of the chamber, which has four holes of 1 mm diameter. These tubings served as inlet and outlet for the introduction of the liquid sample. A schematic of the chamber build-up is shown in Figure 5.1. The process of building a pore can be observed in Movie M3.

For the dAMP and the AImpdA experiments, the cooling system with 50/50 water/ethyleneglycol was set to  $-30^\circ\text{C}$  and the resistance heaters to  $80^\circ\text{C}$ . For the 2',3'-cyclic experiments, the waterbath (50/50 water/ethyleneglycol) was set to  $-20^\circ\text{C}$  and the resistance heaters to  $100^\circ\text{C}$ . To calculate the inner temperatures of the chambers, I measured the temperatures on the outside of the sapphires with a temperature sensor (GTF 300, Greisinger) and a thermometer (GTH 1170 Typ K, Greisinger) and used the steady-state linear heat equation and the conductivities of water 0.6  $\text{W m}^{-1} \text{K}^{-1}$  (at  $20^\circ\text{C}$ ) and sapphire 23  $\text{W m}^{-1} \text{K}^{-1}$  to calculate what temperature this translates to on the inside of the pore. For easy calculation, a self-coded LabVIEW program is provided in Dataset D2 (ThermalGradientCalculator.vi).

The fluorescent microscopy setup consisted of a standard fluorescence microscope (Axiotec, Carl Zeiss Microscopy Deutschland GmbH) equipped with an LED (622 nm, ThorLabs), a dual excitation filter (470 nm/622 nm), a dual emission filter (537 nm/694 nm), a dual band beamsplitter (497 nm/655 nm), a 2x objective (TL2x-SAP, 2x/0.1/350-700 nm/inf/WD56.3 mm, ThorLabs) and a Stingray-F145B ASG camera (ALLIED Vision Technologies GmbH). A self-coded program using the software LabVIEW was used to control the camera and the output voltage to the LED and to the resistance heaters. A cartoon of the setup is shown in Figure 5.2.

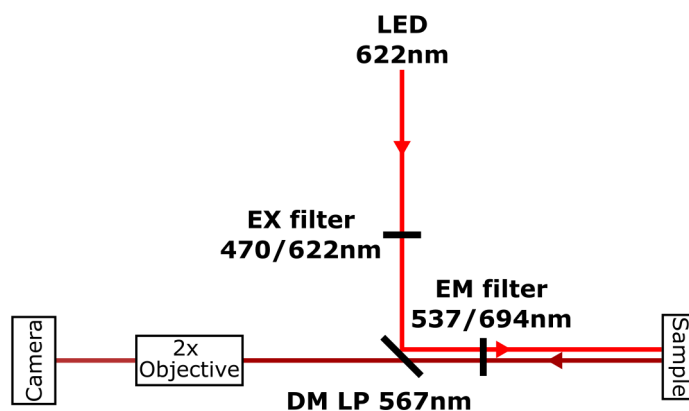


**Figure 5.2: Schematic of the fluorescent microscopy setup.** Light from an LED with wavelength 622 nm went through an excitation filter (622 nm) and onto a longpass dichroic mirror (567 nm), reflecting the light onto the sample. The emitted light went through an emission filter (694 nm), passed the dichroic mirror and a 2x objective and was recorded by a CCD camera.

## 5.2 Sample Preparation

I developed a method to differentially extract all sections of the concentration gradient generated by the pore to study the processes of the combined physicochemical non-equilibrium system: after the run time of the reaction in the thermal gradient, the front heating was turned off, which led to a rapid drop in temperature and finally to the freezing of the pore contents as the waterbath was maintained at  $-20^{\circ}\text{C}$  or  $-30^{\circ}\text{C}$  respectively. After verifying by microscopy that the liquid contents were frozen, the entire pore was removed from the setup and placed it in the  $-80^{\circ}\text{C}$  freezer for 30 min. Then the sapphire-teflon-sapphire sandwich was unscrewed from the metal holders. The sandwich was placed on an aluminum block cooled to  $-80^{\circ}\text{C}$  to prevent melting. The sandwich was opened, and the Teflon was removed using a razor blade. Only the frozen liquid content remained on the sapphires. It was cut into five stripes (for experiments of Chapters 3.1 and 3.2) or three stripes (for experiments of Chapter 3.3) of similar volume and the sapphire was slid stripe by stripe over onto a  $45^{\circ}\text{C}$  aluminium block to melt the frozen sample stripe by stripe. To ensure that two adjacent stripes were not inadvertently mixed during the stripewise thawing, a hydrophobic barrier (glass cover slide wrapped with Teflon foil) was held between each stripe (see Fig. 5.3). The contents of each thawed stripe were pipetted into different low-binding Eppendorf tubes.



**Figure 5.3: Photo of the freeze extraction process.** The sapphire with the frozen sample was slid stripe by stripe over onto a  $45^{\circ}\text{C}$  warm aluminium block to melt the frozen sample stripe by stripe. To ensure that two adjacent stripes were not inadvertently mixed during the stripewise thawing, a hydrophobic barrier (glass cover slide wrapped with Teflon foil) was held between each stripe. The contents of each thawed stripe were pipetted into different low-binding Eppendorf tubes.

After completion of the freeze extraction, the tubes were briefly centrifuged, their liquid contents were weighed, and the percentage of volume of the stripes to the total extracted volume of the pore was calculated. Then, the pH of the samples was measured with Orion VersaStar Pro pH-meter (ThermoFisher Scientific). The process of freeze extraction can be observed in Movie M4. I verified that the freezing process did not disturb the accumulation state of the pore by measurements with fluorescent Cy5-dye (see Figure 5.4).

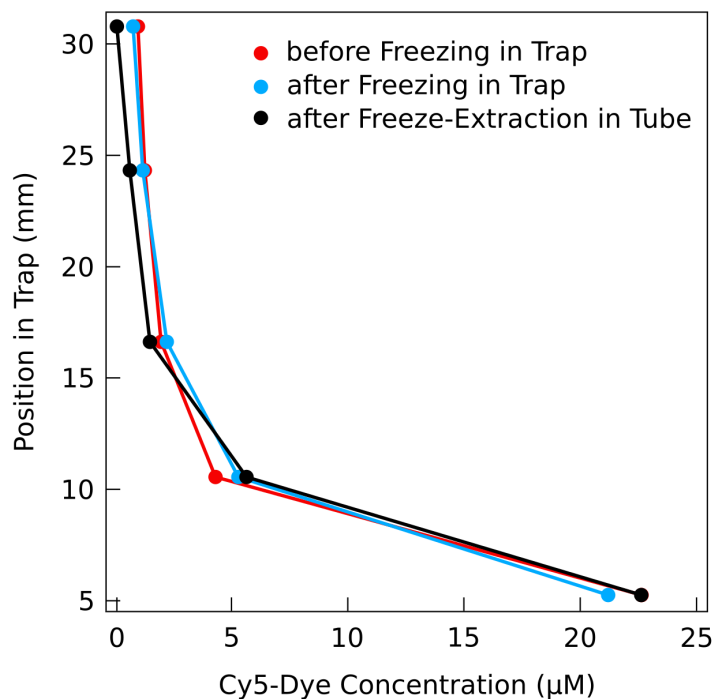


**Figure 5.4: The process of freeze extraction did not disturb the concentration distribution of an accumulated pore.** 10  $\mu\text{M}$  fluorescent Cy5-dye in water was accumulated in a pore of 170  $\mu\text{m}$  thickness for 4 h with a temperature gradient of  $\Delta T = 30^\circ\text{C} - 8^\circ\text{C} = 22^\circ\text{C}$ . Then, the freeze extraction steps described in Chapter 5.2 were performed on this pore. For each step of the process, the concentration of the Cy5-dye was determined via fluorescence microscopy and thickness normalization for each cutout stripe content. It can be observed that the freeze extraction process did not disturb the accumulation state of the pore, as all concentrations stayed the same before and after freezing in the pore as well as after freeze extraction.

For the experiments of Chapters 3.1 and 3.2, the samples were injected directly into the HPLC-MS system without further treatment. For the experiments of Chapter 3.3, the samples were precipitated prior to measurement.

For the precipitation, 10  $\mu\text{L}$  of sample were mixed with 90  $\mu\text{L}$  RNAse free  $\text{H}_2\text{O}$ , 2  $\mu\text{L}$  of 10  $\text{mg mL}^{-1}$  glycogen from oyster (G8751-5G, Sigma-Aldrich) and 10  $\mu\text{L}$  of 5 M Ammonium acetate (CAS 631-61-8, Sigma-Aldrich), then vortexed and spun down. 336  $\mu\text{L}$  of  $-20^\circ\text{C}$  cold ethanol (Art-Nr. 5054.2, Carl Roth GmbH + Co. KG) was added, the mixture was vortexed, spun down and stored overnight in a  $4^\circ\text{C}$  fridge. The next day, the reaction tubes were centrifuged at 15 000 rpm for 30 min at  $4^\circ\text{C}$ , the supernatant was discarded. 100  $\mu\text{L}$  of  $-20^\circ\text{C}$  cold 70/30 ethanol/RNAse-free water mixture were added. The tubes were centrifuged again at 15 000 rpm for 30 min at  $4^\circ\text{C}$ . The supernatant was pipetted off as thoroughly as possible and without further drying the pellet was then dissolved in 40  $\mu\text{L}$  of RNAse-free water. Of this, 38  $\mu\text{L}$  was injected for HPLC-MS measurement in order to make sure to not inject air into the column.

With commercial standards over three orders of magnitude and for oligomer lengths from 2 nt to 10 nt I verified that the precipitation did not disturb the length distribution of the standard mixes and hence did not alter the composition of the sample (see Figure 5.5).

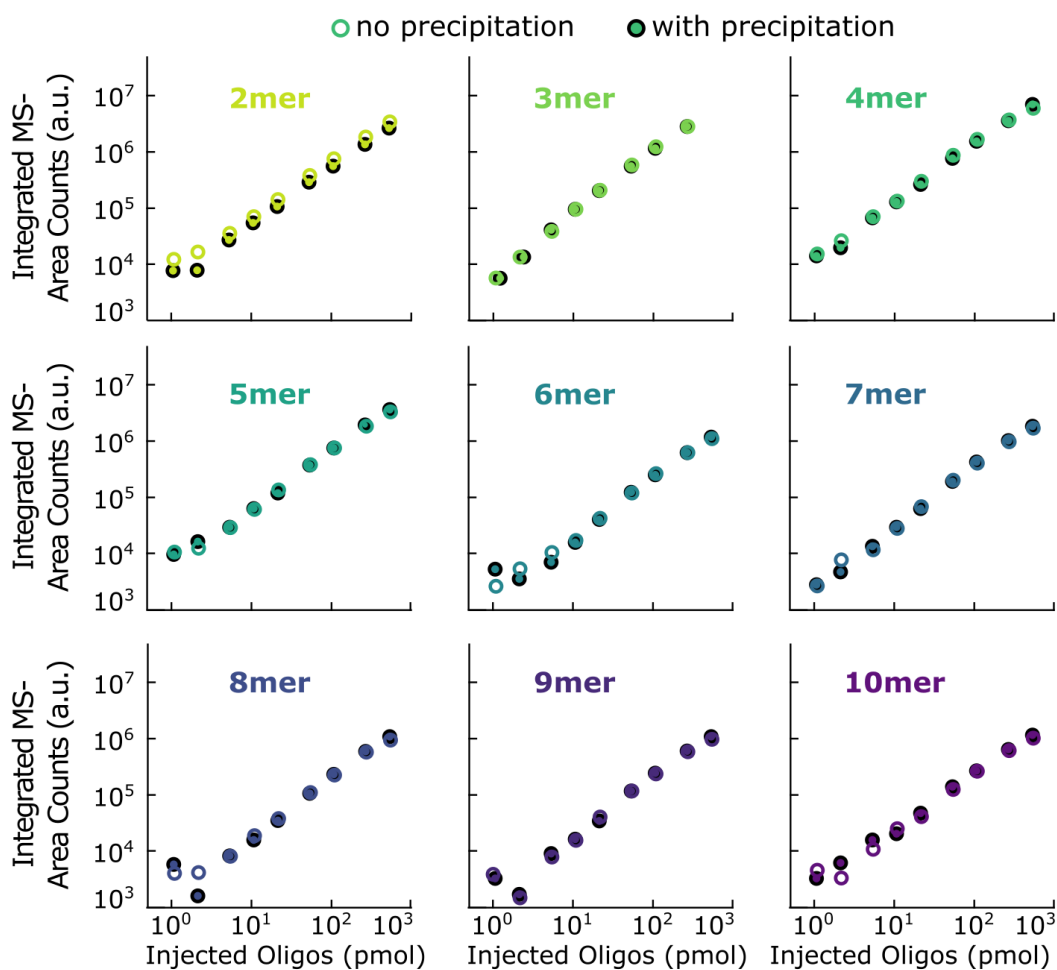


**Figure 5.5: Ethanol precipitation of RNA does not change the strand composition.** Commercially available 2-8mer polyG oligomers (3'-P-G...G-5', 3'-phosphate, biomers.net GmbH, with HPLC purification) with known amounts (1 pmol, 2 pmol, 5 pmol, 10 pmol, 20 pmol, 50 pmol, 100 pmol, 250 pmol, 500 pmol in water) were measured with HPLC/ESI-TOF before and after ethanol precipitation as described in Chapter 5.3. The graphs for the different oligomer lengths above show that the same amount of oligomers before and after precipitation cause the same integrated MS area counts. Hence, the ethanol precipitation treatment does not change the composition of a sample for none of the examined lengths nor concentrations.

## 5.3 Measurements and Analysis

### 5.3.1 HPLC-MS Measurements

The HPLC-MS measurements were performed using a time-of-flight mass spectrometer (TOF-MS) with an electrospray ion source (G6230BA, Agilent Technologies) and a 1260 Infinity II Bioinert high performance liquid chromatograph (HPLC, G5654A, Agilent Technologies). The column was an AdvancedBio Oligonucleotides column (4.6 mm × 150 mm, 2.7 Micron, P.N. 653950-702, Agilent Technologies) and the MS measurements were run in negative mode. For the liquid phase, I used as eluent A: UHPLC-water (CAS No. 7732-18-5, Supelco, Merck KGaA) with 200 mM 1,1,1,3,3,3-Hexafluor-2-propanol (HFIP, Art-Nr 2473.3, Carl Roth GmbH + Co. KG) and 8 mM TEA (CAS No. 603-35-0, Carl Roth GmbH + Co. KG COMPANY) and as eluent B: 50/50 UHPLC-water/methanol (CAS-No 67-56-1, Merck KGaA) with 200 mM HFIP and 8 mM TEA.

### **dAMP Accumulation**

The injection volume was 2  $\mu\text{L}$  for each sample, and the compressibility was set to  $40 * 10^{-6} \text{ L bar}^{-1}$ . A flow of  $0.6 \text{ mL min}^{-1}$  was maintained throughout the 40 min of the method. The column temperature was  $30^\circ\text{C}$ .

The eluent gradients were

0.0 min: 79.0 % A and 21.0 % B

23.0 min: 53.0 % A and 47.0 % B

23.1 min: 0.0 % A and 100 % B

30.0 min: 0.0 % A and 100 % B

30.1 min: 79.0 % A and 21.0 % B

40.0 min: 79.0 % A and 21.0 % B

The recorded diode array detector (DAD) signal was set to 259 nm with a bandwidth of 4 nm. The measured mass range (m/z) was 320-3200 u with a scan rate of  $3 \text{ spectra s}^{-1}$ . The settings were: sheath gas flow:  $11 \text{ L min}^{-1}$ , sheath gas temperature:  $400^\circ\text{C}$ , nebulizer: 45 psig, gas flow:  $5 \text{ L min}^{-1}$ , gas temperature:  $325^\circ\text{C}$ , octupole RF-peak voltage: 800 V, skimmer voltage: 65 V, fragmentor voltage: 250 V, nozzle voltage: 2000 V, V-cap voltage: 4000 V. The reference masses were 1033.988 109 u and 1333.968 947 u (commercially available from Agilent).

### **AImpdA Polymerization**

The method was almost the same as for the dAMP accumulation experiments, except for the mass range, which excluded the monomer masses to obtain a cleaner ion chromatogram with lower background: mass range 550 u-3200 u. Other minor changes were the gas flow:  $8 \text{ L min}^{-1}$  and the gas temperature:  $300^\circ\text{C}$ .

### **2',3'-cyclic Monomer Polymerization**

The injection volume was 38  $\mu\text{L}$  for each sample, and the compressibility was set to  $50 * 10^{-6} \text{ L bar}^{-1}$ . A flow of  $1.0 \text{ mL min}^{-1}$  was maintained throughout the 53 min of the method. The column temperature was  $60^\circ\text{C}$ .

The eluent gradients were

0.0 min: 99.0 % A and 1.0 % B

5.0 min: 99.0 % A and 1.0 % B

27.5 min: 70.0 % A and 30.0 % B

42.5 min: 60.0 % A and 40.0 % B

42.6 min: 0.0 % A and 100.0 % B

47.5 min: 0.0 % A and 100.0 % B

47.6 min: 99.0 % A and 1.0 % B

53.0 min: 99.0 % A and 1.0 % B

The recorded DAD signal was set to 260 nm with a bandwidth of 4 nm. The measured mass range (m/z) was 500-3200 u with a scan rate of  $1 \text{ spectra s}^{-1}$ . The settings were: sheath gas flow:  $11 \text{ L min}^{-1}$ , sheath gas temperature:  $400^\circ\text{C}$ , nebulizer: 45 psig, gas flow:  $8 \text{ L min}^{-1}$ , gas temperature:  $325^\circ\text{C}$ , octupole RF-peak voltage: 750 V, skimmer voltage: 65 V, fragmentor voltage: 175 V, nozzle voltage: 2000 V, V-cap voltage: 3500 V. The reference masses were 601.978 977 u, 1333.968 947 u and 1333.968 947 u (commercially available from Agilent).

### 5.3.2 Masses

For the experiments of Chapters 3.1 and 3.2, the masses were calculated to the fourth decimal using the Agilent Isotope Distribution Calculator. I report the masses of the full isotopic distribution for the first charge state; for the other charge states, I give only the most abundant isotope. For the experiments of Chapter 3.3, the masses were calculated using a self-coded LabVIEW program provided in Dataset D1 (MassListGenerator\_v3.0.vi). I report the masses of the most abundant isotope for all calculated charge states.

#### 1. dAMP

dAMP:  $C_{10}H_{14}O_6N_5P$

m/z (u)	Charge State	Abundance (%)
331.0682	0H	100
330.0609	-1H	100
331.0634	-1H	13.02
332.0654	-1H	2.02
333.0677	-1H	0.19
333.0677	-1H	0.02

#### 2. AImpdA Polymerization

Linear and Pyrophosphate Oligomer Masses:

5'PAA-3':  $C_{20}H_{26}O_{11}N_{10}P_2$

m/z (u)	Charge State	Abundance (%)
644.1258	0H	100
643.1185	-1H	100
644.1210	-1H	25.99
645.1232	-1H	5.51
646.1255	-1H	0.85
647.1277	-1H	0.11
648.1299	-1H	0.01

5'PAAA-3':  $C_{30}H_{38}O_{16}N_{15}P_3$

m/z (u)	Charge State	Abundance (%)
957.1834	0H	100
956.1761	-1H	100
957.1786	-1H	38.96
958.1809	-1H	10.69
959.1832	-1H	2.19
960.1854	-1H	0.38
961.1876	-1H	0.06
962.1898	-1H	0.01
477.5844	-2H	100

5'PAAAA-3': C<sub>40</sub>H<sub>50</sub>O<sub>21</sub>N<sub>20</sub>P<sub>4</sub>

<b>m/z (u)</b>	<b>Charge State</b>	<b>Abundance (%)</b>
1269.2337	-1H	100
1270.2362	-1H	51.93
1271.2385	-1H	17.55
1272.2408	-1H	4.45
1273.2431	-1H	0.93
1274.2453	-1H	0.17
1275.2476	-1H	0.03
634.1132	-2H	100
422.4064	-3H	100

Cyclic Oligomer Masses:

<b>Chemical Formula</b>	<b>m/z (u)</b>	<b>Charge State</b>	<b>Abundance (%)</b>
C <sub>20</sub> H <sub>24</sub> O <sub>10</sub> N <sub>10</sub> P <sub>2</sub> (Dimer)	625.1079	-1H	100
	312.0503	-2H	100
C <sub>30</sub> H <sub>36</sub> O <sub>15</sub> N <sub>15</sub> P <sub>3</sub> (Trimer)	938.1655	-1H	100
	468.5791	-2H	100
	312.0503	-3H	100
C <sub>40</sub> H <sub>48</sub> O <sub>20</sub> N <sub>20</sub> P <sub>4</sub> (Tetramer)	1251.2231	-1H	100
	625.1079	-2H	100
	416.4029	-3H	100
	312.0503	-4H	100

Activated Oligomer Masses:

<b>Chemical Formula</b>	<b>m/z (u)</b>	<b>Charge State</b>	<b>Abundance (%)</b>
C <sub>13</sub> H <sub>17</sub> O <sub>5</sub> N <sub>8</sub> P (Monomer)	395.0987	-1H	100
C <sub>23</sub> H <sub>29</sub> O <sub>10</sub> N <sub>13</sub> P <sub>2</sub> (Dimer)	708.1563	-1H	100
	353.5745	-2H	100
C <sub>33</sub> H <sub>41</sub> O <sub>15</sub> N <sub>18</sub> P <sub>3</sub> (Trimer)	1021.2139	-1H	100
	510.1033	-2H	100
	339.7331	-3H	100
C <sub>43</sub> H <sub>53</sub> O <sub>20</sub> N <sub>23</sub> P <sub>4</sub> (Tetramer)	1334.2715	-1H	100
	666.6321	-2H	100
	444.0856	-3H	100

### 3. 2',3'-cyclic Monomer Polymerization

Oligomers with Open Phosphate Ring:			Oligomers with Closed Phosphate Ring:		
Base Composition	m/z (u)	Charge State	Base Composition	m/z (u)	Charge State
GG	707.0981	-1H	GG	689.0876	-1H
GC	667.092	-1H	GC	649.0814	-1H
CC	627.0859	-1H	CC	609.0753	-1H
GGG	1052.146	-1H	GGG	1034.135	-1H
GGC	1012.139	-1H	GGC	994.1289	-1H
GCC	972.1333	-1H	GCC	954.1227	-1H
CCC	932.1271	-1H	CCC	914.1166	-1H
GGGG	1397.193	-1H	GGGG	1379.183	-1H
	698.0929	-2H		689.0876	-2H
GGGC	1357.187	-1H	GGGC	1339.176	-1H
	678.0898	-2H		669.0845	-2H
GGCC	1317.181	-1H	GGCC	1299.17	-1H
	658.0867	-2H		649.0814	-2H
GCCC	1277.175	-1H	GCCC	1259.164	-1H
	638.0836	-2H		629.0784	-2H
CCCC	1237.168	-1H	CCCC	1219.158	-1H
	618.0806	-2H		609.0753	-2H
GGGGG	1743.244	-1H	GGGGG	1725.233	-1H
	871.1183	-2H		862.113	-2H
	580.4097	-3H		574.4062	-3H
GGGGC	1703.238	-1H	GGGGC	1685.227	-1H
	851.1152	-2H		842.1099	-2H
	567.0744	-3H		561.0708	-3H
GGGCC	1663.232	-1H	GGGCC	1645.221	-1H
	831.1121	-2H		822.1068	-2H
	553.739	-3H	GGCCC	1605.215	-1H
GGCCC	1623.225	-1H		802.1038	-2H
	811.109	-2H	GCCCC	1564.205	-1H
GCCCC	1582.216	-1H		781.599	-2H
	790.6043	-2H	CCCCC	1524.199	-1H
CCCCC	1542.21	-1H		761.5959	-2H
	770.6012	-2H	GGGGGG	2070.281	-1H
GGGGGG	2088.291	-1H		1034.637	-2H
	1043.642	-2H		689.422	-3H
	695.4256	-3H	GGGGGC	2030.275	-1H
GGGGGC	2048.285	-1H		1014.634	-2H
	1023.639	-2H		676.0867	-3H
	682.0902	-3H	GGGGCC	1990.268	-1H
GGGGCC	2008.279	-1H		994.6305	-2H
	1003.636	-2H		662.7513	-3H
	668.7548	-3H	GGGCCC	1950.262	-1H
GGGCCC	1968.273	-1H		974.6275	-2H
	983.6328	-2H		649.4159	-3H
	655.4194	-3H	GGCCCC	1910.256	-1H
GGCCCC	1928.267	-1H		954.6244	-2H

Oligomers with Open Phosphate Ring:			Oligomers with Closed Phosphate Ring:		
Base Composition	m/z (u)	Charge State	Base Composition	m/z (u)	Charge State
	963.6297	-2H		636.0805	-3H
GCCCCC	642.084	-3H	GCCCCC	1870.25	-1H
	1888.261	-1H		934.6213	-2H
	943.6266	-2H		622.7451	-3H
CCCCCC	628.7486	-3H	CCCCCC	1830.244	-1H
	1848.254	-1H		914.6182	-2H
	923.6235	-2H		609.4097	-3H
GGGGGGG	615.4133	-3H	GGGGGGG	2415.328	-1H
	2433.339	-1H		1207.16	-2H
	1216.166	-2H		804.4378	-3H
GGGGGGC	810.4414	-3H	GGGGGGC	603.0766	-4H
	607.5792	-4H		2375.322	-1H
	2393.333	-1H		1187.157	-2H
GGGGGCC	1196.163	-2H	GGGGGCC	791.1025	-3H
	797.106	-3H		593.075	-4H
	597.5777	-4H		2335.316	-1H
GGGGCCC	2353.326	-1H	GGGGCCC	1167.154	-2H
	1176.16	-2H		777.7671	-3H
	783.7706	-3H		583.0735	-4H
GGGGCCC	587.5761	-4H	GGGGCCC	2295.31	-1H
	2313.32	-1H		1147.151	-2H
	1156.157	-2H		764.4317	-3H
GGGCCCC	770.4352	-3H	GGGCCCC	573.072	-4H
	577.5746	-4H		2255.304	-1H
	2273.314	-1H		1127.148	-2H
GGCCCCC	1136.153	-2H	GGCCCCC	751.0963	-3H
	757.0998	-3H		563.0704	-4H
	567.5731	-4H		2215.297	-1H
GGCCCCC	2233.308	-1H	GGCCCCC	1107.145	-2H
	1116.15	-2H		737.7609	-3H
	743.7645	-3H		553.0689	-4H
GCCCCCC	557.5715	-4H	GCCCCCC	2175.291	-1H
	2193.302	-1H		1087.142	-2H
	1096.147	-2H		724.4255	-3H
CCCCCCC	730.4291	-3H	CCCCCCC	2135.285	-1H
	2153.296	-1H		1067.139	-2H
	1076.144	-2H		711.0902	-3H

### 5.3.3 Peak Analysis and Product Quantification

After measurement by HPLC-MS, the masses of the polymerization products were extracted from the raw mass spectrometry data and plotted in single chromatograms (ion count vs. time) with the Agilent software MassHunter Qualitative Analysis. I extracted the mass of the most abundant isotope of the molecule calculated by the Agilent Isotope Distribution Calculator (mass lists and chemical formulas of the polymerization products, see Chapter 5.3.2). For the ion extraction algorithm, I tolerated a symmetric margin of error of  $\Delta m/z = \pm 2.0$  ppm around the target m/z values. Peak identification for integration was performed by an en-

zyme digestion protocol, hydrolysis experiments or by comparing the retention times of the peaks of the sample with the retention times of the peaks from commercially available standards. I additionally verified that the selected peaks corresponded to the correct molecule by checking the isotope distribution signature of the peak in the first charge state (see Chapter 5.3.2 for isotope distributions). The selected peaks were integrated and the background was subtracted either manually using the MassHunter Qualitative Analysis program or with a self-coded LabVIEW program. To retrieve the concentration information from the integrated peak areas, a calibration procedure was used, which is described below.

### dAMP Accumulation

The dAMP peak in the sample was identified by comparison with an injection of commercially available dAMP in water and its retention time. The selected peak was integrated manually using the MassHunter Qualitative Analysis program. To remove the baseline noise, I performed a background subtraction. For that, an injection of RNase-free water was measured along with the samples. Then, the dAMP mass was also extracted from the water injection as described above and its chromatogram was integrated in the same time interval as the dAMP peak of the samples. The resulting integration value was subtracted as background from the integrated area values of the corresponding sample peaks. For calibration, the mass spectrometry data of monomers were measured over a wide range of concentration (0.01 mM, 0.05 mM, 0.1 mM, 0.5 mM, 1 mM, 5 mM, 10 mM, 20 mM, 50 mM, 100 mM, 200 mM, 500 mM, 700 mM in 100 mM MOPS at pH 6.5), then extracted and integrated as described above. The integrated peak area increased with increasing concentration.

Due to the broad measurement range the peak area vs. concentration, the calibration plots had to be fitted in two ranges, 0.01-20 mM and 20-700 mM (see Figure 5.6).

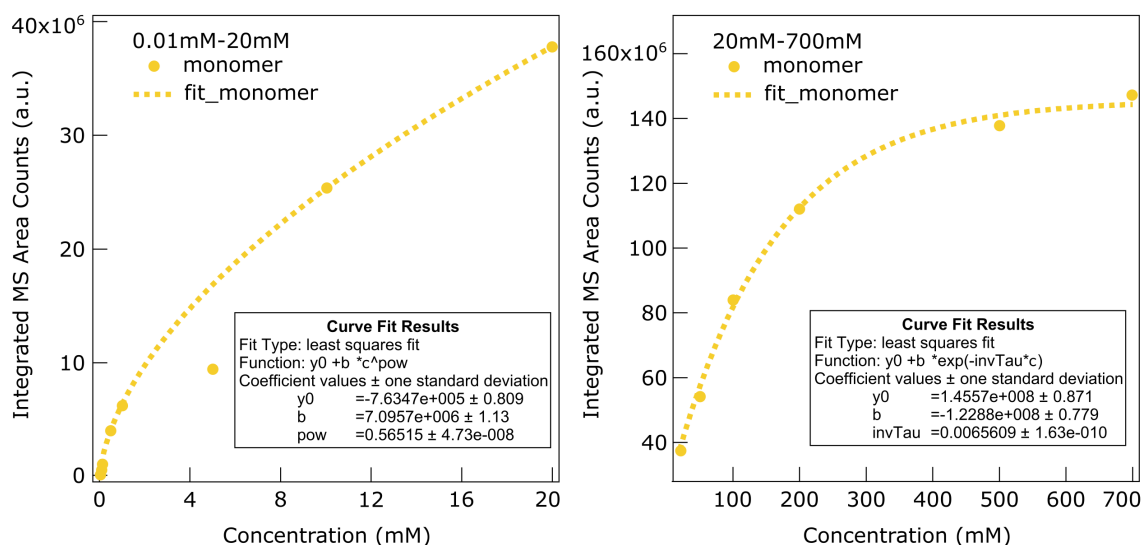


**Figure 5.6: Fitting of monomer calibration measurement data.** Mass spectrometric data from dAMP monomer measurements of known concentration (0.01 mM, 0.05 mM, 0.1 mM, 0.5 mM, 1 mM, 5 mM, 10 mM, 20 mM, 50 mM, 100 mM, 200 mM, 500 mM, 700 mM in 100 mM MOPS at pH 6.5) were extracted and integrated using the same method as for the samples. Concentration vs. peak area data points (circles) were fitted (dashed line) by least square fitting. Due to the wide range of measured concentration, the fit was performed in two intervals (0.01-20 mM and 20-700 mM monomer concentration) using a power-law function and an exponential function, respectively. The fit parameters are given in the box insets and in the text of Chapter 5.3.3.

For the concentration range 0.01-20 mM, the fit function was a power law

$$A(c)/F = y_0 + b \cdot c^{pow}, \quad (5.1)$$

where  $A$  is the area of the integrated peak,  $c$  the concentration of the monomer related to this peak on the day of the measurement,  $F$  is a correction factor and  $y_0 = -763470$ ,  $b = 7095700$  and  $pow = 0.565$  are fitting parameters, determined by least square fitting.

To account for variations in the measurement performance of the HPLC-MS machine between different days (see Figure 5.7), I introduced the correction factor  $F$ .  $F$  is given by the ratio of the integrated peak area of a 20 mM monomer injection measured on a measurement day  $A_{20mMStd}^{today}$  divided by the integrated peak area value of a 20mM monomer injection measured on the day of calibration  $A_{20mMStd}^{Calib} = 56604517$ .  $F$  was calculated anew on each measurement day by measuring a 20 mM standard monomer sample before measuring the actual experimental samples. The integrated peak area of a sample measured on a measurement day was divided by  $F$  to correct it to the value it would have had on the day of calibration.

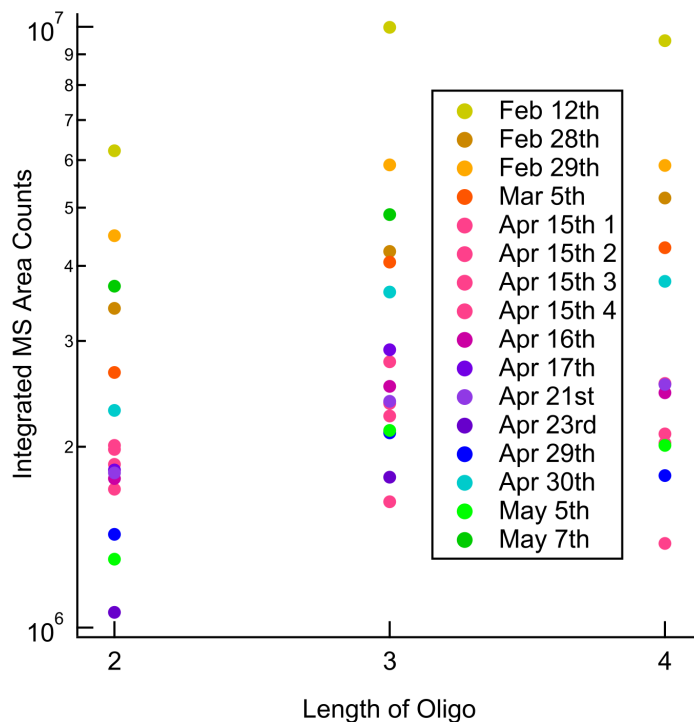


**Figure 5.7: Differences in the integrated MS peak area for the same monomer concentration injection.** 20  $\mu$ M of dAMP monomer standard in water have been injected to the HPLC-MS on different days and months of a year. One sees a significant difference in the integrated peak area counts for different measurement days, which makes the daily correction factor  $F$  necessary.

By inverting equation (5.1) to

$$c(A) = \left[ \frac{(A/F + 763470)}{7095700} \right]^{1.77} \quad (5.2)$$

now the concentration  $c(A)$  from the area  $A$  of a peak could be calculated.

For the concentration range 20-700 mM the same methods were used, but a different fit function was necessary:

$$A(c)/F = y_0 + b \exp\left(-\frac{c}{\tau}\right) \quad (5.3)$$

with the fit parameters  $y_0 = 145570000$ ,  $b = 122880000$ ,  $\tau = 152$  mM determined by least square fitting and the correction factor  $F$ .

By inverting equation 5.3, we obtain

$$c(A) = 152 \text{ mM} \frac{\ln(122880000)}{14557000 - A/F} . \quad (5.4)$$

The decision of which of the two fit functions to use was made by comparing the peak area in question to the area of the 20 mM-standard of a measurement day: peak areas with an area greater or equal to that of the measurement day's 20 mM-standard were inserted into the exponential fit-function, below that into the power-law function. All integrated peak areas of the monomer accumulation experiments were calibrated to concentrations using the procedure described above.

### AImpdA Polymerization

The masses of the AImpdA polymerization products (see Chapter 5.3.2) were extracted in the MassHunter Qualitative Analysis and the chromatograms for the different charge states were added up for each product. The selected peaks from these ion count vs. time chromatograms were integrated manually using the MassHunter Qualitative Analysis program. To remove the baseline noise, I performed a background subtraction. For that, an injection of RNase-free water was measured along with the samples. Then, the oligomer masses were also extracted from the water injection as described above and their chromatograms were integrated in the same time intervals as the peaks of the samples. The resulting integration value was subtracted as background from the integrated area values of the corresponding sample peaks.

In the AImpdA polymerization, two of the possible products - the pyrophosphate-linked and the linear oligomers - had the same masses and therefore their peaks appeared in the same MS-mass-chromatogram. The linear oligomer was identified by comparing the HPLC-retention times of the peaks with commercially available linear oligomer standards (2mers-4mers dA-oligomers with a 5'-phosphate, 3'-dA...dA-5'P, biomers.net GmbH, with HPLC purification) as can be seen in Figure 5.8.

The pyrophosphate oligomer peaks corresponded to those peaks that came down before the linear peaks in the same mass chromatogram following the examples of [57] and [11]. To ensure that the pyrophosphate peaks were correctly identified, I performed an enzyme digestion protocol using a pyrophosphatase (see Figure 5.9, Table 5.2 and Chapter 5.4.2).

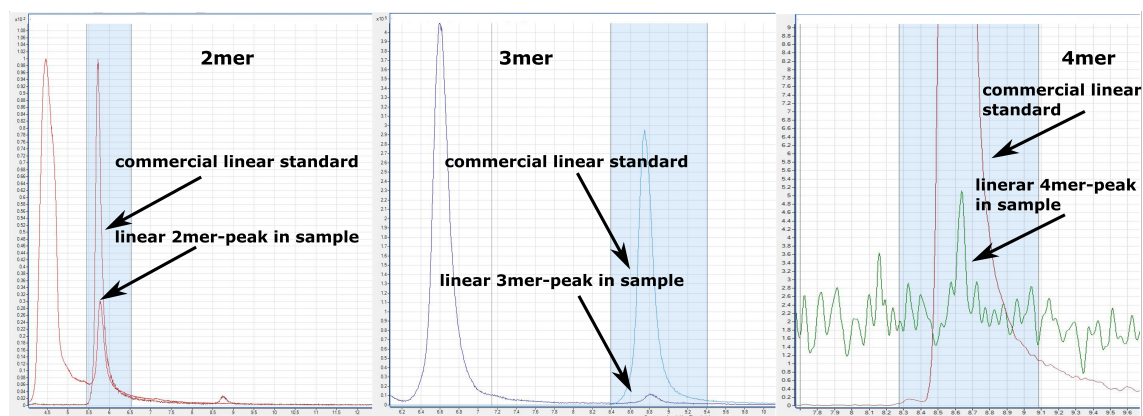


**Figure 5.8: Identification of the linear oligomer peaks by comparison with standards.** Commercially available 3'-dA...dA-5'P oligomer standards (2-4mers) were measured and extracted using the same method as the sample (here exemplarily a 300 mM AImpdA polymerization reaction). The linear oligomer is the one that has the same retention time as the commercially available linear oligomer standard for each length.

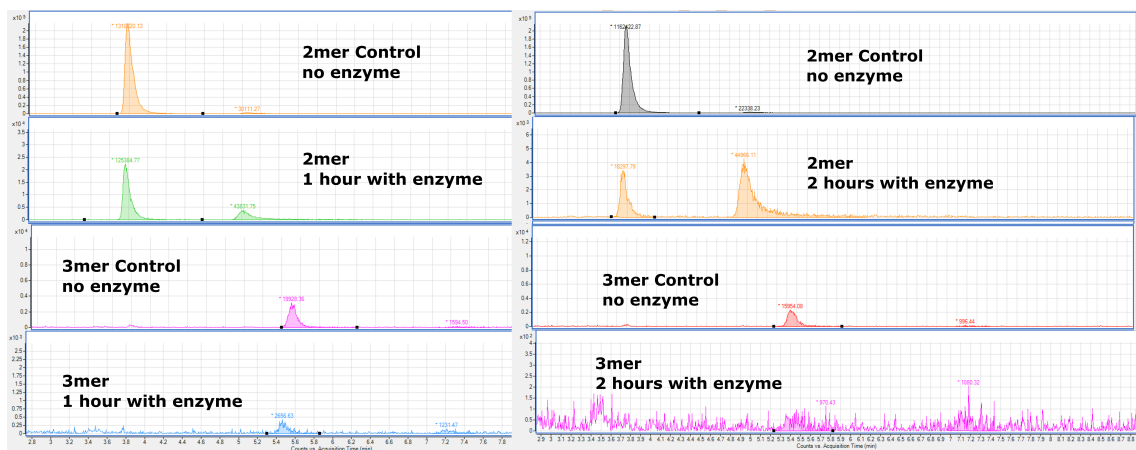


**Figure 5.9: Identification of the pyrophosphate-oligomer peaks by a pyrophosphatase enzyme digestion protocol.** 15  $\mu$ L of an AImpdA-polymerization sample was incubated for 1 h with a pyrophosphatase enzyme, which hydrolyzes pyrophosphate bonds in oligomers and cleaves them into shorter, linear oligomers (see Chapter 5.4.2 for enzyme digestion protocol). Then, both, the digested and the undigested samples were measured and extracted with HPLC-MS and MassHunter. The peak of the linear oligomer was identified by comparison with a commercially available standard (see Figure 5.8) for 2mer and 3mer. The first peak in the 2mer- and 3mer-chromatograms, with the same mass but an earlier retention time, shrank in integrated area counts when incubated with a pyrophosphatase enzyme, while the second, linear peak grew. The same result, but more pronounced, was observed in a second experiment in which I incubated another AImpdA-polymerization sample for 2 h with the pyrophosphatase enzyme. Hence, I concluded that the peaks which decreased in area indeed contained the pyrophosphate-linked oligomers. The linear peaks (at later retention times) grew because the pyrophosphatase enzyme cleaved longer pyrophosphate-oligomers to form shorter, linear oligomers, which then appeared additionally in the linear peaks of the chromatograms of the shorter oligomers and increased the integrated area counts there. The integrated area counts of the decreasing and increasing peaks are given in Table 5.2

Oligomer Length	Protocol	Area Pyrophosphate Peak	Area Linear Peak
2mer	Control	1310720	30111
	1 h enzyme digestion	125385	43831
	Control	1162422	22338
	2 h enzyme digestion	18297	44966
3mer	Control	19928	1594
	1 h enzyme digestion	2656	1231
	Control	15954	996
	2 h enzyme digestion	970	1080

**Table 5.2: Integrated area counts for decreasing and increasing peaks of AImpdA-polymerization products before and after pyrophosphatase enzyme digestion.** Two enzyme digestion experiments were performed in which I incubated 15  $\mu$ L of an AImpdA-polymerization sample for 1 h or 2 h with a pyrophosphatase enzyme. The increase and decrease of the areas of a peak denoted whether the amount of measured products in that peak was higher or lower after the digestion protocol. I saw that the areas of the pyrophosphate peaks shrank, while the area counts of the linear peaks increased after the enzyme digestion (see Figure 5.9). Thus, the pyrophosphate peaks indeed contained the pyrophosphate-linked oligomers from the AImpdA-polymerization reaction as the pyrophosphatase enzyme cleaved them into shorter, linear oligomers.

The activated oligomers had a different mass and were therefore seen individually in a different chromatogram and their peaks were easily identified. I additionally verified that the selected peaks corresponded to the correct molecule by checking the isotope distribution signature of the peak in the first charge state (see Chapter 5.3.2 for the isotope distributions). To obtain the concentration information from the integrated peak areas of the oligomers,

I used a similar calibration method as for the dAMP monomers: mass spectrometric data of oligomers (2-4mers dA-oligomers) of known concentration (0.01  $\mu\text{M}$ , 0.05  $\mu\text{M}$ , 0.1  $\mu\text{M}$ , 0.5  $\mu\text{M}$ , 1  $\mu\text{M}$ , 5  $\mu\text{M}$ , 10  $\mu\text{M}$ , 20  $\mu\text{M}$ , 50  $\mu\text{M}$ , 100  $\mu\text{M}$ , 200  $\mu\text{M}$ , 500  $\mu\text{M}$ , 750  $\mu\text{M}$ , 1000  $\mu\text{M}$  in water) was measured and extracted with the same method as used for the samples.

The integrated peak areas increased with increasing concentration. Concentration vs. peak area (circles) were fitted individually for each oligomer length (dotted lines) using a power-law function (see Figure 5.10) and least square fitting.

$$c(A) = y_0 + b(A/F)^{pow} \quad (5.5)$$

where  $A$  is the area of the integrated peak,  $c(A)$  the concentration of the oligomer related to this peak on the day of the measurement,  $F$  is the factor for the daily correction and  $y_0$ ,  $b$  and  $pow$  are fitting parameters. The fitting parameters for each concentration range and length of oligomer are summarized in the Table 5.3. All integrated peak areas for the AImpdA products where calibrated to concentrations using the procedure described above.

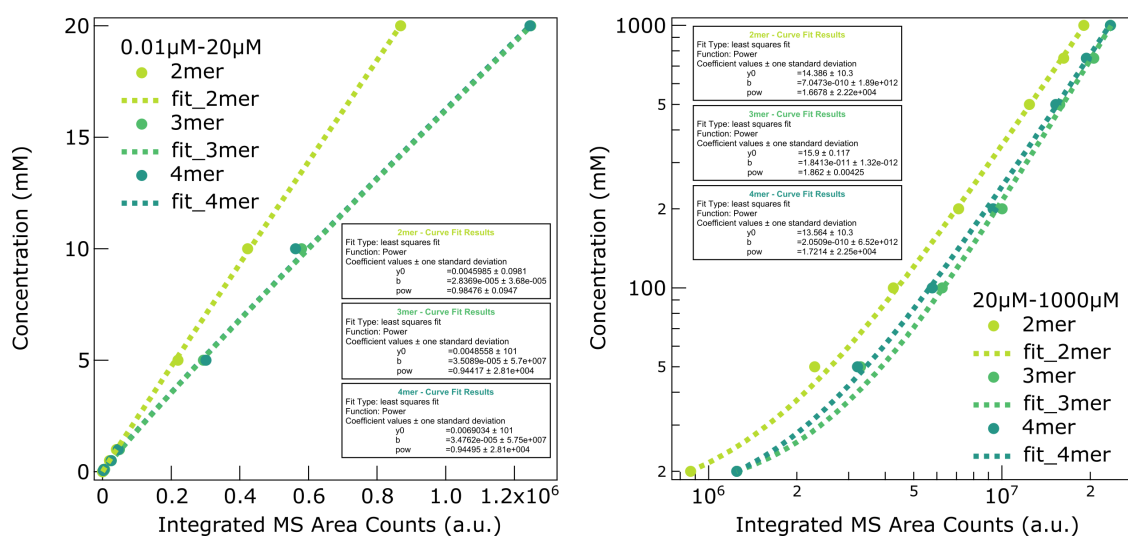


**Figure 5.10: Fitting of dA-oligomer calibration measurement data.** Mass spectrometric data of 3'-dA...dA-5'P oligomer measurements with known concentration (0.01  $\mu\text{M}$  - 1000  $\mu\text{M}$  in water) were extracted and integrated with the same method as the samples. The concentration vs. peak area data points (circles) were fitted (dashed lines) individually for each oligomer length (2mers yellow-green, 3mers light green, 4mers dark green) by least square fitting. Due to the wide range of measured concentration, the fit was performed for two intervals (0.01-20  $\mu\text{M}$  and 20-700  $\mu\text{M}$  monomer concentration) using a power-law function with two different parameter sets. The fit parameters are given in the box insets and in Table 5.3.

Length	Fit Range	$y_0(\mu\text{M})$	$b(\mu\text{M})$	pow	$A_{20\mu\text{MStd}}^{\text{Calib}}$
2mer	0.01-20 $\mu\text{M}$	4.5985e-3	2.8369e-5	0.98476	834081
	20-1000 $\mu\text{M}$	14.38	7.0473e-10	1.6678	
3mer	0.01-20 $\mu\text{M}$	4.8558e-3	3.5089e-5	0.94417	1102110
	20-1000 $\mu\text{M}$	15.9	1.8413e-11	1.862	
4mer	0.01-20 $\mu\text{M}$	6.9034e-3	3.4762e-5	0.94495	1272060
	20-1000 $\mu\text{M}$	13.564	2.0509e-10	1.7214	

**Table 5.3: Fitting parameters for concentration calibration measurements for the AImpdA polymerization products.** Due to the wide range of measured concentration, the least square fit was performed for two intervals (0.01-20  $\mu\text{M}$  and 20-1000  $\mu\text{M}$  oligomer concentration), using different power-law functions for each interval and oligomer length.

## 2',3'-cyclic Monomer Polymerization

For the quantification of polymerization products from 2',3'-cyclic monomers, I used the Agilent software MassHunter Qualitative Analysis and a self-coded LabVIEW program to integrate the product chromatogram peaks. The oligomers formed during the polymerization process 2',3'-cyclic monomers had either an open 2'- or 3'-phosphate end or a closed 2',3'-phosphate ring. The masses of these two types of polymerization products were calculated as described in Chapter 5.3.2. For mass spectrometry analysis, it was necessary to search for both types of oligomers as they differ in weight by one water molecule. Both oligomer types were extracted in single chromatograms for each length and the peaks were integrated and calibrated to concentration one by one. I extracted these  $m/z$  values from the full MS-spectra into an ion counts vs. time chromatogram using MassHunter software, allowing for an imprecision of  $\Delta m/z = \pm 2$  ppm. The chromatograms were saved as .csv ASCII files for further analysis with the LabVIEW program which is provided in Dataset D3 (TOF\_Integrator2.4.vi).

The .csv files were loaded into the LabVIEW program, which summed the chromatograms for different charged states for each possible polymerization product. For integration, the peak selection for the oligomers with an open phosphate ring was performed by comparison to commercially available standards of matching oligomer lengths (2mers-7mers G-oligomers with a 3'-phosphate, 3'-G...G-5'P, biomers.net GmbH, with HPLC purification) as can be seen in Figure 5.11. This control sample with known concentration (10  $\mu$ M per Nmer, mixed 2-7mers) was always measured alongside the samples from the experiment and also served for the concentration calibration later on.

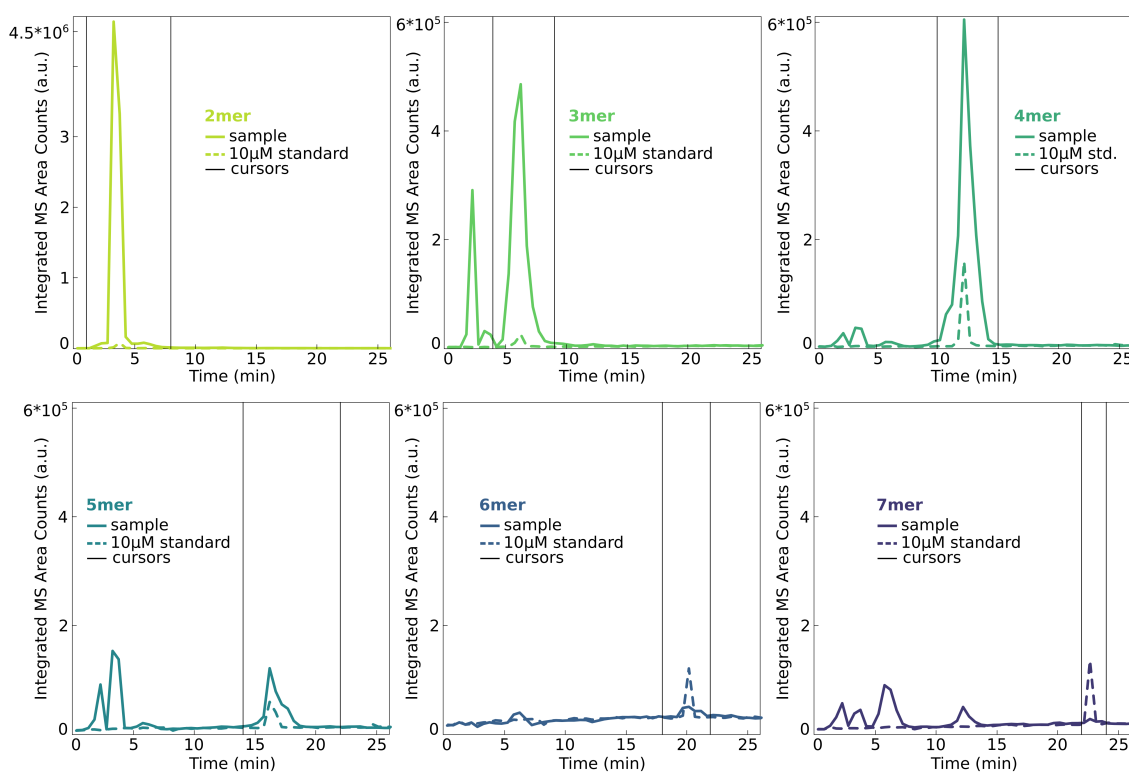


**Figure 5.11: Identification of the linear oligomer peaks by comparison with standards.** Commercially available 3'P-G...G-5' oligomer standards (2-7mers) were measured and extracted using the same method as for the sample (here exemplarily a 10 mM 2',3'-cGMP/50 mM 2',3'-cCMP polymerization reaction). The linear oligomer peak was the one that had the same retention time as the commercially available linear oligomer standard for each length.

The peak selection for the oligomers with a closed phosphate ring was done by selecting the peak with matching mass that came down immediately before the peak of the corresponding oligomer with the open phosphate ring of the same length. This identification was conducted with hydrolysis experiments described in [14]. The identification after the selection by mass is confirmed by checking the isotope pattern of each oligomer with a self-coded LabVIEW program provided in Dataset D3 (SpectraBrowser1.03.vi) which is based on the open source code "IsoSpec2: Ultrafast Fine Structure Calculator" [58]. In the program the theoretical isotope patterns (green) of the products were compared with the measured ones (white) and only chromatograms were used for integration and quantification that showed a quality factor above 2. A closer description of the LabVIEW software can be found in [14]. All isotope patterns are documented as .pngs in Dataset D4.

The selected peaks were integrated in a time interval defined by two cursors set manually to meet the criteria described above. To remove the baseline noise, I performed a background subtraction from the integrated peak area. Depending on the type of the peak, the background subtraction was carried out either by linear extrapolation of a slanted baseline between the two cursor positions (for 3-7mers) or using the chromatogram value at the left cursor position (for 2mers) as the baseline. The integrated peak areas were calibrated daily with a one-point calibration using the 10  $\mu$ M-standards to obtain the concentration values of the oligomers from the HPLC-MS measurements. I used a one-point-calibration because I showed that the oligomer amount (in moles) scaled linearly with the integrated peak area (see Figure 5.12).

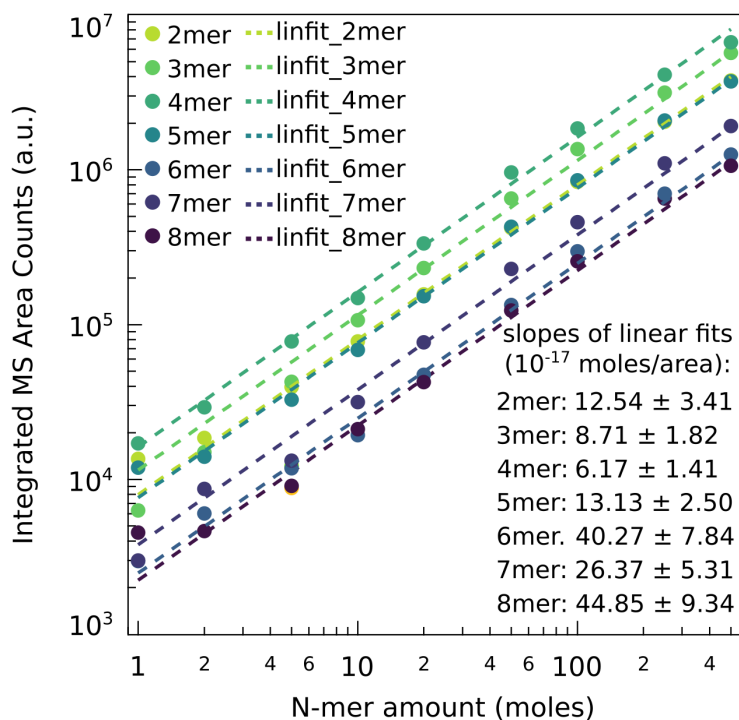


**Figure 5.12: The oligomer amount (in moles) scales linearly with the integrated peak area.** Commercially available 2-8mer polyG oligomers (3'-P-G...G-5', 3'-phosphate biomers.net GmbH, with HPLC purification) with known amounts (1 pmol, 2 pmol, 5 pmol, 10 pmol, 20 pmol, 50 pmol, 100 pmol, 250 pmol, 500 pmol in water) were measured, extracted and integrated with the same method as the RNA polymerization samples. In search for a fit function for the area to mole relationship, I found that the data points (circles) for oligomer amount (in moles) to integrated peak area were best fitted with linear functions for all oligomers lengths (dashed lines).

Thus, I calculated the concentration  $c_{smp}^n$  of an oligomer of a certain length  $n$  in a sample under study via the following equation:

$$c_{smp}^n = \frac{A_{smp}^n}{V_{smp}} * \frac{c_{Std}^n * V_{Std}}{A_{Std}^n}, \quad (5.6)$$

where  $c_{Std}^n$  is the concentration of oligomers of length  $n$  in the injected standard,  $A_{Std}^n$  is the integrated peak area of an oligomer of length  $n$  in the injected standard,  $A_{smp}^n$  is the integrated peak area of an oligomer of length  $n$  in the injected sample,  $V_{smp}$  is the injection volume of the sample and  $V_{Std}$  is the injection volume of the standard.

In this way, I calculated the concentration of each oligomer of each length and ending type (closed or open) in the samples.

## 5.4 Chemistry

### 5.4.1 dAMP Accumulation

For each experiment, deoxyadenosine-5'-monophosphate disodium salt (dAMPNa<sub>2</sub>, CAS No. 2922-74-9, Carbosynth Ltd.) powder was allowed to reach room temperature, weighed into a low-binding test tube and mixed with a 100 mM 3-(N-morpholino)propanesulfonic acid (MOPS) buffer solution to the desired concentration (300 mM, 20 mM, 2.5 mM). No other salts were added. The pH was not adjusted, it naturally settled at pH 6.5. The sample mixture was filled into a thermophoretic pore, which had beforehand been filled with low viscosity oil (3M TM Novec TM 7500, IoLiTec Ionic Liquids Technologies GmbH) to allow complete filling of the pore without introducing any air bubbles. Novec Oil was checked in a separate experiment to not change the polymerization behavior, the filling procedure can be observed in the Movie M1. The pore was operated for 24 h at a temperature gradient of  $\Delta T = 22^\circ\text{C}$ , with the hot temperature at  $30^\circ\text{C}$  and the cold temperature at  $8^\circ\text{C}$  at the front respectively back of the solution.

### 5.4.2 AImpdA DNA Monomers

#### AImpdA Synthesis

3.3 mmol (1 eq) deoxythymidine-5'-monophosphate disodium salt (dTMPNa<sub>2</sub>, CAS No. 33430-62-5, Carbosynth Ltd.) and 16.4 mmol (1 eq) 2-aminoimidazole sulfate salt (SKU No. 197912-2.5G, Sigma Aldrich) were dissolved in 25 mL of RNase free water (Ambion TM Nuclease-Free Water, Ref. No. AM 9932, Life Technologies Corporation) in a 50 mL polypropylene Falcon tube. The pH was adjusted to pH 5.7 by adding a solution of syringe-filtered 1 M hydrogen chloride (HCl, Art. No. K025.1, Carl Roth GmbH + Co. KG). RNase free water was added to give a total volume of 30 mL. The mixture was filtered with a  $0.45\ \mu\text{m}$  filter and aliquoted into two 50 mL polypropylene Falcon tubes, flash-frozen in liquid nitrogen, and lyophilized for two days.

In 250 mL glass round-bottom flasks, a mixture of 50 mL anhydrous dimethyl sulfoxide (SKU No. 276855-1L, Sigma-Aldrich) and 6.2 mL anhydrous triethylamine (CAS No. 121-44-8, Carl Roth GmbH + Co. KG) was stirred under argon. The lyophilized products were added and heated gently in a flame for 30 min. To each flask, 29.5 mmol (9 eq) triphenylphosphine (TEA, CAS No. 603-35-0, Carl Roth GmbH + Co. KG COMPANY) and 32.8 mmol (10 eq) 2,2'-dipyridyldisulfide (SKU No. 8411090005, Sigma-Aldrich) were added. The mixtures were stirred under argon for 30 min. The solutions were poured in an ice-cooled glass bottle containing a mixture of 400 mL acetone (UN No. 1019, Carl Roth GmbH + Co. KG), 250 mL diethyl ether (CAS No. 60-29-7 Carl Roth GmbH + Co. KG company), 30 mL trimethylamine

(UN No. 1296, Carl Roth GmbH + Co. KG) and 1.6 mL acetone saturated with natriumperchlorat ( $\text{NaClO}_4$ ) (SKU No. 410241-500G, Sigma-Aldrich), and stirred until the product flocculated.

Stirring was stopped and the bottle was put on ice for 30 min. The solution was collected in 50ml propylene Falcon tubes and centrifuged at 4000 rpm for 3 min at 10 °C. The supernatant was discarded and the pellets were resuspended in 10ml of a 1 : 8.3 : 13.3 of triethylamine : diethyl ether : acetone mixture. The new solutions were vortexed and centrifuged at 4000 rpm for 3 min at 10 °C. The supernatant was discarded, and the step was repeated. The pellet was washed twice with 10 mL acetone and twice with 10 mL diethyl ether. The pellets were dried overnight under vacuum. The product was stored at -20 °C.

### **AImpdA Polymerization**

For an experiment, the self-synthesized AImpdA powder was allowed to reach room temperature, weighed, put into a low-binding test tube (DNA LoBind Tubes, Eppendorf AG), and mixed with a 100 mM 3-(N-morpholino)propanesulfonic acid (MOPS) buffer solution (CAS No. 1132-61-2, Carl Roth GmbH + Co. KG mixed with RNase-free water) to the desired concentration (300 mM, 20 mM, 2.5 mM). No other salts were added. The pH was not adjusted, it naturally settled at pH 6.5.

The sample mixture was filled into a thermophoretic pore, which had beforehand been filled with low viscosity oil (3M TM Novec TM 7500, IoLiTec Ionic Liquids Technologies GmbH) to allow complete filling of the pore without introducing any air bubbles. Novec Oil was checked in a separate experiment to not change the polymerization behavior, the filling procedure can be observed in the [Movie M1](#). The pore was operated for 24 h at a temperature gradient of  $\Delta T = 22$  °C, with the hot temperature at 30 °C and the cold temperature at 8 °C at the front respectively back of the solution. For the bulk controls, 20  $\mu\text{L}$  of sample was filled in Eppendorf test tubes and covered with 15  $\mu\text{L}$  of paraffin oil (Art. No. 9190.1, Carl Roth GmbH + Co. KG) to prevent any evaporation inside the test tube. Paraffin oil was checked in a separate experiment to not change the polymerization behaviour. The tubes were incubated for 24 h at 30 °C and 8 °C, respectively.

### **Pyrophosphatase Enzyme Digestion Protocol**

I used the NudC Pyrophosphatase Kit (M0607S, New England BioLabs Inc.) for digestion of pyrophosphate-linkages in the AImpdA-polymerization products. After 24 h of incubation at 20 °C in a test tube, 15  $\mu\text{L}$  of a 2.5 mM-AImpdA sample were mixed in a new test tube with the following chemicals, all included in the kit: 2  $\mu\text{L}$  of NEBuffer 3.1 (10x), 1  $\mu\text{L}$  of 100 mM DTT (dithiothreitol) and 2  $\mu\text{L}$  of NudC pyrophosphatase (10  $\mu\text{M}$ ). The tube was vortexed, spun down and incubated for either 1 h or 2 h at 37 °C. Without further treatment, I measured the digested sample with the same HPLC-MS protocol as the undigested sample (see [Chapter 5.3.1](#)) and compared the results of both measurements. Data and analysis are shown in [Figure 5.9](#) and [Table 5.2](#).

### **5.4.3 2',3'-Cyclic RNA Monomers**

2',3'-cCMP (CAS No. 15718-51-1, Sigma-Aldrich) and 2',3'-cGMP (Cat. No. G025-50, Biolog Life Science Institute GmbH and Co. KG) were mixed with RNase free water to create a stock solution of 300 mM. These stocks were stored at -80 °C. For an experiment, the stock solutions were diluted with RNase-free water to the desired concentrations and G/C ratios (10 mM/50 mM, 1 mM/5 mM, 20 mM/20 mM, 2 mM/2 mM). The pH of the solution was adjusted to pH 10.5 with potassium hydroxide (KOH, Art. No. K017.1, Carl Roth GmbH + Co. KG). If visualization of the accumulation process was desired, 10  $\mu\text{M}$  Cy5 fluorescent dye (Cat. 23390, Lumiprobe GmbH, excitation maximum: 649 nm, emission maximum: 666 nm)

were added, which was tested in a separate experiment not to change the polymerization behavior. The sample mixture was filled into an air-filled thermophoretic pore from its top until it filled the upper 4/5 of the chamber volume, the lowest fifth was left air-filled to create the liquid-gas interface. The filling procedure with an air-water interface is shown in [Movie M2](#). The pore was operated for 18 h at a temperature gradient of  $\Delta T = 30\text{ }^{\circ}\text{C}$ , with the hot temperature at  $70\text{ }^{\circ}\text{C}$  and the cold temperature at  $40\text{ }^{\circ}\text{C}$ . For the dry control,  $20\text{ }\mu\text{L}$  of the sample was filled in test tubes and incubated for 18 h at  $70\text{ }^{\circ}\text{C}$  and  $40\text{ }^{\circ}\text{C}$ , respectively, with the tube lid open to allow evaporation. After the 18 h, samples were rehydrated with  $20\text{ }\mu\text{L}$  of RNase free water. For bulk controls,  $20\text{ }\mu\text{L}$  of sample was filled in test tubes and covered with  $15\text{ }\mu\text{L}$  of low viscosity paraffin oil (CAS No. 8042-47-5, Carl Roth GmbH + Co. KG) to prevent any evaporation inside the test tube. The tubes were kept with closed lids for 18 h at  $70\text{ }^{\circ}\text{C}$  and  $40\text{ }^{\circ}\text{C}$ , respectively.

# Bibliography

- [1] S. A. Benner. Defining life. *Astrobiology*, 10(10):1021–30, 2010. <https://www.ncbi.nlm.nih.gov/pubmed/21162682>.
- [2] M. Jauker, H. Griesser, and C. Richert. Spontaneous formation of RNA strands, peptidyl RNA, and cofactors. *Angew Chem Int Ed Engl*, 54(48):14564–9, 2015. <https://www.ncbi.nlm.nih.gov/pubmed/26435376>.
- [3] J. P. Ferris. Mineral catalysis and prebiotic synthesis: Montmorillonite-catalyzed formation of RNA. *Elements*, 1(3):145–149, 2005. <https://pubs.geoscienceworld.org/msa/elements/article-abstract/1/3/145/137565/Mineral-Catalysis-and-Prebiotic-Synthesis?redirectedFrom=fulltext>.
- [4] M. S. Verlander, R. Lohrmann, and L. E. Orgel. Catalysts for the self-polymerization of adenosine cyclic 2',3'-phosphate. *J Mol Evol*, 2(4):303–16, 1973. <https://link.springer.com/article/10.1007/BF01654098>.
- [5] C. B. Mast, S. Schink, U. Gerland, and D. Braun. Escalation of polymerization in a thermal gradient. *Proceedings of the National Academy of Sciences of the United States of America*, 110(20):8030–8035, 2013. <https://www.ncbi.nlm.nih.gov/pmc/articles/PMC3657786/pdf/pnas.201303222.pdf>.
- [6] M. W. Powner, B. Gerland, and J. D. Sutherland. Synthesis of activated pyrimidine ribonucleotides in prebiotically plausible conditions. *Nature*, 459(7244):239–242, 2009. <https://dx.doi.org/10.1038/nature08013>.
- [7] J. S. Teichert, F. M. Kruse, and O. Trapp. Direct prebiotic pathway to DNA nucleosides. *Angewandte Chemie-International Edition*, 58(29):9944–9947, 2019. <https://onlinelibrary.wiley.com/doi/10.1002/anie.201903400>.
- [8] D. J. Ritson and J. D. Sutherland. Conversion of biosynthetic precursors of RNA to those of DNA by photoredox chemistry. *Journal of Molecular Evolution*, 78(5):245–250, 2014. [https://www.ncbi.nlm.nih.gov/pmc/articles/PMC4037592/pdf/239\\_2014\\_Article\\_9617.pdf](https://www.ncbi.nlm.nih.gov/pmc/articles/PMC4037592/pdf/239_2014_Article_9617.pdf).
- [9] A. M. Steer, N. Bia, D. K. Smith, and P. A. Clarke. Prebiotic synthesis of 2-deoxy-d-ribose from interstellar building blocks promoted by amino esters or amino nitriles. *Chem Commun Cambridge*, 53(75):10362–10365, 2017. <https://pubs.rsc.org/en/content/articlepdf/2017/cc/c7cc06083a>.
- [10] R. Lohrmann and L. E. Orgel. Prebiotic activation processes. *Nature*, 244(5416):418–420, 1973. <https://www.nature.com/articles/244418a0>.
- [11] G. Ertem and J. P. Ferris. Synthesis of RNA oligomers on heterogeneous templates. *Nature*, 379(6562):238–240, 1996. <https://www.nature.com/articles/379238a0>.

- [12] B. T. Burcar, M. Jawed, H. Shah, and L. B. McGown. In situ imidazole activation of ribonucleotides for abiotic RNA oligomerization reactions. *Origins of Life and Evolution of Biospheres*, 45(1-2):31–40, 2015. <https://link.springer.com/article/10.1007/s11084-015-9412-y>.
- [13] H. R. Kricheldorf. *Leben Durch Chemische Evolution? Eine Kritische Bestandsaufnahme Von Experimenten und Hypothesen*. Springer Berlin / Heidelberg, Berlin, Heidelberg, 2019. <https://ebookcentral.proquest.com/lib/kxp/detail.action?docID=5785392>.
- [14] A. Dass, S. Wunnavva, J. Langlais, B. von der Esch, M. Krusche, L. Ufer, N. Chrisam, R. Dubini, F. Gartner, S. Angerpointner, F. P. Dirscherl, C. F. Rovó, C. B. Mast, J. E. Šponer, C. Ochsenfeld, E. Frey, and D. Braun. RNA auto-polymerisation from 2',3'-cyclic nucleotides at air-water interfaces. *Submitted to Angewandte in 2022. [Non-peer-reviewed pre-print] in ChemRxiv Cambridge Open Engage*, 2022. <https://doi.org/10.26434/chemrxiv-2022-zwh2t>.
- [15] M. S. Verlander and L. E. Orgel. Analysis of high molecular weight material from the polymerization of adenosine cyclic 2',3'-phosphate. *J Mol Evol*, 3(2):115–20, 1974. <https://link.springer.com/article/10.1007/BF01796557>.
- [16] K. Dose. Peptides and amino acids in the primordial hydrosphere. *Biosystems*, 6(4):224–8, 1975. <https://www.ncbi.nlm.nih.gov/pubmed/1137721>.
- [17] C. de Duve. *Blueprint for a cell: The nature and origin of life*. Portland Press, Burlington, N.C., 1991.
- [18] I. Budin, R. J. Bruckner, and J. W. Szostak. Formation of protocell-like vesicles in a thermal diffusion column. *Journal of the American Chemical Society*, 131(28):9628–9629, 2009. <https://pubs.acs.org/doi/pdf/10.1021/ja9029818>.
- [19] T. Matreux, K. Le Vay, A. Schmid, P. Aikkila, L. Belohlavek, A. Z. Caliskanoglu, E. Salibi, A. Kuhnlein, C. Springsklee, B. Scheu, D. B. Dingwell, D. Braun, H. Mutschler, and C. B. Mast. Heat flows in rock cracks naturally optimize salt compositions for ribozymes. *Nat Chem*, 13(11):1038–1045, 2021. <https://www.ncbi.nlm.nih.gov/pubmed/34446924>.
- [20] W. B. Moore and A. A. Webb. Heat-pipe earth. *Nature*, 501(7468):501–5, 2013. <https://www.nature.com/articles/nature12473>.
- [21] D. S. Kelley, J. A. Karson, G. L. Fruh-Green, D. R. Yoerger, T. M. Shank, D. A. Butterfield, J. M. Hayes, M. O. Schrenk, E. J. Olson, G. Proskurowski, M. Jakuba, A. Bradley, B. Larson, K. Ludwig, D. Glickson, K. Buckman, A. S. Bradley, W. J. Brazelton, K. Roe, M. J. Elend, A. Delacour, S. M. Bernasconi, M. D. Lilley, J. A. Baross, R. E. Summons, and S. P. Sylva. A serpentinite-hosted ecosystem: the lost city hydrothermal field. *Science*, 307(5714):1428–34, 2005. <https://www.ncbi.nlm.nih.gov/pubmed/15746419>.
- [22] D. Niether, D. Afanasenkau, J. K. G. Dhont, and S. Wiegand. Accumulation of formamide in hydrothermal pores to form prebiotic nucleobases. *Proceedings of the National Academy of Sciences of the United States of America*, 113(16):4272–4277, 2016. <https://www.ncbi.nlm.nih.gov/pmc/articles/PMC4843465/pdf/pnas.201600275.pdf>.
- [23] C. B. Mast and D. Braun. Thermal trap for DNA replication. *Physical Review Letters*, 104(18):188102, 2010. <https://link.aps.org/doi/10.1103/PhysRevLett.104.188102>.
- [24] M. Kreysing, L. Keil, S. Lanzmich, and D. Braun. Heat flux across an open pore enables the continuous replication and selection of oligonucleotides towards increasing length. *Nature Chemistry*, 7(3):203–208, 2015. <https://www.nature.com/articles/nchem.2155>.

- [25] L. Keil, M. Hartmann, S. Lanzmich, and D. Braun. Probing of molecular replication and accumulation in shallow heat gradients through numerical simulations. *Physical Chemistry Chemical Physics*, 18(30):20153–20159, 2016. <https://pubs.rsc.org/en/content/articlepdf/2016/cp/c6cp00577b>.
- [26] P. Baaske, F. M. Weinert, S. Duhr, K. H. Lemke, M. J. Russell, and D. Braun. Extreme accumulation of nucleotides in simulated hydrothermal pore systems. *Proceedings of the National Academy of Sciences of the United States of America*, 104(22):9346–9351, 2007. <https://www.ncbi.nlm.nih.gov/pmc/articles/PMC1890497/pdf/zpq9346.pdf>.
- [27] Z. L. Wang, H. Kriegs, and S. Wiegand. Thermal diffusion of nucleotides. *Journal of Physical Chemistry B*, 116(25):7463–7469, 2012. <https://pubs.acs.org/doi/10.1021/jp3032644>.
- [28] D. K. O’Flaherty, N. P. Kamat, F. N. Mirza, L. Li, N. Prywes, and J. W. Szostak. Copying of mixed-sequence RNA templates inside model protocells. *Journal of the American Chemical Society*, 140(15):5171–5178, 2018. <https://pubs.acs.org/doi/pdf/10.1021/jacs.8b00639>.
- [29] H. Peng, A. Lelievre, K. Landefeld, S. Muller, and I. A. Chen. Vesicle encapsulation stabilizes intermolecular association and structure formation of functional RNA and DNA. *Current Biology*, 32(1):86–96.e6, 2022. [https://www.cell.com/current-biology/pdf/S0960-9822\(21\)01491-3.pdf](https://www.cell.com/current-biology/pdf/S0960-9822(21)01491-3.pdf).
- [30] E. Edeleva, A. Salditt, J. Stamp, P. Schwintek, J. Boekhoven, and D. Braun. Continuous nonenzymatic cross-replication of DNA strands with in situ activated DNA oligonucleotides. *Chemical Science*, 10(22):5807–5814, 2019. <https://www.ncbi.nlm.nih.gov/pmc/articles/PMC6568275/pdf/SC-010-C9SC00770A.pdf>.
- [31] T. Lay, J. Hernlund, and B. A. Buffett. Core–mantle boundary heat flow. *Nature Geoscience*, 1(1):25–32, 2008. <https://www.nature.com/articles/ngeo.2007.44>.
- [32] Nicholas T. Arndt and Euan G. Nisbet. Processes on the young earth and the habitats of early life. *Annual Review of Earth and Planetary Sciences*, 40(1):521–549, 2012. <https://doi.org/10.1146/annurev-earth-042711-105316>.
- [33] M. Morasch, J. Liu, C. F. Dirscherl, A. Ianeselli, A. Kuhnlein, K. Le Vay, P. Schwintek, S. Islam, M. K. Corpinot, B. Scheu, D. B. Dingwell, P. Schwillie, H. Mutschler, M. W. Powner, C. B. Mast, and D. Braun. Heated gas bubbles enrich, crystallize, dry, phosphorylate and encapsulate prebiotic molecules. *Nature Chemistry*, 11(9):779–788, 2019. <https://www.nature.com/articles/s41557-019-0299-5>.
- [34] A. Ianeselli, C. B. Mast, and D. Braun. Periodic melting of oligonucleotides by oscillating salt concentrations triggered by microscale water cycles inside heated rock pores. *Angewandte Chemie-International Edition*, 58(37):13155–13160, 2019. <https://onlinelibrary.wiley.com/doi/10.1002/anie.201907909>.
- [35] G. Y. Zhou, G. Sun, X. Wang, C. Y. Zhou, S. G. McNulty, J. M. Vose, and D. M. Amatya. Estimating forest ecosystem evapotranspiration at multiple temporal scales with a dimension analysis approach. *Journal of the American Water Resources Association*, 44(1):208–221, 2008. <https://onlinelibrary.wiley.com/doi/10.1111/j.1752-1688.2007.00148.x>.
- [36] J. D. Toner and D. C. Catling. A carbonate-rich lake solution to the phosphate problem of the origin of life. *Proceedings of the National Academy of Sciences of the United States of America*, 117(2):883–888, 2020. <https://www.ncbi.nlm.nih.gov/pmc/articles/PMC6969521/pdf/pnas.201916109.pdf>.

- [37] B. Damer and D. Deamer. The hot spring hypothesis for an origin of life. *Astrobiology*, 20(4):429–452, 2020. <https://www.liebertpub.com/doi/pdf/10.1089/ast.2019.2045?download=true>.
- [38] K. C. Benison and B. B. Bowen. Extreme sulfur-cycling in acid brine lake environments of western australia. *Chemical Geology*, 351:154–167, 2013. <https://www.sciencedirect.com/science/article/abs/pii/S0009254113002246?via%3Dihub>.
- [39] C. V. Mungi and S. Rajamani. Characterization of RNA-like oligomers from lipid-assisted nonenzymatic synthesis: Implications for origin of informational molecules on early earth. *Life (Basel)*, 5(1):65–84, 2015. <https://www.ncbi.nlm.nih.gov/pubmed/25569237>.
- [40] M. Reichl, M. Herzog, A. Gotz, and D. Braun. Why charged molecules move across a temperature gradient: the role of electric fields. *Phys Rev Lett*, 112(19):198101, 2014. <https://www.ncbi.nlm.nih.gov/pubmed/24877967>.
- [41] S. Dühr and D. Braun. Why molecules move along a temperature gradient. *Proc Natl Acad Sci U S A*, 103(52):19678–82, 2006. <https://www.ncbi.nlm.nih.gov/pubmed/17164337>.
- [42] P. Debye. Zur Theorie des Clusiuschen Trennverfahrens. *Annalen der Physik*, 428(3-4):284–294, 1939. <https://onlinelibrary.wiley.com/doi/abs/10.1002/andp.19394280310>.
- [43] K. Clusius and G. Dickel. Neues Verfahren zur Gasentmischung und Isotopentrennung. *Naturwissenschaften*, 26(33):546–546, 1938. <https://doi.org/10.1007/BF01675498>.
- [44] R. D. Deegan, O. Bakajin, T. F. Dupont, G. Huber, S. R. Nagel, and T. A. Witten. Capillary flow as the cause of ring stains from dried liquid drops. *Nature*, 389(6653):827–829, 1997. <https://doi.org/10.1038/39827>.
- [45] H. Hu and R. G. Larson. Evaporation of a sessile droplet on a substrate. *The Journal of Physical Chemistry B*, 106(6):1334–1344, 2002. <https://doi.org/10.1021/jp0118322>.
- [46] W. Gilbert. Origin of life: The RNA world. *Nature*, 319(6055):618–618, 1986. <https://www.nature.com/articles/319618a0.pdf>.
- [47] R. Lohrmann and L. E. Orgel. Urea-inorganic phosphate mixtures as prebiotic phosphorylating agents. *Science*, 171(3970):490–494, 1971. <https://doi.org/10.1126/science.171.3970.490>.
- [48] M. Morasch, C. B. Mast, J. K. Langer, P. Schilcher, and D. Braun. Dry polymerization of 3',5'-cyclic GMP to long strands of RNA. *Chembiochem*, 15(6):879–83, 2014. <https://chemistry-europe.onlinelibrary.wiley.com/doi/10.1002/cbic.201300773>.
- [49] J. E. Šponer, J. Šponer, A. Giorgi, E. Di Mauro, S. Pino, and G. Costanzo. Untemplated nonenzymatic polymerization of 3',5'-cGMP: a plausible route to 3',5'-linked oligonucleotides in primordia. *J Phys Chem B*, 119(7):2979–89, 2015. <https://pubs.acs.org/doi/10.1021/acs.jpcc.5b00601>.
- [50] A. Salditt, L. M. R. Keil, D. P. Horning, C. B. Mast, G. F. Joyce, and D. Braun. Thermal habitat for RNA amplification and accumulation. *Phys Rev Lett*, 125(4):048104, 2020. <https://www.ncbi.nlm.nih.gov/pubmed/32794805>.
- [51] M. Reichl, M. Herzog, F. Greiss, M. Wolff, and D. Braun. Understanding the similarity in thermophoresis between single- and double-stranded DNA or RNA. *Physical Review E*, 91(6):062709, 2015. <https://link.aps.org/doi/10.1103/PhysRevE.91.062709>.

- [52] B. T. Burcar, L. M. Barge, D. Trail, E. B. Watson, M. J. Russell, and L. B. McGown. RNA oligomerization in laboratory analogues of alkaline hydrothermal vent systems. *Astrobiology*, 15(7):509–22, 2015. <https://www.ncbi.nlm.nih.gov/pubmed/26154881>.
- [53] J. P. Ferris and M. Kamaluddin. Oligomerization reactions of deoxyribonucleotides on montmorillonite clay: the effect of mononucleotide structure on phosphodiester bond formation. *Orig Life Evol Biosph*, 19:609–19, 1989. <https://www.ncbi.nlm.nih.gov/pubmed/11538680>.
- [54] B. A. Anderson and R. Krishnamurthy. Heterogeneous pyrophosphate-linked DNA-oligonucleotides: Aversion to DNA but affinity for RNA. *Chemistry*, 24(26):6837–6842, 2018. <https://www.ncbi.nlm.nih.gov/pubmed/29532524>.
- [55] A. Ianeselli, M. Atienza, P. W. Kudella, U. Gerland, C. B. Mast, and D. Braun. Water cycles in a hadean CO<sub>2</sub> atmosphere drive the evolution of long DNA. *Nature Physics*, 18:579–585, 2022. <https://doi.org/10.1038/s41567-022-01516-z>.
- [56] A. Kühnlein. *Selection and replication of oligonucleotides in early evolution: towards long functional sequences and motifs*. PhD thesis, Ludwig-Maximilians-Universität München, 2021.
- [57] A. Kanavarioti. Dimerization in highly concentrated solutions of phosphoimidazolid activated mononucleotides. *Orig Life Evol Biosph*, 27(4):357–76, 1997. <https://www.ncbi.nlm.nih.gov/pubmed/11536829>.
- [58] M. K. Lacki, D. Valkenborg, and M. P. Startek. Isospec2: Ultrafast fine structure calculator. *Anal Chem*, 92(14):9472–9475, 2020. <https://www.ncbi.nlm.nih.gov/pubmed/32501003>.



# Acknowledgements

Science - by nature - is a group effort that builds on each other's accomplishments, intelligence, helpfulness and willingness to share and teach. In the **Braunie-Lab** I was so lucky to receive this in the most concentrated and vibrant ways one could imagine.

One source of this surely is our professor **Dieter Braun**, so my first **THANKS** go to you. Always up for a compassionate fight but simultaneously equipped with great generosity, a sense for what is really important in science and life and true-lived feminism, you shaped my personality and my brain during the last 6 years of being your PhD student and I wouldn't want to miss a single of the teachings I received. You will be one of the people in my life who will have truly made a difference on my path.

To the emergence of this PhD thesis many more people contributed in mind, hand, heart and soul. So my most heart-felt **THANK YOU** goes to

- **Alex K., Annalena, Patta, Max, Leo, Thommy, Damla, Zhenya** and **Matzi** for your friendship, the right words at the right time, the infinite amount of fun we had together (Kicker!), for your smartness, enthusiasm and down-to-earth-ness. There is so much more to add to this list that it would be beyond of the scope of these acknowledgements, but after the last 6 years "living" together (Dora!), I am sure you know how multibuntly overflowing my heart is towards you. We have made the experience of a lifetime together and I am so glad we left it being not only colleagues but friends!
- **Alan**, who was there for me in the most calm, reassuring, non-judging and helpful manner. You have a beautiful personality and I already now miss your golden one-liners. See you in Brixen, my friend!
- my amazing students and HiWis I had during my 6 years of PhD, namely **Max, Damla, Mathilde, Christina, Sabrina, Nico, Jara** and **Roland**: next to your thoughtful lab-work, I received teachings from you that will accompany me through all my future!
- **Christof, Sree, Paula, Almuth, Alex F., Juliette, Noël, Adriana, Philipp, Newlian, Julian, Alina, Adam, Avinash, Saroj, Victor, Lonzo, Emre, Georg, Barbara, Bobby** and **André**: you are the best colleagues I could wish for - through all of it! If we wouldn't stand so closely and ever-supporting to one another, across all appearing boundaries, none of the great Braunieness would be possible - and a lot of science neither.
- my best friend **Zhenya**, with **Georg**, little **Anton** and the **new baby**: I just love you to the moon and back and I am so looking forward to our common future together, I can't wait for it to start soon!
- **Luise** for a deep-felt companionship since childhood that we are about to add another layer to!

- **Meckie** and **Andreas** who are my soulmates in this world: your deep love towards me is one of the most precious gifts that I am so honoured to receive in my life. You truly have been, are and will be special people to this world and to me!
- **Zümi** and **Dilara**, the best flat mates in the world. It was a gift to have the almost cliché-like perfect WG just at the end of my student-WG-times. Thanks for this experience and for all the love we share. We will stay close in the future!
- **Lea, Lukas, Roman, Andreas, Margret, Philipp** and **Ale** for a sparkling friendship starting in our Bachelor and Master studies at LMU. Becoming a physicist and becoming an adult I only could do alongside of you!
- **Alex G., Nati, Lauri** and my **Erasmus-Crew: Isa, Olli, Pedro** and **Hannes** as well as **Charlotte, Andreas** and **Sigolène** who introduced a deep change to my life: from you I learnt the wonderfulness of being multibunt, hippie and letting people be how they are. You are amazing human beings and you made me a better person for others and myself. I love you!
- all the wonderful people and the institution of **Musikakademie in Brixen** and **Studienstiftung des deutschen Volkes** for all the sharing, caring and daring and for all the opportunities you provide.
- **Stefanie Leister** for taking care of all the siblings out there who are left behind after the death of the life companions that siblings are actually meant to be. You creat truly good in the world with your Geschwister-Wochenenden and the rising of awareness for sibling grief nationwide. You really made a difference in my life and I know in many other lives, too.
- **Melanie** for appearing as one of my rescues in last minute and after that for always finding the right words to raise the good in me. You truly found your calling! I am so glad our ways crossed.
- the great sport of **Voltingieren**, with my best friend there **Janina**, that equipped me with a great sense for the joys of team-spirit, discipline, stamina and being an athlete as well as the wonderful art of **Ballet** which is my anchor and my passion.
- to my beautiful ballet teachers **Eszter** and **Carlos**: you are spreading beauty, strength and love into this world through your dance and through your golden hearts.
- my family **Renate, Jürgen, Markus, Anni, Otto, Josef, Julia, Michael, Idlo, Mike, Lin, Jella, Niki, Kirsten** und **Ursel**: the unbreakable strong love to one another, that is passed on in our family since generations, is the strongest source of my overflowing happiness, sincerity and resilience. This gift and my very conscious gratefulness for it I cannot pay back, but with all my heart and energy I will pass on what I am receiving.
- my unborn **Babies** who taught me so much already now.

# Appendix

## 1 Data Repository

Supplementary data files are provided by the author via the Open Data Repository of Ludwig-Maximilians-Universität and can be downloaded there.

Reference: Christina F. Dirscherl and Dieter Braun. Supplementary Datasets for the Paper “A Heated Rock Pore Promotes Primordial DNA and RNA Polymerization”. *Open Data LMU*, 2022. <https://doi.org/10.5282/ubm/data.351>

### File Descriptions

**Movie M1: Pore filling with help of low viscosity oil.** The sample mixture was filled into a thermophoretic pore, which has beforehand been filled with very low viscosity Novec oil to allow complete filling of the pore without introducing any air bubbles. Novec oil was checked in a separate experiment to not change the polymerization behavior.

**Movie M2: Pore filling with an air-water interface.** The sample mixture was filled into an air-filled thermophoretic pore from its top until it filled the upper 4/5 of the chamber volume, the lowest fifth was left air-filled to create the liquid-gas interface.

**Movie M3: Pore building procedure.** A thin Teflon foil was placed between two transparent sapphires. The sapphires were lined with two heat-conducting graphite foils to ensure a good thermal connection to an aluminum plate at the back and to the resistance rod heaters at the front. The layers were screwed with a steel frame to the back plate, the heater was screwed to the front sapphire. This sandwich is screwed to a waterbath-cooled aluminum block with another graphite foil in between. Three microfluidic teflon tubings were connected with fittings and ferrules to the sapphire back wall of the chamber, which has holes of 1 mm diameter. These tubings served as inlet and outlet for the insertion of the liquid sample.

**Movie M4: Freeze extraction procedure.** After the run time of the reaction in the thermal gradient, the front heating is turned off, which leads to a rapid drop in temperature and finally to freezing of the pore contents. The entire pore was removed from the setup and placed it in the  $-80^{\circ}\text{C}$  freezer for 30 min. Then the sapphire-teflon-sapphire sandwich was unscrewed from the metal holders. The sandwich was placed on an aluminum block cooled to  $-80^{\circ}\text{C}$  to prevent melting. The sandwich was opened, and the Teflon was removed using a razor blade. Only the frozen liquid content remained on the sapphires. This was cut into five stripes (for experiments of Chapters 3.1 and 3.2) or three stripes (for experiments of Chapter 3.3) of similar volume. The sapphire was slid bit by bit over onto a  $45^{\circ}\text{C}$  aluminum block to melt the frozen sample stripe by stripe. To ensure that two adjacent stripes were not

inadvertently mixed during the thawing, a hydrophobic barrier (glass cover slide wrapped with Teflon foil) was held between each stripe. The contents of each thawed stripe were pipetted into different low-binding Eppendorf tubes.

**Movie M5: Thermogravitational accumulation in a water-filled pore.** An out-of-equilibrium hydrothermal pore can localize and concentrate molecules. The thermal gradient induces two physical phenomena inside the pore: the bulk solution undergoes a circular convection motion due to the heat-induced density differences within the liquid and the dissolved molecules within the liquid experience thermophoresis, a drift along the temperature gradient (for DNA/RNA molecules towards the colder side of the pore). The superposition of these two forces leads to a concentration increase of molecules at the bottom cold corner of the pore. The resulting accumulation of molecules is balanced by diffusion, seeking a homogeneous concentration.

**Movie M6: Accumulation and wet-dry cycles in a pore with air-water interface.** In a pore with an air-water interface subjected to a temperature gradient, convection and thermophoresis are joined by evaporation at the hot side and recondensation at the cold side of the pore. In addition to the downward accumulation, the solutes undergo a wet-dry cycling: RNA molecules are deposited in layers on the hot side and are rehydrated by growing water droplets at the cold side, which re-enter the main fluid phase and shift the location of the water-air interface over time.

**Dataset D1: Self-coded LabVIEW program for mass calculation.** The masses of the two types of oligomer products formed in the 2',3'-cyclic polymerization were calculated to the fourth charge state using a self-coded LabVIEW program. The resulting masses are used for further analysis and are displayed in Chapter 5.3.2.

**Dataset D2: Self-coded LabVIEW program for temperature calculations for thermophoretic pores.** To calculate the inner temperatures of the chambers, I measured the temperatures on the outside of the sapphires with a temperature sensor and used the steady-state linear heat equation and the conductivities of water  $0.6 \text{ W m}^{-1} \text{ K}^{-1}$  (at  $20^\circ\text{C}$ ) and sapphire  $23 \text{ W m}^{-1} \text{ K}^{-1}$  to calculate what temperature this translates to on the inside of the pore.

**Dataset D3: Self-coded LabVIEW programs for product peak integration and isotope pattern matching.** For the quantification of polymerization products from 2',3'-cyclic monomers I used two self-coded LabVIEW programs to integrate the product chromatogram peaks and to check the isotope distribution.

**Dataset D4: Isotope pattern documentation.** Screenshots of the isotope patterns for all detected strand lengths and base compositions for the  $10 \text{ mM } 2',3'\text{cCMP} / 50 \text{ mM } 2',3'\text{cGMP}$  experiment for both, thermophoretic pore and drying at  $40^\circ\text{C}$ . The theoretical isotope pattern is displayed in green and was compared with the ESI-TOF-measured isotope pattern in white (A closer description to the software can be found in [14]).

**Dataset D5: Comsol simulation files for all theoretical calculations.** Numerical simulations for the robustness sweep, monomer accumulation, AImpdA accumulation+polymerization for thermophoretic pores and bulk control, 2',3'-cyclic accumulation+polymerization for thermophoretic pores and drying control, 2D-longtime monomer accumulation with and without feeding and 0D-longtime 2',3'-cyclic polymerization with and without feeding.

**Dataset D6: 2',3'-cyclic polymerization rate equations and self-coded LabVIEW program for their calculation.** The rate equations for all strands of the 2',3'-cyclic polymerization with length- and sequence-dependent on-rates are generated with a self-coded LabVIEW program. The resulting equations are used in the combined accumulation and polymerization simulations.



## 2 Associated First Author Publication

**Christina F. Dirscherl**, Alan Ianeselli, Damla Tetiker, Thomas Matreux, Robbin M. Queener, Christof B. Mast, and Dieter Braun. A heated rock crack captures and polymerizes primordial DNA and RNA. *Phys. Chem. Chem. Phys.*, 25, 3375-3386, 2023.

## 3 Associated Co-Author Publications

**M. Morasch**, J. Liu, **C. F. Dirscherl**, A. Ianeselli, A. Kühnlein, K. Le Vay, P. Schwintek, S. Islam, M. K. Corpinot, B. Scheu, D. B. Dingwell, P. Schwille, H. Mutschler, M. W. Powner, C. B. Mast, and D. Braun. Heated gas bubbles enrich, crystallize, dry, phosphorylate and encapsulate prebiotic molecules. *Nature Chemistry*, 11(9):779–788, 2019.  
<https://doi.org/10.1038/s41557-019-0299-5>

**P. W. Kudella**, K. Preißinger, M. Morasch, **C. F. Dirscherl**, D. Braun, A. Wixforth, and C. Westerhausen. Fission of Lipid-Vesicles by Membrane Phase Transitions in Thermal Convection. *Scientific Reports*, 9, 18808, 2019.  
<https://doi.org/10.1038/s41598-019-55110-0>

**S. Wunnava**, **C. F. Dirscherl**, J. Výravský, A. Kovařík, R. Matyášek, J. Šponer, D. Braun, and J. E. Šponer. Acid-Catalyzed RNA-Oligomerization from 3',5'-cGMP. *Chem. Eur. J.*, 27, 17581, 2021.  
<https://doi.org/10.1002/chem.202103672>

**A. V. Dass**, **S. Wunnava**, **J. Langlais**, B. von der Esch, M. Krusche, L. Ufer, N. Chrisam, R. Dubini, F. Gartner, S. Angerpointner, **C. F. Dirscherl**, P. Rovó, C. B. Mast, J. Šponer, C. Ochsenfeld, E. Frey, and D. Braun. RNA auto-polymerisation from 2',3'-cyclic nucleotides at air-water interfaces. *ChemSystemsChem*, 5, e202200026, 2023.  
<https://doi.org/10.1002/syst.202200026>

**M. Stasi**, A. Monferrer, L. Babl, S. Wunnava, **C. F. Dirscherl**, D. Braun, P. Schwille, H. Dietz, and J. Boekhoven. Regulating DNA-Hybridization Using a Chemically Fueled Reaction Cycle. *J. Am. Chem. Soc.*, 144, 48, 21939–21947, 2022.  
<https://doi.org/10.1021/jacs.2c08463>



# Heated gas bubbles enrich, crystallize, dry, phosphorylate and encapsulate prebiotic molecules

Matthias Morasch<sup>1</sup>, Jonathan Liu<sup>1</sup>, Christina F. Dirscherl<sup>1</sup>, Alan Ianeselli<sup>1</sup>, Alexandra Kühnlein<sup>1</sup>, Kristian Le Vay<sup>2</sup>, Philipp Schwintek<sup>1</sup>, Saidul Islam<sup>3</sup>, Mérina K. Corpinot<sup>3</sup>, Bettina Scheu<sup>4</sup>, Donald B. Dingwell<sup>4</sup>, Petra Schwillie<sup>2</sup>, Hannes Mutschler<sup>2</sup>, Matthew W. Powner<sup>3</sup>, Christof B. Mast<sup>1</sup> and Dieter Braun<sup>1\*</sup>

**Non-equilibrium conditions must have been crucial for the assembly of the first informational polymers of early life, by supporting their formation and continuous enrichment in a long-lasting environment. Here, we explore how gas bubbles in water subjected to a thermal gradient, a likely scenario within crustal mafic rocks on the early Earth, drive a complex, continuous enrichment of prebiotic molecules. RNA precursors, monomers, active ribozymes, oligonucleotides and lipids are shown to (1) cycle between dry and wet states, enabling the central step of RNA phosphorylation, (2) accumulate at the gas-water interface to drastically increase ribozymatic activity, (3) condense into hydrogels, (4) form pure crystals and (5) encapsulate into protecting vesicle aggregates that subsequently undergo fission. These effects occur within less than 30 min. The findings unite, in one location, the physical conditions that were crucial for the chemical emergence of biopolymers. They suggest that heated microbubbles could have hosted the first cycles of molecular evolution.**

Life is a non-equilibrium system. Through evolution, life has created a complex protein machinery to maintain the non-equilibrium of crowded molecules inside dividing vesicles. Based on entropy arguments, equilibrium conditions are unlikely to have triggered the evolutionary processes at the origin of life<sup>1</sup>. External non-equilibria had to have been provided for the accumulation, encapsulation and replication of the first informational molecules. These can locally reduce entropy, give rise to patterns<sup>2</sup> and lean the system towards a continuous, dynamic self-organization<sup>3</sup>. Non-equilibrium dynamics can be found in many fluid systems, including gravity-driven instabilities in the atmosphere<sup>4</sup>, the accumulation of particles in nonlinear flow<sup>5,6</sup> and shear-dependent platelet activation in blood<sup>7</sup>. Our experiments discuss whether gas–water interfaces in a thermal gradient could have provided such a non-equilibrium setting for the emergence of life on early Earth.

Non-equilibrium systems in the form of heat flows were a very common and simplistic setting found ubiquitously on early Earth<sup>8</sup>. Hydrothermal activity is considered to have been abundant and intimately linked to volcanic activity<sup>9</sup>. Water was thus circulating through the pore space of volcanic rocks, which was formed by magmatic vesiculation (primary origin) and fractures (secondary origin). These systems have been studied as non-equilibrium driving forces for biological molecules in a variety of processes<sup>10–17</sup>.

Gases originating from degassing of deeper magma bodies percolate through these water-filled pore networks. At shallow depths bubbles are formed by gases dissolved in water and the formation of vapour where sufficient heat is supplied by the hydrothermal system. The bubbles create gas–water interfaces, which

previously have been discussed in connection with atmospheric bubble–aerosol–droplet cycles<sup>18</sup>, the adsorption of lipid monolayers and DNA to the interface<sup>19,20</sup> and the formation of peptide bonds<sup>21</sup>.

In the absence of a temperature gradient, evaporation of a drop of water on a surface exhibits the so-called ‘coffee-ring effect’<sup>22</sup>. Upon evaporation, molecules in the drop are accumulated at its rim by capillary flow. After complete evaporation, a ring of concentrated material is deposited. In the inverted setting studied here, a gas bubble is immersed in water (Fig. 1) and a temperature gradient drives this process continuously.

## Results

**Accumulation at the gas–water interface.** Experimentally, bubbles were created by filling a 240- $\mu\text{m}$ -thick, corrugated microfluidic chamber with solution (Supplementary Fig. 1). As the solution could not fill all the cavities, pinned gas bubbles were created. At higher temperatures, bubbles were found to also form spontaneously anywhere in the system as a result of outgassing. These bubbles were often not restricted by their surrounding geometry and moved along the heated surface.

Accumulation of molecules at these heated gas–water interfaces is caused by a continuous evaporation–recondensation water cycle. The interfaces are held in a constant non-equilibrium state, leading to a steady-state coffee-ring effect that does not end in a fully dry state. Here, we observe six physico-chemical processes, which have all individually been suggested to be relevant for the emergence of prebiotic evolution and are co-located in a single non-equilibrium system: (1) enhanced catalytic activity of ribozymes, amplified by the accumulation of oligonucleotides and ions, (2) condensation of

<sup>1</sup>Physics Department, Center for Nanoscience, Ludwig-Maximilians-Universität München, Munich, Germany. <sup>2</sup>Max Planck Institute of Biochemistry, Martinsried, Germany. <sup>3</sup>Department of Chemistry, University College London, London, UK. <sup>4</sup>Earth and Environmental Sciences, Ludwig-Maximilians-Universität München, Munich, Germany. \*e-mail: [dieter.braun@lmu.de](mailto:dieter.braun@lmu.de)

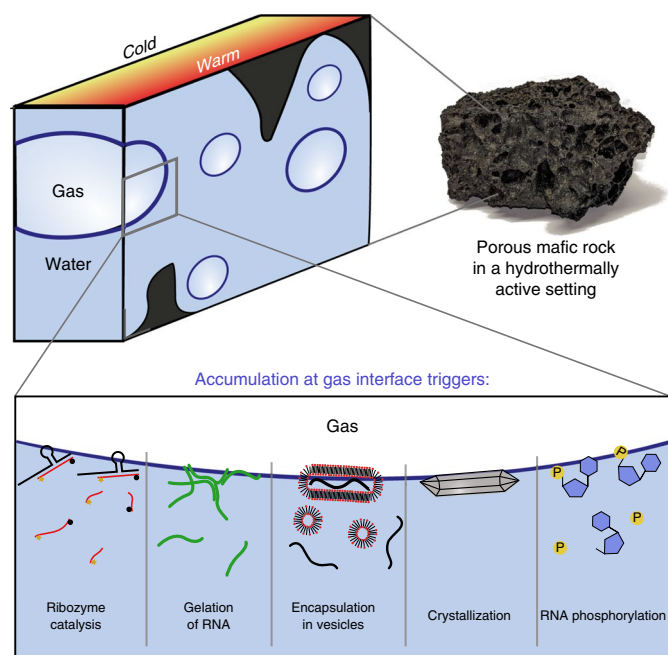


**Fig. 1 | DNA accumulation at gas bubbles in a thermal gradient.** Volcanic rocks in shallow hydrothermal settings are subjected to water cycles in their pore spaces, which are of both primary (magmatic vesicles) and secondary (fractures) origin. Gases, originating from magma degassing at depth, percolate through the water. Heat supplied by the hydrothermal system causes vaporization. At the gas microbubbles, molecules are accumulated by the continuous capillary flow on the warmer side of the gas–water interface. As shown experimentally, this environment can enhance the catalytic activity of ribozymes, trigger the formation of a hydrogel from self-complementary RNA, encapsulate oligonucleotides such as aptamers in vesicle aggregates, trigger their subsequent fission, drive the crystallization of ribose aminooxazoline (RAO)—a prebiotic RNA precursor—and initiate the phosphorylation of RNA nucleosides.

self-complementary RNA 36mers into millimetre-sized hydrogels, (3) vesicle aggregation at the bubble interface along with encapsulation of oligonucleotides in aqueous phases with up to 18-fold enhanced concentration, (4) fission of the vesicle structures in the adjacent micro-convection, (5) formation of euhedral 300  $\mu\text{m}$  crystals from the RNA precursor ribose aminooxazoline (RAO) around bubbles (which also act as seeds for new bubbles) and (6) dry–wet cycles enhancing, for example, the phosphorylation of nucleosides, created by fluctuating and moving interfaces (Fig. 1 and Supplementary Videos 1–6). All six mechanisms were established within 30 min and, importantly, operated in continuous contact with bulk water.

Here, length- and temperature-dependent accumulations were measured at low-salt conditions (0.1-fold PBS buffer: 13.7 mM NaCl, 0.27 mM KCl, 1 mM phosphate buffer). However, DNA and RNA gelation measurements were performed equally well under physiological conditions (1-fold PBS buffer: 137 mM NaCl, 2.7 mM KCl, 10 mM phosphate buffer).

To observe the dynamics at the interface, bubbles were created as described above, using fluorescently labelled molecules in solution (Fig. 2a(i)). The front and back sides of the chamber were heated and cooled, respectively, to generate a temperature gradient. The system was monitored through the warm side using a fluorescence microscope. The optical axis ran along the temperature gradient (Supplementary Figs. 1 and 2) and the quantitative fluorescence was captured with a charge-coupled device (CCD) camera.

Initially, the chamber was filled with a solution of 200 nM 6-Carboxyfluorescein (FAM)-labelled 132-base single-stranded DNA (ssDNA) oligomer in 0.1-fold PBS buffer. When no temperature gradient was applied to the system ( $T_{\text{warm}} = T_{\text{cold}} = 10^\circ\text{C}$ ), we observed no accumulation of DNA near the gas–water interface. The fluorescence signal exhibited a constant small peak at the observed interface, possibly due to a slight adsorption of the DNA to the gas–water interface (Fig. 2a(i), 0 s). Heating one side of the chamber ( $T_{\text{warm}} = 30^\circ\text{C}$ ,  $T_{\text{cold}} = 10^\circ\text{C}$ ) resulted in the rapid accumulation of DNA in a small area on the warm side at the contact line (Fig. 2a(ii), dashed red box, Supplementary Video 1). The chamber-averaged fluorescence at the contact line increased within 6 min by  $\sim 12$ -fold compared to the bulk fluorescence (Fig. 2b). No accumulation was observed on the cold side.

We calculated the local concentration at the contact line from the ratio of the meniscus and bulk fluorescence and the geometry of the curved gas–water interface. Because the fluorescence was averaged over the chamber by the microscope objectives, a 60-fold higher concentration in addition to the higher fluorescence is inferred due to the thinner size of the accumulation region ( $\sim 4 \mu\text{m}$ ) compared to the 240- $\mu\text{m}$ -wide chamber. Therefore, from the observed 12-fold increase in fluorescence, we estimated a concentration increase by a factor of 700, corresponding to 140  $\mu\text{M}$  DNA concentration in the meniscus when starting from a 200 nM bulk solution (Fig. 2c). Simulations suggested that without thermophoresis this accumulation would be only slightly higher, showing that it does not play a significant role in the accumulation process (Fig. 2c, red dotted line).

Further analysis from experiment and theory showed that the accumulation was caused by the focused evaporation of water at the tip of the meniscus<sup>23</sup> (Fig. 2d, orange). A continuous flow of water into the meniscus dragged the molecules with it; because they could not evaporate, they could only escape by diffusion against the one-way capillary flow. The flow was visualized by filling the chamber with a suspension of 200-nm-diameter FAM-labelled polystyrene beads. By particle tracking, we measured the velocity profile in the meniscus (Fig. 2d,e and Supplementary Video 1). Beads moved towards the accumulation region near the hot side of the chamber at the contact line.

We attribute this to capillary flow, which superseded the comparatively weak bulk buoyant convection (Fig. 2e). Temperature gradients have also been demonstrated to create Marangoni flows<sup>23</sup>, in which water is drawn from the warm to the cold side of an interface due to a surface tension gradient. This was difficult to observe because the main temperature gradient was along the viewing axis. However, we observed strong lateral flows at the interface when accumulating vesicles. We attribute these to lateral Marangoni flows and therefore assume also a combination of Marangoni flows and convection along the interface (Fig. 2d, green). Without this flow, our simulation predicts a larger accumulation (Fig. 2c, blue dotted line).

The water that evaporated near the warm chamber wall was found to condense on the cold wall, forming small water droplets. As a result, the gas bubble had less space, expanded, and moved the gas–water interface. Once the condensed ‘rain’ droplets had grown, merged and re-entered into the bulk solution, driven by surface tension, the interface moved back to its initial position (Supplementary Video 1). These fluctuations of the contact line triggered a drying and recondensation of the molecules at the location where the capillary flow initially accumulated them.

A fluid dynamics model was used to describe the main features of the accumulation. We considered a two-dimensional (2D) section perpendicular to the interface. Because the width of the channel was smaller than the capillary length for the water and gas<sup>24</sup>, the interface geometry was approximated by an arc of a circle.

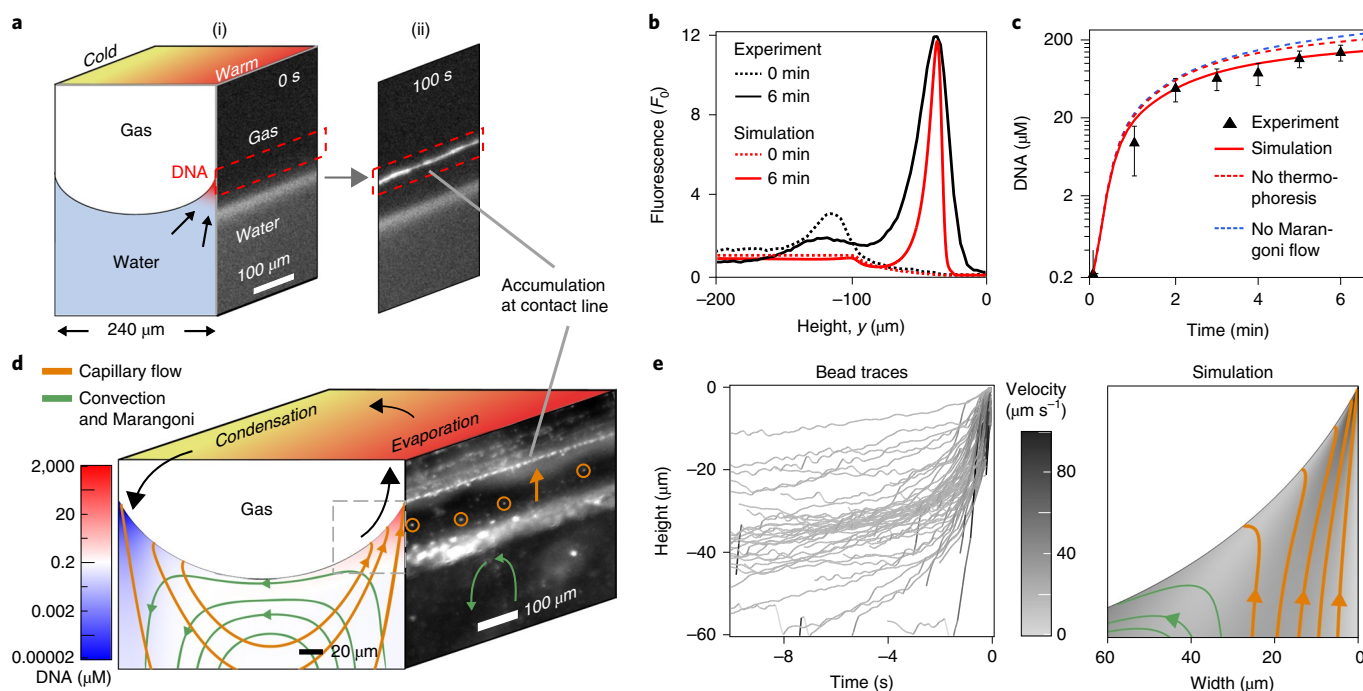


**Fig. 2 | DNA accumulation by capillary flow.** **a**, (i) Gas–water interface imaged by fluorescence microscopy with the contact line area outlined with a red dashed line. The initial higher fluorescence intensity at the contact line originated from adsorbed DNA at the gas–water interface. (ii) After 100 s, the 132mer DNA has accumulated in water near the contact line at the warm temperature side of the chamber ( $T_{\text{warm}} = 30^\circ\text{C}$ ,  $T_{\text{cold}} = 10^\circ\text{C}$ , Supplementary Video 1). **b**, The fluorescence profile reached a 12-fold increase as compared to the bulk fluorescence within 6 min. **c**, Due to the confined meniscus geometry, the accumulated concentration was significantly higher. The 12-fold increase in fluorescence corresponded to a 700-fold increase in DNA concentration, consistent with simulation results (red solid line). Without thermophoresis (red dotted line) or Marangoni flows (blue dotted line), simulations predict a slightly higher accumulation. Error bars were estimated from fluorescence analysis averaged over an  $\sim 200\ \mu\text{m}$  interface width at three positions along the contact line from the shown example measurement. **d**, Fluid flow near the contact line measured by single-particle tracking (Supplementary Video 1). Capillary flow (orange) pulled the beads upwards toward the contact line as water mainly evaporated at the tip of the meniscus. Marangoni and convection flows (green) shuttled the beads between the hot and cold sides. Superposed is the logarithmic concentration profile obtained from the simulation for the accumulation in **a**. **e**, Single-particle tracking of the capillary flow. Peak flow velocities reached  $50\ \mu\text{m s}^{-1}$  in the last second of the water flow before its evaporation (Supplementary Fig. 3).  $T_{\text{cold}} = 10^\circ\text{C}$ ,  $T_{\text{warm}} = 40^\circ\text{C}$ .

The contact line of the interface was pinned in the simulation<sup>25,26</sup>, motivated by the observation that the accumulation kinetics was generally faster than the fluctuating movement of the interface.

The model superposed four water flows, providing the boundary condition for the accumulation of DNA: (1) capillary flow at the meniscus, (2) diffusion of water vapour between the interface and the gas bubble, (3) convection of water and (4) Marangoni flow along the interface. The relative strength of the Marangoni flow—a free parameter due to the unknown presence of surface-active molecules<sup>27</sup>—was adjusted to fit the velocities measured in the experiment.

The interplay of all four flows led to the accumulation of molecules at the meniscus. As only water evaporated on the warm side, dissolved molecules were continuously dragged towards the contact line, where their concentration depended on back-diffusion and the speed of the capillary flow. Convection and Marangoni flow provided a constant cycling of water and new material towards the accumulation region.

DNA accumulation was measured experimentally for various temperature differences and DNA lengths (Supplementary Fig. 4). The accumulation rose with increasing temperature difference ( $\Delta T$ ), reaching a 4,000-fold increase for  $\Delta T = 40^\circ\text{C}$ . We also found that smaller (15mer) DNA molecules accumulated three times less effectively than larger (132mer) DNA, which was attributed to their higher diffusion coefficient. The model predicted a multi-fold

accumulation of mono- and divalent ions (Supplementary Fig. 4), resulting in a higher salt concentration at the meniscus.

**Enhanced ribozyme catalysis at the interface.** The accumulation of larger biomolecules as well as ions at the interface makes it a powerful mechanism to enhance the activity of functional nucleic acids. To test this, we monitored the activity of the Hammerhead ribozyme<sup>28,29</sup>, which cleaves a 12mer RNA substrate strand. The substrate and magnesium concentration determined its activity<sup>30</sup>, and both were accumulated in a  $30^\circ\text{C}$  gradient ( $T_{\text{warm}} = 10^\circ\text{C}$ ,  $T_{\text{cold}} = 40^\circ\text{C}$ ) at low bulk concentrations ( $0.1\ \mu\text{M}$  Hammerhead,  $0.5\ \mu\text{M}$  substrate,  $0.4\ \text{mM}$   $\text{MgCl}_2$ , Fig. 3a). As a control, chambers without gas interfaces were studied. A FAM dye and a black hole quencher were attached on opposite sides of the substrate, inhibiting the fluorescence of the FAM dye. On cleavage, the dye was not quenched anymore and could be detected by fluorescence microscopy. Figure 3a,b and Supplementary Video 2 show the average fluorescence of the chamber over time. The substrate strands were cleaved predominantly at the interface, as seen by the rise of fluorescence there. From here, the cleaved strands were frequently ejected into the bulk solution. After 25 min, samples were extracted from the bulk fluid and analysed by polyacrylamide gel electrophoresis (PAGE, Fig. 3c). We detected up to 50% concentration of the cleaved substrate (bottom band, Supplementary Fig. 5) in a chamber with bubbles.

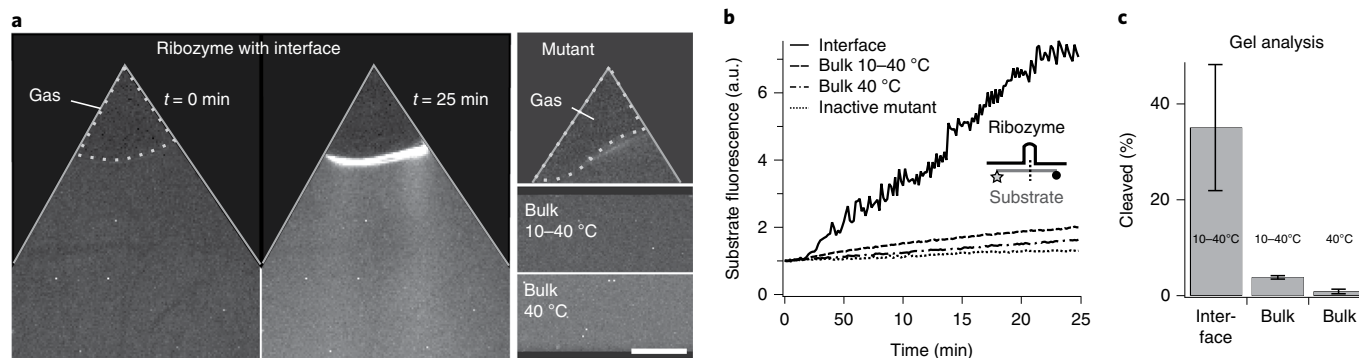


**Fig. 3 | Ribozyme catalysis triggered by an interface.** Fluorescence microscopy and PAGE analysis of Hammerhead ribozyme activity. **a**, Hammerhead in a chamber with a gas–water interface after 0 and 25 min (left and right, respectively;  $T_{\text{warm}} = 40^\circ\text{C}$ ,  $T_{\text{cold}} = 10^\circ\text{C}$ ,  $0.1\ \mu\text{M}$  ribozyme,  $0.5\ \mu\text{M}$  substrate,  $0.4\ \text{mM}$   $\text{MgCl}_2$ ). Fluorescence increased strongly at the interface over time (Supplementary Video 2). Without the interface (bottom right), the Hammerhead shows little activity, both in the same temperature difference and at a homogeneous  $40^\circ\text{C}$ ; an inactive mutant (top right) showed no significant increase in fluorescence. Scale bar,  $500\ \mu\text{m}$ . **b**, Overall fluorescence in the bulk fluid from **a** over time. The illustration shows the ribozyme (black) and substrate (grey) with the cleavage site (dotted line), dye (star) and quencher (black circle). **c**, PAGE analysis results with and without the interface after 25 min (gels in Supplementary Fig. 5). We found a significant increase in cleaved product with the interface ( $35 \pm 13\%$ , five measurements) compared to bulk samples in the same temperature gradient ( $3.79 \pm 0.35\%$ , three measurements) or at  $40^\circ\text{C}$  ( $0.86 \pm 0.49$ , three measurements). Error bars show s.d. from normalized gel band intensities.

In the same temperature gradient, but without interfaces, only 3.8% of the substrate was cleaved. This decreased even further when the bulk temperature was set homogeneously to  $40^\circ\text{C}$ , where only very little activity could be observed. When using an inactive mutant version of the ribozyme, the fluorescence did not increase noticeably (Fig. 3a, top right; Fig. 3b, dotted line), demonstrating that it did not originate from enhanced hydrolysis at the interface. This shows that the accumulation mechanism can enhance the catalytic activity of ribozymes, while maintaining low-salt conditions in the bulk solution. It increases the turnover—the number of strands cleaved per ribozyme—by the accumulation of substrates and ions.

**RNA/DNA gelation.** The length selectivity observed in nucleic acid accumulation could increase the concentration of self-complementary oligonucleotides to the point that hydrogel-forming concentrations could be reached (Fig. 4a). Self-complementary strands were found to form a macroscopic, millimetre-sized hydrogel, a process previously shown for DNA in a thermophoretic accumulation chamber<sup>15</sup>. We observed the formation of hydrogels for self-complementary DNA and RNA and both for GC-only (Fig. 4 and Supplementary Video 3) and AT-only sequences (Supplementary Fig. 6). All oligonucleotides were end-labelled and HPLC purified to minimize the presence of free dye in the experiments.

Starting from uniformly distributed DNA in bulk solution (Fig. 4a(i), initial concentration  $10\ \mu\text{M}$ ; 1-fold PBS buffer), the DNA was quickly accumulated at the interface once the temperature gradient was established. Within 8 min, a hydrogel had formed, after which it quickly detached from the interface and entrained in the convection flow (Fig. 4a(ii)). The hydrogel nature of the DNA was checked by increasing the temperature from  $30^\circ\text{C}$ , below the melting point of the self-complementary sequences, to  $70^\circ\text{C}$ , where the hydrogel dissolved into the convection flow (Fig. 4a(iii)).

The formation of hydrogels from self-complementary RNA was also observed. We co-accumulated two different sequences in a  $20^\circ\text{C}$  temperature difference (Fig. 4b). The red fluorescence channel monitored a 36mer non-complementary ssRNA strand and the green fluorescence channel a self-complementary GC-only 36mer ssRNA strand with three self-complementary binding sites. Based on simulations (Nupack, [www.nupack.org](http://www.nupack.org)), the hydrogel-forming strands bind to each other and form a network of polymers (Fig. 4b,

right). Over the course of the experiment, both the non-complementary and self-complementary strands accumulated at the same interface. However, after 21 min, we only observed a hydrogel for the self-complementary green RNA. No hydrogel could be observed for the non-complementary red RNA, which also accumulated near the surface but was not forming large-scale structures (Supplementary Video 3). Replacing the GC-only strand with a 60mer AU-only RNA with similar self-complementarity gave the same results (Supplementary Fig. 6). This demonstrates that gel formation and separation of the strands is not dominated by G-quadruplex formation.

The red and green strands separated macroscopically based only on their sequence. The self-complementary strands remained at a local high concentration in the hydrogel, which offered reduced hydrolysis rates due to its predominantly double-stranded nature. This sequence-selective gelation was also similarly found for DNA (Supplementary Fig. 6).

**DNA encapsulation in vesicle aggregates.** A key requirement for the emergence of cellular life is the encapsulation of molecules at increased concentration relative to their more dilute external environment. Fatty acids are potential candidates that could separate nucleic acids in vesicles, possibly incorporating phospholipids into their membranes over time<sup>31,32</sup>. For the encapsulation, three autonomous processes need to occur: (1) accumulation of oligonucleotides to meaningful concentrations, (2) accumulation of vesicles to trigger their aggregation or fusion and (3) the combination of both in one location to encapsulate oligonucleotides into vesicular structures. Here, we show that heated gas–water interfaces could fulfil these requirements. The accumulated vesicles do not necessarily form larger, round vesicles, but aggregate. However, we demonstrate in the following that these aggregates enclose DNA and RNA in an aqueous phase, allowing their binding and folding. Shear flows close to the interface as well as in the convection flow were shown to divide these aggregates to form smaller and more round structures.

To introduce lipids in a homogeneous manner, the chamber was filled with small 100-nm-sized vesicles prepared from a 10mM oleic acid solution ( $0.2\ \text{M}$  Na-bicine,  $1\ \text{mM}$  EDTA, pH 8.5) and  $2\ \mu\text{M}$  DNA. These initially small vesicles appeared as a continuous

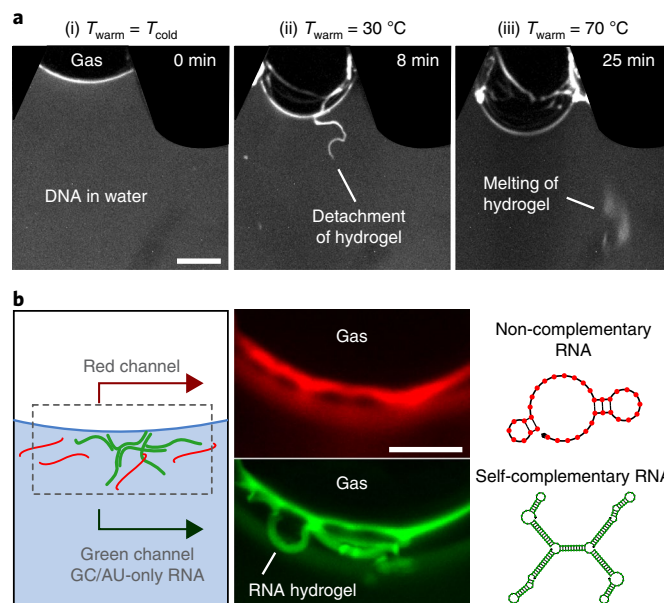


**Fig. 4 | Sequence-selective gelation of RNA and DNA.** Fluorescence microscopy of DNA and RNA revealed the formation of hydrogels at the interface. **a**, Gelation of DNA. (i) Before applying the temperature gradient, DNA accumulated at the interface only due to slight surface adsorption to the gas–water interface. (ii) After applying the temperature gradient, a DNA hydrogel formed and detached from the interface (Supplementary Video 3). (iii) At  $T_{\text{warm}} = 70\text{ }^{\circ}\text{C}$ , the hydrogel melted and redistributed the DNA back into the bulk fluid. We estimated the DNA concentration in the hydrogel to be  $100\text{ }\mu\text{M}$ . Scale bar,  $500\text{ }\mu\text{m}$ . **b**, Gelation of RNA. In a single experiment, non-complementary 36mer ssRNA (red) was accumulated with self-complementary GC-only 36mer ssRNA (green). Both strands accumulated at the interface ( $T_{\text{warm}} = 30\text{ }^{\circ}\text{C}$ ,  $T_{\text{cold}} = 10\text{ }^{\circ}\text{C}$ ), but only the self-complementary RNA formed an elongated, fibrous hydrogel. The same behaviour was found for DNA and AU-only RNA (Supplementary Fig. 6). Scale bar,  $125\text{ }\mu\text{m}$ .

background (Fig. 5a,b and Supplementary Video 4). After turning on the temperature gradient, we observed the accumulation of these vesicles together with DNA within 10 min at the interface ( $T_{\text{warm}} = 70\text{ }^{\circ}\text{C}$ ,  $T_{\text{cold}} = 10\text{ }^{\circ}\text{C}$ ). The vesicles aggregated together and formed larger clusters. It should be noted that this aggregation and cluster formation were strongly increased if  $\sim 0.1\%$  1,2-dioleoyl-*sn*-glycero-3-phosphoethanolamine was added to the lipids (present here to also label the lipids). Interestingly, the co-accumulated DNA was encapsulated into these vesicle aggregates, in which we found an up to 18-fold increase in oligonucleotide concentration compared to the bulk solution. These aggregates were shuttled into the convection and frequently formed thread-like structures. Close to the interface, we observed strong flows (Supplementary Video 4), which we attribute to Marangoni flows. These could originate from lateral temperature gradients across the chamber due to inhomogeneous heating or differences in the thermal conductivity of the chamber material and water. Aggregates were observed to divide and split into smaller compartments in these flows and convection (Supplementary Fig. 4).

Vesicles formed from the phospholipid 1,2-dioleoyl-*sn*-glycero-3-phosphocholine (DOPC) ( $3.6\text{ mM DOPC}$ ,  $0.2\text{ M Na-bicine}$ ,  $1\text{ mM EDTA}$ ,  $\text{pH } 8.5$ ) showed a similar behaviour, but they aggregated more strongly at the interface, and externally applied flow across the microfluidics was sometimes necessary to remove them from the interface. The accumulated  $100\text{-nm}$ -sized vesicles formed larger and more spherical structures compared to the oleic acid aggregates, and encapsulated DNA equally well. They also underwent fission due to shear stress in the convection flow (Fig. 5c and Supplementary Video 4).

The vesicle aggregates (oleic acid or DOPC) concentrated around smaller gas bubbles ( $150\text{ }\mu\text{m}$  in diameter), inducing a clustering of DNA (Supplementary Fig. 7). This was not observed in the absence of lipids. Lipid vesicles therefore significantly enriched the local DNA concentration.

The co-location of DNA and lipids raises the question of whether the oligonucleotides are in an aqueous phase that allows, for example, the folding of RNA or binding of DNA, and whether these compartments are protected from their surrounding. To test the former, we accumulated the RNA aptamer ‘Broccoli’<sup>33</sup> (Fig. 5d), which folds around the fluorophore DFHBI-1T and increases its fluorescence, with DOPC vesicles ( $1\text{ }\mu\text{M}$  aptamer,  $10\text{ }\mu\text{M}$  DFHBI-1T,  $3.6\text{ mM DOPC}$ ,  $50\text{ mM HEPES}$ ,  $\text{pH } 7.6$ ,  $100\text{ mM KCl}$ ,  $1\text{ mM MgCl}_2$ ). Here, we used  $T_{\text{warm}} = 40\text{ }^{\circ}\text{C}$  and  $T_{\text{cold}} = 10\text{ }^{\circ}\text{C}$  to avoid RNA and fluorophore degradation. Again, the RNA, fluorophore and vesicles accumulated at the interface, leading to the formation of aggregates that were visible both in the lipid as well as the fluorophore colour channel. Replacing the Broccoli aptamer with a non-binding RNA strand led to a more than 100-fold reduced fluorescence of the fluorophore. This shows that the aptamer was folded inside the aggregates.

To demonstrate that the accumulated material was protected inside the aggregates, a 72mer double-stranded DNA (dsDNA) was accumulated with DOPC vesicles (Fig. 5e,  $7.1\text{ }\mu\text{M}$  DNA,  $3.6\text{ mM DOPC}$ ,  $0.2\text{ M Na-glycineamide}$   $\text{pH } 8.5$ ,  $6\text{ mM MgCl}_2$ ,  $1\text{ mM CaCl}_2$ ). Each pair of dsDNA strands thereby contained a FAM dye on one strand and a 5-Carboxy-X Rhodamin (ROX) dye opposite to it on the other strand. These dyes form a Förster resonance energy transfer (FRET) pair, in which the excited FAM dye can transfer energy to the ROX dye, which then fluoresces. As this energy transfer works only in close proximity of the dyes, we could use it to measure the amount of dsDNA inside the vesicle aggregates. The higher the signal—between 0 and 1—the more dsDNA was present. After formation of aggregates at the interface, most of the solution was extracted and DNase I was added ( $0.5\text{ units per } \sim 10\text{ }\mu\text{l}$ ). The solution was then put back into the chamber and the FRET signal was observed at  $37\text{ }^{\circ}\text{C}$ . The DNase digested the DNA strands outside the aggregates, where the signal quickly dropped (Fig. 5e, Supplementary Video 4 and Supplementary Fig. 7). The FRET signal of the aggregates reduced only slightly, probably as a consequence of the digestion

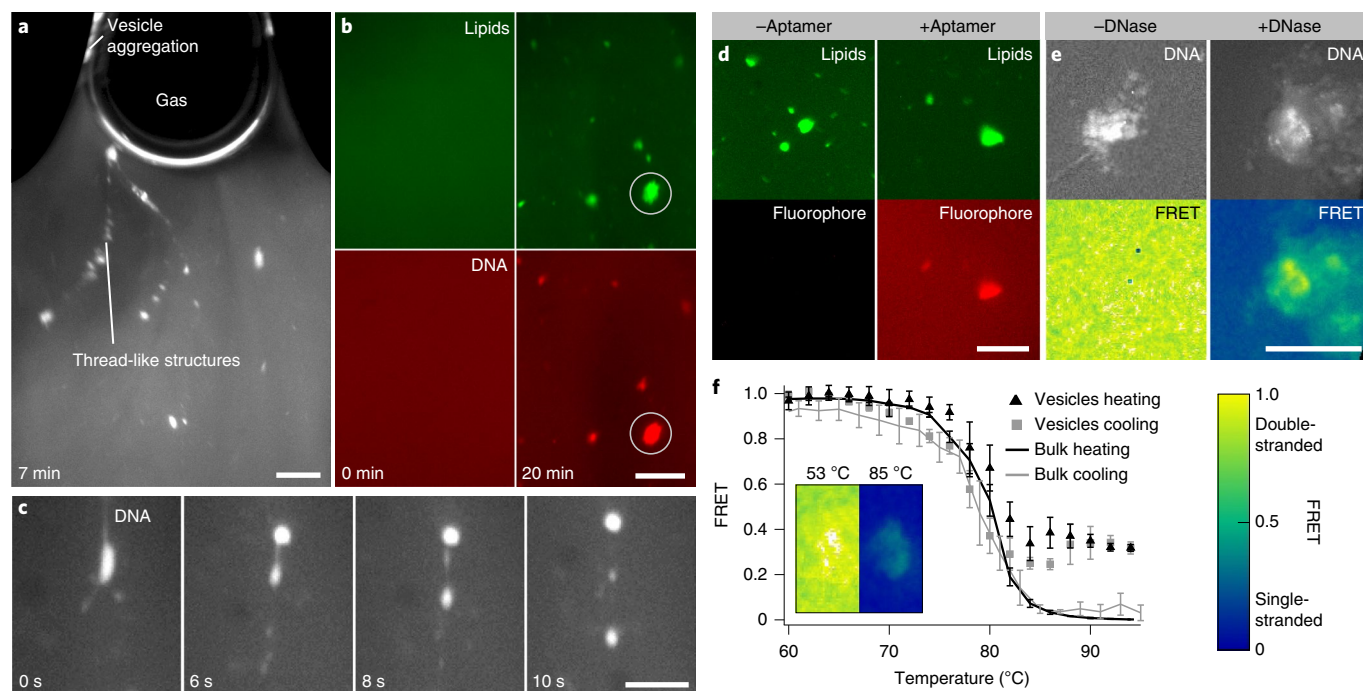


**Fig. 5 | DNA and RNA encapsulation and protection in vesicles formed at the interface.** Fluorescence microscopy images of DNA/RNA and lipid colour channels. **a**, Lipid channel, with 100 nm sized oleic acid vesicles accumulated at the gas-water interface. These formed aggregates of vesicles that were ejected into the bulk and formed thread-like structures (Supplementary Video 4). **b**, Comparison of lipid and DNA colour channels (green, lipid; red, DNA), showing that lipids and DNA co-localize, meaning that the 100 nm-sized vesicles have formed larger clusters and encapsulated DNA at up to 18-fold enhanced concentration compared to the bulk. **c**, DNA channel, with DOPC vesicles accumulated under the same conditions and also encapsulated DNA at enhanced concentrations. Here, a fission of the DOPC vesicles containing DNA was observed in the shear flow. **d**, Encapsulation of fluorophore DFHBI-1T with a non-binding RNA (left) and the Broccoli aptamer (right), which increases its fluorescence. It shows that RNA has folded in an active conformation inside the vesicles. **e**, FRET analysis of dsDNA in aggregates before (left) and after (right) addition of DNase I. DNA inside the aggregates was protected from the DNase (high FRET), whereas it was digested in the bulk solution (low FRET, Supplementary Video 4). **f**, FRET melting curve of dsDNA inside and outside the aggregates, starting from 1.0 (all DNA double-stranded) at 60 °C to 0 (all DNA single-stranded) at 95 °C outside and 0.3 inside the aggregates. Error bars indicate s.d. measured for a larger area of normalized signal of the shown example measurement. Scale bars, 200  $\mu\text{m}$  (**a,b**), 100  $\mu\text{m}$  (**c**), 250  $\mu\text{m}$  (**d,e**).

of solution above/below or DNA sticking to their surface. We thus show that the aggregates protect the molecules inside them.

The FRET signal was also used to observe the melting of dsDNA inside the chamber (Fig. 5f). After accumulation (7.1  $\mu\text{M}$  DNA, 3.6 mM DOPC, 0.2 M Na-glycineamide pH 8.5, 11 mM NaCl, 0.22 mM KCl, 0.8 mM phosphate buffer), the chamber was heated to 95 °C, during which the FRET signal reduced to 0 in the bulk and  $\sim 0.3$  in the aggregates. The remaining signal could stem from aggregated DNA or DNA that is enclosed and stabilized by lipids in a way that did not allow the strands to fully unbind. After cooling, the FRET signal returned to 1 for both aggregates and the bulk solution. The combination of aptamer and FRET analysis demonstrates that oligonucleotides are encapsulated inside the aggregates in an aqueous phase that allows them to melt and fold.

The above experiments assumed the presence of uniformly 100-nm-sized vesicles at the beginning. We also explored the behaviour of the system when it initially contained a range of vesicle sizes, up to  $\sim 30 \mu\text{m}$  in diameter (Supplementary Fig. 8). These exhibited a similar, but often slower accumulation behaviour. Within 20 min, the system again started to form vesicle clusters that contained enhanced DNA concentrations. The formation of oleic acid aggregates was also observed in the absence of DNA, indicating that they were not the result of a DNA/lipid interaction (Supplementary Fig. 8).

**Crystallization at gas bubbles.** The building blocks for the synthesis of single nucleotides, such as the prebiotic RNA precursor ribose

aminoxazoline (RAO), accumulated near gas bubbles to concentrations that triggered its crystallization. For RAO, a crystallization is of fundamental interest because it can be both diastereoisomerically purified by selective sequential crystallization of its precursors and enantiomerically enriched by conglomerate crystallization, where the two enantiomers (D- and L-) of RAO crystallize into discrete independent domains<sup>34,35</sup>. To trigger controlled crystal growth, RAO would need to be accumulated slowly around a growing bubble. In previous experiments, bubbles were artificially created. Here we used elevated temperatures (70 °C warm side, 10 °C cold side) to trigger the spontaneous formation of a bubble. Subsequently, RAO accumulated and crystallized around it (Fig. 6a,b). Therefore, a 40 mM solution of D-RAO, 2.8-fold below the saturation concentration at  $T_{\text{warm}} = 70 \text{ }^\circ\text{C}$  ( $\sim 110 \text{ mM}$ ), was used to fill a chamber without a corrugated geometry and did not create a gas-water interface. For the crystallization to occur at the warm side of the chamber, RAO would have needed to accumulate several fold to overcome the nucleation energy barrier<sup>36</sup>. We monitored the fluorescence of 1  $\mu\text{M}$  Cy5 added to the solution, which co-accumulated at the gas-water interface but was not incorporated into the crystals.

An initially small bubble formed on the warm side and accumulated RAO around it. Within 40 min, the bubble grew while continuously increasing the RAO concentration at its warm side. The crystal shown in Fig. 6a was found at the location where the bubble had formed. No crystals were found on the cold side of the chamber. An X-ray crystal structure determination confirmed that crystals grown on the warm side were indeed D-RAO (Fig. 6c).

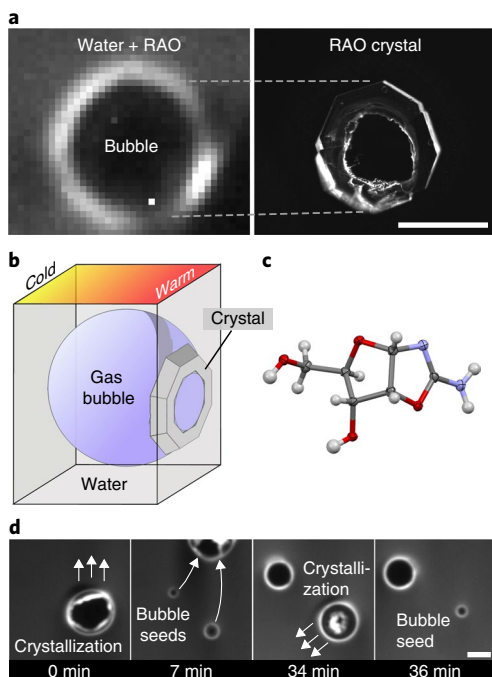


**Fig. 6 | Crystallization and bubble movement.** **a**, RAO accumulated from 40 mM bulk concentration around a growing bubble at the warm side of the chamber (70 °C). After 37 min, an RAO crystal formed below the bubble at the water–gas–solid interface, as indicated. **b**, The crystal shape suggests that it formed successively as the bubble grew, consistent with simulation results (Supplementary Fig. 9). **c**, X-ray crystal structure analysis of a D-RAO crystal grown at a gas–water interface. **d**, Moving bubbles leave behind crystals (7 min) that act as seeds for new bubbles (34 min, Supplementary Video 4). Scale bars, 250  $\mu\text{m}$ .

Interestingly, the formation of RAO crystals led to the later re-formation of gas bubbles near small cavities—a known and well described process of heterogeneous nucleation in supersaturated solutions<sup>36</sup>. We observed this crystal-induced bubble formation in experiments at high  $T_{\text{warm}} = 70\text{ }^{\circ}\text{C}$  (Fig. 6d and Supplementary Video 4). When a gas bubble (around which RAO crystals had formed) moved away, it left behind accumulated material, possibly crystal cavities still filled with gas, which facilitated the growth of new daughter bubbles at the same location. When these daughter bubbles increased in size sufficiently, they started to accumulate RAO, formed crystals and eventually moved away. The remaining crystals again hosted the growth of new bubbles and began the bubble-induced crystallization cycle again.

#### Dry-wet cycles and phosphorylation by moving interfaces.

If bubbles were not confined by their geometry, they tended to move upwards in the chamber (Fig. 7a) due to buoyancy forces. This movement led to a continuous cycling of dry–wet conditions (Fig. 7a), as accumulated material close to the interface entered the bubble, dried and was rehydrated when the bubble moved away. At the same time, accumulated material at the trailing edge was dragged along if the bubble moved slowly enough, keeping high molecule concentrations in the vicinity of the interface (Supplementary Video 6).

At a hydrophilic surface material such as silicon dioxide (quartz), used so far on the cold side in the experiments, the contact angles of the condensed droplets were small, and they re-entered quickly into the bulk water, leading to only little movement of the gas–water interface. To trigger many wet–dry cycles, we placed a Teflon foil

on the warm and cold sides of the chamber. This led to the formation of many droplets on the cold side (Fig. 7b, small round structures inside the dark gas region, Supplementary Video 6), which, if large enough, could also be in contact with the warm side. In this setting, we tested the phosphorylation of nucleosides, a reaction that usually requires dry conditions at elevated temperatures. The reaction is known to be most effective when the solution is dried at 100 °C, a scenario hard to reconcile with typical RNA-world conditions<sup>37,38</sup>. We observed a 20 times more efficient phosphorylation of cytidine nucleosides (Fig. 7c,  $T_{\text{warm}} = 60\text{ }^{\circ}\text{C}$ ,  $T_{\text{cold}} = 37\text{ }^{\circ}\text{C}$ , 240 mM cytidine and ammonium dihydrogen phosphate, 2.4 M urea, similar to the phosphorylation used in ref.<sup>37</sup>) compared to bulk water at average temperatures of 50 °C and 60 °C. The found enhanced in situ phosphorylation reaction would improve the recycling of hydrolysed RNA.

#### Discussion

We have found a general accumulation mechanism of molecules and small vesicles at gas bubbles subjected to heat flow in water. A temperature gradient across a gas–water interface created a continuous process of evaporation and condensation of water between the warm and cold sides. This moved molecules towards the bubble interface and increased their concentration by several orders of magnitude, depending on their diffusion coefficients. Because the contact line between gas and water was mobile, dry–wet cycles were created, in many conditions as often as twice per minute. The molecules studied here have been discussed as prebiotic candidates before the emergence of life<sup>35,37,39</sup>. Fluorescently labelled analogues were used to probe their concentration. We did not elaborate on the types of gas used in this study, because, due to their low concentrations, they did not modify the surface tension and water evaporation significantly<sup>40</sup>.

Our simulation captured the basic characteristics of this accumulation and validated the experimental results. A 4,000-fold DNA accumulation was reached both in experiment and simulation. In comparison with thermophoretic traps, with which the setting could be combined, the accumulation at the interface occurred significantly faster, on the timescale of minutes rather than hours<sup>11</sup>.

We used different temperature gradients adapted to the different scenarios. The magnitude of accumulation depended strongly on the applied temperature difference (Supplementary Fig. 4), which was kept at high values in Figs. 3 and 4 (10–40 °C and 10–30 °C, respectively) to accumulate RNA strongly, but still under cold conditions to keep hydrolysis insignificant. Vesicles aggregated under similar conditions (Fig. 5d), but with faster convective flows from a higher temperature difference (10–70 °C), shuttled aggregated vesicles more efficiently away from the interface for downstream analysis. The creation of crystals from RAO (Fig. 6) required the larger temperature gradients required for an efficient accumulation of the comparably small molecules. The phosphorylation chemistry of monomers (Fig. 7) profited from an overall enhanced temperature.

The co-accumulation of small ions offers additional reactivity. Divalent salts such as  $\text{Mg}^{2+}$  were predicted by our model to accumulate by a factor of 4–5 for temperature differences of 20–30 °C. In high-salt environments, this could enhance the hydrolysis of, for example, accumulated RNA, but the larger temperature differences also increase the movement of the interface by the recondensation of water, decreasing the time accumulated molecules spend dried at high temperatures. On the other side, the enhanced salt concentrations would trigger ribozymatic activity at the interface while the molecules in the bulk are protected by low salt concentrations from hydrolysis.

The system provided, in a single setting, a network of widely different reactions, connected by the fast diffusive transport of these molecules through water between different microbubbles. Ligation<sup>41</sup> chemistry to drive replication could be made possible by

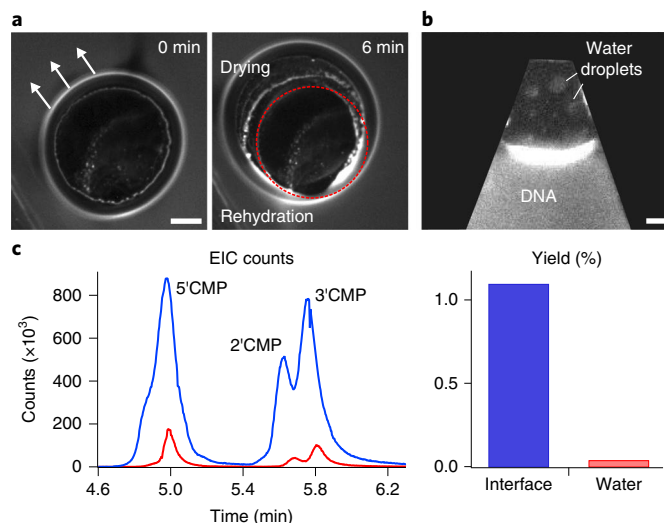


**Fig. 7 | Dry-wet cycles and phosphorylation of nucleosides.** **a**, Movement of bubbles in the chamber left behind dried material in the front that was rehydrated at the back side of the bubble, leading to dry-wet cycles (left, 0 min; right, 6 min). Dotted circle, the position of the accumulation region at  $t = 0$  min. **b**, Using a hydrophobic cold side in the chamber increased the speed of dry-wet cycling by enhancing the formation of circular water droplets on the cold side. As they ‘rained’ into the bulk water, the interface moved periodically, triggering wet-dry cycles at the interface (Supplementary Video 6). **c**, Cytidine nucleosides were phosphorylated in the chamber shown in **b**. Over 12 h, the phosphorylation was, on average, 20 times more effective with the interfaces present (blue,  $T_{\text{warm}} = 60$  °C,  $T_{\text{cold}} = 37$  °C; Cytidine monophosphate (CMP) yield,  $1.1 \pm 0.73\%$  from 12 repeats) compared to bulk water at 60 °C (red; CMP yield,  $0.042 \pm 0.02\%$  from five repeats) or 50 °C ( $0.056 \pm 0.0015\%$  from 15 repeats). Left, extracted-ion chromatogram (EIC) counts (EIC) for CMP peaks after HPLC-MS analysis. Right, yields measured by HPLC and ultraviolet detection. Scale bars, 100  $\mu\text{m}$  (**a**), 250  $\mu\text{m}$  (**b**).

the high local concentrations of substrates, while the drying process in close proximity would trigger the necessary phosphorylation<sup>37,38</sup> and activation chemistry<sup>42</sup> to drive the polymerization<sup>43</sup> of monomers. The dry-wet cycles were implemented continuously at the moving interface and molecules were retained at high concentrations at the interfaces after rehydration. In the adjacent water, molecules thermally cycled between warm and cold via laminar thermal convection.

At the interface, a strongly enhanced ribozymatic activity was demonstrated by the accumulation of the Hammerhead ribozyme. Its activity at the interface clearly dominates the turnover of substrate in the system, with up to 50% of the product being cleaved in a chamber with a gas interface (compared to 3.8% in the bulk). This can be attributed to higher local concentrations of ribozyme, substrate and  $\text{MgCl}_2$  at the interface. Product strands are shuttled back into the bulk solution, where they are protected against the higher salt conditions. The mechanism thereby provides a way to enhance catalytic activity and increase the efficiency of RNA-catalysed processes.

Complex sequence phenotypes of RNA with several self-complementary sites have shown a sequence-selective formation of hydrogels at the interface. These hydrogels maintained a high local RNA concentration in water, an interesting setting to support efficient RNA catalysis<sup>44,45</sup>, also because the high amount of hybridization in the hydrogels could protect oligonucleotides from hydrolysis<sup>46</sup>, even in challenging salt concentrations.

In the presence of lipids such as oleic acid or DOPC, accumulation at the heated gas-water interface led to a continuous encapsulation of oligonucleotides into vesicle aggregates. The local DNA concentration inside these structures increased by a factor of up to 18 compared to the bulk solution. Folded RNA aptamers also accumulated inside the aggregates and dsDNA was shown to melt and re-anneal, demonstrating that aqueous phases readily exist inside the aggregates. As shown with DNase, the vesicles protected the encapsulated DNA from the bulk solution. The encapsulation of

oligonucleotides into lipid membranes is considered to be one of the key elements for more complex life and it has been suggested that lipids facilitated the assembly and polymerization of monomers<sup>47,48</sup>. In the convection flow, the vesicles were subjected to temperature cycles and shear forces that led to vesicle fission. DOPC also produced vesicular structures, showing that modern phospholipids<sup>39</sup> could also accumulate and encapsulate oligonucleotides in the shown conditions.

For the prebiotic synthesis of RNA, crystallization at microbubbles would enable the purification of sugar-nucleobase precursors<sup>34</sup> and possibly also their chiral amplification by the enhanced growth of conglomerate RAO crystals<sup>35</sup>. Interestingly, the sites of crystal formation later triggered, again, the formation of gas bubbles, showing a self-selection for crystallization conditions. If the seed crystal was homochiral, the subsequent bubble formation could accumulate and promote the assembly of more homochiral molecules at the same location. Finally, we found that the prebiotically important dry chemistry of nucleoside phosphorylation was enhanced by the gas interface: cytidine formed CMP 20 times more effectively compared to aqueous conditions.

To conclude, the experiments showed multiple modes of condensation, enrichment, accumulation and increased catalysis at heated gas microbubbles. This led to the physicochemical assembly and localization of prebiotic molecules—such as RNA precursors, lipids and ribozymes. We argue that this accumulation of molecules at a gas-water interface was a robust feature of natural microfluidic systems in porous volcanic rocks in aqueous environments, a setting likely to be ubiquitous on early Earth<sup>9</sup>. The simultaneous occurrence of six synergistic mechanisms for the accumulation and processing of prebiotic molecules, all operating in close proximity, fulfils the requirements for early life to connect a cascade of core reactions in the same non-equilibrium setting.

The setting presented here could therefore have largely helped in an informational polymer world, in which the first simple replicators were evolving. Following a synthesis of life’s first building

blocks, the accumulation at gas–water interfaces offers a mechanism to select polymers and enhance their catalytic activity. The shown continuous encapsulation dynamics of the accumulated molecules at the interface offers a pathway for the emergence of the cellular processes of life. Further experiments will test how this setting can host replication and selection towards early molecular evolution.

## Methods

For the experiments in Fig. 2, a thermal chamber was sandwiched from a thin (>240  $\mu\text{m}$ ) layer of polyethylene terephthalate (PETG) plastic film deposited on a silicon wafer using a 3D printer (Ultimaker 2) in a funnel shape to facilitate a gas–water interface (Supplementary Fig. 1). A sapphire ( $\text{Al}_2\text{O}_3$ ) block sealed the chamber. The chamber was filled through two 240- $\mu\text{m}$ -thick borosilicate capillaries (Vitrocom). The system was annealed at 150 °C and the sapphire pressed down, fixing the thickness to 240  $\mu\text{m}$ . Polydimethylsiloxane was deposited to seal the chamber. For most other experiments, chambers were built with an ultraviolet-curable resin (Photocentric 3D Daylight Resin, flexible, colour amber) through a master obtained by laser printing on a transparency film. Spacers between master and resin defined a chamber thickness of 150  $\mu\text{m}$  or 250  $\mu\text{m}$ . After illumination, sapphire windows were placed on top of the chambers and sealed with resin. Microfluidic access was provided through holes in the sapphire. Similarly, the chamber used for the phosphorylation and Hammerhead experiments was built by replacing the resin with a 254- $\mu\text{m}$ -thick Teflon foil from which the structure was cut out using a cutting plotter. For the phosphorylation, additional Teflon foils were placed on the warm and cold sides of the chamber to mimic a hydrophobic surface. The temperature gradient was produced by heating the sapphire block through copper fixtures using heater cartridges for 3D printers and cooling the silicon side with a water bath. Temperature sensors and proportional–integral–derivative (PID) software maintained the temperatures. The temperature inside the chamber was calculated from the chamber geometry and known material constants with finite element methods (Comsol).

Fluorescence was measured with a fluorescence microscope (Zeiss Axio) through the transparent sapphire heating block using Mitutoyo infinity corrected long working distance objectives ( $\times 2$  and  $\times 10$ ) and a Zeiss Fluor  $\times 5$  objective. The accumulation of DNA was detected with 200 nM FAM-labelled 132-base ssDNA in 0.1-fold PBS (see Supplementary Information for sequence). The silicon substrate was maintained at 10 °C, with the copper heaters initially turned off. The experiment began with the copper heaters set to maintain a desired temperature. Background intensity levels were obtained from the non-fluorescing gas region. The bulk fluorescence signal was obtained from an area far from the free interface. The accumulated DNA fluorescence ratio was averaged perpendicular to the interface and divided by the bulk fluorescence. The flow was visualized with 200 nm FAM-labelled polystyrene beads in 0.1  $\times$  PBS. The positions and velocities of the beads were tracked using ImageJ.

**Simulation protocol.** Simulations were performed using the finite element software COMSOL v4.4. The 2D model solved the convective heat equation, molecule diffusion equation and Navier–Stokes equations perpendicular to the contact line. Marangoni flows were established by implementing a stress boundary condition of the fluid velocity at the interface and by introducing a temperature-dependent surface tension. The water vapour concentration was simulated in the gas region above the interface by a diffusion–convection equation. The gas velocity was calculated from the temperature profile. Its velocity, combined with diffusion, caused an efficient net mass transport of vapour away from the interface into the gas bubble. By coupling a temperature-dependent vapour concentration boundary condition to the interface, a velocity boundary condition for water at the interface was imposed by the state equation of water. This resulted in capillary flow and evaporative mass transport of the water vapour, allowing vapour to enter and escape the water through evaporation or condensation. Thermophoresis was introduced via a thermophoretic drift term in the convection–diffusion equation describing the DNA concentration, and the Soret coefficients of the DNA were taken from experimental data<sup>49</sup>. To incorporate the time lag of the heating process, the sapphire temperature was measured over time and incorporated as a polynomial function for  $T_{\text{warm}}$ .

The above simulation was solved over time, resulting in the time evolution of accumulation at the contact line. To fit the simulation to the observed data, the surface tension dependency on temperature was set within observed values<sup>50</sup> and fine-tuned as a free parameter using the bead tracking data. The geometry of the interface itself was adjusted to moderately tune the DNA accumulation dynamics. Concentrations were determined by averaging the top  $\sim 10 \mu\text{m}$  of the meniscus at the hot side and comparing this to the simulated and experimental fluorescence, establishing a relation between fluorescence and average tip concentration.

To simulate the bubble shown in Supplementary Fig. 9, the simulation was transferred to an axial-symmetric geometry with spherical coordinates. The simulation around a small bubble was closed and gravity was pointed downwards. This removed the slow convection of water in the simulation, which, as expected from our modelling, did not change the accumulation characteristics. Ion and salt diffusion coefficients were taken from refs.<sup>51–53</sup>.

## Data availability

The data supporting the findings of this study are available within the paper and its Supplementary Information. Additional information and files are available from the corresponding author upon reasonable request. X-ray crystallographic data were also deposited at the Cambridge Crystallographic Data Centre (CCDC) under CCDC deposition no. 1847429.

## Code availability

The complete details of both simulations are documented in the html report and mph simulation files in the Supplementary Information.

Received: 7 September 2018; Accepted: 21 June 2019;

Published online: 29 July 2019

## References

- Schrödinger, E. *What is Life? The Physical Aspect of the Living Cell* (Cambridge Univ. Press, 1944).
- Cross, M. C. & Hohenburg, P. Pattern-formation outside of equilibrium. *Rev. Mod. Phys.* **65**, 851–1112 (1993).
- Bodenschatz, E., Pesch, W. & Ahlers, G. Recent developments in Rayleigh–Benard convection. *Annu. Rev. Fluid Mech.* **32**, 709–778 (2000).
- Fritts, D. C. & Alexander, M. J. Gravity wave dynamics and effects in the middle atmosphere. *Rev. Geophys.* **41**, 1003 (2003).
- Eaton, J. K. & Fessler, J. R. Preferential concentration of particles by turbulence. *Int. J. Multiph. Flow* **20**, 169–209 (1994).
- Götendorfer, A., Kruelle, C. A., Rehberg, I. & Svanšek, D. Localized subharmonic waves in a circularly vibrated granular bed. *Phys. Rev. Lett.* **97**, 198001 (2006).
- Chen, J. & Lopez, J. A. Interactions of platelets with subendothelium and endothelium. *Microcirculation* **12**, 235–246 (2005).
- Moore, W. B. & Webb, A. A. G. Heat-pipe Earth. *Nature* **501**, 501–505 (2013).
- Arndt, N. T. & Nisbet, E. G. Processes on the young Earth and the habitats of early life. *Annu. Rev. Earth Planet. Sci.* **40**, 521–549 (2012).
- Duhr, S. & Braun, D. Why molecules move along a temperature gradient. *Proc. Natl Acad. Sci. USA* **103**, 19678–19682 (2006).
- Baaske, P. et al. Extreme accumulation of nucleotides in simulated hydrothermal pore systems. *Proc. Natl Acad. Sci. USA* **104**, 9346–9351 (2007).
- Niether, D., Afanasenkau, D., Dhont, J. K. G. & Wiegand, S. Accumulation of formamide in hydrothermal pores to form prebiotic nucleobases. *Proc. Natl Acad. Sci. USA* **113**, 4272–4277 (2016).
- Kreysing, M., Keil, L., Lanzmich, S. & Braun, D. Heat flux across an open pore enables the continuous replication and selection of oligonucleotides towards increasing length. *Nat. Chem.* **7**, 203–208 (2015).
- Mast, C. B., Schink, S., Gerland, U. & Braun, D. Escalation of polymerization in a thermal gradient. *Proc. Natl Acad. Sci. USA* **110**, 8030–8035 (2013).
- Morasch, M., Braun, D. & Mast, C. B. Heat-flow-driven oligonucleotide gelation separates single-base differences. *Angew. Chem. Int. Ed.* **55**, 6676–6679 (2016).
- Keil, L. M. R., Möller, F. M., Kieß, M., Kudella, P. W. & Mast, C. B. Proton gradients and pH oscillations emerge from heat flow at the microscale. *Nat. Commun.* **8**, 1897 (2017).
- Budin, I., Bruckner, R. J. & Szostak, J. W. Formation of protocell-like vesicles in a thermal diffusion column. *J. Am. Chem. Soc.* **131**, 9628–9629 (2009).
- Lerman, L. Potential role of bubbles and droplets in primordial and planetary chemistry. *Orig. Life Evol. Biosph.* **16**, 201–202 (1986).
- Ariga, K. & Hill, J. P. Monolayers at air–water interfaces: from origins-of-life to nanotechnology. *Chem. Rec.* **11**, 199–211 (2011).
- Eickbush, T. H. & Moudrianakis, E. N. A mechanism for the entrapment of DNA at an air–water interface. *Biophys. J.* **18**, 275–288 (1977).
- Griffith, E. C. & Vaida, V. In situ observation of peptide bond formation at the water–air interface. *Proc. Natl Acad. Sci. USA* **109**, 15697–15701 (2012).
- Deegan, R. D. et al. Capillary flow as the cause of ring stains from dried liquid drops. *Nature* **389**, 827–829 (1997).
- Smith, K. A. On convective instability induced by surface-tension gradients. *J. Fluid Mech.* **24**, 401–414 (1966).
- Batchelor, G. K. *An Introduction to Fluid Dynamics* (Cambridge Univ. Press, 1973).
- Deegan, R. D. Pattern formation in drying drops. *Phys. Rev. E* **61**, 475–485 (2000).
- Larson, R. G. Transport and deposition patterns in drying sessile droplets. *AIChE J.* **60**, 1538–1571 (2014).
- Savino, R., Paterna, D. & Favaloro, N. Buoyancy and marangoni effects in an evaporating drop. *J. Thermophys. Heat Transf.* **16**, 562–574 (2002).
- Drobot, B. et al. Compartmentalised RNA catalysis in membrane-free coacervate protocells. *Nat. Commun.* **9**, 3643 (2018).
- Weinberg, M. S. & Rossi, J. J. Comparative single-turnover kinetic analyses of trans-cleaving hammerhead ribozymes with naturally derived non-conserved sequence motifs. *FEBS Lett.* **579**, 1619–1624 (2005).

30. Dahm, S. C. & Uhlenbeck, O. C. Role of divalent metal ions in the hammerhead RNA cleavage reaction. *Biochemistry* **30**, 9464–9469 (1991).
31. Zhu, T. F. & Szostak, J. W. Coupled growth and division of model protocell membranes. *J. Am. Chem. Soc.* **131**, 5705–5713 (2009).
32. Budin, I. & Szostak, J. W. Physical effects underlying the transition from primitive to modern cell membranes. *Proc. Natl Acad. Sci. USA* **108**, 5249–5254 (2011).
33. Filonov, G. S., Moon, J. D., Svensen, N. & Jaffrey, S. R. Broccoli: rapid selection of an RNA mimic of green fluorescent protein by fluorescence-based selection and directed evolution. *J. Am. Chem. Soc.* **136**, 16299–16308 (2014).
34. Islam, S., Bučar, D.-K. & Powner, M. W. Prebiotic selection and assembly of proteinogenic amino acids and natural nucleotides from complex mixtures. *Nat. Chem.* **9**, 584–589 (2017).
35. Anastasi, C., Crowe, M., Powner, M. W. & Sutherland, J. D. Direct assembly of nucleoside precursors from two- and three-carbon units. *Angew. Chem. Int. Ed.* **45**, 6176–6179 (2006).
36. Jones, S. F., Evans, G. M. & Galvin, K. P. Bubble nucleation from gas cavities—a review. *Adv. Colloid Interface Sci.* **80**, 27–50 (1999).
37. Powner, M. W., Gerland, B. & Sutherland, J. D. Synthesis of activated pyrimidine ribonucleotides in prebiotically plausible conditions. *Nature* **459**, 239–242 (2009).
38. Lohrmann, R. & Orgel, L. E. Urea–inorganic phosphate mixtures as prebiotic phosphorylating agents. *Science* **171**, 490–494 (1971).
39. Gibard, C., Bhowmik, S., Karki, M., Kim, E.-K. & Krishnamurthy, R. Phosphorylation, oligomerization and self-assembly in water under potential prebiotic conditions. *Nat. Chem.* **10**, 2012–2017 (2017).
40. Chow, Y. T. F., Maitland, G. C. & Trusler, J. P. M. Interfacial tensions of the (CO<sub>2</sub>+N<sub>2</sub>+H<sub>2</sub>O) system at temperatures of (298 to 448) K and pressures up to 40 MPa. *J. Chem. Thermodyn.* **93**, 392–403 (2016).
41. Sosson, M. & Richter, C. Enzyme-free genetic copying of DNA and RNA sequences. *Beilstein J. Org. Chem.* **14**, 603–617 (2018).
42. Forsythe, J. G. et al. Ester-mediated amide bond formation driven by wet–dry cycles: a possible path to polypeptides on the prebiotic earth. *Angew. Chem. Int. Ed.* **54**, 9871–9875 (2015).
43. Morasch, M., Mast, C. B., Langer, J. K., Schilcher, P. & Braun, D. Dry polymerization of 3',5'-cyclic GMP to long strands of RNA. *ChemBioChem* **15**, 879–883 (2014).
44. Vaidya, N. et al. Spontaneous network formation among cooperative RNA replicators. *Nature* **491**, 72–77 (2012).
45. Mutschler, H., Wochner, A. & Holliger, P. Freeze–thaw cycles as drivers of complex ribozyme assembly. *Nat. Chem.* **7**, 502–508 (2015).
46. Soukup, G. A. & Breaker, R. R. Relationship between internucleotide linkage geometry and the stability of RNA. *RNA* **5**, 1308–1325 (1999).
47. Topozini, L., Dies, H., Deamer, D. W. & Rheinstädter, M. C. Adenosine monophosphate forms ordered arrays in multilamellar lipid matrices: insights into assembly of nucleic acid for primitive life. *PLoS One* **8**, e62810 (2013).
48. Rajmani, S. et al. Lipid-assisted synthesis of RNA-like polymers from mononucleotides. *Orig. Life Evol. Biosph.* **38**, 57–74 (2008).
49. Reineck, P., Wienken, C. J. & Braun, D. Thermophoresis of single stranded DNA. *Electrophoresis* **31**, 279–286 (2010).
50. Vargaftik, N. B., Volkov, B. N. & Voljak, L. D. International tables of the surface tension of water. *J. Phys. Chem. Ref. Data* **12**, 817–820 (1983).
51. Lide, D. R. *CRC Handbook of Chemistry and Physics* (CRC Press, 2001).
52. Li, Y. & Gregory, S. Diffusion of ions in sea water and in deep-sea sediments. *Geochim. Cosmochim. Acta* **33**, 703–714 (1974).
53. Fell, C. J. D. & Hutchison, H. P. Diffusion coefficients for sodium and potassium chlorides in water at elevated temperatures. *J. Chem. Eng. Data* **16**, 427–429 (1971).

## Acknowledgements

The authors thank L. Keil for help with data analysis. Financial support from the Simons Foundation (318881 to M.W.P. and 327125 to D.B.), the German Research Foundation (DFG) through CRC/SFB 235 Project P07 and SFB 1032 Project A04, DFG Grant BR2152/3-1 and the US–German Fulbright Program is acknowledged. H.M. is supported by the MaxSynBio consortium, which is jointly funded by the Federal Ministry of Education and Research of Germany and the Max Planck Society. H.M. and K.L.V. are supported by the Volkswagen Initiative 'Life?—A Fresh Scientific Approach to the Basic Principles of Life'. A.K. is supported by a DFG fellowship through the Graduate School of Quantitative Biosciences Munich.

## Author contributions

M.M., J.L., C.F.D., A.K., A.I. and Ph.S. performed the experiments. M.M., J.L., K.L.V., S.I., B.S., D.B.D., H.M., Pe.S., M.W.P., C.B.M. and D.B. conceived and designed the experiments. M.M., J.L., K.L.V., S.I., M.K.C., H.M., M.W.P. and D.B. analysed the data. M.M., J.L. and D.B. wrote the paper. All authors discussed the results and commented on the manuscript.

## Competing interests

The authors declare no competing interests.

## Additional information

**Supplementary information** is available for this paper at <https://doi.org/10.1038/s41557-019-0299-5>.

**Reprints and permissions information** is available at [www.nature.com/reprints](http://www.nature.com/reprints).

**Correspondence and requests for materials** should be addressed to D.B.

**Publisher's note:** Springer Nature remains neutral with regard to jurisdictional claims in published maps and institutional affiliations.

© The Author(s), under exclusive licence to Springer Nature Limited 2019

OPEN

# Fission of Lipid-Vesicles by Membrane Phase Transitions in Thermal Convection

Patrick W. Kudella<sup>1,2,3</sup>, Katharina Preißinger<sup>1</sup>, Matthias Morasch<sup>2,3</sup>, Christina F. Dirscherl<sup>2,3</sup>, Dieter Braun<sup>2,3</sup>, Achim Wixforth<sup>1,2</sup> & Christoph Westerhausen<sup>1,2,4\*</sup>

Unilamellar lipid vesicles can serve as model for protocells. We present a vesicle fission mechanism in a thermal gradient under flow in a convection chamber, where vesicles cycle cold and hot regions periodically. Crucial to obtain fission of the vesicles in this scenario is a temperature-induced membrane phase transition that vesicles experience multiple times. We model the temperature gradient of the chamber with a capillary to study single vesicles on their way through the temperature gradient in an external field of shear forces. Starting in the gel-like phase the spherical vesicles are heated above their main melting temperature resulting in a dumbbell-deformation. Further downstream a temperature drop below the transition temperature induces splitting of the vesicles without further physical or chemical intervention. This mechanism also holds for less cooperative systems, as shown here for a lipid alloy with a broad transition temperature width of 8 K. We find a critical tether length that can be understood from the transition width and the locally applied temperature gradient. This combination of a temperature-induced membrane phase transition and realistic flow scenarios as given e.g. in a white smoker enable a fission mechanism that can contribute to the understanding of more advanced protocell cycles.

Before life on earth emerged, only small molecules existed. The development of complex structures or already simple reactions were unlikely and energetically unfavorable simply due to the assumed very dilute settings of early earth<sup>1,2</sup>. Physical non-equilibrium settings can have a profound influence here: sub-sea hydrothermal microenvironments<sup>3</sup> like pores in submerged volcanic rock provide temperature cycling systems and allow for strong accumulation, as the cooperation of convective flow and thermophoresis can enlarge molecule- and particle-concentrations by several orders of magnitude<sup>4</sup>.

An important concept in early earth's cell evolution is compartmentalization. Following Blain, Szostak<sup>5</sup> and Nourian, Danelon<sup>6</sup> a compartment such as a lipid membrane provides a selective barrier between the inner proto-cell content and the surrounding environment. Schrum *et al.* describe a pathway for lipid membrane vesicles made from fatty acids known as prebiotically plausible membrane building blocks<sup>7</sup> to more sophisticated phospholipids. They then raise the question how such structurally simple protocells could accomplish essential membrane functions known from modern cells.

In a model cell cycle for vesicles the two phases, *formation* and *inclusion* of diluted substances, are well understood<sup>5</sup>. The *division*-phase has been the subject of several studies<sup>5,6,8,9</sup>. This division is necessary to redistribute enclosed material or reaction products formed in the protocell. While modern cell division is a complicated mechanism mediated by many complex proteins, an early earth protocell must have had a simple fission mechanism. A basic cell division-like fission could have been driven by the environment and membrane properties only, without any active contribution by the protocell itself. The temperature-dependent hydrophobic effect drives the self-assembly of vesicles from dissolved lipids above a critical concentration and e.g. for dipalmitoylphosphatidylcholine (DPPC) based membranes also causes complex reshaping of the vesicle membrane during several phase transitions<sup>10,11</sup>. Temperature induced morphological transitions of DPPC vesicles have been shown by Leirer *et al.* in absence of additional shear flow. The vesicles showed a pear-shaped morphological transition of previously spherical DPPC vesicles by the DPPC L<sub>3</sub>' - L<sub>α</sub> membrane phase transition<sup>12</sup> by quick temperature changes in a

<sup>1</sup>Chair for Experimental Physics I, University of Augsburg, Augsburg, Germany. <sup>2</sup>Center for NanoScience (CeNS), Ludwig-Maximilian University Munich, Munich, Germany. <sup>3</sup>Systems Biophysics, Ludwig-Maximilian University Munich, Munich, Germany. <sup>4</sup>Chair for Physiology, University of Augsburg, Augsburg, 86159, Germany. \*email: [christoph.westerhausen@gmail.com](mailto:christoph.westerhausen@gmail.com)

static setup. Rapid cooling can fission those vesicles, but the resulting new vesicles differ strongly in size compared to the mother vesicle. They do not result in two or more similarly sized vesicles resembling modern cell division. Moreover, such a temperature setup does not resemble scenarios possible on early earth, as closed fluid compartments with rapid temperature change over some seconds without flow do barely exist in nature.

Zhu, Budin, and Szostak show the growth and division of proto-cell membranes under mild flow<sup>9,13</sup>. Vesicle growth is driven by uptake of micelles by small unilamellar vesicles, the resulting aggregates are tube-shaped due to the large surface-to-volume ratio of the integrated micelles. The low permeability of the fatty acid bilayer inhibits the influx of water and therefore their reshaping to spheres. Already a mild fluid flow induces shear forces by which these aggregates are ruptured. The tube-like structures shown by Zhu *et al.* are fragile and too easily divided to be suitable for the robust transport and enclosure of molecules such as DNA. Alternatively, the surface-to-volume imbalance can be achieved by lipid production in the vesicle<sup>14</sup>. Deshpande *et al.* use the osmotic pressure to increase the surface-to-volume ratio and then use an obstacle in a microfluidic channel to mechanically divide DOPC-vesicles. They note, that the success of vesicle-splitting mainly depends on the surface-to-volume ratio of the mother vesicle and a too small ratio leads to complete rupture of the vesicle<sup>15</sup>.

The concept of a primitive cell cycle with division of cell-sized lipid vesicles is modelled in several studies<sup>16</sup>: in all cases the concept introduces an imbalance of vesicle surface and volume<sup>15,17–19</sup>, as shown above, or shear forces and thermodynamic instability as shown by Szostak *et al.* In combination with a spontaneous growth mechanism, this “[...] could lead to a primitive cell cycle controlled entirely by the biophysical properties of the membrane and environmental forces”<sup>17,20</sup>.

When modern cells like *Bacillus subtilis* are treated by antibiotics they lose their cell wall. In turn, their division mechanism (Z-ring) does not work anymore. In order to proliferate, these cells now grow and undergo a shape transformation to pearl or dumbbell-like shapes and split into multiple cells<sup>21</sup>. This observation shows the ability for an alternative self-driven division mechanism in nowadays cells that is comparable to the division of lipid vesicles<sup>22</sup>.

Here, we describe a simple process of splitting Giant Unilamellar lipid Vesicles (GUV) in homogeneously sized daughter vesicles. In our system this process is driven by environmental conditions of flow induced shear forces in a spatial temperature gradient. The vesicles have a stable membrane with low permeability before and after the fission process and hardly lose any membrane area during fission. In contrast to other mechanisms, here no additional chemical or biological effect or mechanism is necessary.

## Results and Discussion

In temperature-driven convection chambers we first discovered distinctly deformed DPPC vesicles. The chambers are built to mimic hydrothermal microenvironments<sup>3</sup> and sustain flow through the applied temperature gradient. In nature comparable chambers are located in rocks that are heated from the inside (by lava or hot gases) and cooled from the outside (ocean). Figure 1 illustrates such a rock as well as possible capillary or chamber geometries (closed and open channels). Keil *et al.* show, that the geometry of a chamber can vary without altering the convection or accumulation effect significantly<sup>4</sup>.

Figure 2 shows deformed vesicles in the convective flow. The initially spherically shaped vesicles now show non-spherical forms. Some time after the gradient is applied, those shapes disappear. Screening the vesicles in the chamber before and after temperature cycling results in a distinct difference in size distribution. Figure 3a,b show a schematic illustration of the convection chamber and the parabolic flow profile.

The convection driven flow chamber is constructed following the standard procedure shown in the methods section. Vesicles in the chamber travel in the double parabolic flow profile and experience position-dependent velocity and shear-forces. Figure 3c shows the simulated path of two vesicles in the convective flow. The absolute temperature difference was chosen smaller for the second case with elevated temperatures, as the viscosity of water is lower and, therefore, flow speed increases. In d) we show the vesicle volume distribution. When vesicles do not cross the phase transition temperature of their membrane lipids, the size distribution is shifted towards slightly larger volumes, suggesting smaller vesicles loosely adhering to larger ones. In the second case, vesicles shuttle through the chamber and across the phase transition temperature multiple times. Here, the size distribution is shifted to smaller vesicles, suggesting vesicle fission (see Fig. 3d).

In literature, there are several cases of vesicle fission described: vesicles can divide when shear forces are applied<sup>13</sup> or when they are heated in a stationary case<sup>12</sup>. In our case we do only see the shift in size distribution towards smaller vesicle sizes when the transition temperature is exceeded. Combining these reported findings and the statistically significant shift to smaller vesicle sizes suggest the hypothesis of vesicle fission in the convection chamber. While this setup allows to study several thousand vesicles at the same time, tracking of single vesicles is difficult. To check whether indeed vesicle fission happens, we build a capillary setup mimicking the form of the flow profile and the temperature gradient of the convection chamber, however in a linear one-way version. Combined with lower vesicle density and higher magnification we study single vesicles on their way through the temperature profile.

The experiments indeed show vesicle fission as seen in Fig. 4. Figure 4b shows the experimental setup with two copper blocks and a Peltier element for heating and cooling.

Figure 4a shows four states of vesicle deformation, that are reproduced in every fission event we monitored ( $N_{\text{fission}} = 55$  out of  $N_{\text{total}} = 97$ ). The first state is the *static equilibrium*. Here, the membrane is in the gel-like phase as the temperature is below the phase transition temperature. The surface area is in equilibrium with the enclosed volume – an outer force acting on the vesicle would lead to a strain in the membrane acting against that deformation. In the second state *deformation* the vesicle is in the hot part of the capillary and the temperature exceeds the main phase transition temperature of the lipid-membrane. As a result, the membrane expands suddenly while the vesicle volume remains approximatively constant. Additionally, the deformability increases as the bending modulus of the membrane decreases by a factor of about ten<sup>23,24</sup>. The exterior force caused by the parabolic fluid

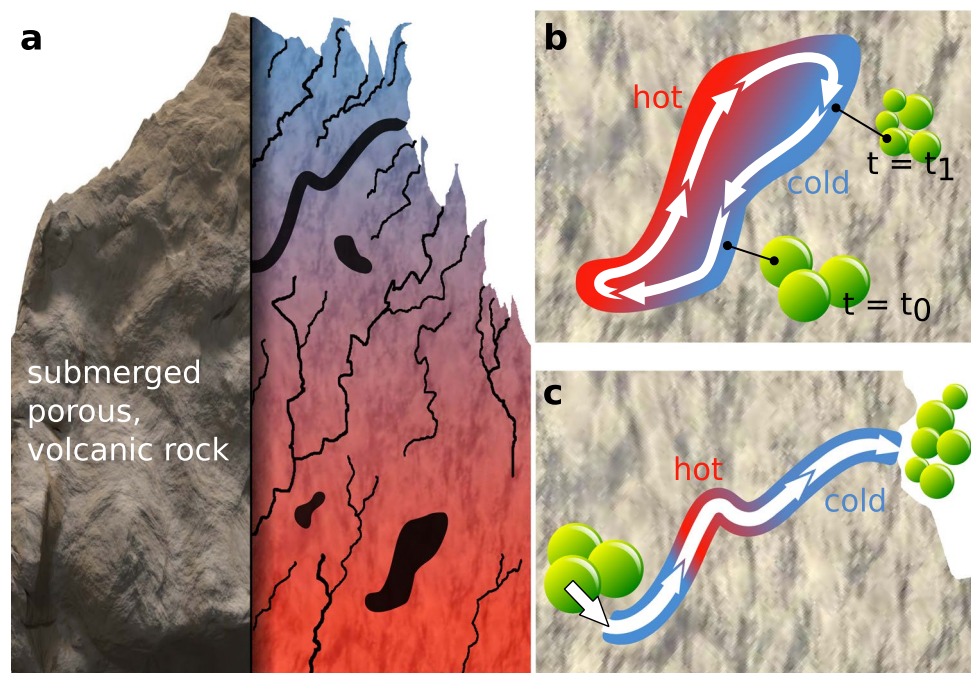


**Figure 1.** Schematic sketch of a subsea hydrothermal microenvironment, (a) Submerged porous (volcanic) rock is a scenario for stable temperature gradients and micro fluidics: water flows through narrow cracks and compartments in the rock where hot parts of thermal vents and the cold ocean create steep temperature gradients on small length scales. (b) Vesicle division in a convection chamber that provides temperature driven flow and temperature cycling. (c) Vesicle division by a fluid flow profile in combination with temperature induced lipid membrane phase transitions.

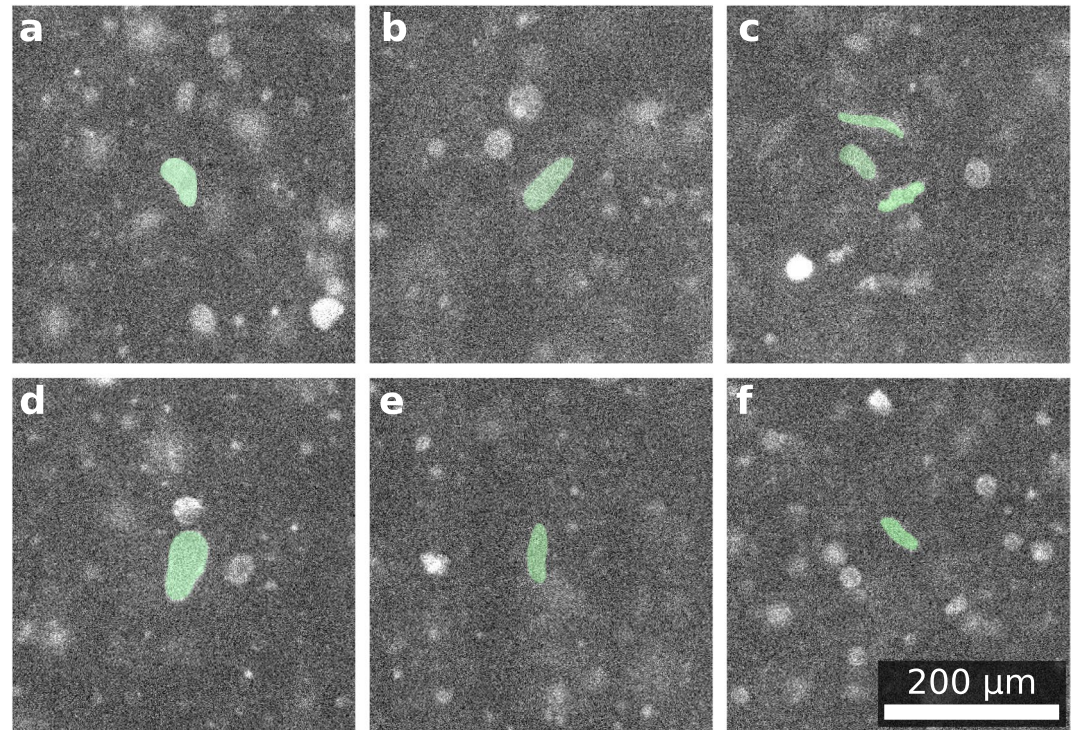


**Figure 2.** Deformed DPPC-DPPG vesicles in a convection chamber: (a–f) deformed vesicles (guide to the eye: green translucent overlay) in a thermally driven convection chamber. Some vesicles are too small or in regions with less shear force and do not deform. Vesicles do only reshape at temperatures above the membrane phase transition temperature. Due to the shallow thickness of the chamber of 400 μm, vesicles in cold and in hot regions are seen sharp simultaneously with the optics used.

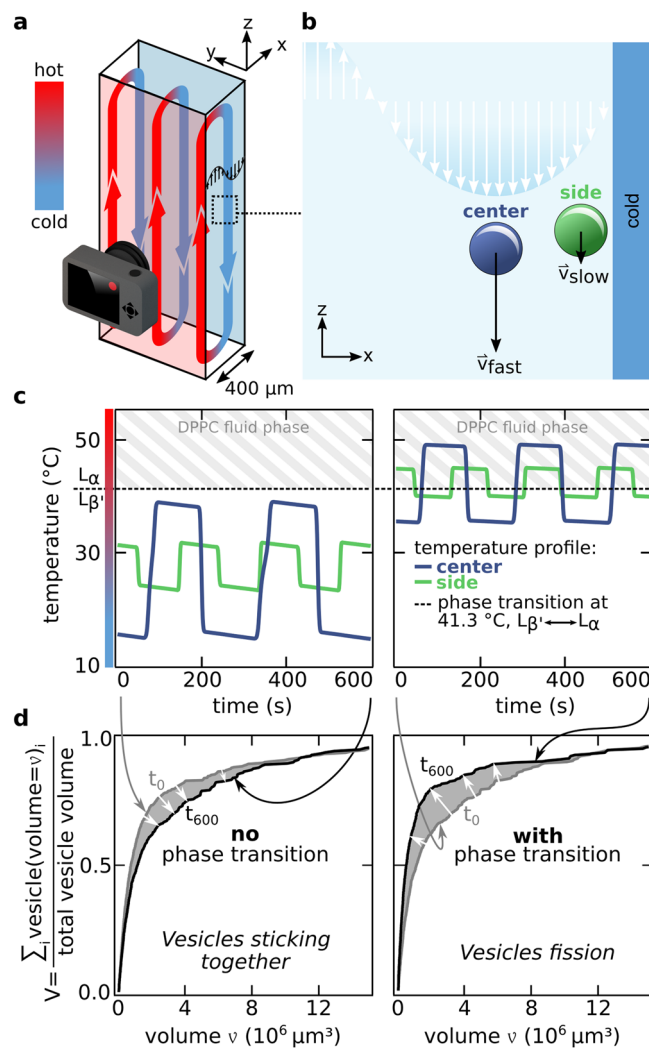


**Figure 3.** Thermally driven convection chamber: (a) The temperature gradient across the 400  $\mu\text{m}$  thick capillary induces a convective flow. Lipid vesicles are carried in this flow and experience hot and cold conditions, as well as shear forces originating from the parabolic flow profile. At the top and the bottom of the chamber, a phase transition of the vesicle membrane can occur. (b) Vesicles in the center of the flow profile are moving the fastest. Near the chamber wall fluid flow is slow. This leads to a different number of experienced phase transitions for each vesicle. (c) The COMSOL simulation of the flow profile in the chamber overlaid by a particle tracker shows the temperature profile in a stream line over time. For elevated temperatures, the streamline crosses the phase transition temperature of DPPC membranes. To achieve similar mean flow velocities,  $\Delta T$  of the temperature gradient is reduced to compensate for the lower viscosity of water at higher temperatures. While at lower temperatures the vesicles simply shuttle in the convective flow, at higher temperatures the vesicles experience two phase transitions for each cycle (simulation and particle tracker from Keil<sup>4</sup>). (d) The vesicle size distribution in the convection chamber before and after cycling. When the applied temperature range does not include the phase transition temperature (silicon: 13  $^{\circ}\text{C}$ , sapphire: 40  $^{\circ}\text{C}$ , see SI) a small shift in the size distribution towards slightly larger vesicles is visible. This can be understood by vesicles sticking together. For higher temperatures (silicon: 34  $^{\circ}\text{C}$ , sapphire: 50  $^{\circ}\text{C}$ ) the size distribution is significantly shifted to smaller sizes.

flow profile is now able to deform the vesicle. Due to the rectangular shape of the capillary the deformation in the  $z$ -direction is several times stronger than in the  $y$ -direction. The formerly rotationally symmetric (with regard to the  $x$ -axis) vesicle is not symmetric in this step and rather flat in the  $z$ -direction compared to the  $y$ -direction and elongated especially in the  $x$ -direction. In the third state *domaining* new lowest energy states of the vesicle shapes develop: volume containing sections are separated by tether sections of negligible volume. Volume containing sections are typically close to a spherical shape and basically encapsulate the entire vesicle volume (see Fig. 4c–e) with parts of the membrane area. The tube-shaped tether sections accommodate the remaining surface area and connect two neighboring volume sections. These vesicle shapes are stable under given conditions as no disruption has been observed and all vesicles adopt to a comparable shape in all performed experiments (for example see SI-Video).

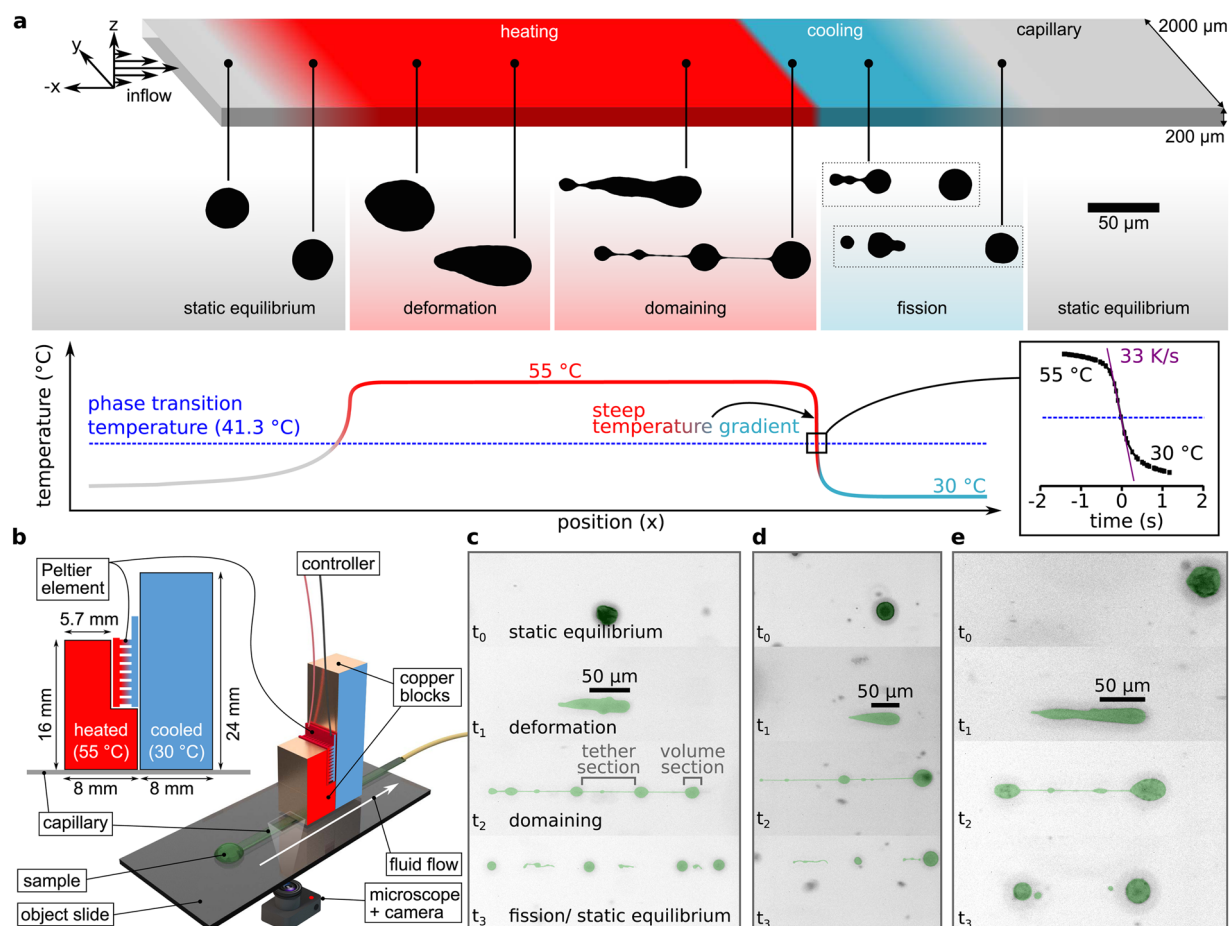


**Figure 4.** Capillary flow chamber to closely monitor vesicles during phase transitions. (a) Processed micrographs show four states of vesicle fission: at temperatures below the phase-transition temperature the vesicles are in static equilibrium and drift with the surrounding medium in the channel without being deformed by the shear force. In the second state, deformation, the vesicles are heated over their phase-transition temperature. The now deformable membrane gains additional surface area and transforms into rain-drop/ comet-tail like shapes. In state three, domaining, the combination of shear force and bending energy minimization leads to the formation of new stable shapes with volume and tether domains. In the phase fission the vesicle is divided by the membrane phase transition back to the gel-like state. The resulting vesicles are again in a spherical shape. The graph shows the temperature profile in the capillary as a function of the channel position. The zoom-in on the right shows the temperature experienced by a vesicle moving in the center stream line as a function of time with flow velocity =  $550 \mu\text{m/s}$  (mean flow velocity:  $367 \mu\text{m/s}$ ). Maximum temperature gradients of up to  $33 \text{ K/s}$  are possible. This data is extracted from a COMSOL simulation. (b) Illustration of the setup: the copper blocks (red, blue) act as heat buffers and contact the capillary from the top. The Peltier element heats the L-shaped copper block and cools the other one. (c–e) Micrographs show vesicles that behave similar to the exemplarily chosen vesicle reshaping and fission in (a).

In the fourth state *fission* the rapid cooling of medium and vesicle membrane below the phase transition temperature of the lipid membrane induces the phase transition from the fluid unordered phase to the gel-like membrane phase. The bilayer surface area shrinks back to its pre-phase transition state. At this state for slow temperature changes and low shear flow velocities the vesicle reshapes back to its spherical starting configuration. However, when a distinct threshold of shear flow velocity and temporal temperature gradient is reached, the tethers break apart. Breaking tethers open energetically unfavorable pores in the membranes of the volume domains. The vesicles close these pores by releasing inner volume into the surrounding medium, as e.g. shown earlier for endocytosis-like nanoparticle uptake<sup>25,26</sup>. By such shrinking to a smaller size and thus decreasing the surface-to-volume ratio, these new smaller vesicles are in a mechanical equilibrium state again. The resulting split-up vesicles are about equal in size in all our experiments (for example Fig. 4).

This mechanism represents a reproducible, controlled way to divide lipid vesicles with a structural membrane phase transition in microfluidic pore setups. Moreover, no processes other than a non-uniform flow profile and a local temperature gradient are necessary for the division process. Most of the vesicle volume is preserved and still enclosed in the unilamellar bilayer vesicle. In control experiments under the same conditions DPPC was replaced by 1,2-dioleoyl-sn-glycero-3-phosphocholine (DOPC), a lipid lacking a phase transition in the respective temperature range. Here, not a single fission event was observed despite high deformability of the

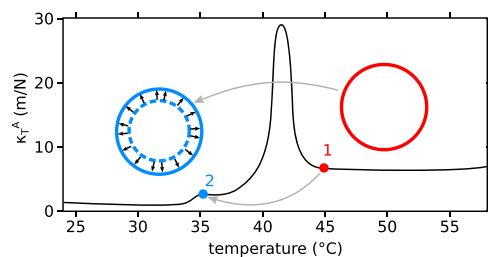


**Figure 5.** Model for energy estimation: area compression modulus as function of temperature. Prior to the temperature gradient the vesicle is at point 1, then quickly passes the transition temperature towards a lower temperature below the main transition (point 2). The vesicle keeps its geometry (blue solid circle) but is in the gel phase at around 35 °C with a smaller equilibrium size (dashed blue circle). The arrows indicate the membrane expansion resulting in membrane tension.

fluid membrane. Following Mercier *et al.*<sup>16</sup> the unbalanced surface-to-volume ratio is key to vesicle division. The main phase transition of DPPC and the resulting increase in surface area provides this imbalance, while DOPC is lacking this property, explaining the lack of fission events described above. For deformed DPPC vesicles the fast phase transition back from fluid to gel-like state enables the vesicle division.

Furthermore, we assume the vesicles in the fluid phase to be equilibrated to the environmental conditions (temperature and shear force), when the front section of a tethered vesicle enters the steep temperature gradient as shown in Fig. 4. The immediate phase transition of the membrane with its accompanied decrease in area leads to a drastic increase in membrane tension. In turn, the increased tension leads to Marangoni flow of lipids from the tether and the rear vesicle section towards the front vesicle section<sup>27</sup>. This is accompanied by a flow of surrounding water, being dragged by the flowing lipid to the front vesicle section. This hinders volume flow towards the back vesicle section what becomes less important with increasing tether radius<sup>27</sup>.

Detailing the fission mechanism, we first investigate the energy necessary for a fission event.

**Energy required for fission.** As the fission event requires the formation of two pores for the rupture of the tether (one in the volume section and one on the tether), we estimate an upper limit for the energy  $E_{\text{pore}}$  necessary for pore formation. We assume a pore radius of  $r = 25$  nm and membrane tension  $\sigma \approx 0$ . Following Taupin *et al.*<sup>28,29</sup>

$$E_{\text{pore}}(r) = \gamma \cdot 2\pi \cdot r - \sigma \cdot \pi \cdot r^2 \quad (1)$$

with the line tension  $\gamma \approx 0.7 \cdot 10^{-11}$  N. This results in  $E_{\text{pore}} \approx 10^{-18}$  J. However, for some finite membrane tension of about 1 mPa,  $E_{\text{pore}}$  can take a maximal value of  $E_{\text{pore}} \approx 10^{-19}$  J for  $r = 7$  nm and becomes even negative for pore radii larger than  $r = 14$  nm.

**Energy supplied by a phase transition of the front vesicle.** We can estimate the energy contributions of this transition following the approach of Heimburg<sup>11</sup> as follows:

The contribution to the Gibbs Free Energy density due to area changes  $g_A$  is

$$g_A = \frac{1}{2} K_A \left( \frac{\Delta A}{A_0} \right)^2 \quad (2)$$

where  $K_A$  is the area compression modulus and  $\Delta A$  the deviation from the equilibrium (here the gel-like phase) area  $A_0$ . Moreover,

$$K_A = \frac{1}{\kappa_A^T} \quad (3)$$

with the area compressibility  $\kappa_A^T$ .

In our experiment prior to the steep temperature gradient from hot to cold the vesicle is in an equilibrium shape as a result of temperature and shear forces. For the following energy estimation, we illustrate the front vesicle of our dumbbell shaped vesicle as a spherical vesicle in Fig. 5.

Starting from point 1 in the graph of area compression modulus as function of temperature, the vesicle quickly passes the transition temperature towards a lower temperature below the main transition (point 2). The vesicle keeps its geometry due to the incompressibility of water and only a minor chance to release volume from the interior during the short moment when the vesicle reaches the main transition temperature. Thus, at point 2 the vesicle still has the area of a fluid phase vesicle but is in the gel phase at around 35 °C. This is equivalent to a stretching of a gel phase vesicle (dashed line) to the size of a fluid phase vesicle (solid line). Thus, accepting the approximate volume conservation (see also Fig. 6), the energy difference between the points 1 and 2 is equal to a membrane expansion of about 25% using the  $K_A$  (35 °C).

Using Eqs. 2 and 3 with  $\frac{\Delta A}{A_0} = \frac{A_{\text{fluid}} - A_{\text{gel}}}{A_{\text{gel}}} \approx 25\%$ <sup>11</sup>,  $\kappa_A^T(35 \text{ °C}) \approx 3 \frac{\text{m}}{\text{N}}$  and  $A_{\text{fluid}} \approx 0.63 \text{ nm}^2$  it follows:

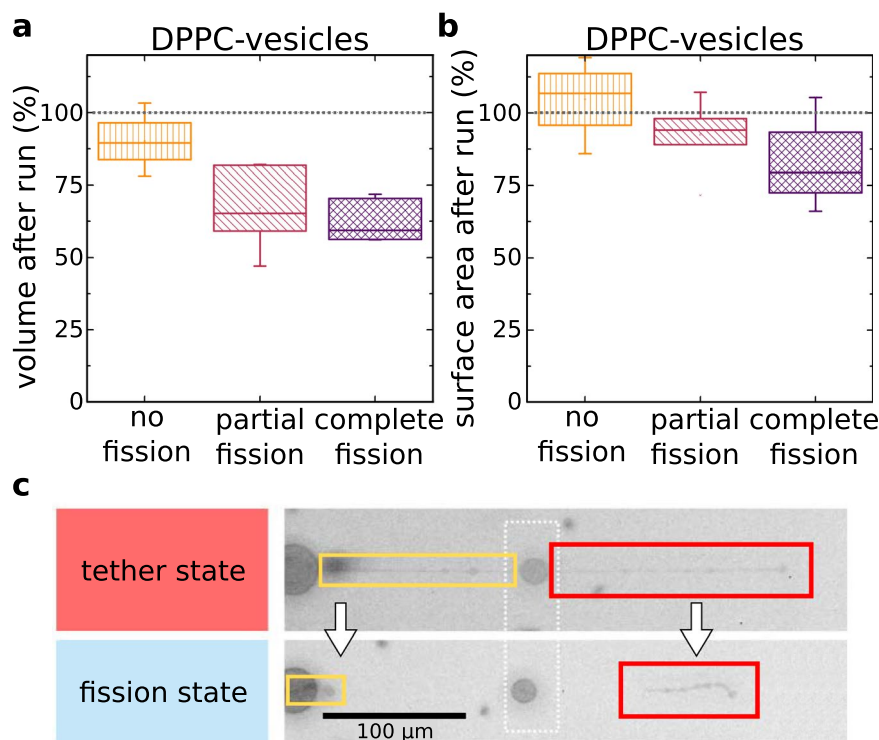


**Figure 6.** Vesicle volume and surface after fission and vesicles with broad phase transition, (a) Volume loss as a function of fission state: completely divided vesicles lose the most volume. Vesicles that do not fission do hardly lose volume. (b) Vesicle membrane area as function of fission state: vesicle lose less than a quarter of surface area by division. The loss of volume is geometrically necessary for the vesicle fission. (c) Microscope image of split off lipid tethers after vesicle fission. Therefore, surface area is lost. The yellow rectangle marks a tether still sticking to a spherical vesicle, the red rectangle marks a completely separated tether-section.

$$g_A = \frac{1}{2} K_A \left( \frac{\Delta A}{A_0} \right)^2 = \frac{1}{2} \cdot \frac{N}{3 \text{ m}} \cdot 0.25^2 = 10 \frac{\text{mN}}{\text{m}} = 10 \frac{\text{mJ}}{\text{m}^2} \quad (4)$$

$$\Delta G_{A_{\text{mol}}} = g_A \cdot A_{\text{fluid}} \approx \frac{3}{2} k_B T \quad (5)$$

Where,  $\Delta G_{A_{\text{mol}}}$  and  $A_{\text{fluid}}$  are the change in Gibbs Free Energy and area per molecule respectively. This energy can be compared with the energy necessary for the formation of a pore with radius  $r$ .

Thus, the Gibbs Free Energy  $\Delta G_{A_{\text{ves}}}$  for a typical vesicle with radius  $R = 10 \mu\text{m}$  is  $\Delta G_{A_{\text{ves}}} \approx 4\pi \cdot (10 \mu\text{m})^2 \cdot \frac{10 \text{ mJ}}{\text{m}^2} = 1.2 \cdot 10^{-11} \text{ J} \gg E_{\text{pore}}$ . This energy easily suffices for arbitrarily large pores, even for vesicles that do not experience shear stress with membrane tension  $\sigma = 0$ .

This estimation shows that all vesicles in our experiments could fission, if the pore formation energy would be the single decisive parameter. However, only a subset of vesicles experiences a fission in the capillary setup. Therefore, we investigate the influence of geometrical parameters like tether length, radius and flow velocity on the fission behavior.

First, we estimate the shear stress  $\sigma$  using a mean shear rate for each vesicle depending on its particular position within the parabolic flow profile in the channel. In the experiments presented here the shear stress typically is  $\sigma_{\text{shear}} = \gamma \eta \approx \frac{1}{s} \cdot 1 \text{ mPa s} = 1 \text{ mPa}$ . Fig. 6c shows boxplots of the estimated shear force  $f$  as a product of  $\sigma$  and the total area of each vesicle for all vesicles categorized as *fission* and *no fission*. The median overall shear force  $f$  for vesicles that do fission during the experiment and those that reshape without fission are  $f_{\text{fission}} = 3.3 \text{ pN}$  and  $f_{\text{no-fission}} = 1.8 \text{ pN}$ , respectively. Vesicles that fission do on average experience an 1.8-fold higher shear stress.

Second, we measure the mean tether radius from the fluorescence micrographs. Figure 6d shows boxplots of the tether radii for all vesicles categorized as *fission* and *no fission*. The median apparent tether radii  $\rho$  for vesicles that are divided during the experiment and those that reshape without fission are  $\rho_{\text{fission}} = 1.1 \mu\text{m}$  and  $\rho_{\text{no-fission}} = 1.3 \mu\text{m}$ , respectively. This is in line with the argumentation on Marangoni flow as discussed above, especially concerning the dependence of flow resistance from the radius  $\sim \rho^4$ . The mean difference of 15 % in radius results in a flow resistance difference by a factor of two.

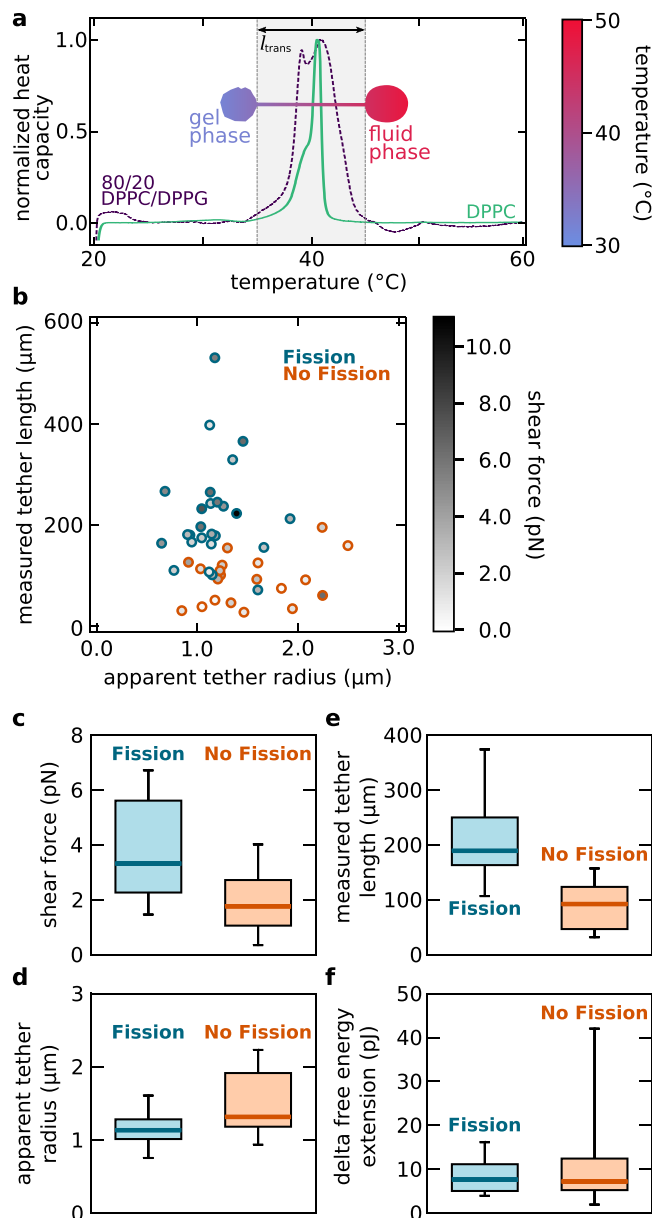


**Figure 7.** Tether length and tether radius are the important parameters determining fission. **(a)** Vesicles made from DPPC and DPPG (80:20 ratio) experience a broader phase transition than vesicles made from DPPC only. The vesicle drawn as an overlay (blue-red color map) shows the temperature distribution over a vesicle moving with a velocity of  $550 \mu\text{m/s}$ . **(b)** Measured tether length as a function of apparent tether radius. Vesicles that fission are marked blue, vesicles that do not fission are marked orange. Fission occurs more often for large tether lengths and small tether diameters. The grey scale filling of the symbols indicates the total shear force experienced by each vesicle. **(c–f)** Boxplots visualize the distribution of shear force, tether length, tether radius and  $\Delta G_{A,ves}$  categorized as fission and no fission. Boxes include 50% of data points, the thick horizontal line marks the median and whiskers mark the range of 80% of the data range.

Third, we measured the tether lengths from the fluorescence micrographs immediately before the vesicles pass the steep temperature gradient from the hot to the cold region. Figure 7e shows boxplots of the tether length for all vesicles categorized as *fission* and *no fission*. The median tether length  $l$  for vesicles are  $l_{fission} = 189 \mu\text{m}$  and  $l_{no\_fission} = 92 \mu\text{m}$ . Therefore, we see a strong correlation of tether length and fission events. Long tethers are prone to fission.

Defining the mean value of  $l_{fission}$  and  $l_{no\_fission}$  as the transition tether length  $l_{trans}$  we can compare  $l_{trans}$  with the width of the phase transition: the setup provides a steep temperature gradient of  $0.07 \text{ K}/\mu\text{m}$  at the phase transition region. Thus, the transition tether length  $l_{trans}$  corresponds to a temperature difference of  $\Delta T = 10 \text{ K}$ . This  $\Delta T$  is about 2.3 times the FWHM of the phase transition temperature width of the used lipid mixture, see Fig. 7a. Even more convincing, 10 K is almost exactly the width of the complete phase transition width.

Summing this discussion up, we conclude that shear forces acting on the vesicles result in a shape change with the formation of a tether of distinct length and radius. The tether radius and length determine the relaxation dynamics of membrane tension after the phase transition of the front vesicle section. In combination with the temperature gradient in the capillary these parameters then determine the Gibbs Free Energy change, that finally leads to the fission event. Or in even simpler words: the shear force decides about the fission indirectly while the phase transition delivers the energy for the fission.

As DOPC-membranes do not have a phase transition in this temperature range, DOPC-vesicles do not change their shape irreversibly and no fission event can be detected. This also holds for vesicles from cholesterol-DPPC mixtures ( $\geq 30\%$  cholesterol, see SI). Thus, the capillary setup experiments proof our hypothesis concluded from the shift in size distribution in the convection driven chamber: a robust vesicles fission takes place under the influence of shear flow and a temperature gradient reaching across a phase transition temperature of the membrane.

Important for protocells, especially for early earth scenarios, is the conservation of its building blocks. In a dilute ocean shell material as well as encapsulated material were scarce<sup>1,2,30</sup>. In Fig. 6 the mean volume and surface of the vesicles before and after passing the capillary are shown. Due to the setup geometry only the 2D-projections in the x-y-plane are analyzed. Vesicles are assumed to be rotationally symmetric. Measurements of vesicles in the capillary setup are classified in three categories: no fission, partial fission and complete fission. Here, partial fission summarizes all irreversible shape deformations including incomplete separation of tether and daughter vesicles.

The total vesicle volume decreases only slightly when there is no fission, decreases for about 35% at partial fission and for about 40% for complete fission. An ideal fission event would not lose any surface area. But the resulting daughter spheres of course have a combined volume smaller than the initial volume. For two and three equally sized daughter vesicles this decrease of volume is about 30% and 42%, respectively. Thus, the fissioned vesicles retain roughly as much volume as geometrically possible (analytical estimation shown in SI).

Along the same line, surface area remains constant if the vesicles do not fission. The slight increase in Fig. 6b points towards a systematic error in the calculation of surface and volume from the 2D-projection (e.g. selection error in fluorescent micrograph). For partial and complete fission, the surface area decreases up to 10% and 25%, respectively. Partially this is due to split off tether-sections as shown in Fig. 6c.

## Conclusion

The mechanism described here shows a division pathway that combines a steep temperature-gradient and a parabolic flow profile, that reliably divides lipid vesicles. Without the need for additional, chemically induced processes, vesicles with a first order membrane phase transition are prone to fission by this mechanism. In a thermal convection chamber we find a significant reduction of the size distribution for a wide range of vesicle sizes. Tracing single vesicles in a capillary we monitored vesicle shape transformations resulting in fission. From these observations we deduce the underlying mechanism: domaining due to the experienced shear forces causes a separation of vesicle volume by tether-like surface domains which rupture during the phase transition back to the gel-like phase.

It would be highly interesting to extend existing theoretical models from Canham, Helfrich, Evans, Seifert, Miao and Döbereiner<sup>31–38</sup> to vesicles experiencing force fields in a scenario as shown here including the non-linear behavior due to membrane phase transitions. Developing this idea further should also consider the sensitivity of these phase transitions to interaction with the enclosed material<sup>39</sup> like proteins or RNA. The temperature cycling is one of the two driving forces of this simple proto-cell division mechanism. But the combination of DNA in the proto-cell with these temperature oscillations can even melt double stranded DNA into single strands and make them accessible for replication mechanism as proposed by Mansy and Szostak<sup>40</sup>. In combination with the fission mechanism discussed in this paper a full cell cycle with included information distribution might be provided.

In a context of Origin of Life, vesicles could be a step on the way to proto-cells that enclose, replicate, transport, shield, and distribute information, e.g. in the form of nucleic acids. Without the sophisticated division mechanisms of evolved modern cells, a much simpler and reliable mechanism for proto-cell division is necessary to have a complete cell cycle of formation, information-inclusion, division, and growth for lipid vesicles. Also, both capillary and convection chamber are experimental realizations of hydrothermal microenvironments. They combine non-uniform flow profiles with rapid temperature-changes, a setting which is plausible in the context of the Origin of Life and is known to have the ability to accumulate dissolved molecules from strongly diluted solutions and provide a mechanism for the formation of lipid-vesicles, a structure that is widely seen as a proto-cell candidate.

Prebiotically plausible protocells probably had multiple different membrane molecules. Membrane phase transitions would not have been as sharp as shown here. The environment in our experiments is also very controlled. Loosening those parameters would probably lead to a lower fission efficiency or the emergence of new division mechanisms which might show similar characteristics. However, the same physics as for our protocell model with a structurally simple membrane would apply. Taken together, a robust fission mechanism can arise from simple gradients, fluid flow and non-linear mechanical membrane properties, as present at temperature induced membrane phase transitions.

## Methods

**Vesicle preparation.** In this paper, we use Giant Unilamellar lipid Vesicles (GUV) with a diameter of up to 100  $\mu\text{m}$ . Their size is comparable to eukaryotic cells<sup>41</sup>. The vesicle formation in the laboratory is achieved by the electro-swelling method<sup>42</sup>: 15  $\mu\text{l}$  of 10 mM dipalmitoylphosphatidylcholine (DPPC) dissolved in chloroform is spread on indium tin oxid (ITO) coated glass. The drop is spread out in between the conductive surfaces of the ITO coated glass plates by pressing them together. They are separated by pulling them away from each other in the plane of slide. The organic solvent is evaporated in a vacuum for 6 h. Two glass slides and a teflon spacer form an

electro-swelling chamber. The conductive ITO surface is connected to a frequency generator to induce an oscillating electric field of 1 mV/mm with a frequency of 10 Hz for 6 hours between the two glass slides. Afterwards, the swelling chamber is placed in a water bath with a temperature above the lipids phase transition temperature (for DPPC: 52 °C).

**Tracking vesicles in the capillary setup.** The vesicles were studied using a *Zeiss Axiovert 200* fluorescence microscope and a *Hamamatsu Orca* camera. The motorized stage of the microscope is controlled with a joystick-controller. The stage is moved at the same speed of the vesicle but in the opposite direction. This keeps the vesicle in the center of the field of view. The movie in the Supporting Information is additionally stabilized using the open-source *Blender*-software.

**Convection chamber and capillary setup.** The bottom of the front opening of the capillary (*CM Scientific Ltd.*, 200 µm by 2000 µm made of borosilicate glass) is glued (*Sekundenkleber Gel, UHU*) to an object slide. The copper contacts are fixed to the object slide with hot glue. A tube is fixed to the back of the capillary with a shrink-tube. A pressure difference reservoir is attached to the tube and enables to suck the sample through the capillary. The heating is done with a Peltier element controlled by a TEC control software from *Meerstetter Engineering*. The convection chamber is 3D printed with a visible light-curing resin on a self-made illumination station. The resin part is pressed in between a silicon wafer (bottom, cold side) and a sapphire crystal (top, hot side). The sapphire is optically transparent and allows to monitor the inside of the chamber, e. g. the vesicles. The sapphire is also a very good heat conductor with a heat conductivity up to 25 W/mK. The heating is done by two copper contacts and a resistance heater and controlled by a *LabView* program. The back side is cooled by a *Julabo CORIO CD-300F* liquid cooling bath.

**Simulation of fluid-flow stream lines.** The paths of vesicles inside the convection chamber are simulated with a combination of *COMSOL* and Brownian motion simulation: *COMSOL* simulates the fluid flow inside the chamber due to the temperature gradient. This fluid flow map is overlaid by a Brownian motion simulation done in *C* and *LabVIEW*, as reported earlier<sup>4</sup>.

**Image transformation for size distribution.** In contrast to the capillary setup where a single vesicle is followed with the motor stage and camera of the microscope, in the chamber setup the entire chamber is scanned. Vesicles are imaged without convective flow, before and after thermo-induced convective cycling. A simple threshold filter creates a binary version of the images with white (0) background and black (1) vesicles. The visualization by accumulated integration has the advantage of not being influenced by a bin size selection as it is the case in standard histograms. The normalization allows to compare the size-distribution of two scans of the same sample before and after temperature cycling.

Received: 26 July 2019; Accepted: 25 November 2019;

Published online: 11 December 2019

## References

- Dose, K. Peptides and amino acids in the primordial hydrosphere. *BioSystems* **6**, 224–228 (1975).
- Mojzsis, S. J., Harrison, T. M. & Pidgeon, R. T. Oxygen-isotope evidence from ancient zircons for liquid water at the Earth's surface 4, 300 Myr ago sources and may therefore provide information about the nature. *Nature* **409**, 178–181 (2001).
- Priye, A., Yu, Y., Hassan, Y. A. & Ugaz, V. M. Synchronized chaotic targeting and acceleration of surface chemistry in prebiotic hydrothermal microenvironments. *Proc. Natl. Acad. Sci.* **114**, 1275–1280 (2017).
- Keil, L., Hartmann, M., Lanzmich, S. & Braun, D. Probing of molecular replication and accumulation in shallow heat gradients through numerical simulations. *Phys. Chem. Chem. Phys.* **18**, 20153–20159 (2016).
- Blain, J. C. & Szostak, J. W. Progress Toward Synthetic Cells. *Annu. Rev. Biochem.* **83**, 615–640 (2014).
- Nourian, Z., Scott, A. & Danelon, C. Toward the assembly of a minimal divisome. *Syst. Synth. Biol.* **8**, 237–247 (2014).
- Schrum, J. P., Zhu, T. F. & Szostak, J. W. The Origins of Cellular Life. *Cold Spring Harb. Perspect. Biol.* **2**, 1–15 (2010).
- Budin, I., Bruckner, R. J. & Szostak, J. W. Formation of protocell-like vesicles in a thermal diffusion column. *J. Am. Chem. Soc.* **131**, 9628–9629 (2009).
- Budin, I., Debnath, A. & Szostak, J. W. Concentration-driven growth of model protocell membranes. *J. Am. Chem. Soc.* **134**, 20812–20819 (2012).
- Janiak, J., Small, M. & Graham, G. (Received for publication, December 5, 1978) *Martin*. **254**, 6068–6078 (1979).
- Heimburg, T. *Thermal Biophysics of Membranes*. *Thermal Biophysics of Membranes*, <https://doi.org/10.1002/9783527611591> (2007).
- Leirer, C., Wunderlich, B., Myles, V. M. & Schneider, M. F. Phase transition induced fission in lipid vesicles. *Biophys. Chem.* **143**, 106–109 (2009).
- Zhu, T. F. & Szostak, J. W. Coupled growth and division of model protocell membranes. *J. Am. Chem. Soc.* **131**, 5705–5713 (2009).
- Murtas, G. Internal lipid synthesis and vesicle growth as a step toward self-reproduction of the minimal cell. *Syst. Synth. Biol.* **4**, 85–93 (2010).
- Deshpande, S., Spoelstra, W. K., Van Doorn, M., Kerssemakers, J. & Dekker, C. Mechanical Division of Cell-Sized Liposomes. *ACS Nano* **12**, 2560–2568 (2018).
- Mercier, R., Kawai, Y. & Errington, J. Excess membrane synthesis drives a primitive mode of cell proliferation. *Cell* **152**, 997–1007 (2013).
- Szostak, J. W. *et al.* Synthesizing life. *Nature* **409**, 387–390 (2001).
- Hanczyc, M. M. & Szostak, J. W. Replicating vesicles as models of primitive cell growth and division. *Curr. Opin. Chem. Biol.* **8**, 660–664 (2004).
- Kurihara, K. *et al.* A recursive vesicle-based model protocell with a primitive model cell cycle. *Nat. Commun.* **6** (2015).
- Norris, V. & Raine, D. J. A fission-fusion origin for life. *Orig. Life Evol. Biosph.* **28**, 523–37 (1998).
- Leaver, M., Domínguez-Cuevas, P., Coxhead, J. M., Daniel, R. A. & Errington, J. Life without a wall or division machine in *Bacillus subtilis*. *Nature* **457**, 849–53 (2009).

22. Koonin, E. V. & Mulkidjanian, A. Y. Evolution of Cell Division: From Shear Mechanics to Complex Molecular Machineries. *Cell* **152**, 942–944 (2013).
23. Kwok, R. & Evans, E. Thermoelasticity of large lecithin bilayer vesicles. *Biophys. J.* **35**, 637–652 (1981).
24. Heimburg, T. & Jackson, A. D. The thermodynamics of general anesthesia. *Biophys. J.* **92**, 3159–3165 (2007).
25. Strobl, F. G. *et al.* Intake of silica nanoparticles by giant lipid vesicles: Influence of particle size and thermodynamic membrane state. *Beilstein J. Nanotechnol.* **5**, 2468–2478 (2014).
26. Strobl, F. G., Czubak, D. M., Wixforth, A. & Westerhausen, C. Ion controlled passive nanoparticle uptake in lipid vesicles in theory and experiment. *J. Phys. D: Appl. Phys.* **52**, 294001 (2019).
27. Dommersnes, P. G., Orwar, O., Brochard-Wyart, F. & Joanny, J. F. Marangoni transport in lipid nanotubes. *Europhys. Lett.* **70**, 271–277 (2005).
28. Taupin, C., Dvolaitzky, M. & Sauterey, C. Osmotic pressure-induced pores in phospholipid vesicles. *Biochemistry* **14**, 4771–4775 (1975).
29. Evans, E. & Kwok, R. Mechanical Calorimetry of Large Dimyristoylphosphatidylcholine Vesicles in the Phase Transition Region. *Biochemistry* **21**, 4874–4879 (1982).
30. Miller, S. L. *Major Events in the History of Life*. (Jones and Bartlett Publ., 1992).
31. Canham, P. B. The minimum energy of bending as a possible explanation of the biconcave shape of the human red blood cell. *J. Theor. Biol.* **26** (1970).
32. Deuling, H. J. & Helfrich, W. Red blood cell shapes as explained on the basis of curvature elasticity. *Biophys. J.* **16**, 861–868 (1976).
33. Helfrich, W. Elastic properties of lipid membranes: theory and possible experiments. *Zeitschrift für Naturforsch. C* **28**, 693703 (1973).
34. Miao, L., Fourcade, B., Rao, M., Wortis, M. & Zia, R. K. P. Equilibrium budding and vesiculation in the curvature model of fluid lipid vesicles. *Phys. Rev. A* **43**, 6843–6856 (1991).
35. Miao, L., Seifert, U., Wortis, M. & Dobreiner, H. Budding transitions of fluid-bilayer vesicles: The effect of area-difference elasticity. *Phys. Rev. E* **49** (1994).
36. Berndt, K., Käs, J., Lipowsky, R., Sackmann, E. & Seifert, U. Shape Transformations of Giant Vesicles: Extreme Sensitivity to Bilayer Asymmetry. *Europhys. Lett.* **13**, 659–664 (1990).
37. Döbereiner, H.-G., Evans, E., Kraus, M., Seifert, U. & Wortis, M. Mapping vesicle shapes into the phase diagram: A comparison of experiment and theory. *Phys. Rev. E* **55**, 4458 (1997).
38. Döbereiner, H. G., Käs, J., Noppl, D., Sprenger, I. & Sackmann, E. Budding and fission of vesicles. *Biophys. J.* **65**, 1396–403 (1993).
39. Westerhausen, C. *et al.* Chemical and mechanical impact of silica nanoparticles on the phase transition behavior of phospholipid membranes in theory and experiment. *Biophys. J.* **102**, 1032–1038 (2012).
40. Mansy, S. S. & Szostak, J. W. Reconstructing the emergence of cellular life through the synthesis of model protocells. *Cold Spring Harb. Symp. Quant. Biol.* **74**, 47–54 (2009).
41. Marshall, W. F. *et al.* What determines cell size? *BMC Biol.* **10**, 101 (2012).
42. Angelova, M. I., Soléau, S., Méléard, P., Faucon, F. & Bothorel, P. Preparation of giant vesicles by external AC electric fields. Kinetics and applications. In *Trends in Colloid and Interface Science VI* (eds. Helm, C., Lösche, M. & Möhwald, H.) 127–131 (Steinkopff, 1992), <https://doi.org/10.1007/BFb0116295>.

## Acknowledgements

The authors would like to acknowledge funding by Nanosystems Initiative Munich (NIM), the Center for NanoScience (CeNS), the CRC 235 Emergence of Life Project P07, the Simons Collaboration on the Origins of Life and the Excellence Cluster Origins. P.W.K. and C.W. thank Andrej Kamenac and Alexander Hupfer for technical support and Florian Strobl for fruitful discussions.

## Author contributions

P.W.K. built the test assembly, measured the convection chamber and capillary data, analyzed all data and drafted the manuscript. K.P. measured the DPPC-DPPG vesicles in the capillary setup and analyzed data. M.M. built the convection chamber assembly, measured the convection chamber data and improved the manuscript. C.F.D. helped to develop the theory and draft the manuscript. D.B. helped to conceive the study, participated in its design and coordination and to draft the manuscript. A.W. participated in the design of the study and helped to draft the manuscript. C.W. participated in design and coordination of the study, participated in measurements, analyzed data and helped to develop the theory as well as the manuscript. All authors read and approved the manuscript.

## Competing interests

The authors declare no competing interests.

## Additional information

**Supplementary information** is available for this paper at <https://doi.org/10.1038/s41598-019-55110-0>.

**Correspondence** and requests for materials should be addressed to C.W.

**Reprints and permissions information** is available at [www.nature.com/reprints](http://www.nature.com/reprints).

**Publisher's note** Springer Nature remains neutral with regard to jurisdictional claims in published maps and institutional affiliations.



**Open Access** This article is licensed under a Creative Commons Attribution 4.0 International License, which permits use, sharing, adaptation, distribution and reproduction in any medium or format, as long as you give appropriate credit to the original author(s) and the source, provide a link to the Creative Commons license, and indicate if changes were made. The images or other third party material in this article are included in the article's Creative Commons license, unless indicated otherwise in a credit line to the material. If material is not included in the article's Creative Commons license and your intended use is not permitted by statutory regulation or exceeds the permitted use, you will need to obtain permission directly from the copyright holder. To view a copy of this license, visit <http://creativecommons.org/licenses/by/4.0/>.

© The Author(s) 2019

 **Acid-Catalyzed RNA-Oligomerization from 3',5'-cGMP**Sreekar Wunnava,<sup>[a]</sup> Christina F. Dirscherl,<sup>[a]</sup> Jakub Výravský,<sup>[b, c]</sup> Aleš Kovařík,<sup>[d]</sup>  
Roman Matyášek,<sup>[d]</sup> Jiří Šponer,<sup>[d]</sup> Dieter Braun,<sup>\*,[a]</sup> and Judit E. Šponer<sup>\*,[d]</sup>

**Abstract:** The assembly of ancient informational polymers from nucleotide precursors is the central challenge of life's origin on our planet. Among the possible solutions, dry polymerization of 3',5'-cyclic guanosine monophosphate (3',5'-cGMP) has been proposed as a candidate to create oligonucleotides of 15–20 units in length. However, the

reported sensitivity of the reaction to the presence of cations raised questions of whether this chemistry could be relevant in a geological context. The experiments in this study show that the presence of cations is not restrictive as long as the reaction is conducted in an acidic environment, in contrast to previous reports that suggested optimal conditions at pH 9.

**Introduction**

One of the major obstacles to the establishment of an RNA world is the progression from nucleotide monomers to oligonucleotide sequences. Several possible prebiotic reactions have been proposed by using high-energy phosphates such as carbodiimide derivatives or phosphorimidazolides for non-enzymatic polymerization of ribonucleotides.<sup>[1–8]</sup> However, due to their reactive nature, these intermediates/precursors are prone to hydrolysis and require feeding or in-situ recycling.<sup>[1,9]</sup> Another class of oligonucleotide precursors is cyclic phosphate-containing nucleotides which, due to the cyclization of the phosphate moiety, can act as mildly activated monomers. Both nucleoside 2',3'- and 3',5'-cyclic phosphates have been used as substrates for polymerization. 2',3'-Cyclic nucleotides have been reported to polymerize moderately in both templated and template-free ways to yield short oligonucleotides in an aqueous and dry state, respectively.<sup>[10,11]</sup> On the other hand

3',5'-cyclic nucleotides (with guanine, adenine, and cytosine) have been shown to polymerize in a template-free manner under dry conditions and rely on the stacked arrangement of the monomers.<sup>[12–15]</sup> Especially for 3',5'-cyclic guanosine monophosphate, investigations have shown that aggregation processes associated with the low solubility of the free-acid form could have played a role in the emergence of the first oligonucleotide sequences on the early Earth.<sup>[16]</sup> Polymerization of cGMP-H has been reported to proceed in a dry state<sup>[14–16]</sup> as well as in a close-to-saturated aqueous solution<sup>[14,16–18]</sup> with optimum conditions being 80 °C and pH 9.<sup>[18]</sup> Under these conditions, a base-catalyzed anionic ring-opening polymerization chemistry has been proposed to take place.<sup>[14]</sup> Quantum chemical calculations<sup>[14]</sup> have shown that a stacked supramolecular architecture reminiscent of the one found in the crystal structures<sup>[19,20]</sup> of Na-salt (hereafter, cGMP-Na) and free-acid form (hereafter H-form or cGMP-H, the form in which all acidic groups are fully protonated) of 3',5'-cGMP may provide favorable steric conditions for this reaction. However, while cGMP-H polymerizes on drying, cGMP-Na does not.<sup>[14,18]</sup> The previous report on the base-catalyzed mechanism explained this with the high propensity of Na<sup>+</sup> ions to bind to the anionic phosphate oxygen inactivating the nucleophile and thus silencing the polymerization reaction.<sup>[14]</sup>

**Results and Discussion**

When cGMP-H is polymerized in the presence of NaCl, only a large excess (~50x) of NaCl stops the reaction (see Figure 5c in ref. [14]). We re-evaluated the effect of Na<sup>+</sup> ions on cGMP-H polymerization like the one described in ref. [14]. Solutions of cGMP-H containing 1 μmol of the monomer were dried at 80 °C in the presence of different amounts of NaCl for 20 h in a vacuum evaporator. Figure 1 shows the electrophoretic profile (for qualitative assessment) and the HPLC ESI-TOF MS quantification of oligonucleotides in the prepared samples. Our current results agree with those from ref. [14] and show that only a large excess of NaCl leads to deterioration of the oligomerization process. Nonetheless, lower Na<sup>+</sup> concentrations do not

[a] S. Wunnava, C. F. Dirscherl, Prof. D. Braun  
Department of Physics, NanoSystems Initiative Munich and Center for Nanoscience  
Ludwig-Maximilians-Universität München  
Amalienstrasse 54, 80799 Munich (Germany)  
E-mail: dieter.braun@lmu.de

[b] J. Výravský  
Tescan Brno s.r.o.  
Libušina třída 1, 62300 Brno (Czech Republic)

[c] J. Výravský  
Department of Geological Sciences, Faculty of Science  
Masaryk University  
Kotlářská 2, 61137 Brno (Czech Republic)

[d] Dr. A. Kovařík, Dr. R. Matyášek, Prof. J. Šponer, Dr. J. E. Šponer  
Institute of Biophysics Academy of Sciences of the Czech Republic  
Královopolská 135, 61265 Brno (Czech Republic)  
E-mail: judit@ncbr.muni.cz

 Supporting information for this article is available on the WWW under <https://doi.org/10.1002/chem.202103672>

 © 2021 The Authors. Chemistry - A European Journal published by Wiley-VCH GmbH. This is an open access article under the terms of the Creative Commons Attribution Non-Commercial License, which permits use, distribution and reproduction in any medium, provided the original work is properly cited and is not used for commercial purposes.

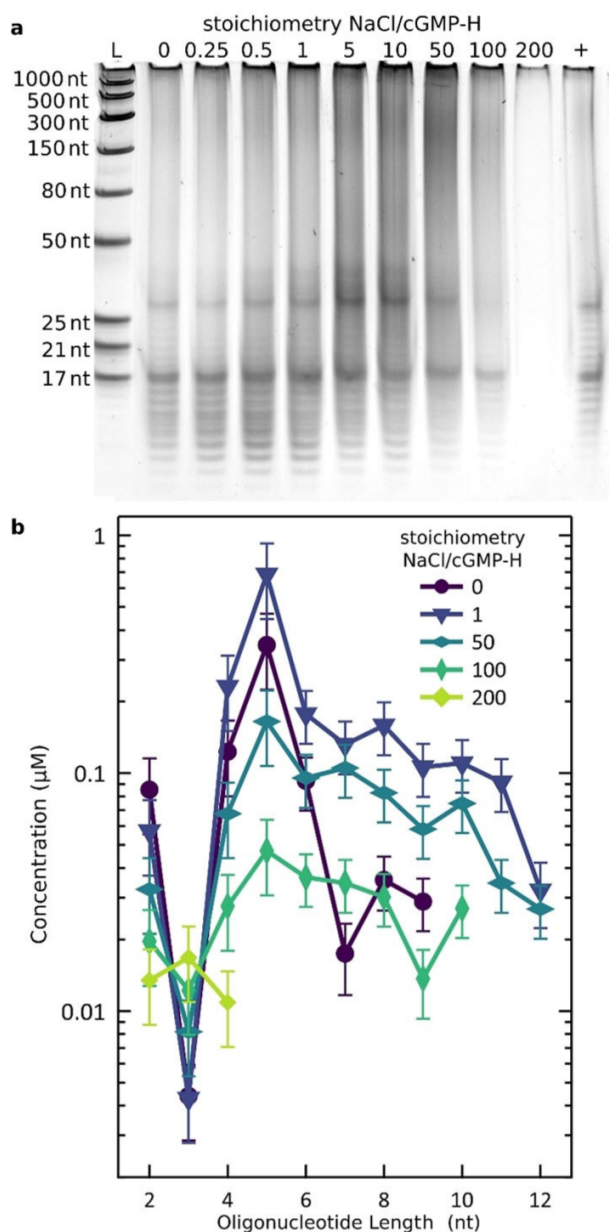


**Figure 1.** Polymerization of cGMP-H in presence of added  $\text{Na}^+$  ions. A solution containing  $1 \mu\text{mol}$  3',5'-cGMP-H (pH 3.1) was mixed with NaCl and dried for 20 h at  $80^\circ\text{C}$  under vacuum and redissolved in  $100 \mu\text{L}$  nuclease-free water. a) The polymerization was analyzed qualitatively by gel electrophoresis and SYBR-Gold staining. Polymerization of cGMP is observed in the presence of 0–100 molar equiv. NaCl but inhibited at 200 molar equiv. Lanes: L denotes mixed-sequence ssRNA ladder with sizes given on the left; 0–200 indicate the added micromoles of NaCl; + denotes positive control [dried 3',5'-cGMP-H (G7504 from Sigma–Aldrich) has preformed oligomers that were ethanol precipitated]. Correspondence of the oligonucleotide sizes in the reference ladder to those of oligoG sequences is presented in Figure S1 in the Supporting Information. b) HPLC ESI-TOF quantification of the selected samples was done after ethanol precipitation. Concentrations are reported for  $100 \mu\text{L}$  injection volume. A UV chromatogram and corresponding mass spectra for tetra- to hexamers isolated from the sample with 0 equiv. NaCl is given in Figure S2 along with the MS spectrum from the void volume of the column showing monomer aggregates.

hinder the polymerization of cGMP-H and hence the silencing effect of  $\text{Na}^+$  ions added in large excess cannot explain the inability of cGMP-Na to polymerize and the issue requires further analysis. Furthermore, a base-catalyzed mechanism<sup>[14]</sup> with an optimum pH of 9<sup>[18]</sup> fails to explain how the low starting pH of cGMP-H in the experiments reported recently by Costanzo et al.<sup>[16]</sup> (pH 3.7, measured at room temperature) could still enable the polymerization. Under these low-pH conditions, the equilibrium favors the free-acid form of the molecule which is electrically neutral. Thus, these monomers are not suited to support an anionic, that is, base-catalyzed polymerization. However, being a transesterification reaction, it is very likely that a complementary acid-catalyzed polymerization mechanism might also exist.<sup>[21,22]</sup>

This motivated us to revisit the role of pH on the polymerization reaction of 3',5'-cGMP-H. We hypothesized that the inability of cGMP-Na to polymerize upon drying is due to the different starting pH of the solution. While 1 mM solution of 3',5'-cGMP-H has an acidic pH (ca. 3.1) and polymerizes on drying, a 1 mM cGMP-Na solution has a neutral pH (ca. 6.7–7) and does not polymerize. We confirmed this hypothesis by testing the polymerization of cGMP at different starting pH by the addition of NaOH and HCl to cGMP-H and cGMP-Na, respectively.

Figure 2a shows the dependence of polymerization on the amount of NaOH added to 1 mM cGMP-H solution before drying at  $80^\circ\text{C}$  under vacuum for 20 h. We have found that already equimolar amounts of NaOH are sufficient to extinguish the polymerization reaction (Figure 2a). With the addition of 0.5 or fewer equivalents of NaOH, the resulting solution acts as a buffer with a stable pH of around 3, and, as a result, the polymerization proceeds. Similarly, starting from cGMP-Na, the solution was acidified with different molar equivalents of HCl.

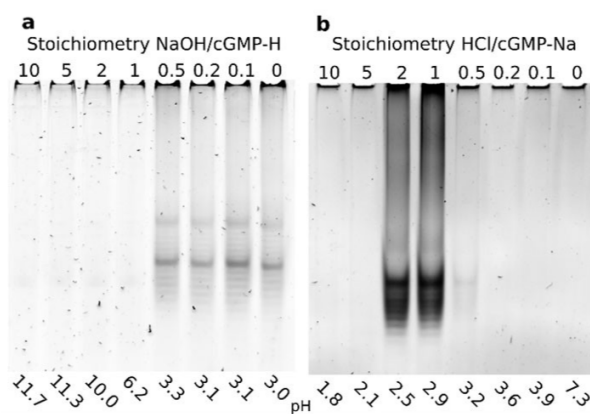


**Figure 2.** Polymerization of 3',5'-cGMP depends on the pH of the starting solution. a) 1 mM cGMP-H solution was mixed with NaOH in 0.1–10 molar equiv. The resulting solutions were dried at  $80^\circ\text{C}$  for 20 h under vacuum. Polymerization of cGMP is inhibited in samples with 1 or more molar equiv. of NaOH (i.e., at  $\text{pH} \geq 6.2$ ). b) 1 mM cGMP-Na solution was dried ( $80^\circ\text{C}$  under vacuum, 20 h) after the addition of 0.1–10 molar equiv. of HCl. Polymerization is visible only in samples with 0.5–2.0 molar equiv. of HCl ( $\text{pH} \sim 3$ ). Both gels were stained with SYBR-Gold. Lanes: 0–10 denote equivalents of HCl or NaOH added to the solution; the pH of the resulting solution is given under the lane.

Upon drying at 80 °C under vacuum for 20 h, only the solutions with 0.5–2 equivalents of HCl showed polymerization (Figure 2b). Further acidification below pH 2.5 (starting from 5 molar equiv. of added HCl), however, leads to a loss in oligomers presumably due to depurination reactions. Similar depurination reactions have also been observed for the lipid-assisted polymerization of 5'- nucleotides under dehydrating acidic conditions.<sup>[23]</sup>

The addition of weaker bases like NH<sub>4</sub>OH, triethylamine or tris(hydroxymethyl aminomethane) [hereafter, Tris] has the same inhibitory effect on the polymerization of cGMP-H as the addition of NaOH (Figure S3), thus suggesting that the pH of the cGMP solution before drying must be acidic to allow polymerization. However, the previous report<sup>[18]</sup> has shown that if Tris-HCl buffer is used instead, the polymerization proceeds even though the starting pH 8.4 was alkaline. The reported experiment<sup>[18]</sup> involved polymerization in aqueous conditions starting from a close-to-saturated solution of cGMP-H in a relatively small volume (15 µL).

On repeating the experiment as described in ref. [18], oligomer formation was indeed detected (Figure 3a). We propose the following arguments for this anomalous observation. First, due to such a small starting volume and high concentration of monomers, the reaction most likely proceeded in a semi-dry state as the liquid evaporated. Second, the pH of Tris-HCl buffer falls rapidly with increasing temperature.<sup>[24]</sup> Thus, heating from 20 to 80 °C might easily revert a weakly basic buffer to a weakly acidic one.

Finally, in the experiment in ref. [18], the concentration of cGMP-H (a weak acid) was 10 mM in 20 mM Tris-HCl buffer.

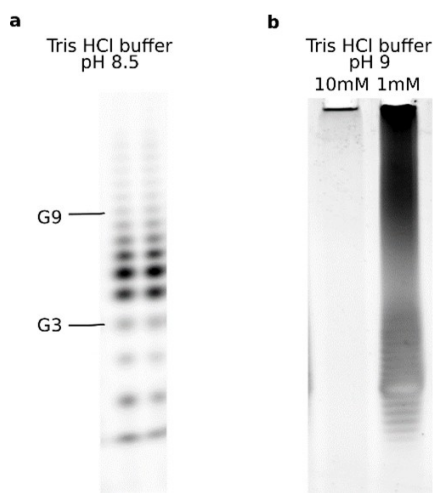


**Figure 3.** Polymerization of 3',5'-cGMP in a Tris-HCl buffer. a) Two parallel samples were prepared according to ref. [18]: 150 µL 1 mM cGMP-H was dried and dissolved in 15 µL of 20 mM Tris-HCl pH 8.5 buffer. The samples were polymerized for 5 h at 85 °C in closed tubes. The polymerization products were radioactively labeled with  $\gamma$ -<sup>32</sup>P-ATP and separated by electrophoresis on a denaturing gel. G3 and G9 denote band positions of G<sub>3</sub> and G<sub>9</sub> oligonucleotide standards. b) A 1 mM solution of cGMP-H was mixed with Tris-HCl buffer to give final buffer concentrations of 10 and 1 mM at pH 9 before being dried at 80 °C for 20 h under vacuum. Polymers were observed only at 1 mM buffer concentration. The gel was stained with SYBR Gold.

Under such concentration ratios, the buffering capacity of Tris-HCl can be questioned. We tested this by drying a 1 mM cGMP-H solution in Tris-HCl buffer pH 9 at 1 and 10 mM buffer concentration at 80 °C under vacuum for 20 h. Polymerization was only observed (Figure 3b) for the solution with 1 mM buffer concentration. In light of the above arguments, it is likely that under the experimental conditions of ref. [18], the polymerization occurred from a weakly acidic solution under drying conditions. Coupled with a high concentration of cGMP-H in the solution and evaporation of the solvent, the monomers become concentrated in an acidic environment, enhancing the polymerization.

Earlier quantum chemical calculations by some of us<sup>[14]</sup> suggested that the crystal structure of cGMP (Na- as well as H-form)<sup>[19,20]</sup> provides favorable steric conditions for the transphosphorylation reactions leading to oligonucleotide formation. Using the theoretically derived optimum nucleotide arrangement from ref. [14], we found the potential acid-catalyzed polymerization mechanism described in Figure S4. It is thus reasonable to assume that the ability of the monomers to crystallize under given conditions might dramatically influence the experimentally observed polymerization rates. The very first step of this process is nucleation, a process in which intermolecular contacts are established between the solute molecules at the expense of disrupting interactions with the surrounding solvent environment. This process is strongly dependent on the protonation state of the nucleotide monomers and thus the pH of the chemical environment.

While cGMP-Na has a solubility of 136 mM (supplier specified value 50 mg/mL), the H-form material has a much lower solubility (predicted value 10.9 mM<sup>[25]</sup>). Unlike the sodium salt, which dissociates completely in water giving the nucleotide a negative charge, the free acid form, being a weak acid, only partially dissociates. Thus, in an aqueous solution of the free-acid form material, a large part of solute molecules is neutral (Figure 4a) and more prone to aggregation due to hydrophobic stacking interactions.

Similar behavior has been reported for aromatic carboxylic acids where it has been revealed that stacking might be a more important driving force for nucleation than H-bonding and electrostatic interactions.<sup>[26]</sup> In contrast to their free acid form, the solubility of the sodium salts of aromatic carboxylic acids is much higher and upon quick evaporation of the solvent, these materials often form amorphous phases rather than crystalline materials.<sup>[27]</sup>

This is the case for cGMP-Na as well which forms an amorphous material upon drying. In contrast, the H-form material forms well-developed crystals under the same drying conditions (Figure 4b). The transition between the H- and Na-form materials is smooth: precipitates are observed upon acidification of the Na-form material (Figure 4c). This indicates that charge neutralization of the nucleotide monomers helps the stacking-assisted nucleation process and hence crystallization. Monomer assembly in well-developed crystals of 3',5'-cGMP then provides optimum steric conditions for the polymerization reaction.

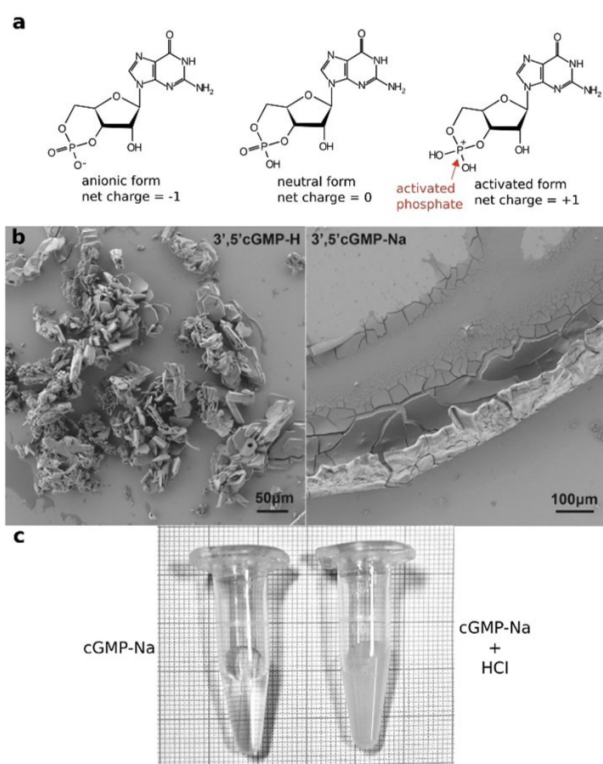


**Figure 4.** a) Protonation states of 3',5'-cGMP. The phosphate group can have either a  $-1$  charge, a  $+1$  charge, or no charge. b) Electron microscope images of H- and Na-form 3',5'-cGMP dried under the same conditions. Samples were deposited on glass microscope slides by dropwise evaporation of 1 mM aqueous solutions at 80 °C. While the H-form material is dominated by large (several tens of  $\mu\text{m}$  long) crystals, 3',5'-cGMP-Na forms an amorphous mass. c) 3',5'-cGMP-Na is more soluble than the H form. 3',5'-cGMP-Na is soluble at a concentration of 50 mM (left). Upon addition of equivalent moles of HCl, the solubility of 3',5'-cGMP is significantly reduced, and the solution becomes turbid (right). The low solubility of the H-form material is due to its ability to form stacking-assisted aggregate structures similar to aromatic carboxylic acids.<sup>[26]</sup>

## Conclusion

To summarize, we have demonstrated that the nonenzymatic oligomerization of 3',5'-cGMP in a dry state depends critically on the pH of the solution it dries in. We show that acidic conditions aid polymerization in two ways. Primarily, they enable the formation of stacked supramolecular architectures made of neutral free-acid-form monomers. This process could serve as an efficient selection force for the accumulation of 3',5'-cGMP-H from a complex prebiotic broth. Furthermore, under acidic conditions, the monomer can be activated by binding an additional proton to the P=O group of the neutral cyclic phosphate, which, when coupled to the crystalline structure, enables polymerization. Overall, our study suggests that protonation in a drying acidic environment could have served as a simple strategy for activation on the primordial Earth and might provide the long-sought clue for the question of how the first oligonucleotide sequences formed from cyclic nucleotide precursors.

## Experimental Section

**Polymerization of 3',5'-cGMP:** Monomer solutions were dried such that the total amount of dried cGMP (free-acid, Biolog G001H and Na-salt, Sigma G6129) was 1  $\mu\text{mol}$ . To test the effect of various ions and pH, test ions were added to the monomer solution in required stoichiometry prior to drying. The solutions were then dried in a centrifugal vacuum evaporator (Genevac EZ-2 Elite) at 80 °C for 20 h. The drying time was found to be ca. 2 h for 1 mL solution, thus the 20 h of vacuum drying includes ca. 2 h of drying followed by ca. 18 h of incubation in the dry state. The dry products were then dissolved in 100  $\mu\text{L}$  of nuclease-free water such that the final cGMP concentration would be 10 mM. All reactions were done in unbuffered solutions unless specific buffer interactions were being studied. This was done to limit the interactions of buffers and other ions apart from the test ion with cGMP. The resulting solutions were solubilized by intermittent heating at 60 °C and vigorous vortexing and immediately used (without precipitation) for electrophoresis on a polyacrylamide gel.

**Gel electrophoresis:** Denaturing polyacrylamide gels were made at  $\sim 25\%$  acrylamide concentration from a 40% acrylamide/bis-acrylamide (29:1) stock solution (Carl Roth A515.1) and contained 50 wt% urea and 1x TBE (from 10x, Carl Roth 3050.1). Gel staining was done with 1x SYBR Gold (from 10000x, Invitrogen, S11494) in 1x TBE (from 10x, Carl Roth 3061.1) for 5 min and rinsed with 1x TBE.

The stained gel was visualized in BIORAD ChemiDoc Gel imaging system.

**Ethanol precipitation:** To the dissolved samples, 20  $\mu\text{g}$  of glycogen (Sigma G8751) and 500 mM ammonium acetate (Sigma A7262) was added. To this, 3 volumes of cold 100% ethanol (Carl Roth 9065.4) were added and the samples were incubated at 4 °C for 18 h. The samples were centrifuged at 15000 rpm for 30 min at 4 °C and the pellet was washed with cold 70% ethanol and centrifuged at 15000 rpm for 30 min at 4 °C. The resulting pellets were air-dried and dissolved in the required volume of nuclease-free water for downstream analysis.

**HPLC-ESI TOF analysis:** Agilent 1260 Infinity II LC System coupled with a 6230B Time of Flight was used for HPLC-MS analysis. Agilent AdvanceBio Oligo C18 column (4.6x150 mm, 2.7  $\mu\text{m}$ ) was used as the stationary phase and the elution was done under a gradient of methanol (Merk 1060352500) with 200 mM hexafluoroisopropanol (Carl Roth 2473.3) and 8 mM triethylamine (Carl Roth X875.1) as ion-pairing agents. Time-of-flight mass spectrometry was done in negative ion mode.

**Scanning electron microscopic (SEM) analysis:** The SEM imaging of the dried 3',5'-cGMP, H- and Na- form samples was performed on the TESCAN CLARA SEM in high-vacuum mode with 2kV acceleration voltage, 10 pA beam current and 5 mm working distance.

## Acknowledgements

The authors would like to acknowledge funding by the Advanced Grant (EvoTrap #787356) PE3, ERC-2017-ADG from the European Research Council and the Deutsche Forschungsgemeinschaft (DFG, German Research Foundation) through the CRC 235 Emergence of Life (Project ID 364653263). Open Access funding enabled and organized by Projekt DEAL.

## Conflict of Interest

The authors declare no conflict of interest.

## Data Availability Statement

The data that support the findings of this study are available from the corresponding author upon reasonable request.

**Keywords:** cGMP · nonenzymatic polymerization · nucleotides · prebiotic chemistry

- [1] M. Jauker, H. Griesser, C. Richert, *Angew. Chem. Int. Ed.* **2015**, *54*, 14559–14563; *Angew. Chem.* **2015**, *127*, 14767–14771.
- [2] B. J. Weimann, R. Lohrmann, L. E. Orgel, H. Schneider-Bernloehr, J. E. Sulston, *Science* **1968**, *161*, 387–387.
- [3] M. Dorr, P. Löffler, P.-A. Monnard, *Curr. Org. Synth.* **2013**, *9*, 735–763.
- [4] L. E. Orgel, R. Lohrmann, *Acc. Chem. Res.* **1974**, *7*, 368–377.
- [5] P. Wright, D. Lloyd, W. Rapp, A. Andrus, *Tetrahedron Lett.* **1993**, *34*, 3373–3376.
- [6] R. Lohrmann, P. K. Bridson, L. E. Orgel, *Science* **1980**, *208*, 1464–1465.
- [7] T. Walton, W. Zhang, L. Li, C. P. Tam, J. W. Szostak, *Angew. Chem. Int. Ed.* **2019**, *58*, 10812–10819; *Angew. Chem.* **2019**, *131*, 10926–10933.
- [8] A. Mariani, D. A. Russell, T. Javelle, J. D. Sutherland, *J. Am. Chem. Soc.* **2018**, *140*, 8657–8661.
- [9] J. D. Ibanez, A. P. Kimball, J. Oró, *Science* **1971**, *173*, 444–446.
- [10] M. S. Verlander, R. Lohrmann, L. E. Orgel, *J. Mol. Evol.* **1973**, *2*, 303–316.
- [11] M. Renz, R. Lohrmann, L. E. Orgel, *Biochim. Biophys. Acta Nucleic Acids Protein Synth.* **1971**, *240*, 463–471.
- [12] G. Costanzo, S. Pino, A. M. Timperio, J. E. Šponer, J. Šponer, O. Nováková, O. Šedo, Z. Zdráhal, E. Di Mauro, *PLoS One* **2016**, *11*, e0165723.
- [13] G. Costanzo, A. Giorgi, A. Scipioni, A. M. Timperio, C. Mancone, M. Tripodi, M. Kapralov, E. Krasavin, H. Kruse, J. Šponer, J. E. Šponer, V. Ranc, M. Otyepka, S. Pino, E. Di Mauro, *ChemBioChem* **2017**, *18*, 1535–1543.
- [14] J. E. Šponer, J. Šponer, A. Giorgi, E. Di Mauro, S. Pino, G. Costanzo, *J. Phys. Chem. B* **2015**, *119*, 2979–2989.
- [15] M. Morasch, C. B. Mast, J. K. Langer, P. Schilcher, D. Braun, *ChemBioChem* **2014**, *15*, 879–883.
- [16] G. Costanzo, J. E. Šponer, J. Šponer, A. Cirigliano, P. Benedetti, V. Giliberti, R. Polito, E. Di Mauro, *ChemSystemsChem* **2021**, *3*, e202000011.
- [17] G. Costanzo, S. Pino, F. Ciciello, E. Di Mauro, *J. Biol. Chem.* **2009**, *284*, 33206–33216.
- [18] G. Costanzo, R. Saladino, G. Botta, A. Giorgi, A. Scipioni, S. Pino, E. Di Mauro, *ChemBioChem* **2012**, *13*, 999–1008.
- [19] A. K. Chwang, M. Sundaralingam, *Acta Crystallogr. Sect. B Struct. Crystallogr. Cryst. Chem.* **1974**, *30*, 1233–1240.
- [20] K. A. Šlepokura, *Acta Crystallogr. Sect. C Struct. Chem.* **2016**, *72*, 465–479.
- [21] J. Otera, *Chem. Rev.* **1993**, *93*, 1449–1470.
- [22] F. A. Carey, R. J. Sundberg, *Advanced Organic Chemistry*, Springer, Boston, **2007**.
- [23] C. V. Mungi, N. V. Bapat, Y. Hongo, S. Rajamani, *Life* **2019**, *9*, 1–11.
- [24] K. Reineke, A. Mathys, D. Knorr, *Int. J. Food Prop.* **2011**, *14*, 870–881.
- [25] I. V. Tetko, J. Gasteiger, R. Todeschini, A. Mauri, D. Livingstone, P. Ertl, V. A. Palyulin, E. V. Radchenko, N. S. Zefirov, A. S. Makarenko, V. Y. Tanchuk, V. V. Prokopenko, *J. Comput.-Aided Mol. Des.* **2005**, *19*, 453–463.
- [26] A. J. Cruz-Cabeza, R. J. Davey, S. S. Sachithanathan, R. Smith, S. K. Tang, T. Vetter, Y. Xiao, *Chem. Commun.* **2017**, *53*, 7905–7908.
- [27] C. Butterhof, T. Martin, W. Milius, J. Breu, *Z. Anorg. Allg. Chem.* **2013**, *639*, 2816–2821.

Manuscript received: October 12, 2021

Accepted manuscript online: November 2, 2021

Version of record online: November 23, 2021

# RNA Oligomerisation without Added Catalyst from 2',3'-Cyclic Nucleotides by Drying at Air-Water Interfaces\*\*

Avinash Vicholous Dass<sup>+, [a]</sup>, Sreekar Wunnava<sup>+, [a]</sup>, Juliette Langlais<sup>+, [a]</sup>, Beatriz von der Esch,<sup>[b]</sup> Maik Krusche,<sup>[a]</sup> Lennard Ufer,<sup>[a]</sup> Nico Chrisam,<sup>[a]</sup> Romeo C. A. Dubini,<sup>[d]</sup> Florian Gartner,<sup>[f]</sup> Severin Angerpointner,<sup>[f]</sup> Christina F. Dirscherl,<sup>[a]</sup> Petra Rovó,<sup>[d, e]</sup> Christof B. Mast,<sup>[a]</sup> Judit E. Šponer,<sup>[g]</sup> Christian Ochsenfeld,<sup>[b, c]</sup> Erwin Frey,<sup>[f]</sup> and Dieter Braun<sup>\*[a]</sup>

For the emergence of life, the abiotic synthesis of RNA from its monomers is a central step. We found that in alkaline, drying conditions in bulk and at heated air-water interfaces, 2',3'-cyclic nucleotides oligomerised without additional catalyst, forming up to 10-mers within a day. The oligomerisation proceeded at a pH range of 7–12, at temperatures between 40–80 °C and was marginally enhanced by K<sup>+</sup> ions. Among the canonical ribonucleotides, cGMP oligomerised most efficiently. Quantification was performed using HPLC coupled to ESI-TOF by fitting

the isotope distribution to the mass spectra. Our study suggests a oligomerisation mechanism where cGMP aids the incorporation of the relatively unreactive nucleotides C, A and U. The 2',3'-cyclic ribonucleotides are byproducts of prebiotic phosphorylation, nucleotide syntheses and RNA hydrolysis, indicating direct recycling pathways. The simple reaction condition offers a plausible entry point for RNA to the evolution of life on early Earth.

## Introduction

The central and multifunctional role of RNA within biology points towards RNA as a chief informational biopolymer for the onset of molecular evolution.<sup>[1]</sup> Polymerisation involving more than a single type of canonical nucleotide, generating a varied pool of RNA strands, has not been achieved under aqueous conditions.<sup>[2–6]</sup> Chemical activation strategies are deployed to trigger RNA polymerisation<sup>[3,7,8]</sup> and template-directed primer extension of sequences.<sup>[9,10]</sup> In the earliest self-replicating systems, the formation of complementary strands for replication and transfer of genetic information by non-enzymatic processes is believed to be important and homopolymers are not considered very useful as genes.<sup>[11]</sup> Short RNA strands, especially from dimers<sup>[11]</sup> to tetramers<sup>[12,13]</sup> have been shown to enhance the copying of mixed-sequence templates in comparison to

monomers. Thus, it is necessary to have a oligomerisation mechanism that is able to generate short mixed-sequences that later function as primers and templates for copying of longer sequences.

We base this study on 2',3'-cyclic mononucleotides (cNMP) which (a) possess an intrinsically activated phosphate; (b) are products of several prebiotic phosphorylation and nucleotide syntheses;<sup>[14–18]</sup> and (c) are products of neutral to alkaline chemical and enzymatic hydrolyses of RNA.<sup>[19–23]</sup> In comparison, the dry oligomerisation of 3',5'-cGMP<sup>[24–26]</sup> did not foster the oligomerisation of the other ribonucleotides.<sup>[26]</sup> Orgel and coworkers, reported conditions for 2',3'-cAMP oligomerisation by drying for 40 days with a 5-fold excess of ethane-1,2-diamine and yields up to 0.67 % of 14-mers.<sup>[4,6]</sup> Other catalysts such as imidazole or urea required temperatures up to 85 °C and offered lower yields.<sup>[4,6]</sup>

[a] Dr. A. V. Dass,<sup>+</sup> S. Wunnava,<sup>+</sup> J. Langlais,<sup>+</sup> M. Krusche, L. Ufer, N. Chrisam, C. F. Dirscherl, Dr. C. B. Mast, Prof. Dr. D. Braun  
Faculty of Physics, Systems Biophysics  
Ludwig-Maximilians-Universität München  
Amalienstraße 54, 80799, Munich, Germany  
E-mail: dieter.braun@lmu.de

[b] B. von der Esch, Prof. Dr. C. Ochsenfeld  
Chair of Theoretical Chemistry, Department of Chemistry,  
Ludwig-Maximilians-Universität München  
Butentandtstraße 5–13, 81377, Munich, Germany

[c] Prof. Dr. C. Ochsenfeld  
Max Planck Institute for Solid State Research  
Heisenbergstr. 1, 70569 Stuttgart, Germany

[d] R. C. A. Dubini, Dr. P. Rovó  
Faculty of Chemistry and Pharmacy,  
Ludwig-Maximilians-Universität München  
Butentandtstraße 5–13, 81377, Munich, Germany

[e] Dr. P. Rovó  
Institute of Science and Technology Austria  
c/o NMR Facility, Am Campus 1, 3400 Klosterneuburg, Austria

[f] Dr. F. Gartner, S. Angerpointner, Prof. Dr. E. Frey  
Faculty of Physics, Statistical and biological physics,  
Ludwig-Maximilians-Universität München,  
Theresienstraße. 37, D-80333, Munich, Germany

[g] Dr. J. E. Šponer  
Institute of Biophysics Academy of Sciences of the Czech Republic  
Královopolská 135, 61265 Brno, Czech Republic

[\*] These authors contributed equally to this work.

[\*\*] A previous version of this manuscript has been deposited on a preprint server (<http://doi.org/10.26434/chemrxiv-2022-zwh2-t-v2>).

 Supporting information for this article is available on the WWW under <https://doi.org/10.1002/syst.202200026>

 © 2022 The Authors. ChemSystemsChem published by Wiley-VCH GmbH. This is an open access article under the terms of the Creative Commons Attribution Non-Commercial NoDerivs License, which permits use and distribution in any medium, provided the original work is properly cited, the use is non-commercial and no modifications or adaptations are made.

We found that 2',3'-cGMP oligomerised spontaneously under alkaline (pH 7–12) drying conditions (40–80 °C), within a day. The other canonical cNMP were relatively inert under similar conditions. Our observations of cAMP and cUMP forming up to trimers are consistent with literature.<sup>[27,28]</sup> The oligomerisation is demonstrated in the presence of bulk water at the air-water interface, within a microfluidic thermal chamber. The chamber mimics conditions of a heated, water filled volcanic rock pore that includes a gas bubble.

In an oligomerisation mixture of cNMP, we observed oligomers rich in G nucleotides, but with C, A and U incorporated at lower concentrations. Computational and modelling results suggest that the oligomers of cGMP form a self-assembled scaffold in the dry state, which could incorporate the nucleotides C, A and U to form short mixed-sequence oligomers.

## Results

### Polymerisation of cGMP

An aqueous solution of the sodium salt of 2',3'-cGMP (20 mM) was dried for 18 hours at 40 °C in the presence of 40 mM KCl. Since the monomers are monosodium salts, there was an equal concentration of Na<sup>+</sup> ions when in solution (20 mM). All the reported concentrations throughout the article are calculated for a volume of 100 μL. The total concentration of each n-mer (oligomer) is a sum of oligomers containing the linear-phosphate (-P) and the cyclic-phosphate (-cP) on the n-mer terminus. Both endings are well discriminated by HPLC as the n-mer-cP is eluted before a n-mer-P of the same length (S2d). Typically, about 90% of the n-mers consisted of -P endings (S5d). Due to propensity of purines to form non-covalent aggregates in mass spectrometry detection,<sup>[29]</sup> a combination of HPLC and ESI-TOF techniques were used for detection of oligonucleotides. The non-covalent stacked n-mers (eg. two 4-mers) are discriminated from covalent n-mers (eg. an 8-mer) due to the higher mass of the stacked n-mers by one H<sub>2</sub>O in the MS and the corresponding HPLC retention times of n-mers under denaturing HPLC conditions.<sup>[30–32]</sup>

The denaturing conditions of the HPLC column at 60 °C efficiently resolved synthetic oligoG n-mers without signs of aggregation, as shown in Figure 1c. It must be noted that an n-mer-cP and a cyclised n-mer of the same length would have the same mass, but are unlikely not to be discriminated by the HPLC retention times. The presence of n-mer-cP is established from the <sup>31</sup>P NMR peak at ~20 ppm in Figure 1d. Oligomers from 2- to 15-mers (S8a) were detected by HPLC-MS for cGMP oligomerisation. For quantification, only 2- to 10-mers were considered throughout the study.

The error bars can be estimated based on plots of cGMP oligomerisation (5 replicates) in S8a, with a mean standard deviation of 2.95 μM between independent runs of the experiment. The error bars are not indicated in the figures as they would appear insignificant on the log scale. For quantification, the HPLC retention times of the oligomer standards of G were

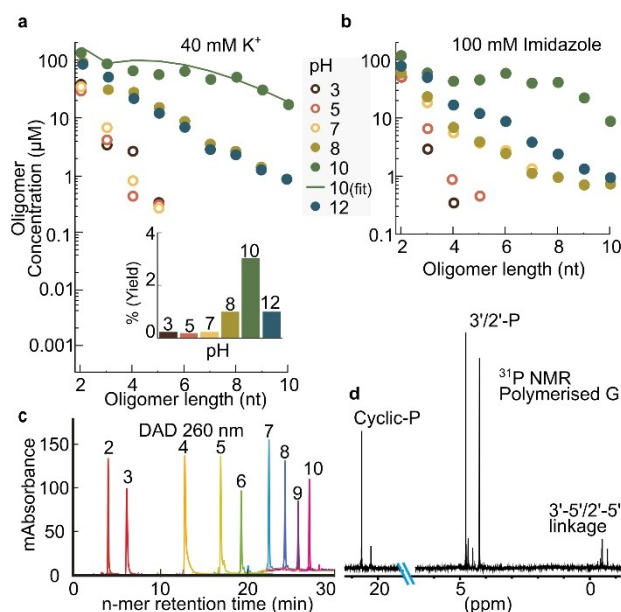


**Figure 1.** Oligomerisation of Guanosine-2',3'-cyclic monophosphate (cGMP-Na). A 20 mM cGMP-Na solution was heat-dried with 40 mM K<sup>+</sup> at 40 °C for 18 hours, under ambient pressure in 100 μL volume. (a) Polymerisation was screened over a range of pH 3–12. The reported concentrations were the sum of terminal cyclic (-cP) and linear phosphate (-P) containing oligomers. Oligomers without terminal phosphates were not detected. Polymerisation was optimal at pH 10 with total oligomer yields of ~3.5% (inset). The solid line shows results of the polymerisation model based on stacked assembly (S19). (b) pH screen with 100 mM imidazole under similar conditions. No significant increase in oligomerisation was found by adding imidazole. (c) Diode array detector (DAD) absorbance at 260 nm for 50 μM oligoG standards (-P endings) and 100 μM KCl used for confirming HPLC separation and the determination of retention time for quantification with ion counts. (d) <sup>31</sup>P proton-decoupled NMR spectrum (10% D<sub>2</sub>O, pH 10), of oligomerised G sample: the signals corresponding to phosphodiester linkages for both 3'-5' and 2'-5' are between -0.8 and -1.1 ppm.

first optimised on an RP C-18 HPLC column coupled to ESI-TOF. Figure 1c shows the HPLC chromatogram of 2- to 10-mers for oligoG standards (with 1 eqv. of KCl) with their respective retention times. We found efficient separation and no evidence for the formation of aggregates. The ion counts of the n-mer with their HPLC retention times are shown in S2b. By comparing the ion counts, we confirmed the high efficiency of the post-polymerisation ethanol precipitation protocol and its negligible influence (S3). However, the precipitation was used to remove excess monomers which would otherwise saturate the HPLC column, yielding a robust method for the quantification of the complex oligonucleotide mixtures (S2c).

The calculated isotope probabilities of the n-mers in the various charge states were fitted to the raw mass spectra using a self-written LabView program. This allowed us to identify salt adducts formed in the mass spectrometer and to fit overlapping isotope patterns. The retention times of the oligoG standards were used to obtain time-brackets to sum the mass spectra. Further details on the calibration used for the quantification within the program and the functional modes of the program are elaborated in S1–S6. Based on preliminary enzymatic digestion experiments, we estimated that the formed G

oligomers were linked by 2'-5' and 3'-5' phosphodiester linkages in about 1:1 ratio (S21–S23). The linkage type in the oligomerisation was also confirmed by  $^{31}\text{P}$  NMR (Figure 1d) and the peaks were assigned based on the literature values.<sup>[33,34]</sup>

Figures 1a and 1b compare the effect of pH on the lengths and concentrations of the n-mers formed by drying with  $\text{K}^+$  ( $\text{Cl}^-$ ) and imidazole respectively. We determined the optimal reaction temperature to be  $40^\circ\text{C}$  (S5, S8b). Imidazole and its derivatives are used in the literature as nucleotide activation agents for templated primer extension reactions,<sup>[9]</sup> as a buffering agent and a catalyst for oligomerisation.<sup>[4]</sup> The addition of imidazole did not enhance the length and concentration of n-mers in comparison to oligomerisation with  $\text{K}^+$ .

### Polymerisation from cNMP

We also tested the polymerisation tendencies of cAMP, cUMP and cCMP under the same heat-drying conditions and found that these monomers did not polymerise to the same lengths and concentrations as cGMP. Figure 2a shows that the polymerisation trend decreases in the order  $\text{cGMP} > \text{cUMP} > \text{cAMP} > \text{cCMP}$ . The dominance of G-polymerisation prompted us to investigate the copolymerisation of these moderately reactive mononucleotides under the influence of the well oligomerising cGMP. We found that a mixture of two or four different monomers was capable of generating mixed sequence oligomers, where the majority of the mixed oligomers were rich in G. We probed if the oligomerisation of a G and C mixture could reach levels where hybridisation between strands could be possible. Thus, we oligomerised a binary mixture of cGMP and cCMP (20 mM each), under heat-drying conditions ( $40^\circ\text{C}$ ) in the presence of 40 mM KCl. Comparing quantities of  $\text{C}_2$  in Figure 2a and 2b, the concentration of  $\text{C}_2$  is enhanced 2 fold and  $\text{C}_3$  became detectable; besides the fact that mixed GC oligomers are formed (Figure 2b). The detailed sequence composition for GC mixed polymerisation is seen in Figure 2e, showing that the  $\text{G}_2$  to  $\text{G}_{10}$  contribute to the bulk of the oligomers formed in the polymerisation mixture. Up to two C's were incorporated into oligomers  $\leq 4$ -mers, one C is incorporated into 5-mers and none were detectable beyond them. A similar analysis of GA and GU binary mixtures is available in S9a, b.

GC mixed polymerisation was favoured at temperatures ranging from  $40^\circ\text{C}$  to  $80^\circ\text{C}$  (Figure 2c), similar to cGMP (S5b, S8b). It must be noted that in reactions at  $30^\circ\text{C}$  for 18 hours, the drying was incomplete within the polypropylene tubes used for the experiment and the reaction kinetics in the dry state was reduced. Higher temperatures on the other hand possibly contributed to the degradation of the monomers (S4c) and the formed oligomers as seen in the trace comparisons under 80, 60 and  $40^\circ\text{C}$  in Figure 2c.

Specific cations also influenced cNMP oligomerisation. We found that  $\text{K}^+$  ions yielded higher concentrations and lengths of the oligomers in comparison to  $\text{Na}^+$  ions at the same concentrations. The presence of  $\text{Mg}^{2+}$  ions in the reaction mixture inhibited polymerisation (Figure 2d). The dependence

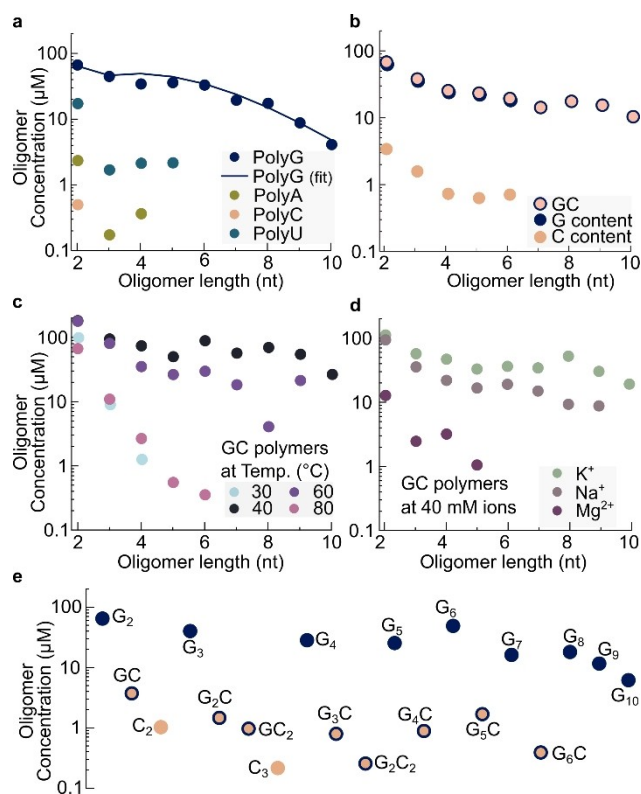


**Figure 2.** Oligomerisation of mixed Nucleotide 2',3'-cyclic monophosphate (cNMP). (a) Homooligomers of cGMP-Na, cAMP-Na, cCMP-Na, cUMP-Na were individually produced from a 20 mM solution at  $40^\circ\text{C}$  for 18 hours. Oligomers of G were formed in far higher concentrations than polyC, A and U. The solid line shows results of the polymerisation model based on stacked assembly (S18). The approximately 3x lower yield for oligoG compared to Figure 1a is attributed to the lack of  $\text{K}^+$  ions. (b) Oligomerisation of cGMP and cCMP at  $40^\circ\text{C}$  with 40 mM  $\text{K}^+$ . The base C is incorporated into the sequences in the presence of cGMP while only dimers were detected without it. (c) Temperature screening over a range of  $30\text{--}80^\circ\text{C}$  for GC oligomerisation. Reduced concentration of n-mers  $> 3$  is observed for  $80^\circ\text{C}$ , possibly due to ring opening of the cyclic phosphate monomers (S4c). (d) The presence of 40 mM  $\text{K}^+$  increased the concentration of n-mers while added  $\text{Mg}^{2+}$  quenched polymerisation (S10a). (e) Sequence composition of cGMP and cCMP mixed oligomers at 40 mM  $\text{K}^+$ . Oligomers show G-rich n-mers and suggest the presence of all possible combinations in trimer sequences.

of polymerisation on  $\text{K}^+$ ,  $\text{Na}^+$  and  $\text{Mg}^{2+}$  salt concentrations is shown in S10, indicating that 1–3 eqv. of the same cation display similar results, but the type of cation affected the efficiency of oligomerisation.

### Polymerisation of cNMP in a heated rock pore mimic

Wet-dry cycles in surface-based geological settings are subjected to a drift in salt and pH conditions due to the imbalance caused by the evaporation of pure water and the rehydration of the fluid that contains salt. Wet-dry cycling can also occur in a closed chamber, subjected to a temperature gradient.<sup>[35]</sup> The water that evaporates on the warm side re-enters the fluid on its cold side. This causes interface shifts and the dew droplet dynamics on the cold side, offering wet-dry cycles under

constant pH and salt conditions. The geological analogues of such a setting would be volcanic rock pores which are partially filled with fluids and are subjected to a thermal gradient. We have previously reported prebiotically important processes such as accumulation, phosphorylation, encapsulation, gelation, strand separation, enzymatic DNA replication and crystallisation within such settings.<sup>[35–37]</sup>

For the polymerisation within this setting, we started with 20 mM total monomers (5 mM each of cG, cC, cA and cU). After the chamber was loaded with the monomer solution, a thermal gradient was applied which drove continuous wet-dry cycles just above the air-water interface inside the chamber (Figure 3a). Over time, the meniscus of the bulk liquid receded in an oscillatory manner depending on how many dew droplets formed above the interface; and dried material precipitated on the warm side as a consequence (Figure 3b). The dew droplets grew at the cooler side of the chamber by surface-tension driven fusion and made contact with the warm side, rehydrating the dried material and transporting it back into the bulk.<sup>[37]</sup> This phenomenon was allowed to continue for 18 hours, after which the setup was dismantled and the remaining bulk liquid

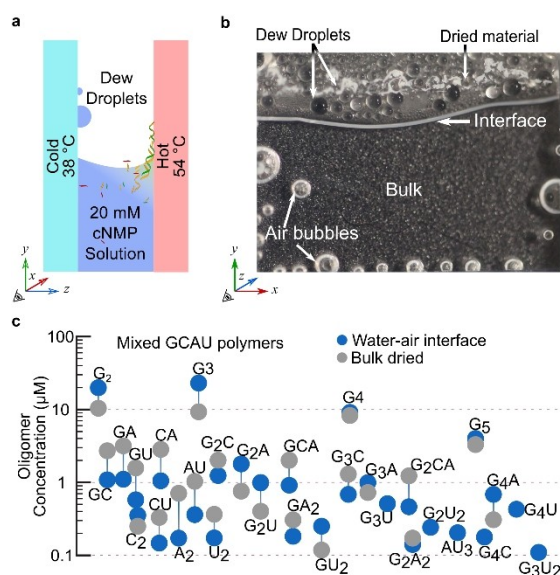


**Figure 3.** RNA oligomerisation in the vicinity of air inclusions in a heated simulated volcanic rock pore. (a) Side view. The chamber is 500 µm in depth and subjected to a heat flow with a temperature gradient of 38–54 °C. (b) Front view. The thermal gradient drives continuous evaporation and recondensation in the air inclusions, triggering accumulation and wet-dry cycles. Molecules accumulated at the interface are dried from a receding interface due to evaporation. Rehydration is provided by dew droplets on the cold side which merge with the bulk solution due to surface tension. (c) Oligomerisation of four canonical monomers: cGMP, cCMP, cAMP and cUMP, 5 mM each, 40 mM KCl at pH 10 for 18 hours. Especially for the longer strands, the oligomerisation in the simulated rock pore shows improved yields over the dry reaction. The physically triggered wet-dry cycling and length selectivity in this environment has been shown to drive efficient replication and selection cycles,<sup>[37]</sup> making the finding of oligomerisation to provide the raw material for templated ligation very interesting. Moreover, this shows that oligomerisation under simulated geological conditions is possible without the need for arid conditions on early Earth. The trends show a rich set of mixed short sequences when all four nucleotides are mixed together for oligomerisation.

and the dried flakes (after dissolution) were sampled for analysis.

The pH of the samples at the end of the reaction was found to be lowered by a pH unit, indicating the formation of acidic species in the reaction mixture. A likely cause of the pH drop is the acidification by the ring opening of the cyclic phosphate in the mononucleotides and the oligomers (S4e, S5c, d). At higher temperatures, the pH drop was 1.5 to 2 pH units (S4e).

Despite the presence of bulk water, the oligomerisation inside the simulated volcanic-rock pore showed comparable yields as that of the heat-dried conditions. This indicates that the heated interface can access conditions favourable for polymerisation similar to bulk dried polymerisation conditions. The constant feeding of monomers from the bulk fluid could also be an important factor. A length-selective enzymatic DNA replication was reported recently within this setting, indicating the possible continuity of prebiotic chemistry in such a setting.<sup>[37]</sup>

We observed all the dimer sequence combinations and most of the trimers (Figure 3c). However, the tetramers and pentamers are predominantly sequences rich in G. The length selectivity of the HPLC allowed the detection of longer sequences. However, the isotopic fit to the raw mass spectra provided by our LabView-based analysis showed that longer species with concentrations lower than 0.2 µM were lost in the background noise of the mass spectra. Moreover, different oligomers can have similar masses (eg. Table S3 and S4), so to avoid false positives, sequences with mass overlaps were not included here. This is in addition to the rigid selection criteria, based on fitting of the isotopic distribution (S12) and only considering mass spectra within the optimised n-mer retention times of the HPLC. A full sequence composition analysis for GC and GCAU mixtures with comparison between dry polymerisation and simulated rock-pore polymerisation is provided in S11. In comparison, CAU reaction mixture yielded only dimers (S9c), indicating again the central role of G in the copolymerisation process.

### Computational study of the proposed intercalated stacked arrangement

Based on the hypothesis that a stack-assisted geometry is triggering the oligomerisation of 3',5'-cGMP,<sup>[26]</sup> we studied the suitability of intercalated stack arrangements for the oligomerisation of 2',3'-cNMP. We explored the stability of the stack arrangements, and the incorporation of cNMP monomers into polymerised cGMP scaffold, based on minimum energy structures and molecular dynamics simulations (Figure 4a–c and S24–34).

To investigate the suggested intercalated stack arrangement for several possible species, we have computed the stacking interaction energies and evaluated the minimum energy geometries obtained at ωB97 M-V/def2-TZVPD level of theory.<sup>[38–41]</sup> All systems were studied in the gas phase as well as with implicit solvation (C-PCM).<sup>[42]</sup> The quantum mechanical

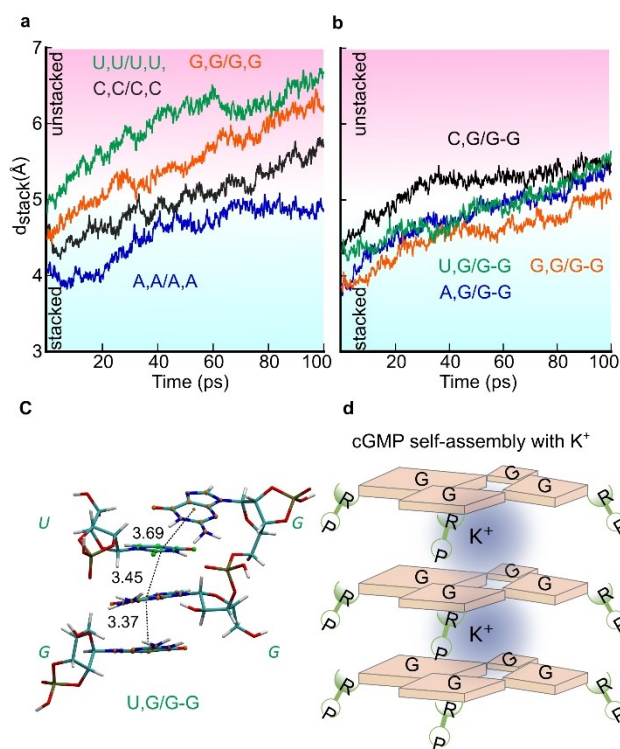


**Figure 4.** Possible supramolecular assemblies facilitating polymerisation of cNMP. Molecular dynamics simulations suggest polymerisation of A, U and C by intercalating into stacks of oligoG. (a) Distances between bases in the complex of unpolymerised nucleotides show that polymerisation is disfavoured due to drifting away of the complex. (b) The assembly formed when the bases are templated by covalently linked G–G (2′–5′) dimers, forms the most stable complexes and make possible the incorporation of the G, C, A, and U within the n-mers observed in our experiments. (c) Snapshot after energy minimization of stacking interaction between an oligomerised scaffold of cGMP (G–G) to template the cGMP and cUMP monomers (U,G). The dotted lines mark distances between the bases used to evaluate the stability of the complex. (d) However, the self-oligomerisation of oligoG could also be based on stacks of G-tetrads, stabilised by inner  $K^+$  ions, coinciding with the promotion of oligoG formation by  $K^+$  ions. R denotes the ribose of RNA.

computations were performed using FermiONS+ +<sup>[43–45]</sup> in combination with Chemshell.<sup>[46]</sup>

These computations were complemented by GFN-FF molecular dynamics simulations,<sup>[47]</sup> for the systems encapsulated in an explicit water sphere using xtb.<sup>[48]</sup> The stacking of homogeneous monomers were tested (N,N/N,N) with N = A, U, G, C and the incorporation of monomers into a dimer and trimer scaffold of G was probed (N,N/G–G or N,N/G–G–G). The 3′–5′ linked G–G and G–G–G accommodate A, U and G monomers into the scaffold providing a stable arrangement for the initiation of polymerisation. For C an alternate arrangement involving hydrogen bonding with a G within the scaffold is observed (S28). We found that a 2′–5′ oligoG scaffold seemed to enhance the alignment (Figure 4a, b, c), confirmed both by static and dynamic computations (S30, S31).

## Theoretical model of cGMP polymerisation

Additional evidence supporting a stacked polymerisation mechanism comes from the observed non-exponential length distribution of the oligomer concentrations. This supports the idea that the formation of dimers is the rate limiting step: the concentration drop from monomers to dimers was most significant. For the cGMP oligomerisation in Figure 1a, the 20 mM monomer concentrations drop to 0.15 mM for  $G_2$ , then forming a flat concentration plateau, in contrast to the typical exponential length distribution in homogeneous polymerisation.<sup>[49]</sup>

To test this idea, we fit the concentration distribution of G homooligomers with a stacked polymerisation model (solid line Figure 1a and 2a). The model assumed a three-step polymerisation reaction: i) a monomer of length  $i$  and a oligoG scaffold  $k$  can stack together with rate  $\nu$ , ii) the de-stacking rate  $\delta_{k,i}$  decreases exponentially with the number of stacked bases  $n_{k,i}$ , iii) another monomer of length  $j$  can stack to the complex. If the stacks persist long enough, the polymerisation reaction ligates the two monomers with rate  $\rho$  (see for details S18–S19). The model fits the experimental data, suggesting a rate limiting step for the formation of short oligomers due to the required mutual alignment. It should be noted that it is difficult to distinguish between inter-base stacking or a plausible G-tetrad arrangement suggested based on the enhanced polymerisation observed with  $K^+$  (Figure 4d).

## Discussion

Our data suggests that cGMP oligomerises in dry state at moderate temperatures and pH. The oligomerisation occurs over a range of temperatures (40–80 °C) and pH (7–12) and does not require additional catalysts, making this reaction robust. Dissolved gases and salts could adjust the pH of the environment, making RNA formation more probable under early Earth models.<sup>[50,51]</sup> We also showed polymerisation in the wet-dry cycling environment at a heated air-water interface, adding RNA polymerisation to the pool of prebiotic processes possible within such a setting.<sup>[35–37]</sup> The tested conditions of wet-dry cycles at an air-water interface or direct drying keep the reaction out of equilibrium. The cyclic monomers undergo polymerisation and ring-opening (Figure 1d), of which the ring-opening is still the dominant product at the tested temperatures (S4). Under the tested conditions, the reaction yielded oligomers up to 15-mers. The formed oligoG incorporated cCMP, cAMP and cUMP monomers, albeit in lower concentration, which did not homooligomerise significantly. As a rough comparison to the yields achieved by Verlander and Orgel with homooligomers of cAMP in the presence of ethane-1,2-diamine, we observed ~0.35% for a 6-mer of oligoG in 18 hours compared to 0.81% for polyA in 40 days.<sup>[6]</sup>

An important feature of this oligomerisation is that the 2′,3′-cyclic phosphate group, under alkaline pH, is sufficient to trigger oligomerisation without ex-situ or in-situ activation mechanism or added catalysts, and under low salt conditions.

The finding that the oligomerisation starts without added catalysts – and that the reaction site is not yet blocked by a catalyst – is a very good starting point for Darwinian evolution to speed up this reaction rate. Low salt conditions are interesting for RNA evolution since they notably help strand separation and reduce RNA degradation.<sup>[36]</sup>

cNMP oligomerisation is found to be a relatively clean reaction under the tested conditions. In comparison, *in situ* EDC activation yields side products, especially at high temperatures.<sup>[52]</sup> We did not detect any major side products with ESI-TOF, other than the salt adducts of sodium and potassium.

The abiotic formation and recyclability of the cNMP monomers is feasible, as they are known to be produced under several phosphorylation conditions, nucleotide syntheses and are common degradation products of RNA.<sup>[19–23]</sup> Thus, with the likelihood of finding catalytic boosts for this found reaction mode, a cycle of reactions involving polymerisation, oligomer extension, polymer hydrolysis and reactivation of monomers under early Earth conditions becomes conceivable. Furthermore, recombination and templated ligation involving 2',3'-cyclic ending oligomers<sup>[53]</sup> have been observed.

For our studies, we compared two monovalent ions ( $K^+$ ,  $Na^+$ ) and one divalent cation ( $Mg^{2+}$ ). They were chosen for their relevance in contemporary cytosolic media, their abundance on the early Earth<sup>[54]</sup> and for the role of  $Mg^{2+}$  in ribozyme activity.<sup>[55]</sup> Polymerisation is enhanced in the presence of  $K^+$  in comparison to  $Na^+$  ions. The inhibition by  $Mg^{2+}$  ions possibly occurs by a combination of base catalysis mechanism, the deactivation of -cP ends of the reactant, products and enhanced oligomer hydrolysis. Despite its role in ribozyme functionality, at high concentrations  $Mg^{2+}$  inhibits RNA replication by creating strong RNA duplexes, limiting thermal denaturation and enhancing temperature dependent hydrolysis.<sup>[56]</sup> It is also known that the presence of  $\sim 1.5$  mM  $Mg^{2+}$  is sufficient to inhibit the membrane self-assembly of fatty acids and this has been considered an incompatible aspect for the co-emergence of RNA and fatty acid membranes.<sup>[57,58]</sup> However, under the discussed reaction conditions of cNMP oligomerisation, RNA formation and encapsulation with fatty acids might be conceivable within freshwater locations on the primordial Earth. Moreover, we have shown that efficient strand separation can be achieved by low sodium concentrations, triggered by microscale water cycles within heated rock pores.<sup>[36,37]</sup>

Our very preliminary digestion studies and  $^{31}P$  NMR results suggest a considerable backbone heterogeneity (2'-5' and 3'-5') within the oligomers. However, a full quantitative treatment is beyond the scope of this study. It has been demonstrated that the presence of 2'-5' linkages allow efficient strand separation by reducing the melting temperature ( $T_m$ ) of oligomers, which is pertinent in the case of G-rich sequences that are observed in this oligomerisation.<sup>[59]</sup> Lowering of  $T_m$  is critical to replication of sequences.<sup>[59,60]</sup> These studies also show that the presence of 2'-5' linkages allow the folding of RNA into three-dimensional structures, similar to native linkages and do not hinder the evolution of functional RNAs, such as ribozymes. The susceptibility towards enhanced hydrolysis of the 2'-5' over the 3'-5'

linkages could select the latter in wet-dry cycling conditions, similar to the reported backbone selection of RNA and DNA.<sup>[59,61,62]</sup>

Mechanistically, molecular dynamics studies indicated that cGMP oligomerisation could be due to the formation of intercalated stacks of cGMP as a consequence of hydrophobic interactions between the guanine bases. On attaining a stable intermolecular arrangement, the 5'-OH of a nucleotide can attack the cyclic phosphate of the neighbouring nucleotide. This could allow the formation of oligomeric G-scaffolds (Figure 4c, d, S25). However, the formation of tetrad stacks over one another with a central  $K^+$  ion between the stacks could also promote oligomerisation (Figure 4d).

The notion of multi-molecular assemblies is supported by the presence of slow-diffusing species observed in  $^1H$ ,  $^{31}P$  diffusion ordered spectroscopy (DOSY) of cGMP-KCl solution (S15, S16). Reports in literature point to self-assembly of 5'-GMP and 3'-GMP into helical stacks.<sup>[63]</sup> The presence of several slow-diffusing species indicate a range of molecular environments, making it impossible to identify a single type of self-assembly by NMR. It has also been reported that G-quadruplex structures could be stable up to a pH of  $\sim 10.8$  at ambient temperatures.<sup>[64,65]</sup>

The formation of dimers appears to be a limiting step in the oligomerisation. Such a threshold behaviour is known to be an optimal control strategy for self-assembly processes.<sup>[66]</sup> With this, monomers remain available in high concentration, leading to long-tailed, non-exponential polymer distributions. This limits the total efficiency of the polymerisation but favours the formation of the oligomers, important for downstream reactions such as templated replication.

It should be noted that an efficient generation of very long and random RNA sequences would make hybridisation and replication inconceivable. At this point, the generated G-rich sequences might not seem optimal for hybridisation and replication. However, a biased pool of short oligomers (10- to 15-mers) further constrains the sequence space, favouring selectivity and making templated replication plausible.<sup>[11,67,68]</sup> We think that the findings are a first step to provide oligonucleotides for templated ligation and the emergence of an evolutionary dynamics with RNA.

## Conclusion

We report the oligomerisation of canonical nucleotides that produced RNA of mixed sequences under drying conditions in bulk and at heated air-water interface. A wide range of temperatures (40–80 °C) and pH (7–12) promoted oligomerisation. Best yields were reported by mild heating (40 °C) of monomers at low salt concentrations and under alkaline drying conditions (pH 10). The reaction proceeded best at 1–2 equivalents of  $K^+$  and  $Na^+$ , while  $Mg^{2+}$  ions inhibited it. In an equal mixture of four nucleotides, equal incorporation of all four was not observed and the mixed sequences were dominated by G. However, 2',3'-cGMP fostered the incorporation of the otherwise scarcely reactive C, A, and U, generating short, mixed

sequences. This reaction under the tested temperatures, pH and salt conditions provide a novel route to fresh water oligomerisation towards short RNA strands, an important intermediate step towards providing the raw materials for an RNA-based emergence of life.

## Acknowledgements

We would like to thank Ulrich Gerland, Tobias Göppel, Joachim Rosenberger and Bernhard Altaner for their helpful remarks and discussions; Thomas Matreux, Alexandra Kühnlein, Noël Yeh Martin and Maximilian Weingart for comments on the manuscript. The authors thank J. Kussmann (LMU Munich) for providing a development version of the FermiONs ++ program package. Financial support was provided by the European Research Council (ERC Evotrap, grant no. 787356, the Simons Foundation (grant no. 327125), the Deutsche Forschungsgemeinschaft (DFG, German Research Foundation) – Project-ID 364653263 – TRR 235 (CRC 235), the Deutsche Forschungsgemeinschaft (DFG, German Research Foundation) under Germany's Excellence Strategy – EXC-2094 – 390783311, and the Center for NanoScience. Open Access funding enabled and organized by Projekt DEAL.

## Conflict of Interest

The authors declare no conflict of interest.

## Data Availability Statement

The data that support the findings of this study are available from the corresponding author upon reasonable request.

**Keywords:** RNA · Polymerisation · Prebiotic chemistry · Non-equilibrium · Air-water interfaces

- [1] H. S. Bernhardt, *Biol. Direct* **2012**, *7*, 1–10.
- [2] G. Costanzo, S. Pino, A. M. Timperio, J. E. Šponer, J. Šponer, O. Nováková, O. Šedo, Z. Zdráhal, E. Di Mauro, *PLoS One* **2016**, *11*, 1–14.
- [3] J. P. Ferris, A. R. Hill, R. Liu, L. E. Orgel, *Nature* **1996**, *381*, 59–61.
- [4] M. S. Verlander, R. Lohrmann, L. E. Orgel, *J. Mol. Evol.* **1973**, *2*, 303–316.
- [5] C. V. Mungli, N. V. Bapat, Y. Hongo, S. Rajamani, *Life* **2019**, *9*, 1–11.
- [6] M. S. Verlander, L. E. Orgel, *J. Mol. Evol.* **1974**, *3*, 115–120.
- [7] A. Luther, R. Brandsch, G. Von Kiedrowski, *Nature* **1998**, *396*, 245–248.
- [8] S. J. Zhang, D. Duzdevich, D. Ding, J. W. Szostak, *Proc. Nat. Acad. Sci.* **2022**, *119*, 2021.09.07.459201.
- [9] T. Walton, W. Zhang, L. Li, C. P. Tam, J. W. Szostak, *Angew. Chem. Int. Ed.* **2019**, *58*, 10812–10819; *Angew. Chem.* **2019**, *131*, 10926–10933.
- [10] E. Kervio, M. Sosson, C. Richert, *Nucleic Acids Res.* **2016**, *44*, 5504–5514.
- [11] C. Richert, G. Leveau, D. Pfeffer, B. Altaner, E. Kervio, U. Gerland, F. Welsch, *Angew. Chem. Int. Ed.* **2022**, 202203067, 1–6.
- [12] L. Li, N. Prywes, C. P. Tam, D. K. Oflaherty, V. S. Lelyveld, E. C. Izgu, A. Pal, J. W. Szostak, *J. Am. Chem. Soc.* **2017**, *139*, 1810–1813.
- [13] D. K. O'Flaherty, N. P. Kamat, F. N. Mirza, L. Li, N. Prywes, J. W. Szostak, P. Sheeringa, *J. Am. Chem. Soc.* **1997**, *119*, 1–5.
- [14] E. I. Jiménez, C. Gibard, R. Krishnamurthy, *Angew. Chem. Int. Ed.* **2020**, *60*, 19, 1077–10783, DOI 10.1002/anie.202015910.
- [15] Z. Liu, L. F. Wu, J. Xu, C. Bonfio, D. A. Russell, J. D. Sutherland, *Nat. Chem.* **2020**, *12*, 3–10.
- [16] H. J. Kim, S. A. Benner, *Astrobiology* **2021**, *21*, 298–306.
- [17] M. W. Powner, B. Gerland, J. D. Sutherland, *Nature* **2009**, *459*, 239–242.
- [18] Y. Yamagata, H. Inoue, K. Inomata, *Origins Life Evol. Biospheres* **1995**, *25*, 47–52.
- [19] R. Breslow, *Acc. Chem. Res.* **1991**, *24*, 317–324.
- [20] Y. Li, R. R. Breaker, *J. Am. Chem. Soc.* **1999**, *121*, 5364–5372.
- [21] H. Peng, B. Latifi, S. Müller, A. Lupták, I. A. Chen, *RSC Chem. Biol.* **2021**, *2*, 1370–1383.
- [22] A. M. Pyle, *Science* **1993**, *261*, 709–714.
- [23] S. I. Nakano, D. M. Chadalavada, P. C. Bevilacqua, *Science* **2000**, *287*, 1493–1497.
- [24] M. Morasch, C. B. Mast, J. K. Langer, P. Schilcher, D. Braun, *ChemBioChem* **2014**, *15*, 879–883.
- [25] J. E. Šponer, J. Šponer, A. Giorgi, E. Di Mauro, S. Pino, G. Costanzo, *J. Phys. Chem. B* **2015**, *119*, 2979–2989.
- [26] S. Wunna, C. F. Dirscherl, J. Výravský, A. Kovařík, R. Matyášek, J. Šponer, D. Braun, J. E. Šponer, *Chem. A Eur. J.* **2021**, *27*, 70, 17581–17585, DOI 10.1002/chem.202103672.
- [27] C. M. Tapiero, J. Nagyvary, *Nature* **1971**, *231*, 42–43.
- [28] S. Dagar, S. Sarkar, S. Rajamani, *RNA* **2020**, *26*, 756–769.
- [29] J. E. Šponer, J. Šponer, A. Kovařík, O. Šedo, Z. Zdráhal, G. Costanzo, E. Di Mauro, *Life* **2021**, *11*, 1–13.
- [30] A. Premstaller, P. J. Oefner, *LCGC Eur.* **2002**, *15*, 7, 410–422.
- [31] A. Premstaller, P. J. Oefner, *Denaturing High-Performance Liquid Chromatography*, Humana Press, New Jersey, n.d.
- [32] P. B. Danielson, R. Kristinsson, R. J. Shelton, G. S. LaBerge, *Expert Rev. Mol. Diagn.* **2005**, *5*, 53–63.
- [33] H. R. Palmer, J. J. Bedford, J. P. Leader, R. A. J. Smith, *J. Biol. Chem.* **2000**, *275*, 27708–27711.
- [34] S. Motsch, D. Pfeffer, C. Richert, *ChemBioChem* **2020**, *21*, 2013–2018.
- [35] M. Morasch, J. Liu, C. F. Dirscherl, A. Ianeselli, A. Kühnlein, K. Le Vay, P. Schwintek, S. Islam, M. K. Corpinot, B. Scheu, D. B. Dingwell, P. Schwill, H. Mutschler, M. W. Powner, C. B. Mast, D. Braun, *Nat. Chem.* **2019**, *11*, 779–788.
- [36] A. Ianeselli, C. B. Mast, D. Braun, *Angew. Chem. Int. Ed.* **2019**, *58*, 13155–13160; *Angew. Chem.* **2019**, *131*, 13289–13294.
- [37] A. Ianeselli, M. Atienza, P. W. Kudella, U. Gerland, C. B. Mast, D. Braun, *Nat. Phys.* **2022**, *18*, 579–585, DOI 10.1038/s41567-022-01516-z.
- [38] N. Mardirossian, M. Head-Gordon, *J. Chem. Phys.* **2016**, *144*, DOI 10.1063/1.4952647.
- [39] O. A. Vydrov, T. Van Voorhis, *J. Chem. Phys.* **2010**, *133*, DOI 10.1063/1.3521275.
- [40] F. Weigend, *Phys. Chem. Chem. Phys.* **2006**, *8*, 1057–1065.
- [41] F. Weigend, R. Ahlrichs, *Phys. Chem. Chem. Phys.* **2005**, *7*, 3297–3305.
- [42] M. Cossi, N. Rega, G. Scalmani, V. Barone, *J. Comput. Chem.* **2003**, *24*, 669–681.
- [43] J. Kussmann, C. Ochsenfeld, *J. Chem. Phys.* **2013**, *138*, DOI 10.1063/1.4796441.
- [44] J. Kussmann, C. Ochsenfeld, *J. Chem. Theory Comput.* **2015**, *11*, 918–922.
- [45] J. Kussmann, C. Ochsenfeld, *J. Chem. Theory Comput.* **2017**, *13*, 3153–3159.
- [46] P. Sherwood, A. H. De Vries, M. F. Guest, G. Schreckenbach, C. R. A. Catlow, S. A. French, A. A. Sokol, S. T. Bromley, W. Thiel, A. J. Turner, S. Billeter, F. Terstegen, S. Thiel, J. Kendrick, S. C. Rogers, J. Casci, M. Watson, F. King, E. Karlsen, M. Sjøvoll, A. Fahmi, A. Schäfer, C. Lennartz, *J. Mol. Struct.* **2003**, *632*, 1–28.
- [47] S. Spicher, S. Grimme, *Angew. Chem.* **2020**, *132*, 15795–15803; *Angew. Chem. Int. Ed.* **2020**, *59*, 15665–15673.
- [48] C. Bannwarth, E. Caldeweyher, S. Ehlert, A. Hansen, P. Pracht, J. Seibert, S. Spicher, S. Grimme, *Wiley Interdiscip. Rev.: Comput. Mol. Sci.* **2021**, *11*, 1–49.
- [49] C. B. Mast, S. Schink, U. Gerland, D. Braun, *Proc. Natl. Acad. Sci. USA* **2013**, *110*, 8030–8035.
- [50] J. F. Kasting, M. T. Howard, *Philos. Trans. R. Soc. London Ser. B* **2006**, *361*, 1733–1741.
- [51] J. Krissansen-Totton, G. N. Arney, D. C. Catling, *Proc. Natl. Acad. Sci. USA* **2018**, *115*, 4105–4110.
- [52] E. Edeleva, A. Salditt, J. Stamp, P. Schwintek, J. Boekhoven, D. Braun, *Chem. Sci.* **2019**, *10*, 5807–5814.
- [53] A. V. Lutay, E. L. Chernolovskaya, M. A. Zenkova, V. V. Vlasov, *Dokl. Biochem. Biophys.* **2005**, *401*, 163–166.
- [54] S. Maurer, *Life* **2017**, *7*, DOI 10.3390/life7040044.
- [55] T. S. Lee, C. S. López, G. M. Giambaşu, M. Martick, W. G. Scott, D. M. York, *J. Am. Chem. Soc.* **2008**, *130*, 3053–3064.

- [56] A. Salditt, L. M. R. Keil, D. P. Horning, C. B. Mast, G. F. Joyce, D. Braun, *Phys. Rev. Lett.* **2020**, *125*, 48104.
- [57] I. A. Chen, K. Salehi-Ashtiani, J. W. Szostak, *J. Am. Chem. Soc.* **2005**, *127*, 13213–13219.
- [58] K. Adamala, J. W. Szostak, *Science* **2013**, *342*, 1098–1100.
- [59] A. E. Engelhart, M. W. Powner, J. W. Szostak, *Nat. Chem.* **2013**, *5*, 390–394.
- [60] J. Sheng, L. Li, A. E. Engelhart, J. Gan, J. Wang, J. W. Szostak, *Proc. Natl. Acad. Sci. USA* **2014**, *111*, 3050–3055.
- [61] S. Bhowmik, R. Krishnamurthy, *Nat. Chem.* **2019**, *11*, 1009–1018.
- [62] A. Mariani, J. D. Sutherland, *Angew. Chem. Int. Ed.* **2017**, *56*, 6563–6566; *Angew. Chem.* **2017**, *129*, 6663–6666.
- [63] M. Gellert, M. N. Lipsett, D. R. Davies, *Proc. Natl. Acad. Sci. USA* **1962**, *48*, 2013–2018.
- [64] Y. Y. Yan, J. H. Tan, Y. J. Lu, S. C. Yan, K. Y. Wong, D. Li, L. Q. Gu, Z. S. Huang, *Biochim. Biophys. Acta Gen. Subj.* **2013**, *1830*, 4935–4942.
- [65] R. Del Villar-Guerra, R. D. Gray, J. B. Chaires, *Curr. Protoc. Nucleic Acid Chem.* **2017**, *2017*, 17.8.1–17.8.16.
- [66] F. M. Gartner, I. R. Graf, E. Frey, *Proc. Natl. Acad. Sci. USA* **2022**, *119*, DOI 10.1073/pnas.2116373119.
- [67] P. W. Kudella, A. V. Tkachenko, A. Salditt, S. Maslov, D. Braun, *Proc. Natl. Acad. Sci. USA* **2021**, *118*, DOI 10.1073/pnas.2018830118.
- [68] S. Toyabe, D. Braun, *Phys. Rev. X* **2019**, *9*, 11056.

---

Manuscript received: July 29, 2022

Accepted manuscript online: September 19, 2022

Version of record online: ■■■, ■■■■

# Regulating DNA-Hybridization Using a Chemically Fueled Reaction Cycle

Michele Stasi, Alba Monferrer, Leon Babl, Sreekar Wunnava, Christina Felicitas Dirscherl, Dieter Braun, Petra Schwille, Hendrik Dietz, and Job Boekhoven\*



Cite This: *J. Am. Chem. Soc.* 2022, 144, 21939–21947



Read Online

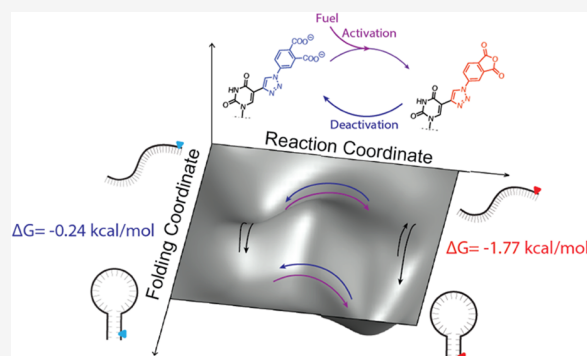
ACCESS |

Metrics & More

Article Recommendations

Supporting Information

**ABSTRACT:** Molecular machines, such as ATPases or motor proteins, couple the catalysis of a chemical reaction, most commonly hydrolysis of nucleotide triphosphates, to their conformational change. In essence, they continuously convert a chemical fuel to drive their motion. An outstanding goal of nanotechnology remains to synthesize a nano-machine with similar functions, precision, and speed. The field of DNA nanotechnology has given rise to the engineering precision required for such a device. Simultaneously, the field of systems chemistry developed fast chemical reaction cycles that convert fuel to change the function of molecules. In this work, we thus combined a chemical reaction cycle with the precision of DNA nanotechnology to yield kinetic control over the conformational state of a DNA hairpin. Future work on such systems will result in out-of-equilibrium DNA nanodevices with precise functions.



## INTRODUCTION

Nucleic acids have proven to be outstanding building blocks for molecular self-assembly. The precision and fidelity of base-pairing allow for predicting self-assembly patterns and optimizing the strength of the interaction. The advent of DNA origami<sup>1–4</sup> has pushed further the boundaries of the possible structures designed with DNA, opening the door for the easy bottom-up assembly of user-defined three-dimensional structures with unprecedented accuracy. Although initial works in the field have mainly focused on developing static structures, the so-called structural DNA nanotechnology, a strong interest is now diverted toward developing dynamic systems that reshape and actively interact with their surroundings.<sup>5–8</sup>

If structural DNA nanotechnology enables virtually building of any architecture on the nanometer scale, the combination with actuation mechanisms could fulfill the dream of a fully synthetic biomolecular machine.<sup>7,9,10</sup> Several strategies to control the actuation of DNA nanodevices have been employed. Toehold-mediated strand displacement reaction<sup>11–17</sup> is a popular approach that relies on user-designed DNA sequences with partial complementarity, making it easy to implement. A limiting factor in this strategy is the second-order kinetic hybridization between DNA sequences that require high concentrations of DNA strands to achieve operational speed in seconds. Alternative approaches for actuation of DNA-based nanodevices include light-responsive molecules,<sup>18</sup> redox stimuli,<sup>19,20</sup> pH-dependent secondary

structures,<sup>21–23</sup> actuation by varying the ionic strength of the medium<sup>24</sup> or the temperature and thus controlling the stacking interaction of nucleobases in blunt ends,<sup>8</sup> through the use of external electric or magnetic fields,<sup>9,25,26</sup> or biomolecules such as antibodies<sup>27</sup> and enzymes.<sup>28–31</sup> Most of these strategies, except for the enzyme-driven ones, proceed stepwise, *i.e.*, the structure switches from one static state to another upon application of the stimulus. Additionally, they operate profoundly differently than naturally occurring biomolecular machines in harnessing the energy required to function. Specifically, the actuation process in dynamic DNA nanotechnology results from a change in the overall energy landscape (*e.g.*, by changing the pH or ionic strength), thereby driving the system into the new global minimum. Conversely, natural molecular machines, such as ATPases or motor proteins, couple the catalysis of a chemical reaction, *e.g.*, the hydrolysis of nucleotide triphosphates, to their conformational change: they incessantly consume fuel to drive their motion.<sup>32</sup> Recently, Del Grosso and co-workers introduced the concept of dissipative DNA nanotechnology to distinguish those systems that do not strictly operate under thermodynamic

Received: August 9, 2022

Published: November 28, 2022

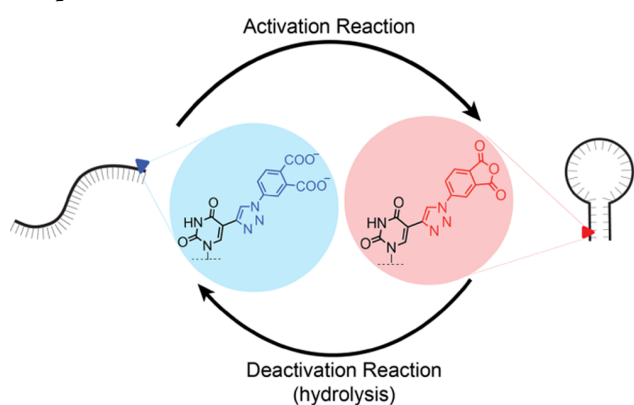


control but instead require the presence of an additional element: a chemical reaction as an energy-dissipative element.<sup>33</sup> The examples reported rely on ATP-consuming enzymes to ligate and excise DNA strands, thereby controlling their hybridization behavior<sup>30,34–36</sup> or RNases to degrade RNA strands.<sup>29,37</sup>

Outside of dissipative DNA nanotechnology, the constant conversion of fuels to drive the function of molecules has been successfully applied to the self-assembly of small molecules.<sup>38,39</sup> In such a chemically fueled system, molecular assembly is regulated by a fuel-driven reaction cycle that comprises at least two reactions, *i.e.*, an activation and deactivation reaction. In the activation reaction, a precursor reacts with a chemical fuel which activates it for self-assembly. In the deactivation, the activated product spontaneously reverts to the precursor. In its finite lifetime, the activated product can be temporarily part of a dynamic assembly, which is thus regulated by the kinetics of the reaction cycle. This strategy has resulted in chemically fueled dynamic fibers,<sup>40,41</sup> droplets,<sup>42</sup> and colloids.<sup>43</sup> More recently, chemically fueled reaction cycles have also been used to operate small molecular machines and motors.<sup>44–46</sup> Developments in chemically fueled self-assembly have resulted in fast reaction cycles in which activated products have half-lives of tens of seconds. Nevertheless, chemically fueled self-assembly of small molecules still lacks precision and designability compared to DNA nanotechnology.

In this work, we combined a fast reaction cycle with the precision of DNA nanotechnology to achieve kinetic control over the conformational state of a DNA hairpin (Scheme 1).

**Scheme 1. Schematic Representation of a Fuel-Driven Hairpin<sup>a</sup>**



<sup>a</sup>The hairpin is mostly unfolded in its precursor state (dicarboxylic acid, blue). The folded state becomes more stable upon activation (anhydride, red).

We harness the energy of hydration of carbodiimide to shift the population of hybridized DNA versus single-stranded DNA. We reach a distribution not allowed at thermodynamic equilibrium. The system spontaneously reverts to its initial state once the fuel is fully consumed, and the nonequilibrium distribution cannot be further sustained. Our molecular design is versatile, can be quickly introduced in commercially available DNA sequences, and provides a strategy for nonequilibrium self-assembly and actuation in DNA nanotechnology. We demonstrate its applicability in both a unimolecular and a bimolecular setting, *i.e.*, develop a strategy for chemically

fueled strand displacement reaction based entirely on an abiotic fuel, potentially orthogonal to previously reported strategies.

## RESULTS AND DISCUSSION

We used a versatile, well-described chemical reaction cycle<sup>47–49</sup> in which a phthalic acid-based precursor is transiently activated into its corresponding anhydride at the expense of a molecule of EDC (1-ethyl-3-(3-dimethylaminopropyl)carbodiimide, Figure 1A). In the activation reaction, the precursor reacts with EDC to yield the precursor's anhydride state and EDU (1-(3-(dimethylamino)propyl)-3-ethylurea). The anhydride product rapidly hydrolyzes to its precursor state in the aqueous environment, *i.e.*, the deactivation reaction. In its finite lifetime, the hydrophobization and rigidification of the molecule can induce self-assembly or, in our design, affect the stability of a DNA hairpin. Using a copper-catalyzed alkyne–azide cycloaddition reaction, we modified an alkyne-bearing thymine to carry two carboxylates that serve as the precursor for our reaction cycle (modified thymine, Figure 1A).

First, we tested the reaction cycle's kinetics of the nucleotide itself, *i.e.*, without incorporating it in a DNA hairpin (modified thymine, Figure 1A). The addition of 4 mM EDC to 8 mM of the modified thymine in 200 mM MES at pH 6 yielded the formation of the corresponding anhydride product, as evidenced by HPLC. As the reaction progressed, the concentrations of fuel and anhydride decayed (Figure S1). The kinetics of the reaction cycle could be accurately captured with a kinetic model (see Supporting Note 1), which allowed us to calculate the half-life of the anhydride product ( $t_{1/2}$ ) to be 23 s.

Next, we incorporated the modified thymine into a molecular beacon comprising a Cy3 dye on the 5' end and a black hole quencher (BHQ-2) on the 3' end of a 30-base oligomer (Figure 1B). We measured its melting temperature by fluorescence spectroscopy (see Figure S2). The molecular beacon we chose is based on a hairpin that, without any artificial modification, has a melting temperature ( $T_m$ ) of 40.4 °C under the applied conditions (H-0, Figure 1D). We anticipated that incorporating one modified thymine would decrease the  $T_m$  due to steric hindrance and electrostatic repulsion of the modified thymine compared to regular thymine. Thus, we designed H-1, which is H-0 with a point mutation of one thymine for modified thymine in the stem region of the molecular beacon. As expected, we found that its melting temperature was 10.5 °C lower than H-0. This decrease in  $T_m$  was independent of where the mutation was performed (H-2), provided it was in the stem region, *i.e.*, H-3 was modified in the loop region. Its  $T_m$  was almost equal to the unmodified H-0. If we added two mutations in the stem region,  $T_m$  decreased by 20.6 °C (H-4, Figure 1D).

The destabilizing effect of the modified thymine can be attributed to the electrostatic repulsion of the carboxylates and/or steric hindrance of the phthalic acid and triazole in the crowded environment of the duplex. To test which of these forces was the dominant one, we synthesized the methyl ester of modified thymine which lacks the anionic nature compared to modified thymine but is similar in size (Figure 1C). When incorporated in the molecular beacon (H-5), we found a slight drop in  $T_m$  (4.4 °C) compared to nonmodified H-0. This observation suggests that both a steric hindrance and the

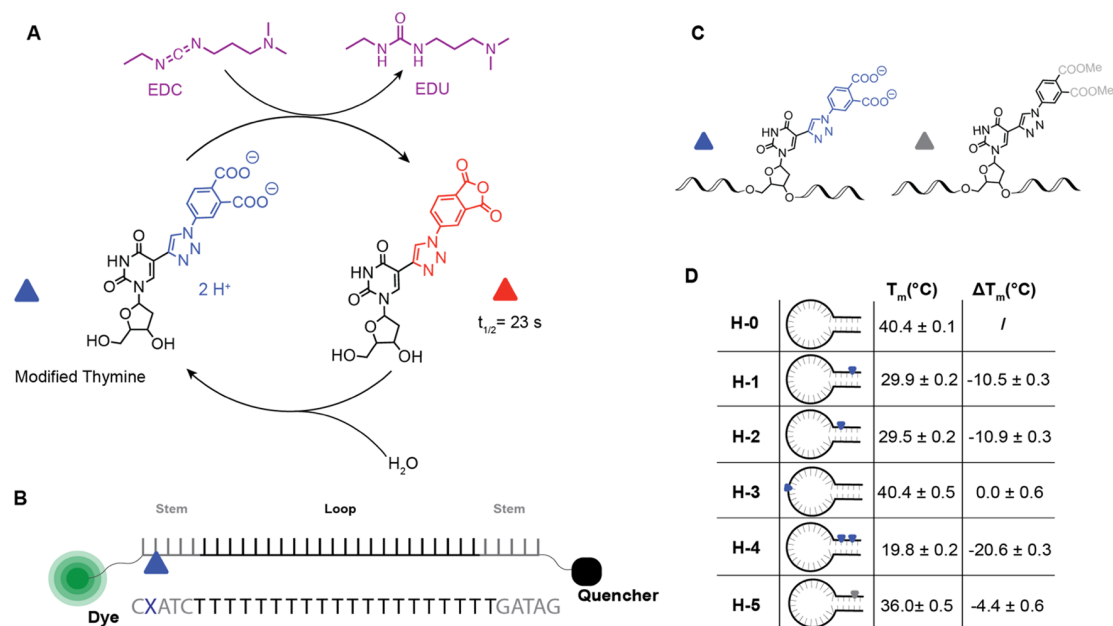


**Figure 1.** Molecular design of the dynamically folding hairpins. (A) Chemical reaction cycle activates modified thymine at the expense of a carbodiimide-based fuel. (B) Sequence of the oligomer in which the modified thymine is incorporated. The dye is Cy3, the quencher is a Black Hole Quencher 2, and the blue triangle represents the modified thymine. (C) Schematic representation of an oligomer with the modified thymine incorporated and an oligomer with a control compound, *i.e.*, the methyl ester of the modified thymine, is represented as a gray triangle. (D) Table of oligonucleotides (H-0 to H-5) with the location of their modification (blue triangles), their melting temperature ( $T_m$ ), and the difference in  $T_m$  compared to nonfunctionalized H-0 as measured by fluorescence melting experiments (see Figure S2).

presence of negative charges are responsible for the change in the  $T_m$  upon incorporating modified thymine.

Next, we tested the ability of the fuel-driven chemical reaction cycle to induce the folding of the hairpin. We added 20 mM EDC to 0.2  $\mu$ M H-1 (*i.e.*, a 100,000-fold excess) and monitored the fluorescence intensity of the molecular beacon as a function of time (Figure 2A,B). The experiment was performed at the  $T_m$  of H-1 (30 °C). We can thus assume that roughly 50% of the hairpin was in its folded state before fuel addition. Immediately after the EDC addition, the fluorescence intensity dropped, indicating that the population of folded hairpins had increased. Ten minutes after the EDC addition, we added 10 mM *N*-acetyl aspartate (Ac-D-OH) as a scavenger, *i.e.*, a competing dicarboxylate that can also cyclically react with EDC and rapidly consume all fuel. Consequently, the hairpin fluorescence returned to a value close to the original level. We attribute the lack of a complete return due to the change in ionic strength of the solution caused by the positively charged group present in both EDC and its byproduct of hydration, *i.e.*, the waste EDU (Figure 2C).

These results suggest that adding a chemical fuel creates a steady state of anhydride, which changes the dynamic population of the folded hairpins and unfolded oligonucleotide. The reason for the high amount of fuel lies in the different rates of the reactions and the low concentration of DNA. In our reaction cycle, the activation reaction and the deactivation are simultaneously operating. The activation however follows a second-order kinetics, while the deactivation follows a pseudo-first-order kinetics. To sustain a constant level of anhydride, high enough to show a change in the population of hybridized species, we balance the effect with a great excess of fuel. We quantified the change in the folding caused by the fuel by

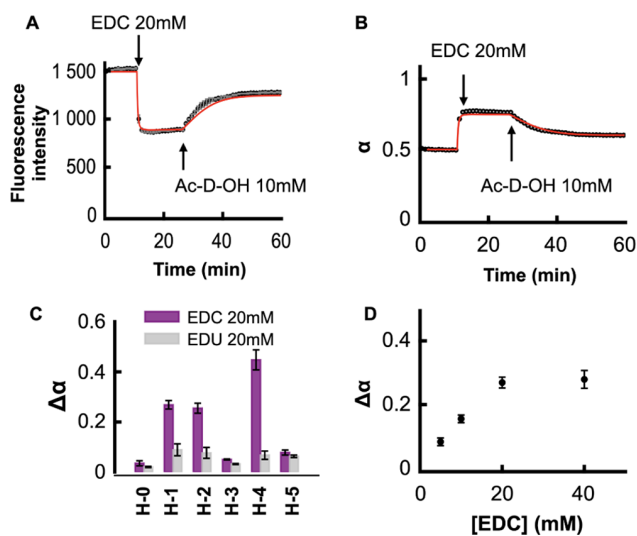


**Figure 2.** Response of the molecular beacon to chemical fuel. (A) Fluorescence intensity as a function of time for H-1. At 10 min, 20 mM EDC is added. After 15 min, 10 mM *N*-acetyl aspartate is added to consume the remaining EDC. Black markers represent the experimental data. The standard deviation of duplicate experiments is shown as an error bar. The red line represents a prediction with our kinetic model. (B) Evolution of  $\alpha$  for the experiment described in panel A. (C) Comparison of the effect of fuel (EDC, 20 mM) and waste (EDU, 20 mM) on the folding of the different oligonucleotides. (D) Effect of different amounts of fuel on the folding of H-1.

calculating the amount of folded hairpins as a fraction of the total concentration of oligonucleotides ( $\alpha$ )

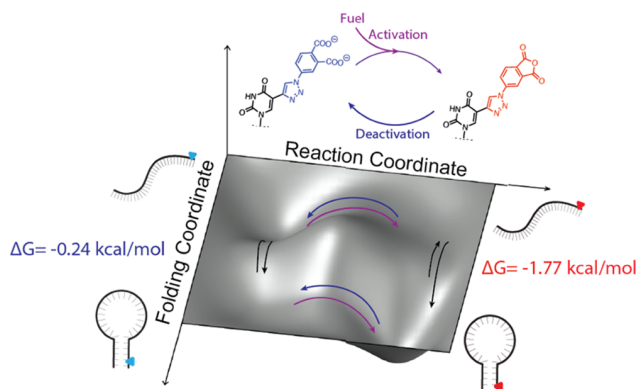
$$\alpha = \frac{[\text{folded hairpin}]}{[\text{total hairpin}]} \quad (1)$$

We determined the concentration of folded hairpins by fluorescence spectroscopy by comparing the fluorescence intensity to two reference points, *i.e.*, the fluorescence intensity of a sample where all of the hairpins were folded and the fluorescence intensity at 30 °C before the addition of fuel. We prepared the sample where all of the hairpins were folded by adding 20 mM MgCl<sub>2</sub> while the corresponding  $\alpha$  at 30 °C is known from the melting curve of each H (Supporting Table 1). From these two reference points, the  $\alpha$  was calculated using the equation described in Supporting Notes 2.

We measured the  $\alpha$  increase upon adding fuel or EDU for all of the hairpins in this work (Figure 2C). As expected, for the nonmodified hairpin H-0, the increase in  $\alpha$  was minimal. Moreover, it was similar to the increase upon the addition of EDU. The same trend is observed for H-3, *i.e.*, the molecular beacon with the modified thymine in the loop region. For the final control compound, H-5, where the carboxylic acids are protected as methyl esters, the change induced by the fuel and the waste was modest. In contrast, H-1, H-2, and H-4 displayed a striking difference between adding EDC or EDU. In the case of H-4, we started with an almost open state before applying fuel ( $\alpha = 0.21$ ). The addition of fuel pushed the system toward a closed state ( $\alpha = 0.66$ ). In other words, the fuel switched the system from a condition where the open state is dominant to a new, temporary distribution where the closed state is in excess. We then explored the effect of different amounts of fuel on the folding of H-1. We chose to focus on H-1 because it has only one modified thymine, thus reducing the number of transient species. When increasing amounts of fuel are added, a greater degree of folding is achieved (Figure 2D), mainly attributed to the higher anhydride yield in a steady state. In contrast, when a similar amount of EDU was added, the change in  $\alpha$  was much lower (Figure S3). These combined experiments conclude that adding fuel increases the folded hairpin population by activating the modified thymine.

The fluorescence data provided information about the overall fraction of the folded hairpin. However, precursor and activated states are simultaneously present, and each can form hairpins (see Scheme 2). Our system was designed so that the activated state is more likely to form a hairpin. We were interested in understanding the contributions of each of the

### Scheme 2. Proposed Energy Landscape of the Chemically Fueled Hairpin<sup>a</sup>



<sup>a</sup>A hairpin in our system can toggle between four positions in our energy landscape: unactivated and unfolded, unactivated and folded, activated and unfolded, and activated and folded. Chemical activation makes folding more favorable.

two possible hairpin species to the overall fraction of folded hairpins.

We can rewrite eq 1 as the sum of two terms like in the following

$$\begin{aligned}\alpha &= \frac{[\text{folded hairpins}]}{[\text{total hairpins}]} = \frac{[\text{anhydride}_{\text{folded}}] + [\text{acid}_{\text{folded}}]}{[\text{total hairpins}]} \\ &= \frac{\alpha_1 \cdot [\text{total hairpins}] \cdot y + \alpha_0 \cdot [\text{total hairpins}] \cdot (1 - y)}{[\text{total hairpins}]} \\ &= \alpha_1 \cdot y + \alpha_0 \cdot (1 - y)\end{aligned}$$

where  $\alpha_0$  and  $\alpha_1$  are the folding ratios of the acid and the anhydride state, respectively, and  $y$  is the steady-state yield of the reaction cycle. To determine those two  $\alpha$  values, we thus have to determine the steady-state concentration of anhydride, which we measured by HPLC. As a precursor, we used a short oligonucleotide equipped with our modified thymine, and we applied different amounts of fuel to induce different steady-state levels. We quenched these samples after 1 min with a previously established quenching method.<sup>50</sup> In brief, we added EDC to a solution of unlabeled oligo (1  $\mu$ M) in MES buffer at pH 5.5, and after 1 min, 2  $\mu$ L of 1-pentylamine was added to the sample. We found that two new peaks appeared in the chromatogram, which we attributed to the products of the anhydride reacting with 1-pentylamine (see Figure S18). By comparing the areas of the peaks, we calculated the yield of anhydride in a steady state, which we used in our kinetic model to fit the fluorescence data as a function of time (see Supporting Note 1 and Figure S4). From the model, we derived a value for  $\alpha_1$ , which we estimated to be 0.95. In other words, 95% of the activated oligos are in their folded state, whereas only 50% of the nonactivated oligos are in their folded state.

The obtained data creates a clearer picture of the energy landscape of our dynamic hairpins (Scheme 2). In the energy landscapes, four states exist: a DNA strand can either be folded or unfolded, or it can either be activated or deactivated. Pathways exist between these states. However, only the eight dominant ones are shown: an unactivated strand can fold and unfold, and an activated strand can fold and unfold (pathways along the folding coordinate). Along the reaction coordinate, a folded or unfolded strand can become activated, and a folded and unfolded activated strand can become deactivated. While it is technically possible that a folded oligonucleotide simultaneously deactivates and unfolds, it is unrealistic and complicates the landscape.

We found that the activated state has a half-life of 23 s (*vide supra*). We also found that its degree of folding is in the range of 95%. Thus, in its lifetime, the activated oligomer will spend roughly 95% of its time in the folded state. However, the half-life for folding a DNA strand such as the one used in our experiments is reported to be in the range of milliseconds.<sup>51–53</sup> That means that even though an activated state will spend roughly 95% of its time in a folded state, it will unfold and refold 100 s of times in its lifetime.

Interestingly, the anhydride state was significantly more folded than the methyl ester control compound (activated H-1 vs H-5,  $\alpha = 0.95$  vs  $\alpha = 0.71$ , under the same conditions) even though both species lack the negative charges. A possible explanation is that the formation of the anhydride increases the overall planarity of the functional group, thus facilitating intercalation and stacking into the DNA helix. We also

observed a modest increase in the activation rate constant ( $k_1$  in the kinetic model, see Supporting Table 2) for the modified thymine when embedded in the oligo, in agreement with the previous report from our group that a densely charged local environment can affect the reactivity of dicarboxylic acid.<sup>41</sup>

In the experiments above, we changed the fraction of folding of hairpins in a steady state by adding fuel. The addition of a fuel scavenger allows controlling of the steady state by rapidly depleting all fuel reversibly. Next, we introduce the idea of a permanently present fuel scavenger that consumes most fuel and thus controls the lifetime of the folded population. Such an approach opens the door to self-regulating DNA nanodevices with time-dependent behavior. When fuel is added to such a competition experiment, the majority of the fuel is consumed by the scavenger, and the conformation change of the hairpin is only temporary (Figure 3A). A simulation by our kinetic

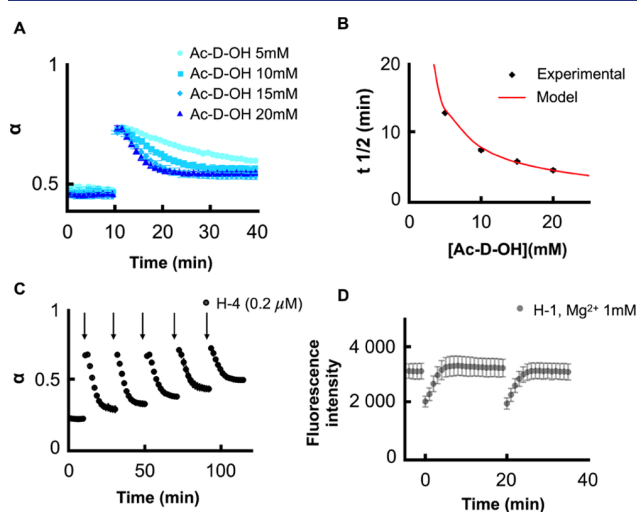


**Figure 3.** Regulating the lifetime of the folded hairpin population by introducing a fuel scavenger. (A) Variation of fraction folded ( $\alpha$ ) of H-1 ( $0.2 \mu\text{M}$ ) fueled with 20 mM EDC as a function of time in the presence of different amounts of Ac-D-OH (5, 10, 15, 20 mM, respectively). (B) Half-life of fluorescence recovery for experiment in (B). (C) Sequential addition of EDC 20 mM to H-4 ( $0.2 \mu\text{M}$ ). Each purple arrow indicates one 20 mM batch of fuel addition. (D) Evolution of fluorescence signal of H-1 with 20 mM of EDC in the presence of  $\text{Mg}^{2+}$  1 mM and Ac-D-OH 20 mM.

model demonstrated the validity of this approach and showed that lifetimes of the folded population could be tuned from a few minutes to hours, depending on the amount of scavenger that is added (Figure 3B).

We carried out these experiments using  $0.2 \mu\text{M}$  of H-1 in an MES buffer containing variable concentrations of Ac-D-OH as a scavenger at  $30^\circ\text{C}$ . When 20 mM EDC was added to the system with 20 mM of scavenger, we observed a marked drop in the fluorescence, followed by a rapid signal recovery. The kinetic profile of the fluorescence recovery correlates with the experimentally determined consumption of the EDC (Figure S6). Moreover, our kinetic model accurately modeled the fluorescence signal and correlated with the predicted anhydride concentration (Figures S7 and S8). The scavenger concentration could be used to tune the half-life of recovery of the folded states from 4 min to over 13 min, in agreement with the predicted half-life of recovery (Figure 3B). The ability of the system to stop autonomously allows for operating multiple

cycles with minimal intervention, which we demonstrate by adding five batches of 20 mM of EDC, which resulted in a transient change in the population of folded and unfolded molecules each time (Figure 3C). In contrast, most of the DNA dynamic system reported so far requires either extensive manipulation, such as buffer exchange, or at least two stimuli to move between the different states.

To demonstrate that our new chemically fueled hybridization can be incorporated into more sophisticated DNA structures than hairpins, we tested its resistance to magnesium ions.  $\text{Mg}^{2+}$  is a critical component for the folding of DNA origami and the operation of DNA nanotechnology. We analyzed the melting curve of our model hairpin H-1 in the presence of 1 mM and 10 mM  $\text{MgCl}_2$  (Figure S2). The modified thymine can still destabilize the duplex, but  $\Delta T_m$  decreased to 8 from  $10^\circ\text{C}$  compared to sodium-only buffer. In the case of higher concentrations of  $\text{MgCl}_2$ , the difference is reduced to only  $1.1^\circ\text{C}$ . However, the presence of Ac-D-OH widened the window to  $4.4^\circ\text{C}$ , potentially leaving a margin for operation. Aspartic acid is a weak chelator for  $\text{Mg}^{2+}$  ions while stabilizing the secondary structure.<sup>54</sup> Lastly, we tested the response of H-1 to fuel in the presence of a low concentration of  $\text{Mg}^{2+}$  (1 mM) and scavenger (Figure 3D). We found the expected behavior of the fluorescence signal corresponding to transient folding.

In the first part of the work, we demonstrated the possibility of chemically fueled hybridization on a simple, unimolecular construct. In dynamic DNA nanotechnology, strand displacement is the primary strategy for actuation.<sup>14</sup> Thus, to demonstrate that our chemically fueled hybridization can be used to power strand displacement, we repurposed a strand displacement circuit, where a short invader strand can control the folding state of a hairpin via hybridization to the stem.<sup>55</sup> The chemical state of the invader (active or inactive) controls the folding state of the target, thus behaving as an actuator that converts the chemical energy of the fuel into a conformational change. We installed the modified Thymine in the inner part of the sequence (I-1, Figure 4) or at the 5' end (I-2, Figure 4). We determined the  $T_m$  of the hairpin in the presence of 2 equivalents of invader strands. I-1 showed the most drastic destabilization, with a decrease of  $11.4^\circ\text{C}$  of the melting temperature compared to the unmodified control I-0. On the other hand, I-2 showed only a modest decrease in the stability of the duplex due to a minor relevance of the 5' end base to the overall 12bp duplex.

Next, we tested the system's response to chemical fuel and quantified the hairpin's degree of folding by monitoring the fluorescence intensity of the dual-labeled construct. We performed all experiments at  $36^\circ\text{C}$ , i.e., above the melting temperature of I-1 and close to the  $T_m$  of I-0 and I-2. The invader strand displaces the stem of the hairpin and forces it to open, increasing the fluorescence signal. Upon adding fuel, I-1 immediately shows an increase of the fraction open due to the invasion of the double-stranded region, moving from 0.13 to 0.21. The signal increases for 5 minutes and gradually decreases over 1 h. Similarly, I-2 is responsive to the fuel and induces an increase in the open fraction of the hairpin, even though it did not significantly decrease the stability of the duplex in its precursor state. The formation of the more hydrophobic anhydride likely promotes  $\pi$ -stacking interactions and, potentially, intercalation of planar phthalic anhydride, stabilizing the duplex even at the 5'-end. The scavenger consumes the fuel within 20 min after its addition, but an

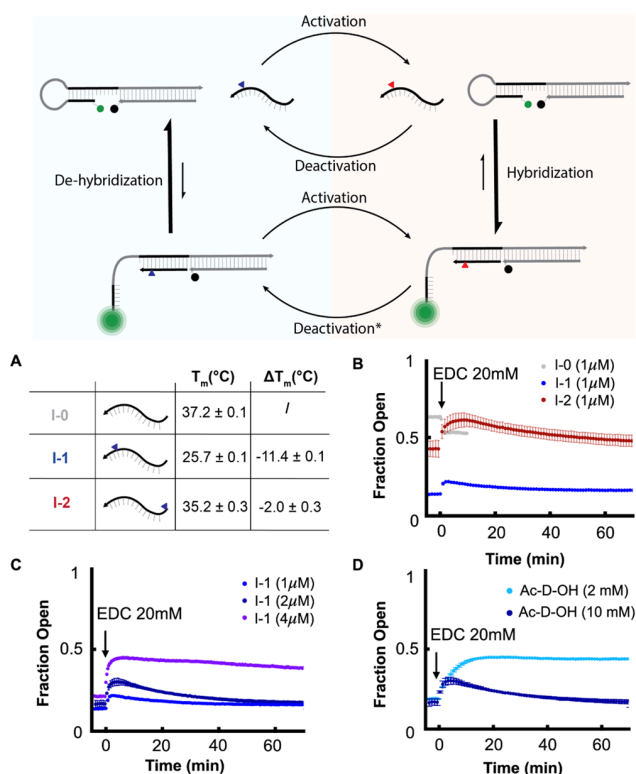


**Figure 4.** Chemically Fueled Strand Displacement. Schematic representation of the strand displacement circuit used in the experiments. (A) Melting temperature of the hairpin with invader strand (Hairpin  $0.5 \mu\text{M}$ , I-1, I-2, I-0  $1 \mu\text{M}$ ; the melting temperature refers to the transition for the dissociation of the Hairpin-Invader duplex). (B) Evolution of open fraction of the hairpin ( $0.5 \mu\text{M}$ ) with I-0 ( $1 \mu\text{M}$ , gray), I-1 ( $1 \mu\text{M}$ , blue), and I-2 ( $1 \mu\text{M}$ , red) when  $20 \text{ mM}$  of EDC are added. Buffer MES  $200 \text{ mM}$ , pH 5.6, Ac-D-OH  $10 \text{ mM}$ , ( $T = 36 \text{ }^\circ\text{C}$ ). (C) Evolution of the open fraction of the hairpin when an increasing amount of I-1 ( $1 \mu\text{M}$  blue,  $2 \mu\text{M}$  dark blue,  $4 \mu\text{M}$  violet) is fueled with  $20 \text{ mM}$  EDC. (D) Effect of different amounts of Ac-D-OH ( $10 \text{ mM}$  dark blue,  $2 \text{ mM}$  cyan) on strand displacement with I-1 ( $1 \mu\text{M}$ ). Measurement was performed at  $36 \text{ }^\circ\text{C}$ . Error bars are the standard deviations of duplicate experiments.

increased fluorescence signal can still be measured until 40 min from fuel addition for I-1. Indeed, we could detect by HPLC (Figure S9) the presence of the anhydride on the strand at 40 min. The combined evidence points toward hybridization acting as a protection mechanism that slows down the anhydride hydrolysis. It further corroborates that the anhydride resides in a more hydrophobic environment, such as the bases' interface or the helix's inner part. The unmodified strand I-0, as a control, shows a permanent decrease in the open fraction of the hairpin, probably due to the change in the ionic strength of the medium caused by the fuel and waste.

We tested the effect of an increasing concentration of invader strands (Figure 4C) and a lower concentration of scavenger (Figure 4D). A higher concentration of invader strand ( $4 \mu\text{M}$  of I-1 instead of  $1 \mu\text{M}$ ) leads to a higher concentration of activated invader, which increased the open fraction of the hairpin when  $20 \text{ mM}$  of EDC was supplied (Figure 4C). Moreover, the open state persisted much longer as more anhydride can be protected by hybridization. Likewise, when the amount of scavenger is reduced from  $10 \text{ mM}$  (standard conditions) to  $2 \text{ mM}$ , the system's response to the fuel increases the efficiency of strand displacement. According

to our kinetic model, the maximum yield of anhydride is only slightly higher, with a lower concentration of Ac-D-OH. However, the concentration of the active strand can be sustained for much longer since the fuel is only slowly depleted. Indeed, with  $2 \text{ mM}$  of scavenger, the open fraction increases over 15 min before plateauing (Figure 4D). In contrast, with  $10 \text{ mM}$  of scavenger, the open fraction declines after 5 min.

The strand displacement experiments above demonstrate that our chemical reaction cycle can be used to control the secondary structure of a target DNA construct by modulating the affinity of a complementary strand. In the case of the unimolecular system, there is no delay between fuel consumption and the secondary structure change. In contrast, with the bimolecular system, we have evidence of a mechanism for protecting the active state, thereby suggesting a dependence of the reaction rates of the cycle on the conformational state. In other words, the horizontal pathways in Figure 4 differ from top to bottom. The reason why the same effect is not detected on the unimolecular hairpin is most likely because of the different kinetics of unfolding. It is known that a longer duplex has slower dissociation kinetics, with half-lives that range from minutes for a 10-mer to hundreds of years for a 20-mer.<sup>56</sup> The hairpin used in the first part of the work has a stem of 5 bp. Therefore, the active state will constantly be exposed to the solvent because of the rapid equilibration of the hairpin between the two states. In contrast, we can expect the duplex resulting from strand invasion -12nt- not to undergo such a fast exchange, and therefore, the active state can be protected.

## CONCLUSIONS

In this work, we bridged the field of DNA nanotechnology and chemical-fueled self-assembly. We implemented a chemical reaction cycle based on a carbodiimide fuel to control the hybridization of DNA in both uni- and a bimolecular setting. We used a non-natural nucleotide functionalized with a dicarboxylic acid that undergoes the reaction cycle. The formation of the neutral and planar anhydride increases the strand's affinity for hybridization. The main difference from previous works on the autonomous or dissipative actuation of DNA is in the way energy is used.

In our work, the DNA structure plays an active role in the fuel-to-waste conversion, and the high energy state is, per se, thermodynamically not stable. In general, this approach is conceptually similar to the operational mode of biomolecular machines in the sense that the energy of a chemical fuel—an abiotic one in our case—is used to drive a conformational change of the device in a nonequilibrium fashion. The system presented in this work is not in itself a molecular machine but rather a strategy to potentially actuate DNA nanodevices in an out-of-equilibrium fashion. We envision that implementing this strategy in more complex supramolecular structures, such as DNA origami, allows us to develop machines that can convert chemical energy into work. Crucial to perform work is to overcome two challenges. First, we characterize the ratcheting constant,<sup>57,58</sup> which is a measure of the degree of kinetic asymmetry. In other words, we determine whether the rate of fuel consumption and deactivation change between the two states of the system. We know that the modified oligonucleotide is an active element in the dissipation process, which constitutes the first necessary requirement for kinetic asymmetry, and we have the first evidence that the rate of deactivation is lower in the hybridized state than on the free

strand. Additionally, the carbodiimide reaction cycle has proven successful in operating information ratchets<sup>44–46,59</sup> that are fundamentally based on kinetic asymmetry. The second challenge is related to the operational conditions of the system. The activation of a single modification induces a moderate change in the melting temperature, but the coupling of several modifications strategically placed in a modular object, such as a DNA Origami, would multiply the effect upon activation. The presence of divalent cations required for DNA Origami, which is detrimental for our system, can be avoided by stabilization of the nanostructure to survive at low-ionic strength environments<sup>60–63</sup> better suited for the effective performance of our reaction cycle. Taken together, we will install multiple modified thymines in DNA nanostructures to develop a machine that converts chemical energy into work.

## ■ ASSOCIATED CONTENT

### SI Supporting Information

The Supporting Information is available free of charge at <https://pubs.acs.org/doi/10.1021/jacs.2c08463>.

Materials and methods description, additional fluorescence data, and HPLC data (PDF)

## ■ AUTHOR INFORMATION

### Corresponding Author

**Job Boekhoven** – School of Natural Sciences, Department of Chemistry, Technical University of Munich, Garching 85748, Germany; [orcid.org/0000-0002-9126-2430](https://orcid.org/0000-0002-9126-2430);  
Email: [job.boekhoven@tum.de](mailto:job.boekhoven@tum.de)

### Authors

**Michele Stasi** – School of Natural Sciences, Department of Chemistry, Technical University of Munich, Garching 85748, Germany

**Alba Monferrer** – School of Natural Sciences, Department of Physics, Technical University of Munich, Garching 85748, Germany; Munich Institute of Biomedical Engineering, Technical University of Munich, Garching 85748, Germany

**Leon Babl** – Max Planck Institute of Biochemistry, Martinsried 82152, Germany

**Sreekar Wunnava** – Center for NanoScience (CeNS) and Systems Biophysics, Ludwig-Maximilian University Munich, Munich 80799, Germany

**Christina Felicitas Dirscherl** – Center for NanoScience (CeNS) and Systems Biophysics, Ludwig-Maximilian University Munich, Munich 80799, Germany

**Dieter Braun** – Center for NanoScience (CeNS) and Systems Biophysics, Ludwig-Maximilian University Munich, Munich 80799, Germany; [orcid.org/0000-0001-7751-1448](https://orcid.org/0000-0001-7751-1448)

**Petra Schwill** – Max Planck Institute of Biochemistry, Martinsried 82152, Germany; [orcid.org/0000-0002-6106-4847](https://orcid.org/0000-0002-6106-4847)

**Hendrik Dietz** – School of Natural Sciences, Department of Physics, Technical University of Munich, Garching 85748, Germany; Munich Institute of Biomedical Engineering, Technical University of Munich, Garching 85748, Germany; [orcid.org/0000-0003-1270-3662](https://orcid.org/0000-0003-1270-3662)

Complete contact information is available at: <https://pubs.acs.org/doi/10.1021/jacs.2c08463>

## Author Contributions

The manuscript was written through the contributions of all authors. All authors have approved the final version of the manuscript.

## Notes

The authors declare no competing financial interest.

## ■ ACKNOWLEDGMENTS

J.B. and H.D. are grateful for support from the TUM Innovation Network—RISE, funded through the Excellence Strategy. This research was conducted within the Max Planck School Matter to Life, supported by the German Federal Ministry of Education and Research (BMBF) in collaboration with the Max Planck Society. J.B. is grateful for funding from the European Research Council (ERC Starting Grant 852187) and the Deutsche Forschungsgemeinschaft (DFG, German Research Foundation) under Germany's Excellence Strategy—EXC-2094—390783311 and project 411722921. H.D. is grateful for funding from the European Research Council (ERC Consolidator Grant 724261). This project has received funding from the European Union's Horizon 2020 Research and Innovation Program under the Marie Skłodowska-Curie Grant Agreement No. 765703 (to H.D. and A.M.). J.B. is grateful for an extensive discussion with R. Dean Astumian (Univ. Maine).

## ■ ABBREVIATIONS USED

EDC 1-ethyl-3-(3-dimethylaminopropyl) carbodiimide  
EDU 1-(3-(dimethylamino)propyl)-3-ethylurea  
Ac-D-OH N-acetyl aspartic acid

## ■ REFERENCES

- (1) Rothmund, P. W. K. Folding DNA to create nanoscale shapes and patterns. *Nature* **2006**, *440*, 297–302.
- (2) Douglas, S. M.; Dietz, H.; Liedl, T.; Högberg, B.; Graf, F.; Shih, W. M. Self-assembly of DNA into nanoscale three-dimensional shapes. *Nature* **2009**, *459*, 414–418.
- (3) Dietz, H.; Douglas, S. M.; Shih, W. M. Folding DNA into Twisted and Curved Nanoscale Shapes. *Science* **2009**, *325*, 725.
- (4) Hong, F.; Zhang, F.; Liu, Y.; Yan, H. DNA Origami: Scaffolds for Creating Higher Order Structures. *Chem. Rev.* **2017**, *117*, 12584–12640.
- (5) Dong, J.; Zhou, C.; Wang, Q. Towards Active Self-Assembly Through DNA Nanotechnology. *Top. Curr. Chem.* **2020**, *378*, No. 33.
- (6) Teller, C.; Willner, I. Functional nucleic acid nanostructures and DNA machines. *Curr. Opin. Biotechnol.* **2010**, *21*, 376–391.
- (7) Ramezani, H.; Dietz, H. Building machines with DNA molecules. *Nat. Rev. Genet.* **2020**, *21*, 5–26.
- (8) Gerling, T.; Wagenbauer, K. F.; Neuner, A. M.; Dietz, H. Dynamic DNA devices and assemblies formed by shape-complementary, non-base pairing 3D components. *Science* **2015**, *347*, 1446.
- (9) Pumm, A.-K.; Engelen, W.; Kopperger, E.; Isensee, J.; Vogt, M.; Kozina, V.; Kube, M.; Honemann, M. N.; Bertolin, E.; Langecker, M.; Golestanian, R.; Simmel, F. C.; Dietz, H. A DNA origami rotary ratchet motor. *Nature* **2022**, *607*, 492–498.
- (10) Bertolin, E.; Maffeo, C. M.; Drexler, T.; Honemann, M. N.; Aksimentiev, A.; Dietz, H. A nanoscale reciprocating rotary mechanism with coordinated mobility control. *Nat. Commun.* **2021**, *12*, No. 7138.
- (11) Zhang, D. Y.; Winfree, E. Control of DNA Strand Displacement Kinetics Using Toehold Exchange. *J. Am. Chem. Soc.* **2009**, *131*, 17303–17314.
- (12) Simmel, F. C.; Yurke, B.; Singh, H. R. Principles and Applications of Nucleic Acid Strand Displacement Reactions. *Chem. Rev.* **2019**, *119*, 6326–6369.

- (13) Li, J.; Johnson-Buck, A.; Yang, Y. R.; Shih, W. M.; Yan, H.; Walter, N. G. Exploring the speed limit of toehold exchange with a cartwheeling DNA acrobat. *Nat. Nanotechnol.* **2018**, *13*, 723–729.
- (14) Zhang, D. Y.; Seelig, G. Dynamic DNA nanotechnology using strand-displacement reactions. *Nat. Chem.* **2011**, *3*, 103–113.
- (15) Del Grosso, E.; Ragazzon, G.; Prins, L. J.; Ricci, F. Fuel-Responsive Allosteric DNA-Based Aptamers for the Transient Release of ATP and Cocaine. *Angew. Chem., Int. Ed.* **2019**, *58*, 5582–5586.
- (16) Gentile, S.; Del Grosso, E.; Prins, L. J.; Ricci, F. Reorganization of Self-Assembled DNA-Based Polymers using Orthogonally Addressable Building Blocks. *Angew. Chem., Int. Ed.* **2021**, *60*, 12911–12917.
- (17) Groeer, S.; Walther, A. Switchable supracolloidal 3D DNA origami nanotubes mediated through fuel/antifuel reactions. *Nanoscale* **2020**, *12*, 16995–17004.
- (18) Kuzyk, A.; Yang, Y.; Duan, X.; Stoll, S.; Govorov, A. O.; Sugiyama, H.; Endo, M.; Liu, N. A light-driven three-dimensional plasmonic nanosystem that translates molecular motion into reversible chiroptical function. *Nat. Commun.* **2016**, *7*, No. 10591.
- (19) Del Grosso, E.; Ponzio, I.; Ragazzon, G.; Prins, L. J.; Ricci, F. Disulfide-Linked Allosteric Modulators for Multi-cycle Kinetic Control of DNA-Based Nanodevices. *Angew. Chem., Int. Ed.* **2020**, *59*, 21058–21063.
- (20) Del Grosso, E.; Prins, L. J.; Ricci, F. Transient DNA-Based Nanostructures Controlled by Redox Inputs. *Angew. Chem., Int. Ed.* **2020**, *59*, 13238–13245.
- (21) Göpflich, K.; Urban, M. J.; Frey, C.; Platzman, I.; Spatz, J. P.; Liu, N. Dynamic Actuation of DNA-Assembled Plasmonic Nanostructures in Microfluidic Cell-Sized Compartments. *Nano Lett.* **2020**, *20*, 1571–1577.
- (22) Heinen, L.; Walther, A. Temporal control of i-motif switch lifetimes for autonomous operation of transient DNA nanostructures. *Chem. Sci.* **2017**, *8*, 4100–4107.
- (23) Mariottini, D.; Del Giudice, D.; Ercolani, G.; Di Stefano, S.; Ricci, F. Dissipative operation of pH-responsive DNA-based nanodevices. *Chem. Sci.* **2021**, *12*, 11735–11739.
- (24) Marras, A. E.; Shi, Z.; Lindell, M. G.; Patton, R. A.; Huang, C.-M.; Zhou, L.; Su, H.-J.; Arya, G.; Castro, C. E. Cation-Activated Avidity for Rapid Reconfiguration of DNA Nanodevices. *ACS Nano* **2018**, *12*, 9484–9494.
- (25) Lauback, S.; Mattioli, K. R.; Marras, A. E.; Armstrong, M.; Rudibaugh, T. P.; Sooryakumar, R.; Castro, C. E. Real-time magnetic actuation of DNA nanodevices via modular integration with stiff micro-levers. *Nat. Commun.* **2018**, *9*, No. 1446.
- (26) Kopperger, E.; List, J.; Madhira, S.; Rothfischer, F.; Lamb, D. C.; Simmel, F. C. A self-assembled nanoscale robotic arm controlled by electric fields. *Science* **2018**, *359*, 296–301.
- (27) Ranallo, S.; Sorrentino, D.; Ricci, F. Orthogonal regulation of DNA nanostructure self-assembly and disassembly using antibodies. *Nat. Commun.* **2019**, *10*, No. 5509.
- (28) Green, L. N.; Subramanian, H. K. K.; Mardanlou, V.; Kim, J.; Hariadi, R. F.; Franco, E. Autonomous dynamic control of DNA nanostructure self-assembly. *Nat. Chem.* **2019**, *11*, 510–520.
- (29) Yehl, K.; Mugler, A.; Vivek, S.; Liu, Y.; Zhang, Y.; Fan, M.; Weeks, E. R.; Salaita, K. High-speed DNA-based rolling motors powered by RNase H. *Nat. Nanotechnol.* **2016**, *11*, 184–190.
- (30) Deng, J.; Walther, A. Fuel-Driven Transient DNA Strand Displacement Circuitry with Self-Resetting Function. *J. Am. Chem. Soc.* **2020**, *142*, 21102–21109.
- (31) Deng, J.; Walther, A. Pathway Complexity in Fuel-Driven DNA Nanostructures with Autonomous Reconfiguration of Multiple Dynamic Steady States. *J. Am. Chem. Soc.* **2020**, *142*, 685–689.
- (32) Feng, Y.; Ovalle, M.; Seale, J. S. W.; Lee, C. K.; Kim, D. J.; Astumian, R. D.; Stoddart, J. F. Molecular Pumps and Motors. *J. Am. Chem. Soc.* **2021**, *143*, 5569–5591.
- (33) Del Grosso, E.; Franco, E.; Prins, L. J.; Ricci, F. Dissipative DNA nanotechnology. *Nat. Chem.* **2022**, *14*, 600–613.
- (34) Deng, J.; Walther, A. Autonomous DNA nanostructures instructed by hierarchically concatenated chemical reaction networks. *Nat. Commun.* **2021**, *12*, No. 5132.
- (35) Deng, J.; Liu, W.; Sun, M.; Walther, A. Dissipative Organization of DNA Oligomers for Transient Catalytic Function. *Angew. Chem., Int. Ed.* **2022**, *61*, No. e202113477.
- (36) Deng, J.; Walther, A. Programmable ATP-Fueled DNA Coacervates by Transient Liquid-Liquid Phase Separation. *Chem* **2020**, *6*, 3329–3343.
- (37) Del Grosso, E.; Irmisch, P.; Gentile, S.; Prins, L. J.; Seidel, R.; Ricci, F. Dissipative Control over the Toehold-Mediated DNA Strand Displacement Reaction. *Angew. Chem., Int. Ed.* **2022**, *61*, No. e202201929.
- (38) Boekhoven, J.; Hendriksen, W. E.; Koper, G. J.; Eelkema, R.; van Esch, J. H. Transient assembly of active materials fueled by a chemical reaction. *Science* **2015**, *349*, 1075–1079.
- (39) Tena-Solsona, M.; Riess, B.; Grotsch, R. K.; Lohrer, F. C.; Wanzke, C.; Kasdorf, B.; Bausch, A. R.; Müller-Buschbaum, P.; Lieleg, O.; Boekhoven, J. Non-equilibrium dissipative supramolecular materials with a tunable lifetime. *Nat. Commun.* **2017**, *8*, No. 15895.
- (40) Dai, K.; Fores, J. R.; Wanzke, C.; Winkeljann, B.; Bergmann, A. M.; Lieleg, O.; Boekhoven, J. Regulating Chemically Fueled Peptide Assemblies by Molecular Design. *J. Am. Chem. Soc.* **2020**, *142*, 14142–14149.
- (41) Kriebisch, B. A. K.; Jussupow, A.; Bergmann, A. M.; Kohler, F.; Dietz, H.; Kaila, V. R. I.; Boekhoven, J. Reciprocal Coupling in Chemically Fueled Assembly: A Reaction Cycle Regulates Self-Assembly and Vice Versa. *J. Am. Chem. Soc.* **2020**, *142*, 20837–20844.
- (42) Späth, F.; Donau, C.; Bergmann, A. M.; Kranzlein, M.; Synatschke, C. V.; Rieger, B.; Boekhoven, J. Molecular Design of Chemically Fueled Peptide-Polyelectrolyte Coacervate-Based Assemblies. *J. Am. Chem. Soc.* **2021**, *143*, 4782–4789.
- (43) Wanzke, C.; Jussupow, A.; Kohler, F.; Dietz, H.; Kaila, V. R. I.; Boekhoven, J. Dynamic Vesicles Formed by Dissipative Self-Assembly. *ChemSystemsChem* **2020**, *2*, No. e1900044.
- (44) Borsley, S.; Leigh, D. A.; Roberts, B. M. W. A Doubly Kinetically-Gated Information Ratchet Autonomously Driven by Carbodiimide Hydration. *J. Am. Chem. Soc.* **2021**, *143*, 4414–4420.
- (45) Borsley, S.; Kreidt, E.; Leigh, D. A.; Roberts, B. M. W. Autonomous fuelled directional rotation about a covalent single bond. *Nature* **2022**, *604*, 80–85.
- (46) Borsley, S.; Leigh, D. A.; Roberts, B. M. W.; Vitorica-Yrezabal, I. J. Tuning the Force, Speed, and Efficiency of an Autonomous Chemically Fueled Information Ratchet. *J. Am. Chem. Soc.* **2022**, *144*, 17241–17248.
- (47) Kariyawasam, L. S.; Hartley, C. S. Dissipative Assembly of Aqueous Carboxylic Acid Anhydrides Fueled by Carbodiimides. *J. Am. Chem. Soc.* **2017**, *139*, 11949–11955.
- (48) Schnitter, F.; Bergmann, A. M.; Winkeljann, B.; Rodon Fores, J.; Lieleg, O.; Boekhoven, J. Synthesis and characterization of chemically fueled supramolecular materials driven by carbodiimide-based fuels. *Nat. Protoc.* **2021**, *16*, 3901–3932.
- (49) Tena-Solsona, M.; Janssen, J.; Wanzke, C.; Schnitter, F.; Park, H.; Rieß, B.; Gibbs, J. M.; Weber, C. A.; Boekhoven, J. Accelerated Ripening in Chemically Fueled Emulsions\*\*. *ChemSystemsChem* **2021**, *3*, No. e2000034.
- (50) Schnitter, F.; Boekhoven, J. A Method to Quench Carbodiimide-Fueled Self-Assembly. *ChemSystemsChem* **2021**, *3*, No. e2000037.
- (51) Tsukanov, R.; Tomov, T. E.; Berger, Y.; Liber, M.; Nir, E. Conformational Dynamics of DNA Hairpins at Millisecond Resolution Obtained from Analysis of Single-Molecule FRET Histograms. *J. Phys. Chem. B* **2013**, *117*, 16105–16109.
- (52) Wallace, M. I.; Ying, L.; Balasubramanian, S.; Klenerman, D. Non-Arrhenius kinetics for the loop closure of a DNA hairpin. *Proc. Natl. Acad. Sci. U.S.A.* **2001**, *98*, 5584–5589.
- (53) Grunwell, J. R.; Glass, J. L.; Lacoste, T. D.; Deniz, A. A.; Chemla, D. S.; Schultz, P. G. Monitoring the Conformational

Fluctuations of DNA Hairpins Using Single-Pair Fluorescence Resonance Energy Transfer. *J. Am. Chem. Soc.* **2001**, *123*, 4295–4303.

(54) Yamagami, R.; Bingaman, J. L.; Frankel, E. A.; Bevilacqua, P. C. Cellular conditions of weakly chelated magnesium ions strongly promote RNA stability and catalysis. *Nat. Commun.* **2018**, *9*, No. 2149.

(55) Adam, V.; Prusty, D. K.; Centola, M.; Škugor, M.; Hannam, J. S.; Valero, J.; Klöckner, B.; Famulok, M. Expanding the Toolbox of Photoswitches for DNA Nanotechnology Using Arylazopyrazoles. *Chem. – Eur. J.* **2018**, *24*, 1062–1066.

(56) Morrison, L. E.; Stols, L. M. Sensitive fluorescence-based thermodynamic and kinetic measurements of DNA hybridization in solution. *Biochemistry* **1993**, *32*, 3095–3104.

(57) Astumian, R. D. Kinetic asymmetry allows macromolecular catalysts to drive an information ratchet. *Nat. Commun.* **2019**, *10*, No. 3837.

(58) Das, K.; Gabrielli, L.; Prins, L. J. Chemically Fueled Self-Assembly in Biology and Chemistry. *Angew. Chem., Int. Ed.* **2021**, *60*, 20120–20143.

(59) Mo, K.; Zhang, Y.; Dong, Z.; Yang, Y.; Ma, X.; Feringa, B. L.; Zhao, D. Intrinsically unidirectional chemically fuelled rotary molecular motors. *Nature* **2022**, *609*, 293–298.

(60) Bertolin, E.; Stömmer, P.; Feigl, E.; Wenig, M.; Honemann, M. N.; Dietz, H. Cryo-Electron Microscopy and Mass Analysis of Oligolysine-Coated DNA Nanostructures. *ACS Nano* **2021**, *15*, 9391–9403.

(61) Ponnuswamy, N.; Bastings, M. M. C.; Nathwani, B.; Ryu, J. H.; Chou, L. Y. T.; Vinther, M.; Li, W. A.; Anastassacos, F. M.; Mooney, D. J.; Shih, W. M. Oligolysine-based coating protects DNA nanostructures from low-salt denaturation and nuclease degradation. *Nat. Commun.* **2017**, *8*, No. 15654.

(62) Gerling, T.; Kube, M.; Kick, B.; Dietz, H. Sequence-programmable covalent bonding of designed DNA assemblies. *Sci. Adv.* **2018**, *4*, No. eaau1157.

(63) Rajendran, A.; Endo, M.; Katsuda, Y.; Hidaka, K.; Sugiyama, H. Photo-Cross-Linking-Assisted Thermal Stability of DNA Origami Structures and Its Application for Higher-Temperature Self-Assembly. *J. Am. Chem. Soc.* **2011**, *133*, 14488–14491.

## Recommended by ACS

### DNA-Based Molecular Machines

Xiuhai Mao, Xiaolei Zuo, *et al.*

OCTOBER 21, 2022  
JACS AU

READ 

### Programming Dissipation Systems by DNA Timer for Temporally Regulating Enzyme Catalysis and Nanostructure Assembly

Zhaohui Qin, Xin Su, *et al.*

SEPTEMBER 14, 2022  
ACS NANO

READ 

### Reaction–Diffusion Patterning of DNA-Based Artificial Cells

Adrian Leathers, Lorenzo Di Michele, *et al.*

SEPTEMBER 14, 2022  
JOURNAL OF THE AMERICAN CHEMICAL SOCIETY

READ 

### Self-Assembly of DNA Tiles with G-Quadruplex DNzyme Catalytic Activity for Sensing Applications

Lin Wang, Simon Chi-Chin Shiu, *et al.*

AUGUST 02, 2022  
ACS APPLIED BIO MATERIALS

READ 

Get More Suggestions >



